NONEQUILIBRIUM DYNAMICS OF DRIVEN DISSIPATIVE RYDBERG GASES

Dissertation

Fabian Letscher

Vom Fachbereich Physik der Technischen Universität Kaiserslautern zur Verleihung
des akademischen Grades „Doktor der Naturwissenschaften“ genehmigte Dissertation

Betreuer: Prof. Dr. Michael Fleischhauer
Zweitgutachter: Prof. Dr. Herwig Ott
Drittgutachter: Prof. Dr. Igor Lesanovsky

Datum der wissenschaftlichen Aussprache: 18.05.2018

D 386

Contents

Contents 3

Abstract 5

Kurzfassung 7

1 Introduction 11
- 1.1 Open Quantum Systems 11
- 1.2 Rydberg Atoms 19
- 1.3 Fractional Quantum Hall Effect 22

2 Bistability vs. Metastability 27
- 2.1 Bistability in Open Quantum Systems 30
- 2.2 Characterization of the Experiment 36
- 2.3 Single Cluster Model & Dynamics in a 1D lattice 42
- 2.4 Experimental Results & Cluster Dynamics in 3D Lattices 50

3 Hole Dynamics in a Chain of Rydberg Superatoms 61
- 3.1 1D Chain of Superatoms 62
- 3.2 Transient Relaxation Dynamics 71
- 3.3 Steady State Hole Dynamics 73

4 Anomalous Excitation Facilitation 81
- 4.1 Two Particle Dynamics: Usual Case 81
- 4.2 Inhomogeneous Broadening 83
- 4.3 Two & Many Particle Dynamics: Anomalous Case 84

5 Mobile Bound States of Rydberg Excitations in a Lattice 89
- 5.1 Extended XXZ Model 90
- 5.2 Effective Rydberg-dressed Spin Lattice Model 91
- 5.3 Magnon Dynamics and Bound States 102

5.4 Experimental Considerations 107

6 Laughlin State Preparation for Cavity Rydberg Polaritons 111

6.1 Photonic Cavity Setup and Rydberg Polaritons 112

6.2 Growing Scheme 116

6.3 Flux Insertion in a Photonic Cavity 118

6.4 Exact Diagonalization of Small Systems 127

List of publications 131

Appendices 135

A A single atom in an optical lattice 135

References 137

Lebenslauf 151

Danksagung 153

Abstract

More than 20 years ago, the first Bose-Einstein condensate was observed experimentally [1]. This marked the beginning of a new research area in physics focusing on quantum gases in the regime of ultracold temperatures. While first experiments demonstrated the coherent control on the single particle level, nowadays we reach a regime of realizing interesting many-body states of atomic matter [2, 3]. Solid state systems typically lack the potential to coherently control and manipulate the system parameters at will and they are moreover impure. In contrast to this, quantum gases allow to realize condensed matter analogues with high precision and control. To give an example, single atoms or arrays of single atoms can be trapped in configurable lattice structures [4, 5]. Their internal states can be controlled and detected locally providing a full state tomography.

For many applications such as quantum computation [6–9] and quantum simulation [10–12] long coherence times are essential. To this end, much progress has been done in isolating quantum systems from their environment. Another compelling approach is to incorporate the coupling to the environment or even to engineer a proper environment to stabilize interesting quantum states. This is the research area of open many-body systems. In particular, the competition between reservoir coupling and external drive with the internal atomic interactions may lead to steady states exhibiting novel properties, which lie beyond possible realizations in solid state systems. Therefore, it is of current interest to study nonequilibrium steady states, their relaxation dynamics as well as possible critical behavior.

A particularly interesting platform exploiting strong and quasi long-range interactions are Rydberg atoms [13]. On the one hand, these systems are inherently open as their internal states are controlled by an external coherent laser field and the finite Rydberg state lifetime. On the other hand, the large dipole-dipole interactions between Rydberg states offer the study of many-body systems. This makes them an ideal platform to study quantum optics [14–17], ultracold chemistry [18–20] and many-body physics of correlated matter [21, 22]. One consequence of the strong interactions between Rydberg states manifests itself in the so-called dipole blockade [23, 24]. Here, a single Rydberg atom suppresses the excitation of neighboring atoms to the Rydberg state within a certain volume. This regime was studied extensively over the past years and the creation of long-range ordered states was investigated. In turn, the presence of a Rydberg excitation can also enhance the atomic transition rates. This is the so called antiblockade regime [25, 26], where an off-resonant excitation laser compensates the Rydberg induced level shift.

In the present thesis, I will study nonequilibrium dynamics of driven dissipative Rydberg gases. Starting with an introduction of the basic concepts used throughout this thesis, I discuss Rydberg gases in the antiblockade regime. Based on an experiment-theory collaboration with the group of Herwig Ott, the possibility of a bistable phase in an open many-body system is explored. The experiment analyzes the excitation dynamics of large Rydberg lattice gases using a continuous off-resonant laser excitation. I contribute to the characterization of the experiment and develop a simple model for understanding the highly correlated excitation dynamics. The results indicate that the system consists of many small excitation clusters, which are incompatible with a phase transition to a global bistable phase. However, the prolongation of the characteristic timescale indicates that the system is in a metastable state. I support the experimental results with numerical simulations obtaining qualitative and partially quantitative agreement.

The dipole blockade of a mesoscopic atomic ensemble represents an effective spin model and leads to the concept of a superatom. In the regime of strong dissipation, the excitation rates to the single excited Rydberg state are collectively enhanced. I study a regular array of these superatoms in the antiblockade regime resulting in a high, almost universal, Rydberg excitation density 2/3. Furthermore, I characterize the transient relaxation towards the steady state exploiting a coarse-grained excitation model and the steady state itself. It is shown that the non-trivial nonequilibrium dynamics can be understood in terms of excitation holes, i.e., ground state atoms surrounded by two excited superatoms. Numerical simulations were performed using a newly developed superatom rate equation model.

The superatom concept already shows that the impact of dissipation and dense atomic ensembles can lead to exaggerated excitation dynamics compared to the few particle case. This leads to an anomalous facilitation mechanism in an inhomogeneously broadened Rydberg gas. It is shown that facilitation is possible although the detuning does not compensate the interaction-induced level shift.

A key tool to the investigation of coherent lattice spin models is a controllable interaction strength. I discuss the realization of a tunable XXZ model using Rydberg atoms and the existence of mobile bound states of Rydberg excitations. It is shown that this spin model can be realized by a regular array of driven atoms, where the excited state represents the spin-up state and a Rydberg-dressed ground state the spin-down state. I discuss bound states of excitations and their increased mobility due to resonant two-site hopping processes. The increased mobility allows to study the competition between kinetic and interaction effects, which was however not subject of the present thesis.

While photons do barely interact with each other, the coupling to Rydberg states in a configuration supporting electromagnetically induced transparency, allows to transfer the strong interactions to a mixture of matter and quantized light – a Rydberg polariton. Recent progress in the field of artificial gauge fields demonstrated the creation of photonic Landau levels in a twisted cavity setup. The combination of both, strong interactions and artificial magnetic fields in a photonic cavity, is a promising setup for the preparation of fractional quantum Hall states for photons. To this end, a growing scheme is discussed, which consists of adiabatic transfer of flux quanta using a dense atomic medium as a mediator and a single photon pump.

Kurzfassung

Vor über 20 Jahren wurde das erste Bose-Einstein Kondensat experimentell beobachtet [1]. Dies eröffnete das neue Forschungsfeld der ultrakalten Quantengase. Bereits erste Experimente demonstrierten die kohärente Kontrolle eines Quantensystems auf Einteilchenebene. Heutzutage erreichen wir einen Bereich, in dem es möglich ist interessante Vielteilchenzustände der atomaren Materie zu erzeugen [2, 3]. Während viele Festkörpersysteme unrein sind und keine kohärente Kontrolle und Manipulation der Systemparameter ermöglichen, erlauben Quantengase die Realisierung von Modellen aus der kondensierten Materie mit hoher Präzision. Ein Beispiel ist das Fangen einzelner Atome und Anordnen von diesen in konfigurierbaren Gitterstrukturen [4, 5]. Eine lokale Kontrolle der internen Zustände dieser Atome erlaubt sogar eine volle Zustandstomographie.

Für viele Anwendungen, wie etwa Quantencomputer [6–9] oder Quantensimulatoren [10–12], werden lange Kohärenzzeiten benötigt. Um das zu erreichen wird versucht Quantensysteme immer besser von ihrer Umwelt zu isolieren. Ein anderer beeindruckender Ansatz befasst sich mit offenen Vielteilchensystemen und nimmt dabei die Umgebung mit in die Beschreibung des Systems auf oder versucht eine Umgebung zu schaffen, die interessante Quantenzustände erzeugen kann. Insbesondere das Zusammenspiel zwischen externer Kopplung und der Wechselwirkung mit einer Umgebung gegenüber den internen atomaren Wechselwirkungen kann zu stationären Zuständen mit neuen Eigenschaften führen, welche in Festkörpersystemen nicht realisiert werden können. Darum ist es interessant Nichtgleichgewichtszustände, deren Relaxationsverhalten, sowie mögliches kritisches Verhalten zu studieren.

Eine besonders interessante Plattform macht sich die starke und quasi langreichweitige Wechselwirkung von Rydbergatomen zunutze [13]. Auf der einen Seite sind diese Systeme intrinsisch offen, da ihre internen Zustände mithilfe eines externen, kohärenten Lichtfeldes kontrolliert werden können und Rydbergzustände eine endliche Lebensdauer haben. Auf der anderen Seite ermöglicht die starke Dipol-Dipol-Wechselwirkung das Studium von Vielteilcheneffekten. Beides macht Rydbergatome zu einer idealen Plattform um Fragestellungen aus Quantenoptik [14–17], ultrakalter Chemie [18–20] und Vielteilchenphysik der korrelierten Materie [21, 22] zu untersuchen. Eine direkte Konsequenz aus der starken Wechselwirkung zwischen Rydbergzuständen ist die sogenannte Dipolblockade [23, 24]. Hierbei unterdrückt eine Rydberganregung die Anregung von benachbarten Grundzustandsatomen in den Rydbergzustand in einem endlichen Volumen. Dieses Phänomen wurde in den letzten Jahren ausgiebig diskutiert und die Möglichkeit langreichweitiger Ordnung wurde untersucht. Im Gegenzug dazu kann eine Rydberganregung auch zu einer erhöhten Übergangswahrscheinlichkeit führen. Dies ist das sogenannte Antiblockade-Regime [25, 26], indem eine verstimmte Laseranregung die Energieverschiebung durch den Rydbergzustand ausgleicht.

In der vorliegenden Doktorarbeit studiere ich die Nichtgleichgewichtsdynamik getriebener dissipativer Rydberggase. Nach einer Einführung in die für diese Arbeit benötigten grundlegenden Konzepte, diskutiere ich zunächst Rydberggase im Antiblockade-Regime. Basierend auf der Zusammenarbeit mit der Experimentalgruppe von Prof. Herwig Ott, wird die Möglichkeit einer bistabilen Phase in einem offenen Vielteilchensystem untersucht. Das Experiment analysiert die Anregungsdynamik von Rydbergatomen in einem Gitter unter dem Einfluss eines verstimmten kontinuierlichen Laserfeldes. Ich trage zu der Charakterisierung des Experiments, sowie der Erstellung eines vereinfachten Modells zur Erklärung der korrelierten Anregungsdynamik bei. Die Resultate deuten darauf hin, dass das System aus vielen kleinen Anregungsclustern besteht, was im Gegensatz zu einer globalen, bistabilen Phase steht. Die Zunahme der charakteristischen Zeitskala lässt darauf schließen, dass das System in einem metastabilen Zustand ist. Die experimentellen Befunde werden durch numerische Simulationen untermauert, die sowohl qualitative als auch teilweise quantitative Übereinstimmung aufzeigen.

Die Dipolblockade eines mesoskopischen, atomaren Ensembles lässt sich auf ein effektives Spin-Modell zurückführen und wird durch das Konzept eines Superatoms beschrieben. Im Fall starker Dissipation wird die Anregungsrate zum angeregten Rydbergzustand kollektiv verstärkt. Ich studiere ein eindimensionales Gitter aus Superatomen im Antiblockade-Regime und zeige, dass die Rydberganregungsdichte einen hohen, nahezu konstanten Wert von 2/3 annimmt. Zusätzlich charakterisiere ich die Relaxation in den stationären Zustand durch ein makroskopisches Modell sowie den stationären Zustand selbst. Es zeigt sich, dass die nicht triviale Nichtgleichgewichtsdynamik durch die Einführung von Anregungslöchern, d.h. Grundzustandsatomen umgeben von je zwei benachbarten angeregten Superatomen, verstanden werden kann. Auf Basis eines neuentwickelten Superatom-Ratengleichungsmodells wurden numerische Simulationen durchgeführt.

Die Einführung eines Superatoms zeigt bereits, dass der Einfluss von Dissipation und dichter atomarer Ensembles zu interessanter Anregungsdynamik führen kann, gegenüber dem Fall weniger Teilchen. Dies zeigt sich in einem anomalen Anregungsmechanismus im Antiblockade-Regime bei inhomogen, verbreiterten Rydberggasen. Es wird gezeigt, dass die verstärkte Anregung möglich ist in einem Bereich, indem die Verstimmung des Laserfeldes nicht die Energieverschiebung durch die Wechselwirkung kompensieren kann.

Eine wichtige Eigenschaft für die Untersuchung kohärenter Spin-Modelle ist die Fähigkeit die Wechselwirkungsstärke zu regulieren. Ich diskutiere eine Realisierung eines durchstimmbaren XXZ Spin-Modells basierend auf Rydbergatomen und zeige, dass darin bewegliche, gebundene Zustände von Rydberganregungen existieren. Es wird gezeigt, dass das Spin-Modell in einem getriebenen System einer eindimensionalen atomaren Kette entsteht, wobei ein Spinzustand eine Mischung aus Grundzustand und Rydberganregung ist und der andere Spinzustand ein weiterer Rydbergzustand ist. Ich diskutiere den Einfluss langreichweitiger Hüpfprozesse auf die Beweglichkeit gebundener Zustände von Spin-Anregungen. Dies erlaubt die Untersuchung von konkurrierenden Effekten von

kinetischer Energie und Wechselwirkungsenergie, was allerdings nicht Bestandteil dieser Arbeit ist.

Während Photonen nicht miteinander wechselwirken, kann deren Ankopplung an Rydbergzustände mithilfe der elektromagnetisch induzierten Transparenz zu einer Wechselwirkung zwischen sogenannten Rydberg-Polaritonen, d.h. einer Mischung zwischen Materie und quantisiertem Licht, führen. In einem Experiment wurde gezeigt, dass künstliche Magnetfelder für Photonen und damit die Realisierung photonischer Landau-Niveaus durch geschickte Anordnung optischer Resonatoren möglich ist. Die Kombination von starker Wechselwirkung und magnetischen Feldern für Photonen in einem optischen Resonator kann die Präparation von fraktionalen Quanten-Hall-Zuständen ermöglichen. Es wird ein Protokoll zum Wachsen dieser Zustände diskutiert, welches zum einen aus dem adiabatischen Einführen von Flussquanten mittels eines dichten atomaren Mediums besteht und zum anderen aus einer Ein-Photonen-Pumpe.

Chapter 1

Introduction

1.1 Open Quantum Systems

Although many theoretical studies assume isolated quantum systems, which are decoupled from their environment, this can only be an approximation for sufficiently small timescales. In practice, there are no completely isolated quantum systems. Besides the measurement process, which in quantum mechanics projects the system to a specific state, all systems interact with their environment – a *reservoir* with many degrees of freedom. Typically, this introduces a decoherence mechanism of the system. In particular the coherent control of quantum systems required for applications, such as quantum computation and quantum simulation, poses the challenge of isolating and interacting with the system at the same time. Therefore, for quantum technology applications proper isolation is required.

In recent years, a paradigm shift occurred, which incorporates the reservoir as a tool for manipulating the system. While the coupling to the reservoir typically introduces decoherence of the system, it can also lead to novel and interesting features in the steady state of the system. Moreover, these stationary states may be more robust against perturbations compared to a pure quantum state.

Below, we introduce a description of open quantum systems. A full characterization of the interaction between reservoir and the system is challenging. Typically, we do not have knowledge about all microscopic details of the reservoir and thus the coupling to the system. The large number of degrees of freedom of the reservoir makes a solution of the system and reservoir equations of motion almost impossible. Nevertheless we can find an effective description of a system in contact with an environment without detailed knowledge of the underlying reservoir couplings. This section is based on Ref. [27–30].

1.1.1 Master Equation

Formally, system and reservoir can be described by a density matrix χ. By eliminating the degrees of freedom of the reservoir

$$\hat{\rho} = \mathrm{tr}_r\{\chi\}, \tag{1.1}$$

i.e. calculating the partial trace over all reservoir degrees of freedom, we obtain the density matrix $\hat{\rho}$ of the system. Now, $\hat{\rho}$ contains only information about the system, but not the reservoir. For $\hat{\rho}$ to be a proper density matrix, we demand the following conditions:

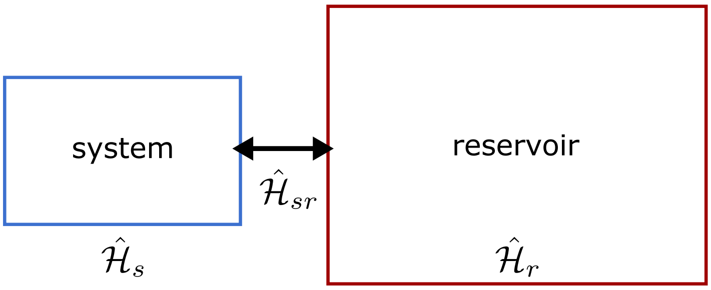

Figure 1.1: Sketch of the system-reservoir approach. It is assumed that the reservoir has many more degrees of freedom than the system. Furthermore, we assume the reservoir is in a stationary state, e.g. a thermal state.

(i) The density matrix is a hermitian operator, i.e. $\hat{\rho} = \hat{\rho}^\dagger$ and thus all eigenvalues are real.

(ii) $\hat{\rho}$ is positive semi-definite, i.e. all eigenvalues are larger or equal to zero.

(iii) We demand that

$$\mathrm{tr}\{\hat{\rho}\} \equiv \sum_n \langle \Psi_n | \, \hat{\rho} \, | \Psi_n \rangle = 1,$$

where $\{|\Psi_n\rangle\}$ is an orthogonal basis for the system. The normalization allows an interpretation in terms of probabilities. The total probability is conserved, since $\frac{\mathrm{d}}{\mathrm{d}t}\mathrm{tr}\{\hat{\rho}\} = 0$.

Using the density matrix $\hat{\rho}$ we can calculate the expectation value of all relevant physical observables $\hat{\mathcal{O}}$ with $\langle \hat{\mathcal{O}} \rangle = \mathrm{tr}\{\hat{\rho}\hat{\mathcal{O}}\}$. Two-time correlations can be calculated using the regression theorem [28].

In many quantum optical setups, the coupling to reservoirs is Markovian and thus the time evolution of the system can be described by a master equation in Lindblad form for the density matrix $\hat{\rho}$,

$$\partial_t \hat{\rho} = -\frac{i}{\hbar}[\hat{\mathcal{H}}_s, \hat{\rho}] + \frac{1}{2}\sum_\mu \left(2\hat{L}_\mu \hat{\rho} \hat{L}_\mu^\dagger - \hat{L}_\mu^\dagger \hat{L}_\mu \hat{\rho} - \hat{\rho} \hat{L}_\mu^\dagger \hat{L}_\mu \right) \equiv \mathcal{L}[\hat{\rho}]. \tag{1.2}$$

The first part accounts for the coherent evolution of the system with Hamiltonian $\hat{\mathcal{H}}_s$. The latter part includes Lindblad jump operators $\hat{L}_\mu$ describing the impact of the coupling between system and reservoir. These jump operators can be deduced from first principle calculations or may be constructed by analyzing the underlying physical processes. Examples of both will be discussed within this thesis. Now we will review the main steps and approximations in the derivation of the master equation.

Derivation of the master equation

Suppose we can describe the full system and reservoir with a Hamiltonian $\hat{\mathcal{H}} = \hat{\mathcal{H}}_s + \hat{\mathcal{H}}_r + \hat{\mathcal{H}}_{sr}$, as illustrated in Fig. 1.1. In the interaction picture, rotating with the Hamiltonian of the system $\hat{\mathcal{H}}_s$ and reservoir $\hat{\mathcal{H}}_r$, the evolution of the full system-reservoir is described by the von Neumann equation

$$\partial_t \hat{\chi}(t) = -\frac{i}{\hbar}[\hat{\mathcal{H}}_{sr}(t), \hat{\chi}(t)], \tag{1.3}$$

where $\hat{\chi}(t)$ is the density matrix for both, system and reservoir. The coupling between the system and reservoir is denoted by the Hamiltonian $\hat{\mathcal{H}}_{sr}$, as indicated in Fig. 1.1. By formally integrating Eq. (1.3) and reinserting, this equation can be rewritten as an integro-differential equation

$$\partial_t \hat{\chi}(t) = -\frac{i}{\hbar}[\hat{\mathcal{H}}_{sr}(t), \hat{\chi}(0)] - \frac{1}{\hbar^2}\int_0^t \mathrm{d}\tau \, \left[\hat{\mathcal{H}}_{sr}(t), [\hat{\mathcal{H}}_{sr}(\tau), \hat{\chi}(\tau)]\right]. \tag{1.4}$$

Let us assume that initially at time $t = 0$, system and reservoir are decoupled, i.e.

$$\hat{\chi}(0) = \hat{\rho}(0) \otimes \hat{\rho}_r(0), \tag{1.5}$$

where $\hat{\rho}_r$ is the reservoir density matrix. Since we are only interested in the system dynamics, we furthermore assume that $\mathrm{tr}_r\{[\hat{\mathcal{H}}_{sr}(t), \hat{\rho}(0) \otimes \hat{\rho}_r(0)]\} = 0$. For instance, when the reservoir is in a thermal state, this is fulfilled since the coupling elements are typically linear in the system and reservoir operators. Equation (1.4) is the starting point for further approximations:

Born approximation We assume that the system and the reservoir are weakly coupled in their time evolution. Thus, in second order of $\hat{\mathcal{H}}_{sr}$, we can set $\hat{\chi}(\tau) \simeq \hat{\rho}(\tau) \otimes \hat{\rho}_r(\tau)$. Furthermore, since the reservoir is large, having many degrees of freedom, it is almost unaltered by the coupling to the system. We assume that the reservoir stays in a stationary state and thus approximate

$$\hat{\chi}(\tau) \simeq \hat{\rho}(\tau) \otimes \hat{\rho}_r(0). \tag{1.6}$$

Markov approximation On top of that we assume that reservoir correlations decay on a timescale which is short compared to the intrinsic timescales of the system. In other words, the reservoir has no memory. In Eq. (1.4), the impact of the past is hidden in the integration over previous times $\tau \in (0, t)$. The Markov approximation assumes

$$\hat{\chi}(\tau) \simeq \hat{\rho}(t) \otimes \hat{\rho}_r(0). \tag{1.7}$$

We obtain the master equation in Born-Markov approximation by tracing over the reservoir degrees of freedom

$$\partial_t \hat{\rho}(t) = -\frac{1}{\hbar^2}\int_0^t \mathrm{d}\tau \, \mathrm{tr}_r \left\{ \left[\hat{\mathcal{H}}_{sr}(t), [\hat{\mathcal{H}}_{sr}(\tau), \hat{\rho}(t) \otimes \hat{\rho}_r(0)]\right] \right\}. \tag{1.8}$$

The validity of the approximations made above have to be justified for each specific system. For many experiments in the regime of ultracold gases, the Born-Markov approximation is justified. A further evaluation requires knowledge of the system and reservoir. For simplicity, we discuss a coupling between the reservoir and the system of the form

$$\hat{\mathcal{H}}_{sr} = \hbar \hat{S} \cdot \hat{R}, \tag{1.9}$$

where $\hat{S}$ and $\hat{R}$ are hermitian operators acting on the system and the reservoir, respectively. For generic bosonic or spin systems we refer to Ref. [28]. Inserting into Eq. (1.8), we obtain

$$\begin{aligned} \partial_t \hat{\rho}(t) = \int_0^t \mathrm{d}\tau \, \Big[& \langle \hat{R}(t)\hat{R}(\tau)\rangle \left(\hat{S}(t)\hat{\rho}(t)\hat{S}(\tau) - \hat{S}(t)\hat{S}(\tau)\hat{\rho}(t)\right) \\ & \langle \hat{R}(\tau)\hat{R}(t)\rangle \left(\hat{S}(\tau)\hat{\rho}(t)\hat{S}(t) - \hat{\rho}(t)\hat{S}(\tau)\hat{S}(t)\right) \Big]. \end{aligned} \tag{1.10}$$

Within the Markov approximation we assume that the reservoir operators are δ-correlated in time, i.e. $\langle \hat{R}(t)\hat{R}(\tau)\rangle = (\Gamma + i\Delta)\delta(t-\tau)$, where $\Gamma, \Delta \in \mathbb{R}$. Then, replacing the upper limit of the integration by $t \to \infty$, we obtain

$$\partial_t \hat{\rho}(t) = -\frac{i}{\hbar}[\hbar\Delta \hat{S}(t)\hat{S}(t), \hat{\rho}(t)] + \Gamma\big(2\hat{S}(t)\hat{\rho}(t)\hat{S}(t) - \hat{S}(t)\hat{S}(t)\hat{\rho}(t) - \hat{\rho}(t)\hat{S}(t)\hat{S}(t)\big), \tag{1.11}$$

which has the form of a Lindblad master equation (1.2). The coupling to a reservoir may result in coherent (Δ) and incoherent (Γ) contributions to the time evolution. Equation (1.2) serves as a prototype for various systems discussed within this thesis. A detailed derivation and justification for all systems presented here is beyond the scope of this thesis. Importantly, the master equation in Lindblad form preserves the properties (i)-(iii) for the density matrix $\hat{\rho}$. The Lindblad jump operators will be motivated by the underlying physical processes.

1.1.2 Rate Equation Model

Single atom dynamics

In atomic systems it is common to model the light-matter interaction using a two-level approximation. For a coherent drive with a laser in the optical wavelength regime, this is typically a good approximation when the energy difference ω_{ge} between the two relevant states, denoted by $|g\rangle$ and $|e\rangle$, is nearly resonant with the laser carrier frequency ω and all other transition frequencies are far detuned. A detailed derivation and discussion of the relevant approximations, namely the dipole and rotating wave approximation, can be found in standard textbooks, see e.g. Ref. [30]. This results in the Hamiltonian ($\hbar = 1$)

$$\hat{\mathcal{H}} = \Omega\left(\hat{\sigma}_{ge} + \hat{\sigma}_{eg}\right) - \Delta \hat{\sigma}_{ee}, \tag{1.12}$$

where we defined the atomic transition operator $\hat{\sigma}_{ge} = |g\rangle\langle e|$ and the projection operator $\hat{\sigma}_{ee} = |e\rangle\langle e|$. The coupling strength Ω (*Rabi frequency*) between the two states includes the electric field strength and the relevant dipole moment. When the laser frequency ω is resonant with the atomic transition frequency ω_{ge}, the detuning $\Delta = \omega - \omega_{ge}$ vanishes. Additionally, we consider a finite lifetime of the excited state, which decays with rate Γ_s. Therefore, it is convenient to introduce a Lindblad jump operator,

$$\hat{L}_s = \sqrt{\Gamma_s}\hat{\sigma}_{ge}, \tag{1.13}$$

which describes the impact of the coupling between the atomic system to its environment. The decay rate Γ_s mainly originates from the coupling to the vacuum of the electromagnetic field. However, other sources, such as collisions, leading to a finite excited state lifetime can be included. Similarly, we include in the description dephasing of the excited state with respect of the ground state by a Lindblad jump operator,

$$\hat{L}_d = \sqrt{\Gamma_d}\hat{\sigma}_{ee}. \tag{1.14}$$

Sources of dephasing are e.g. fluctuations in the laser frequency ω as well as thermal motion of the atoms. As will be seen below, dephasing leads to a decay of coherence in the system. While dephasing preserves the energy, a spontaneous decay of the excited state does not.

In terms of the master equation in Lindblad form, the equations for the density matrix can be cast as

$$\partial_t \rho = \hat{\mathcal{L}}\rho, \tag{1.15}$$

with a vector representation $\rho = (\rho_{gg}, \rho_{ee}, \rho_{eg}, \rho_{ge})^T$ of the elements of the density matrix and Lindblad superoperator (*Lindbladian*)

$$\hat{\mathcal{L}} = \begin{pmatrix} 0 & \Gamma_s & i\Omega & -i\Omega \\ 0 & -\Gamma_s & -i\Omega & i\Omega \\ i\Omega & -i\Omega & -i\Delta - \gamma & 0 \\ -i\Omega & i\Omega & 0 & i\Delta - \gamma \end{pmatrix}. \tag{1.16}$$

The decoherence rate $\gamma = \frac{1}{2}(\Gamma_s + \Gamma_d)$ describes the relaxation of the coherences ρ_{ge} and ρ_{eg}. Solving for the steady state, i.e. $\partial_t \rho = 0$, we obtain the steady state excited state population

$$\rho_{ee} = \frac{2\Omega^2\gamma}{4\Omega^2\gamma + \Gamma_s\left(\gamma^2 + \Delta^2\right)}, \tag{1.17}$$

and the corresponding linewidth

$$w = \sqrt{4\Omega^2\gamma/\Gamma_s + \gamma^2}. \tag{1.18}$$

Clearly, the steady state population is bounded by $\rho_{ee} \leq 0.5$ even for resonant laser excitation.

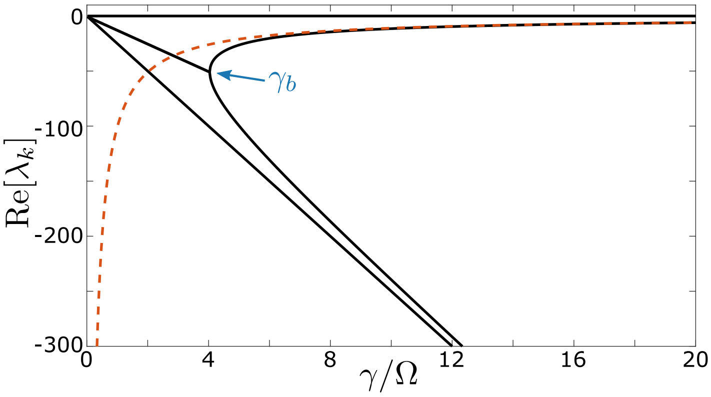

Figure 1.2: Real parts of the eigenvalues λ_k of the matrix $\hat{\mathcal{L}}$ in Eq. (1.16) versus the decoherence rate γ for $\Omega/\Gamma_s = 25$ and $\Delta = 0$. The relaxation rate $-(\Gamma_{\mathrm{ex}} + \Gamma_{\mathrm{de}})$ (with a minus sign) of the rate equation model is indicated by a red dashed line and the bifurcation point γ_b by a blue arrow. For strong decoherence rate γ, the rate equation approximation matches well the exact relaxation rate of the system.

For large rate $\gamma \gg \Omega$, the coherences decay on a fast timescale compared to the coherent dynamics and it is justified to adiabatically eliminate them. Setting $\partial_t \rho_{ge} = \partial_t \rho_{eg} = 0$, we obtain rate equations for the transitions between the populations ρ_{gg} and ρ_{ee},

$$\partial_t \rho_{gg} = -\Gamma_{\mathrm{ex}} \rho_{gg} + \Gamma_{\mathrm{de}} \rho_{ee}, \tag{1.19a}$$

$$\partial_t \rho_{ee} = +\Gamma_{\mathrm{ex}} \rho_{gg} - \Gamma_{\mathrm{de}} \rho_{ee}, \tag{1.19b}$$

with excitation and deexcitation rates

$$\Gamma_{\mathrm{ex}} = \frac{2\Omega^2 \gamma}{\gamma^2 + \Delta^2}, \qquad \Gamma_{\mathrm{de}} = \Gamma_{\mathrm{ex}} + \Gamma_s. \tag{1.20}$$

The rate equation model Eq. (1.19) preserves the total population $\rho_{gg} + \rho_{ee} = 1$. Within this approximation the relaxation of the two-level system is given by the sum of both rates, $\Gamma_{\mathrm{ex}} + \Gamma_{\mathrm{de}}$.

Let us compare the rate equation model to the exact relaxation rates. To this end, we diagonalize the matrix in Eq. (1.16), which determines the evolution of the density matrix $\rho(t)$. The corresponding eigenvectors $\hat{\rho}_k$ and eigenvalues $\lambda_k \in \mathbb{C}$ with $k = 0, 1, 2, 3$ fully characterize the two-level dynamics. Importantly, the real parts $\mathrm{Re}[\lambda_k] \leq 0$ (apart from a minus sign) determine the relaxation rates of the system. Explicitly, we have for the case $\Delta = 0$,

$$\lambda_0 = 0, \tag{1.21a}$$

$$\lambda_{1,2} = -\tfrac{1}{2}\gamma - \tfrac{1}{2}\Gamma_s \pm \tfrac{1}{2}\sqrt{(\gamma - \Gamma_s)^2 - 16\Omega^2}, \tag{1.21b}$$

$$\lambda_3 = -\gamma. \tag{1.21c}$$

The value λ_0 corresponds to the stationary state, since $\partial_t \hat{\rho}_0 = 0$ and determines the steady state values for the populations ρ_{gg}, ρ_{ee} and the coherences ρ_{ge}, ρ_{eg}. The smallest value $|\mathrm{Re}[\lambda_{k\geq 1}]|$ describes the slowest timescale for relaxation. In Fig. 1.2 the exact relaxation rates are shown and compared to the total relaxation rate $\Gamma_{\mathrm{ex}} + \Gamma_{\mathrm{de}}$ of the rate equation model. The bifurcation point $\gamma_b = 4\Omega + \Gamma_s$ indicates a transition where all eigenvalues λ_k become real for $\gamma \geq \gamma_b$. This is the regime where we expect excellent agreement with the rate equation model in Eq. (1.19). However, already for $\gamma/\Omega \gtrsim 2$ we obtain similar relaxation rates in the exact model and the rate equation approximation. For $\gamma < \gamma_b$ coherent dynamics can be observed in the form of damped Rabi oscillations.

Many-body dynamics and numerical simulation

Now, we extend the rate equation description to the case of many atoms within the two-level approximation. Besides the atom-light coupling introduced before we include interactions between atoms in the excited state. These interactions stem from coupling to Rydberg states and will be discussed in the next section. For a system with L atoms we consider the Hamiltonian ($\hbar = 1$),

$$\hat{\mathcal{H}} = \sum_{i}^{L} \left[\Omega\left(\hat{\sigma}_{eg}^{i} + \hat{\sigma}_{ge}^{i}\right) - \Delta \hat{\sigma}_{ee}^{i}\right] + \sum_{i<j}^{L} V_{ij}\, \hat{\sigma}_{ee}^{i} \otimes \hat{\sigma}_{ee}^{j}. \tag{1.22}$$

Here, V_{ij} is the interaction strength between the ith and jth atom in the excited state. As discussed in Ref. [31–33], the level shift due to the interaction can be cast as an effective detuning in the rate equation approximation. To be specific, the resulting detuning of the ith atom in the presence of all other atoms j is,

$$\Delta_i \equiv \Delta - \sum_{j\neq i} V_{ij} \hat{\sigma}_{ee}^{j}. \tag{1.23}$$

The effective detuning Δ_i depends on the current state of all atoms and changes in time. In the limit $\gamma \gg \Omega$, we replace the detuning Δ in the single atom rates in Eq. (1.20) by the effective detuning Δ_i. This leads to a set of $2L$ nonlinear equations,

$$\partial_t \rho_{gg}^{(i)} = -\Gamma_{\mathrm{ex}}^{(i)} \rho_{gg}^{(i)} + \Gamma_{\mathrm{de}}^{(i)} \rho_{ee}^{(i)}, \tag{1.24a}$$

$$\partial_t \rho_{ee}^{(i)} = +\Gamma_{\mathrm{ex}}^{(i)} \rho_{gg}^{(i)} - \Gamma_{\mathrm{de}}^{(i)} \rho_{ee}^{(i)}, \tag{1.24b}$$

with the constraint $\rho_{ee}^{(i)} + \rho_{gg}^{(i)} = 1$ and transition rates

$$\Gamma_{\mathrm{ex}}^{(i)} = \frac{2\Omega^2 \gamma}{\gamma^2 + \Delta_i^2}, \qquad \Gamma_{\mathrm{de}}^{(i)} = \Gamma_{\mathrm{ex}}^{(i)} + \Gamma_s, \qquad \text{with} \quad \Delta_i \equiv \Delta - \sum_{j\neq i} V_{ij} \rho_{ee}^{j}. \tag{1.25}$$

We include the interaction shift Δ_i from all excited atoms in the denominator. Note that we replaced in the rate equation approximation the operator-valued effective detuning in Eq. (1.23) by a real number. While an analytic solution is challenging, this system can be easily solved numerically. An efficient algorithm is a Monte Carlo technique, which we describe below.

At a given time, the classical state of the system can be described by a vector s of length L, where each element, $s_i \in \{0,1\}$ with $i = 1, \dots, L$, is either 1 if site i is an excited state or 0 if site i is a ground state. We have 2^L different configurations and thus a simulation in terms of the full density matrix is infeasible for large systems. Instead, using a Monte Carlo approach we simulate a set of states $\{\mathrm{s}^k(t)|k = 1, \dots, N\}$ for a specific time t. We can use each representation $\mathrm{s}^k(t)$ and calculate expectation values $\langle \mathcal{O}(t) \rangle_k$ of any observable $\mathcal{O}$. Then, the average $\langle \mathcal{O}(t) \rangle = \frac{1}{N} \sum_k \langle \mathcal{O}(t) \rangle_k$ is used as an approximation to the exact solution of Eq. (1.24). The complexity is hereby hidden in the simulation of many $N \gg 1$ faithful representations.

The given initial configuration s_0 is the same for all different trajectories. We describe now the numerical procedure how we obtain a single trajectory $\mathrm{s}(t_j)$ with time steps t_j. The time t_j denotes the point in time, where one element of the vector $\mathrm{s}(t_{j-1})$ has changed ($0 \leftrightarrow 1$). The algorithm produces a Markov chain $\{t_j, \mathrm{s}(t_j)\}$ until a given time $t_j > T$ is reached, where T is the longest time of interest. Essentially, the algorithm consists of two iterative steps:

1. *Determine the next point in time* t_{j+1}

   First, we calculate the total rate of change Γ. Each element s_i, corresponding to the ith atom, in the vector s is flipped with a rate

   $$\Gamma_i = \Gamma_{\mathrm{ex}}^{(i)}(1 - s_i) + \Gamma_{\mathrm{de}}^{(i)} s_i. \tag{1.26}$$

   Thus, the total rate of change is $\Gamma = \sum_i \Gamma_i$. We calculate a waiting time τ for the next event using a random number generator from a Poisson distribution with mean waiting time $1/\Gamma$. Then, the next point in time is given by $t_{j+1} = t_j + \tau$.

2. *Calculate the updated configuration* $\mathrm{s}(t_{j+1})$

   To decide which atom i flips its state, we calculate the corresponding weights $w_i = \Gamma_i/\Gamma$ for any transition. Using a random number between 0 and 1 we choose one atom i according to the weights w_i and change its internal state ($0 \leftrightarrow 1$).

The algorithm can be repeated many times and averages over many trajectories can be used to calculate the relevant observables. Further information on the algorithm and its validity can be found in Ref. [25, 32–34].

1.2 Rydberg Atoms

While the typical interaction between atoms in quantum gases is short-range, the use of so called *Rydberg atoms* offers a way to generate strong and quasi long-range interactions. The study of Rydberg atoms is an active research field, which includes quantum optics [14–16], ultracold chemistry [18–20, 35] and many-body physics [10, 21, 22, 36]. This section is based on Ref. [37, 38]. For a detailed discussion see also Ref. [13].

Single Particle Physics

Rydberg atoms are atoms where the valence electron is in a state with a high principal quantum number $n \gg 1$. The typical size of the electronic wavefunction scales as $r_n \propto n^2 a_0$, where a_0 is the Bohr radius, and can reach large values $r_n \sim 100\,\mathrm{nm}$ for $n = 20 - 100$. Since the valence electron is classically far away from the nucleus and the remaining electrons, Rydberg atoms are similar to hydrogen atoms. In particular, the energy of an atom in state $|\alpha\rangle = |n, l, s, j, m_j\rangle$ is given by

$$E_\alpha = -\frac{\mathrm{Ry}}{(n - \delta_{nl})^2}, \tag{1.27}$$

where $\mathrm{Ry} \simeq 13.6\,\mathrm{eV}$ is the Rydberg constant and δ_{nl} denotes the quantum defect. The latter is a correction to the bare hydrogen energy formula and includes the interaction of the valence electron with the nucleus and the inner electrons. Rydberg atoms show extreme properties in their scaling behavior with the principal quantum number n, such as a long lifetime $\tau_s \propto n^3$ and a large polarizability $\alpha_p \propto n^7$. While long lifetimes make Rydberg atoms an interesting platform for quantum optical applications, the huge polarizability means that they are very sensitive to electric fields.

Two Particle Physics

Let us consider two Rydberg atoms in the frozen gas approximation [39] at positions $\mathbf{R}_1$ and $\mathbf{R}_2$ with relative position $\mathbf{R} = \mathbf{R}_2 - \mathbf{R}_1$. When the distance $R = |\mathbf{R}|$ is larger than the size of the electronic wavefunction, the interaction between two Rydberg atoms can be cast in the dipole-dipole approximation

$$\hat{\mathcal{H}}_{dd} = \frac{1}{4\pi\epsilon_0} \frac{\hat{\mathbf{d}}_1 \cdot \hat{\mathbf{d}}_2 - 3(\hat{\mathbf{d}}_1 \cdot \hat{\mathbf{r}})(\hat{\mathbf{d}}_2 \cdot \hat{\mathbf{r}})}{R^3}, \tag{1.28}$$

where $\hat{\mathbf{r}} = \mathbf{R}/R$ and $\hat{\mathbf{d}}_i$ is the electric dipole operator of the ith atom. Three different regimes can be distinguished.

van der Waals regime In the absence of interactions, two atoms in the same state $|\alpha,\alpha\rangle \equiv |\alpha\rangle \otimes |\alpha\rangle$ have an energy $E_{\alpha\alpha} = E_\alpha + E_\alpha$. We assume that the state $|\alpha,\alpha\rangle$ is not degenerate with any other state $|\beta,\gamma\rangle$ with energy $E_{\beta\gamma}$ and that the Hamiltonian Eq. (1.28) can be treated as a perturbation. While the first order correction typically vanishes, we obtain in second order perturbation theory an energy correction to the state $|\alpha,\alpha\rangle$

$$\Delta E_{\alpha\alpha} = \sum_{\beta,\gamma} \frac{|\langle\alpha,\alpha|\,\hat{\mathcal{H}}_{dd}\,|\beta,\gamma\rangle|^2}{E_{\alpha\alpha} - E_{\beta\gamma}}. \tag{1.29}$$

The resulting energy shift scales as $\Delta E_{\alpha\alpha} \simeq \frac{\hbar C_6}{R^6}$ with distance R and can be interpreted as a van der Waals type interaction. The coefficient C_6 may depend on the angle between the two dipoles and scales as $C_6 \propto n^{11}$ with the principal quantum number n. The interaction between two Rydberg atoms can be directly measured [40] and the interaction strength can be on the order of several MHz at a distance of several microns.

One implication of the strong interaction between atoms in their Rydberg state is the phenomenon of the *dipole blockade* [23, 24]. Let us consider two atoms excited to the Rydberg state as is sketched in Fig. 1.3a. When the distance R between the two atoms is large, we can neglect interactions and both atoms can be resonantly excited. However, for small distances $R \lesssim a_\mathrm{B}$, where a_B is the blockade distance, the interaction induced level shift cannot be disregarded. The state with two Rydberg excitations is shifted out of resonance and the system shares at most one excitation. The blockade radius is defined by the distance where the interaction lineshift exceeds the linewidth w,

$$a_\mathrm{B} = \left(\frac{C_6}{w}\right)^{1/6}. \tag{1.30}$$

Due to the van der Waals scaling this transition appears typically rather sharp as a function of the separation of the atoms and thus often allows to approximate the interaction with a hard sphere model [33] in cold gases or with a nearest neighbor approximation in lattice systems [32].

When a mesoscopic ensemble of atoms is confined within the blockade radius, the system is termed *superatom* [41, 42]. Again, resonant excitation of the ensemble drives a transition between a state with zero excitation and maximal one excitation. Rydberg superatoms were already realized in several experiments [22, 36, 43–45]. A detailed description and physical consequences are discussed in Chapter 3.

Förster resonance If the two atom state $|\alpha,\alpha\rangle$ is degenerate with another pair state $|\beta,\gamma\rangle$, then one can neglect the contributions from second order perturbation theory with other nonresonant states. The corresponding level shift from resonant dipole-dipole interaction scales as $\frac{\hbar C_3}{R^3}$. In general, these states are not degenerate, but have a small energy mismatch $\hbar\delta w = E_{\alpha\alpha} - E_{\beta\gamma}$ which is called

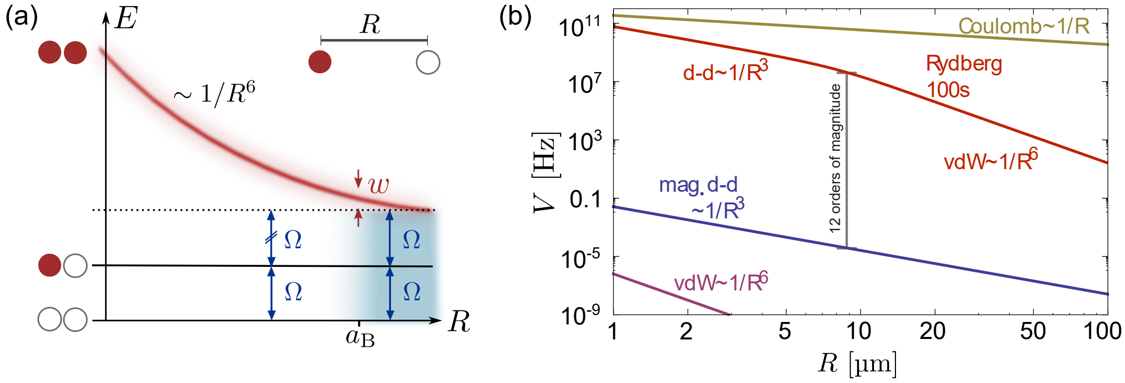

Figure 1.3: (a) Illustration of the dipole blockade [23, 24] using a resonant excitation laser with Rabi frequency Ω. Red filled circles denote Rydberg state atoms and open circles ground state atoms. The excitation of two atoms with distance R smaller than the blockade radius a_B is suppressed due to the strong Rydberg-Rydberg interaction induced level shift exceeding the linewidth w. (b) Typical interaction strength V of the dipole-dipole interaction between Rydberg atoms versus the distance R. Also shown are Coulomb interactions (highest interaction strength), magnetic and van der Waals interactions between ground state atoms (smallest interaction strength). The figure is taken from Ref. [38].

Förster defect. Due to different polarizabilities of the atomic states $|\alpha\rangle, |\beta\rangle, |\gamma\rangle$, their energies can be tuned by applying electric fields [46]. For a fixed Förster defect δw, there is a transition from the Förster resonance regime for small distances R to a van der Waals regime for large R. The crossover between the two regimes occurs around $R_c \simeq (C_3/\delta w)^{1/3}$.

In Fig. 1.3b a typical example of the interaction strength between atoms in their Rydberg state is shown. While the Rydberg-Rydberg interaction is clearly smaller than the Coulomb interaction for charged particles, it can be many orders of magnitude larger than interactions between neutral ground state atoms. For small distances in the Förster resonance regime the interaction scales as $\propto 1/R^3$ and for large distances in the van der Waals regime it scales as $\propto 1/R^6$.

Resonant dipole-dipole interaction Finally, consider the case where two atoms are initially in two different Rydberg states $|\alpha\beta\rangle$ [47]. This state is directly coupled by the dipole-dipole interaction to the state $|\beta\alpha\rangle$. Since both states have the same energy $E_{\alpha\beta} = E_{\beta\alpha}$, this process is resonant and we have

$$\hat{\mathcal{H}}_{dd} \simeq \frac{\hbar C_3}{R^3}\big(|\alpha\beta\rangle\langle\beta\alpha| + |\beta\alpha\rangle\langle\alpha\beta|\big), \tag{1.31}$$

where the interaction coefficient scales with the principal quantum number n as $C_3 \propto n^4$. Interpreting the two different Rydberg states as two pseudo-spin states, this realizes a long-range XY spin Hamiltonian.

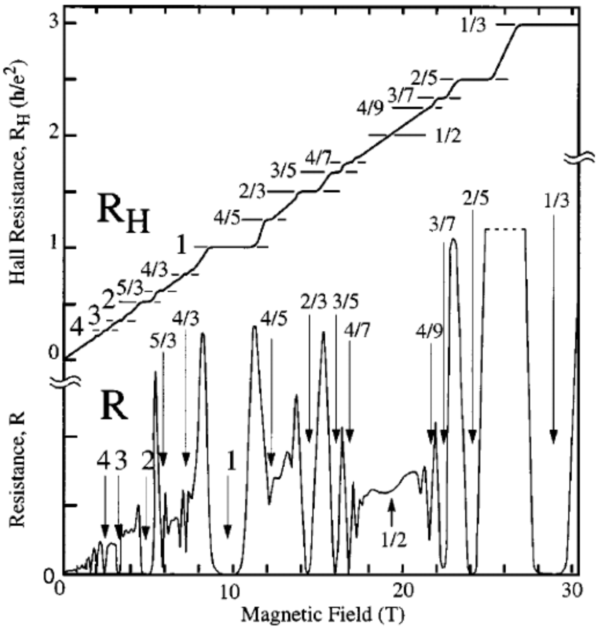

Figure 1.4: Measurement of the Hall resistance $R_{\mathrm{H}} = 1/\sigma_{\mathrm{H}}$ and and the longitudinal resistance R versus the magnetic field, taken from Ref. [52]. The fractions follow a sequence $f = n/(2n+1)$, where n is an integer.

1.3 Fractional Quantum Hall Effect

In this section we summarize the main concepts of the fractional quantum Hall effect. A full explanation of quantum Hall physics is beyond the scope of this thesis. For detailed discussions of the underlying mechanisms we refer to Ref. [48, 49].

In 1982 – only two years after the discovery of the integer quantum Hall effect by von Klitzing [50] – Tsui, Stormer and Gossard [51] discovered precisely quantized plateaus of the Hall conductivity at

$$\sigma_{\mathrm{H}} = f\frac{e^2}{h}, \tag{1.32}$$

where f is a fraction. In the following years a hole sequence of fractions f was observed, see Fig. 1.4. While the integer quantum Hall effect could be explained by noninteracting electrons in a magnetic field, the occurrence of fractions required to take the Coulomb interaction between electrons into account.

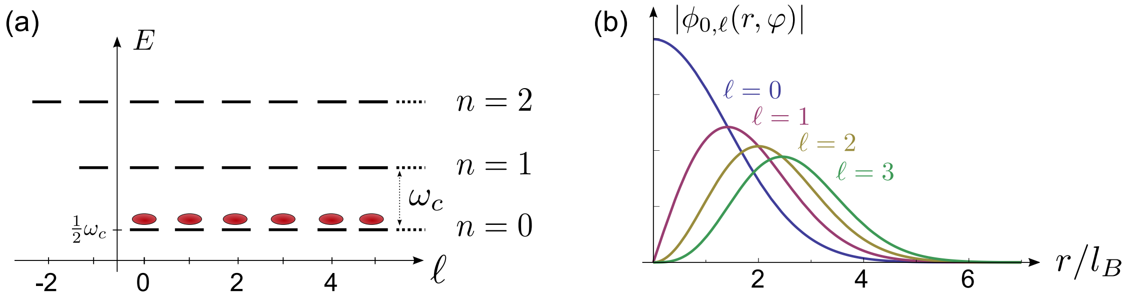

Figure 1.5: (a) Sketch of the Landau level energy structure. The quantum number n labels the Landau level and ℓ the angular momentum. Landau levels are gapped by the cyclotron frequency ω_c. The lowest Landau level ($n=0$) is fully occupied with electrons realizing a magnetic filling $\nu=1$ integer quantum Hall phase. (b) Eigenstates $\phi_{n,\ell}(r,\varphi)$ in the lowest Landau level ($n=0$) with different angular momentum ℓ versus the distance r in units of the magnetic length ℓ_B. Only the $\ell=0$ mode has a nonvanishing amplitude at the center of the system $r=0$.

Model Consider N electrons confined in a two-dimensional disc geometry with a strong magnetic field. The system is described by the Hamiltonian,

$$\hat{\mathcal{H}} = \sum_i \frac{1}{2m_e}\left(\mathbf{p}_i - e\mathbf{A}(\mathbf{r}_i)\right)^2 + \sum_{i<j} V(|\mathbf{r}_i - \mathbf{r}_j|), \tag{1.33}$$

where m_e is the electron mass and $\mathbf{A}(\mathbf{r}) = B/2(-y,x,0)^T$ the vector potential in symmetric gauge, which leads to a magnetic field in z-direction of strength B. The electrons interact via a repulsive Coulomb interaction

$$V(r) = \frac{e^2}{4\pi\varepsilon_0 r}, \tag{1.34}$$

which depends only on the mutual distance r between two electrons. Here, ε_0 is the permittivity. This model assumes spin-polarized particles without additional disorder.

1.3.1 Noninteracting Case & Integer Quantum Hall Effect

Let us first neglect interactions between electrons, setting $V(r)=0$. Then, the spectrum of the Hamiltonian (1.33) is described in terms of Landau levels $E_n = \hbar\omega_c(n+\frac{1}{2})$ with cyclotron frequency $\omega_c = eB/m_e$ as shown in Fig. 1.5a. The corresponding eigenfunctions $\phi_{n,\ell}$ are labeled by the Landau level $n=0,1,\dots$ and the angular momentum $\ell=-n,-n+1,\dots$. Note that the eigenenergies E_n do not depend on the angular momentum ℓ and have therefore a large degeneracy.

Consider N electrons occupying an area A with density $\rho = N/A$. The extent of the cyclotron orbits $2\pi\ell_B^2$ is determined by the magnetic length

$$\ell_B = \sqrt{\hbar/eB}. \tag{1.35}$$

Comparison of the density to the area of a cyclotron orbit leads to the definition of the magnetic filling factor

$$\nu = 2\pi\ell_B^2\rho = \frac{N}{N_\phi}, \tag{1.36}$$

where N_ϕ counts the number of flux quanta in the system. In particular, for ν being an integer, electrons fill all $\nu - 1$ Landau levels. This is an incompressible state gapped by the cyclotron frequency ω_c and gives a first hint for the quantization of the Hall conductivity σ_{H} at integer values of the magnetic filling ν.

At low temperatures $k_B T \ll \hbar\omega_c$ and $\nu = 1$, all electrons occupy states within the lowest Landau level (LLL) $n = 0$. The corresponding single-particle wavefunctions are

$$\phi_{0,\ell}(z, z^*) = \frac{z^\ell}{\sqrt{2\pi\ell_B^{2(\ell+1)}2^\ell\ell!}} \exp\left(-\frac{|z|^2}{4\ell_B^2}\right), \tag{1.37}$$

where we used the complex coordinate $z = x - iy$. For the case of N electrons, we can construct the fermionic many-body wavefunction using the Slater determinant and obtain

$$\Psi_{\nu=1}(z_1, \ldots, z_N) = \mathcal{N}\prod_{i<j}(z_i - z_j)\exp\left(-\sum_j \frac{|z_j|^2}{4\ell_B^2}\right), \tag{1.38}$$

where $\mathcal{N}$ is a normalization constant. Besides the Gaussian factor, the wavefunction depends only on the relative distances $z_i - z_j$ between the particles. The product $\prod_{i<j}(z_i - z_j)$ is termed Jastrow factor.

1.3.2 Interacting Case & Fractional Quantum Hall Effect

Let us discuss the case of interacting electrons. We assume that we are in a regime of low temperatures compared to typical interaction energies Δ_{int} and the cyclotron frequency ω_c, i.e. $k_B T \ll \hbar\Delta_{\mathrm{int}} \ll \hbar\omega_c$. Furthermore, we discuss here only the case of magnetic filling $\nu \leq 1$. Then, it is sufficient to project the Hamiltonian (1.33) to the LLL,

$$\hat{\mathcal{P}}_{\mathrm{LLL}}\hat{\mathcal{H}}\hat{\mathcal{P}}_{\mathrm{LLL}} = N\frac{1}{2}\hbar\omega_c + \hat{\mathcal{P}}_{\mathrm{LLL}}\sum_{i<j}V(|\mathbf{r}_i - \mathbf{r}_j|)\hat{\mathcal{P}}_{\mathrm{LLL}}, \tag{1.39}$$

where $\hat{\mathcal{P}}_{\mathrm{LLL}}$ is the projector to the LLL. Now, the only relevant energy scale is given by the repulsive Coulomb interaction and we cannot solve the problem perturbatively.

Haldane's pseudopotentials A method to quantify the interaction $V(r)$ between electrons in the LLL was presented by Haldane in 1983 [53]. Consider the case of two particles with relative angular momentum m and center of mass angular momentum M. Evaluating the interaction part in Eq. (1.39) yields

$$\begin{aligned}\hat{\mathcal{P}}_{\mathrm{LLL}} V(r) \hat{\mathcal{P}}_{\mathrm{LLL}} &= \sum_{M,M'} \sum_{m,m'} |M,m\rangle \langle M,m| V(r) |M',m'\rangle \langle M',m'| \\ &= \sum_{M,m} V_m |M,m\rangle \langle M,m| , \end{aligned} \tag{1.40}$$

where we used that the interaction potential depends only on the relative coordinate r and angular momentum is a conserved quantity. The values $V_m = \langle m| V(r) |m\rangle$ are called *Haldane's pseudopotentials*. For the case of Coulomb interaction, we explicitly have

$$V_m = \frac{e^2}{8\pi\varepsilon\ell_B} \frac{\Gamma(m+\frac{1}{2})}{\Gamma(m+1)}, \tag{1.41}$$

where $\Gamma(x)$ is the Gamma function. The pseudopotentials quickly drop with increasing relative angular momentum m.

Laughlin's wavefunction The first successful attempt to describe the ground state in the case of fractional filling $\nu = f$ was made by Laughlin in 1983 [54]. Using the variational wavefunction (*Laughlin wavefunction*),

$$\Psi_{\mathrm{LN}}(z_1, \dots, z_N) = \mathcal{N}_{\mathrm{LN}} \prod_{i<j} (z_i - z_j)^m \exp\left(- \sum_j \frac{|z_j|^2}{4\ell_B^2} \right), \tag{1.42}$$

the Hall resistance series with fractions $f = 1/m$, where m is an odd integer, could be explained. In the case of interacting fermions, m has to be an odd integer to maintain the anti-symmetry. The Laughlin wavefunction has a similar form as in the case of noninteracting electrons as per Eq. (1.38), but with additional Jastrow factors. Since a Jastrow factor with power m increases the relative particle distance and thus screens the pseudopotentials $V_0, \dots, V_m$, it reduces the interaction energy. Additionally, it attaches m flux quanta to each particle. Note that a Laughlin state can also exist for bosonic particles with m being an even integer [55, 56].

Quasi-excitations Finally, let us comment on the low-energy excitations of the Laughlin wavefunction, which are termed quasi-hole excitation. For a system with few, i.e. $m \ll N$ quasi-hole excitations, the state can be described by the wavefunction

$$\Psi_{m\mathrm{qh}}(z_1, \ldots, z_N) = \prod_j z_j^m \Psi_{\mathrm{LN}}. \tag{1.43}$$

Due to the factor $\prod_j z_j^m$ additional flux is attached to the center of the system and thus produces a hole excitation.

Chapter 2

Bistability vs. Metastability

The transition between different phases of matter, such as between a liquid and a gas, is an active and interesting research field in physics. For many years, two different categories of phase transitions, classified by the nature of fluctuations, were explored: On the one hand, *quantum phase transitions* [57] occur at zero (or very low) temperatures, when the system is in its ground state. Upon system parameter changes the ground state properties may change drastically, which indicates a phase transition. Examples are supraconductivity, the superfluid-to-Mott-insulator transitions [2] and the quantum Ising model [57]. Hereby, the transition is driven purely by quantum fluctuations. On the other hand, a system in its thermal equilibrium can undergo a *classical* or *thermal phase transition* upon changes in the temperature T [58]. This transition is driven by thermal fluctuations. For a finite temperature T, the system can no longer be described by a pure ground state. Rather, the system is in a thermal (Gibbs) state. Prominent examples are a liquid-gas transition, the emergence of a Bose-Einstein condensate at low temperatures and the Ising model. The latter plays a fundamental role in the explanation of ferromagnetism and describes a transition from a disordered spin configuration with zero magnetization to an ordered ferromagnetic phase. In the case of continuous (or second order) phase transitions different physical systems behave in a universal fashion when approaching a critical point. Then, the correlation length ξ and correlation time τ_c diverge upon reaching a critical point Δ_c,

$$\xi \propto (\Delta - \Delta_c)^{-\nu}, \qquad \tau_c \propto \xi^z \propto (\Delta - \Delta_c)^{-\nu z}, \tag{2.1}$$

where Δ is a tuning parameter and ν, z are the critical exponents.

While quantum and thermal phase transitions occur in equilibrium, much less is known about the transition between different phases in nonequilibrium systems. We are particularly interested in open quantum systems, where the competition between coherent drive, interactions and dissipation may lead to novel steady states, so called *nonequilibrium steady states.* Upon system parameter changes a phase transition may occur driven by both, quantum and classical fluctuations. While these states can strongly differ from a thermal state [59, 60], they may show similar critical behavior as seen in thermal and quantum phase transitions. However, also novel properties can emerge as shown in Ref. [61].

In contrast to thermal equilibrium, where the state is determined solely by maximizing the entropy at a given temperature, in a nonequilibrium system the steady states are obtained by solving a partial differential equation. This makes a full theoretical description challenging. Starting from early considerations of phase transitions in open many-body quantum systems [61, 62], many theoretical approaches were developed. Due to the large size of the Hilbert space, exact numerical methods are limited to small system sizes [63, 64]. Therefore, advanced numerical methods such as open system TEBD (time evolving block decimation algorithm) [34, 65], cluster mean field descriptions [66] and variational approaches [67, 68] were developed. However, these methods are often restricted to low dimensions and require that correlations decay on a short length scale. The method employed in this chapter is based on a rate equation model, as discussed in Sec. 1.1.2, which is only valid in the strongly dissipative regime [31, 32]. Since rate equation models are amenable to efficient Monte Carlo simulations this approach does allow to model large systems even on long time scales. A promising analytical approach uses a Keldysh technique for open quantum systems [69–71]. This approach considers the long wavelength properties of the system and may thus be applicable to describe phase transitions. Another commonly used technique is mean field theory [72–76], which typically results in a set of nonlinear equations for the steady state. In this case, multiple steady state solutions may exist, which is of particular interest for what follows. However, it is already known from thermal phase transitions that mean field approximations can result in wrong predictions. These results should thus be contrasted with those from advanced numerical methods. The nonlinear character of mean-field equations may lead to the prediction of bistable or multi-stable solutions in the steady state, while an exact numerical treatment suggests a unique steady state [65, 67, 68, 77].

The notion of bistability in a driven dissipative environment was already discussed several years ago in the context of optical systems [78]. In a nonlinear single mode cavity subject to photon losses two disjunct states of the semi-classical dynamics can occur, one with low and one with high photon number. The steady state of the full quantum dynamics is however unique. Starting with either one of the bistable states, quantum tunneling to the unique steady state occurs on very long timescales. It was shown that two stable steady states emerge under a proper thermodynamic limit [64]. This thermodynamic limit is however artificial as it requires a diverging photon number in the considered mode. Later, the single photonic cavity was extended to an array of coupled cavities, where a thermodynamic limit in the conventional sense can be introduced which requires the number of coupled cavities to go to infinity [65, 76, 79–81]. It was argued that the competition between strong interactions and photon losses may lead to a global bistable phase in large cavity systems.

Similarly the possibility of bistable steady states was discussed in interacting spin models with dissipation [69, 82]. Rydberg lattice systems are one interesting platform for studying dissipative spin models. Here, the strong van der Waals interaction between atoms in their Rydberg state and the coherent drive compete with dephasing and the Rydberg state lifetime. Due to the large flexibility of the individual parameters, Rydberg systems are an ideal platform to study open many-body systems. An essential ingredient thereby is the large separation of timescales and the quasi long-range interactions realizing spin models with kinetic constraints [71, 83–88].

The possibility of the existence of bistable steady states attracted much attention in the case of off-resonantly driven Rydberg gases. In the so called *facilitation* or *antiblockade regime* an off-resonant seed excitation triggers an excitation cascade and leads to interesting dynamics and microscopic structures [89–91]. First theoretical approaches [72–74] showed that the resulting state exhibits strong fluctuations. While exact numerical simulations were limited to small system sizes, analytical mean field theories predicted the existence of a bistable steady state. Experimental investigations of this regime further supported this idea: Firstly, in cold atom experiments [92, 93], the counting statistics of Rydberg excitations was measured. A bimodal distribution with a peak at low and high number of Rydberg excitations and strong Rydberg state number fluctuations was observed. These are indications for the existence of a bistable phase. However, as argued in Ref. [77] the experiments were performed on short timescales and therefore do not probe the steady state. Secondly, in thermal vapor cells [94–97] a hysteresis was observed. Here, parameter sweeps of the detuning in forward and backward direction yield a finite hysteresis area and a slowing down of the relaxation timescale. In Ref. [97] it was argued that the underlying interaction mechanism stems from ions rather than interacting Rydberg atoms. More advanced theoretical approaches precluded the existence of two disjunct steady states [67, 68, 77]. However, in Ref. [98] it was argued that bistable states may exist in experiments with mixed power law interactions in combination with atomic motion, which support the mean field prediction. Whether or not true bistability exists in Rydberg systems under conditions of facilitation is still an open question and we will address this issue in the following.

In the work presented here we use a combined theory-experiment approach to study the question of bistability in off-resonantly driven Rydberg gases on a lattice. The experiment allows to observe the long time dynamics of a driven Rydberg gas and thus should reflect the true stationary state of the system. Based on measuring an in-situ Rydberg ion signal, temporal correlation functions are analyzed. This yields insight into the underlying structure of the system and allows to make a comparison to a theoretical model for the formation of small excitation clusters. These clusters originate from initial seed excitations and act as independent parts of the steady state for small Rydberg excitation densities. Within this model we estimate the typical cluster size and lifetime as well as the number of clusters in the system. Furthermore, we perform advanced numerical simulations using a many-body rate equation approach. This allows us to access microscopic details and we calculate a counting distribution and hysteresis sweeps. Altogether, we conclude that the underlying phase is a metastable [99, 100] rather than a bistable state.

This chapter is organized as follows: We start with a definition of bistability and metastability in open many-body systems in Sec. 2.1 and discuss their direct consequences for phase transitions upon system parameter changes. In Sec. 2.2 we describe the experiment and the underlying microscopic model, which is the basis of our further discussion. In Sec. 2.3, we start with a discussion of a simplified model of the Rydberg excitation dynamics. Specifically, we introduce a single cluster model, which can explain various features of the steady state. Finally, we use this model to explain the experimental findings in Sec. 2.4. We further support the experimental results with numerical studies.

The present chapter is based on the publication [FL4], partially with text overlap.

2.1 Bistability in Open Quantum Systems

2.1.1 Definition

Let us start by defining *bistability* in open quantum systems and contrast it to *metastability*. We assume a system coupled to a large reservoir, which is described by a master equation in Lindblad form for the density matrix $\hat{\rho}$ [29, 101]. The Lindblad master equation and the corresponding approximations were already discussed in Sec. 1.1. We can cast the time evolution of a state ρ (vector of density matrix elements) using a Lindblad superoperator $\hat{\mathcal{L}}$ as

$$\partial_t \rho = \hat{\mathcal{L}} \rho. \tag{2.2}$$

The so called *Lindbladian* $\hat{\mathcal{L}}$ is the generator of the dissipative system dynamics. It includes both, a coherent part described by a Hamiltonian $\hat{\mathcal{H}}$ as well as couplings to reservoirs described by jump operators $\hat{L}_\mu$. The superoperator $\hat{\mathcal{L}}$ is not necessarily hermitian, i.e. $\hat{\mathcal{L}} \neq \hat{\mathcal{L}}^\dagger$. Nevertheless, we assume that $\hat{\mathcal{L}}$ can be diagonalized,

$$\hat{\mathcal{L}} \hat{\rho}_k = \lambda_k \hat{\rho}_k, \tag{2.3}$$

where $\hat{\rho}_k$ denotes the right eigenstate and $\lambda_k \in \mathbb{C}$ the corresponding eigenvalue. We will assume that k is an ordered index with $\mathrm{Re}[\lambda_k] \geq \mathrm{Re}[\lambda_{k+1}]$ and the largest eigenvalue is $\lambda_0 = 0$. The states $\hat{\rho}_k$ are in general no proper density matrices, since $\mathrm{tr}\{\hat{\rho}_k\} = 0$ for $\lambda_k \neq 0$. However, there is a subset of states

$$\mathcal{S} = \{\hat{\rho}_k \,|\, \lambda_k = 0,\ \mathrm{tr}\{\hat{\rho}_k\} = 1\} \tag{2.4}$$

having a vanishing real eigenvalue and a trace equal to one. These are the stationary states of the system, since $\partial_t \hat{\rho}_k = 0$. Now, if $\mathcal{S}$ contains exactly one state $\hat{\rho}_0$, it is the unique steady state of the system and we call the system *monostable*. If $\mathcal{S}$ contains exactly two linear independent stationary solutions $\hat{\rho}_0, \hat{\rho}_1$, both of which are true density matrices, we call the system *bistable*. For the case where $\mathcal{S}$ contains more than two stationary states, we call the system *multistable*.

The solution of Eq. (2.2) with initial value $\rho(t=0)$ can be formally written as

$$\rho(t) = e^{\hat{\mathcal{L}} t} \rho(0) = \sum_k c_k \hat{\rho}_k e^{\lambda_k t}, \tag{2.5}$$

with coefficients $c_k = \mathrm{tr}\{\check{\rho}_k \rho(0)\}$ and $\check{\rho}_k$ being a left eigenstate of $\hat{\mathcal{L}}$, i.e. $\check{\rho}_k \hat{\mathcal{L}} = \lambda_k \check{\rho}_k$. Here, we used the orthogonality relation $\mathrm{tr}\{\check{\rho}_k \hat{\rho}_l\} = \delta_{kl}$. Clearly, the real parts of the eigenvalues $\mathrm{Re}[\lambda_k] \leq 0$

correspond to the relaxation rates (with a minus sign) of the system and characterize the damping spectrum. Consider the long time limit $t \to \infty$, where a system approaches a steady state ρ_{ss}. The impact of all states $\hat{\rho}_k$ with nonvanishing relaxation rates decays to zero. For a monostable system, we have a unique steady state $\rho_{ss} = \rho_0$ with $c_0 = 1$. Conditions on the uniqueness of steady states are discussed in Refs. [102–104]. The steady state of a bistable system can be described by a convex sum of the two stationary states,

$$\rho_{ss} = p\hat{\rho}_0 + (1-p)\hat{\rho}_1, \tag{2.6}$$

where $p = \mathrm{tr}\{\check{\rho}_0 \rho(0)\}$. In this case, the final steady state depends on the initial condition $\rho(0)$ of the system.

Here, we are interested in many-body systems with a linear system size L. We assume that interactions as well as reservoir couplings are local, i.e. independent reservoirs act only on a finite space of the system. As an example, the spontaneous decay of an atom is a local process. In general, these systems have a unique steady state as long as the system is finite and the reservoir couplings are not fine-tuned (see e.g. Ref. [105] for a system where symmetries generate multiple degenerate stationary states).

Experiments are always performed in a finite system within a finite observation time. Thus, the question is how can we determine whether a system is bistable or not? To this end, we consider the damping spectrum and assume a finite system $L < \infty$ with a unique steady state. The spectral gap $|\mathrm{Re}[\lambda_1]|$ determines the longest timescale $\tau = |\mathrm{Re}[\lambda_1]|^{-1}$ for relaxation towards the steady state. For times $t \gg \tau$, the system is essentially in the steady state $\rho_{ss} \simeq \hat{\rho}_0$. On top of that, if the system has a separation of relaxation rates

$$|\mathrm{Re}[\lambda_1]| \ll |\mathrm{Re}[\lambda_k]| \quad \text{for } k \geq 2, \tag{2.7}$$

we call it *metastable*. Then the transient relaxation is determined by a much shorter timescale $\tau' = |\mathrm{Re}[\lambda_2]|^{-1} \ll \tau$. For times $\tau' \lesssim t \lesssim \tau$ the system may appear stationary, as was discussed in Ref. [99, 100].

2.1.2 Long-range order and critical slowing-down

Upon increasing the linear system size L, the relaxation rate $|\mathrm{Re}[\lambda_1]|$ may decrease. Nevertheless, for any finite size the system is metastable. If in the thermodynamic limit $|\mathrm{Re}[\lambda_1]|$ vanishes, we obtain a truly bistable system with two stationary states. The relaxation rate may also approach an asymptotic value when the system size is increased and exceeds some length scale. In this case the system is metastable. As we will argue below true bistability requires the absence of such a critical length scale and is thus connected to long-range order. The two possibilities of a metastable and a bistable system are indicated in Fig. 2.1. The transition to a bistable regime constitutes a phase

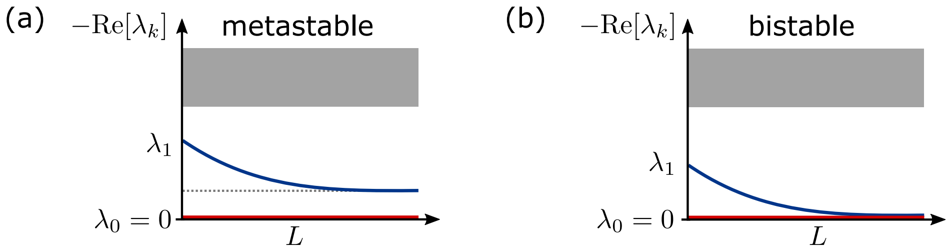

Figure 2.1: Schematic damping spectrum $-\mathrm{Re}[\lambda_k]$ depending on the system size L for (a) a metastable system and (b) a bistable system. In the case of a metastable system, the spectral gap $|\mathrm{Re}[\lambda_1]|$, which determines the slowest timescale for relaxation, approaches a finite value in the thermodynamic limit $L \to \infty$. For the bistable case, the spectral gap vanishes and we obtain two stable states $\hat{\rho}_0$, $\hat{\rho}_1$ with $\partial_t \hat{\rho}_0 = \partial_t \hat{\rho}_1 = 0$.

transition in an open quantum system. Similar to the case of thermal and quantum phase transitions [57, 58] we expect an algebraic scaling of the relaxation time

$$\tau \sim L^{\alpha > 0} \tag{2.8}$$

diverging with the system size L. The exponent α thereby depends on the system. An indication of a bistable phase is therefore a critical slow down of the relaxation dynamics with increasing system size L. True bistability can be distinguished from a metastable system by considering the scaling of the relaxation timescale with the system size. In a metastable system, the slowest relaxation time approaches a constant value $\tau < \infty$ in the thermodynamic limit $L \to \infty$, see Fig. 2.1a.

Let us consider a bistable system, which has two stationary states in the thermodynamic limit $L \to \infty$. We assume that each of the possible stationary states is characterized by a different order parameter. As will be shown below, this implies long-range order. However, in the corresponding finite system in the scenario of Fig. 2.1b we have a unique steady state and expect also a finite correlation length ξ. Thus, approaching the thermodynamic limit we presume that correlation lengths ξ diverge algebraically with the system size L,

$$\xi \sim L^{\beta > 0}, \tag{2.9}$$

where β is a system dependent parameter.

Bistable steady state and long-range order

Here, we proof that a translational invariant system which supports a bistable steady state has long-range order. To this end, consider the bistable state Eq. (2.6). We assume that a local observable $\hat{x}_j$ exists which distinguishes both stationary states $\hat{\rho}_0$ and $\hat{\rho}_1$. Here the index j represents a position or compact region in space. Without loss of generality we set

$$\langle \hat{x}_j \rangle_0 \equiv \mathrm{tr}\{\hat{x}_j \hat{\rho}_0\} = +1 \quad \forall j, \tag{2.10}$$

$$\langle \hat{x}_j \rangle_1 \equiv \mathrm{tr}\{\hat{x}_j \hat{\rho}_1\} = -1 \quad \forall j. \tag{2.11}$$

Thus, the expectation value of the local operator $\hat{x}_j$ of the steady state in Eq. (2.6) is given by

$$\langle \hat{x}_j \rangle_{ss} = p\langle \hat{x}_j \rangle_0 + (1-p)\langle \hat{x}_j \rangle_1 \tag{2.12}$$

$$= p - (1-p) = 2p - 1. \tag{2.13}$$

The *covariance* for two operators $\hat{X}$ and $\hat{Y}$ is defined as

$$\langle\langle \hat{X}, \hat{Y} \rangle\rangle \equiv \left\langle \left(\hat{X} - \langle \hat{X} \rangle\right) \left(\hat{Y} - \langle \hat{Y} \rangle\right) \right\rangle = \langle \hat{X}\hat{Y} \rangle - \langle \hat{X} \rangle \langle \hat{Y} \rangle. \tag{2.14}$$

Since the covariance is positive semi-definite we have $\langle\langle \hat{X}, \hat{X} \rangle\rangle \geq 0$. If we define an operator $\hat{X} = \sum_j \hat{x}_j$, then we have explicitly,

$$\begin{aligned} \langle\langle \hat{X}, \hat{X} \rangle\rangle &= \sum_{j,k} \left(\langle \hat{x}_j \hat{x}_k \rangle - \langle \hat{x}_j \rangle \langle \hat{x}_k \rangle\right) \\ &= \sum_{j,k} \langle\langle \hat{x}_j, \hat{x}_k \rangle\rangle \geq 0. \end{aligned} \tag{2.15}$$

Since this holds for both stationary states $\hat{\rho}_0$ and $\hat{\rho}_1$, we can estimate

$$\sum_{j,k} \langle \hat{x}_j \hat{x}_k \rangle_{0,1} \geq \sum_{j,k} \underbrace{\langle \hat{x}_j \rangle_{0,1}}_{=\pm 1} \underbrace{\langle \hat{x}_k \rangle_{0,1}}_{=\pm 1} = L^2 \tag{2.16}$$

Note that the two expectation values have always the same sign. Inserting the estimate in Eq. (2.15), we obtain for the steady state

$$\begin{aligned} \langle\langle \hat{X}, \hat{X} \rangle\rangle_{ss} &\geq L^2(p + (1-p)) - L^2(2p-1)^2 \\ &= L^2 4p(1-p). \end{aligned} \tag{2.17}$$

In a translational invariant system, only the relative distance $d = j - k$ should be relevant. Thus, we can cast the covariance for the steady state as

$$\begin{aligned} \langle\langle \hat{X}, \hat{X} \rangle\rangle_{ss} &= L \sum_d \langle \hat{x}_0 \hat{x}_d \rangle_{ss} - \langle \hat{x}_0 \rangle_{ss} \langle \hat{x}_d \rangle_{ss} \\ &= L \sum_d \langle\langle \hat{x}_0, \hat{x}_d \rangle\rangle_{ss} \end{aligned} \tag{2.18}$$

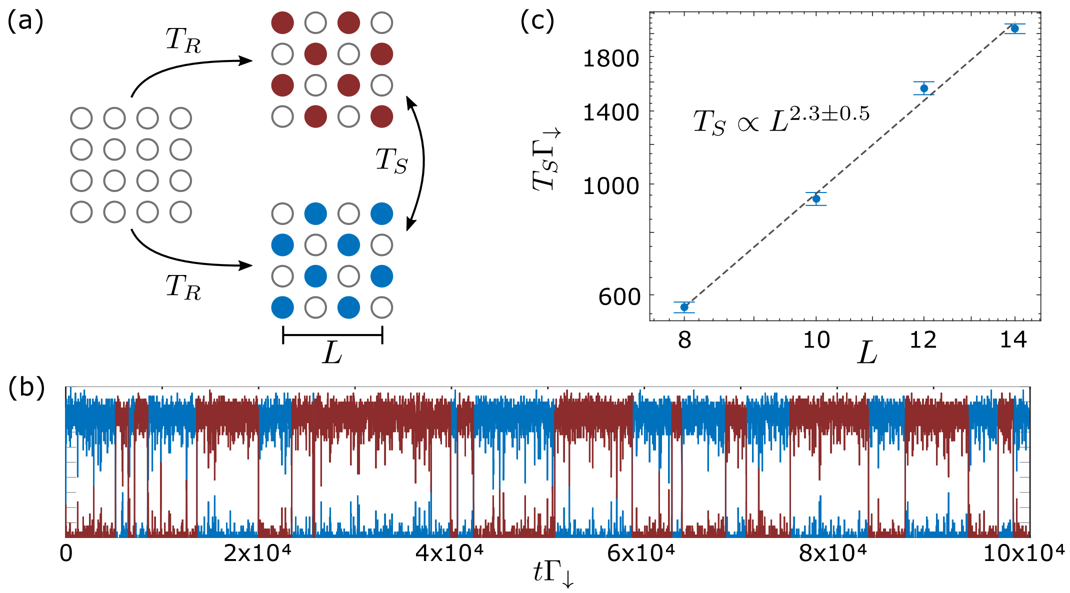

Figure 2.2: (a) Schematic relaxation behavior of the antiferromagnetic open quantum system described in Ref. [59]. The timescale T_R denotes the relaxation timescale to one of the two checkerboard configurations. The timescale T_S describes the switching between the two checkerboard configurations. (b) The time evolution of a single trajectory shows the switching in the occupation number of each sublattice as indicated by the color code in (a). (c) Scaling of the switching time T_S indicated in (a) with linear system size L. The error bars indicate the stochastic uncertainty in the retrieved switching time and the dashed line indicates an algebraic fit function in the system size L. We used $\Gamma_\uparrow/\Gamma_\downarrow = 4$ and thus $p_0 = 0.8$ with periodic boundary conditions.

In total, combining the last two equations we obtain the inequality

$$\sum_d \langle\langle \hat{x}_0, \hat{x}_d \rangle\rangle_{ss} \geq L\, 4p(1-p). \tag{2.19}$$

In general, this can only be fulfilled when $\langle\langle \hat{x}_0, \hat{x}_d \rangle\rangle_{ss}$ approaches a constant value for $d \to \infty$ in the thermodynamic limit $L \to \infty$. Otherwise, for vanishing $\langle\langle \hat{x}_0, \hat{x}_d \rangle\rangle_{ss}$ we can always find a system size L, which violates the above inequality. Unless $p = 0$ or $p = 1$ we have long-range order.

2.1.3 Example: Antiferromagnetic Order in Rydberg Superatom Lattices

To give an example of a phase transition to a bistable mixed steady state, we discuss the Rydberg superatom model of Ref. [59]. It was shown that this system hosts a phase transition from an unordered to an ordered state upon increasing the resonant excitation probability p_0. A 2D lattice composed of Rydberg superatoms is continuously excited to the Rydberg state under conditions of nearest neighbor blockade. In the strong driving regime $p_0 \geq 0.749$ the translational lattice symmetry is spontaneously broken and the Rydberg excitations arrange in one of two checkerboard-type sublattices [106, 107], as indicated in Fig. 2.2a. As will be discussed in Chapter 3, Rydberg superatoms allow for a strong driving strength $p_0 \to 1$. For simplicity, we assume a strong nearest neighbor interaction (hard core) and neglect the quasi long-range van der Waals interaction on the next nearest neighbors. Within this hard core approximation, we can describe the system dynamics with the following Lindblad jump operators

$$\begin{aligned}\hat{L}_{\downarrow}^{(x,y)} &= \sqrt{\Gamma_{\downarrow}}\hat{\sigma}_{gr}^{(x,y)},\\ \hat{L}_{\uparrow}^{(x,y)} &= \sqrt{\Gamma_{\uparrow}}\hat{\sigma}_{rg}^{(x,y)}(\hat{\sigma}_{rr}^{(x-1,y)}-1)(\hat{\sigma}_{rr}^{(x+1,y)}-1)(\hat{\sigma}_{rr}^{(x,y-1)}-1)(\hat{\sigma}_{rr}^{(x,y+1)}-1).\end{aligned} \tag{2.20}$$

This model is reminiscent of a hard core lattice gas [107, 108] with excitation probability $p_0 = \Gamma_{\uparrow}/(\Gamma_{\uparrow}+\Gamma_{\downarrow})$. It is however a stochastic model, where the number of excited hard spheres fluctuates dynamically. For large driving strength $\Gamma_{\uparrow} \gg \Gamma_{\downarrow}$ an antiferromagnetic state emerges, which has long-range order. For any finite system, we have a unique steady state with equal weights for both checkerboard configurations. The initial relaxation time T_R to one of both checkerboard configurations was extracted in Ref. [59] and is schematically sketched in Fig. 2.2a. This time scales with the linear system size L as $T_R \propto L^{2.22\pm0.10}$, where the uncertainty stems from the algebraic fit function. Observing the system on an even longer timescale, we extract a switching time T_S between both checkerboard configurations. As an example, a single trajectory of the system dynamics governed by Eq. (2.20) is shown in Fig. 2.2b. We extract a switching time scaling with the linear system size as

$$T_S \propto L^{2.3\pm0.5} \tag{2.21}$$

and is shown in Fig. 2.2c. Note that both the exponents for relaxation and switching are compatible within their uncertainty in the algebraic fit and diverge in the thermodynamic limit. This indicates a phase transition to a bistable steady state, where the system may relax to any of the two checkerboard configurations. For times $t \lesssim T_R$, the system appears metastable and the state is an admixture of the stationary state $\hat{\rho}_0$ and the first eigenstate $\hat{\rho}_1$ [99].

The results for the exponents are compatible with the dynamical critical exponent in kinetic Ising models without long-range interactions [109, 110]. A simple argument for $\alpha = 2.3 \pm 0.5$ is as follows: To switch the checkerboard configuration a defect line (domain wall) has to move through the whole 2D lattice which implies $\alpha = 2$ and $\alpha > 2$ including fluctuations of the specific system. However, as argued in Ref. [111–113] the switching time attains an exponential correction in the linear system size scaling as $T_S \propto L^{\alpha}\exp(\kappa L)$ in the case of a two-dimensional kinetic Ising model. This is a result of the interfacial tension (included in the constant κ) of one-dimensional domain walls. For the driven Rydberg lattice gas and within the error bars of our numerical data in Fig. 2.2c we cannot verify the existence of exponential corrections which become dominant for large system sizes L.

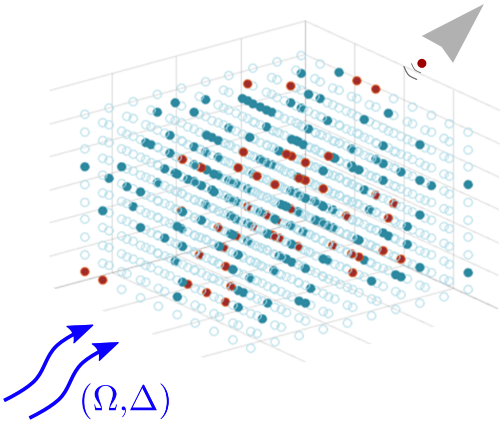

Figure 2.3: Schematic sketch of the experimental setup: Atoms in a large 3D optical lattice are continuously driven to a Rydberg state with Rabi frequency Ω and detuning $\Delta > 0$. Open circles denote atoms in the ground state, red circles in the Rydberg state and blue circles indicate vacancies due to ionization. Ions are guided to a detector by applying a small electric field.

2.2 Characterization of the Experiment

In what follows we describe an experiment performed in the group of Herwig Ott. The study addresses the question whether the observed dynamics in an off-resonantly driven Rydberg gas resembles a metastable or bistable system. This question was discussed inconclusively in many experiments [92–95, 97] and theoretical works [67, 72, 77, 98, 114, 115]. We start with a description of the experiment and a microscopic model. The microscopic model cannot be solved exactly and thus we first construct a simplified cluster model for the excitation dynamics. The model will then be supported by numerical simulations of the full model using a rate equation approximation.

2.2.1 Experiment and Measurement

Rubidium atoms are prepared in a Mott insulating phase in a 3D optical lattice with unit filling. The lattice constant in x- and y-direction is $a_{x,y} = 374\,\mathrm{nm}$ and in z-direction $a_z = 529\,\mathrm{nm}$. The number of atoms in the system is approximately $N_{\mathrm{at}} \simeq 20\,000$. The atomic ground state $|g\rangle = |5S_{1/2}\rangle$ is coupled continuously to a Rydberg state $|e\rangle = |25P_{1/2}\rangle$ via a one-photon transition at a wavelength of $\lambda = 297\,\mathrm{nm}$. The corresponding transition Rabi frequency Ω is varied in the range of $2\pi \times 10\,\mathrm{kHz}$ to $2\pi \times 500\,\mathrm{kHz}$ and the laser is blue detuned up to $\Delta = 2\pi \times 100\,\mathrm{MHz}$. Atoms in the Rydberg state interact with a potential $V(r) = C_p/r^p$. In Fig. 2.3 the experiment is sketched. Additionally we assume the following incoherent contributions: First, the Rydberg state has an effective lifetime of $\tau_s = \Gamma_s^{-1} \simeq 20\,\mu\mathrm{s}$. This lifetime includes black-body induced transitions to other Rydberg states. Second, we estimate a bare decoherence rate of $\gamma_0 \geq 300\,\mathrm{kHz}$. Additional dephasing due to the

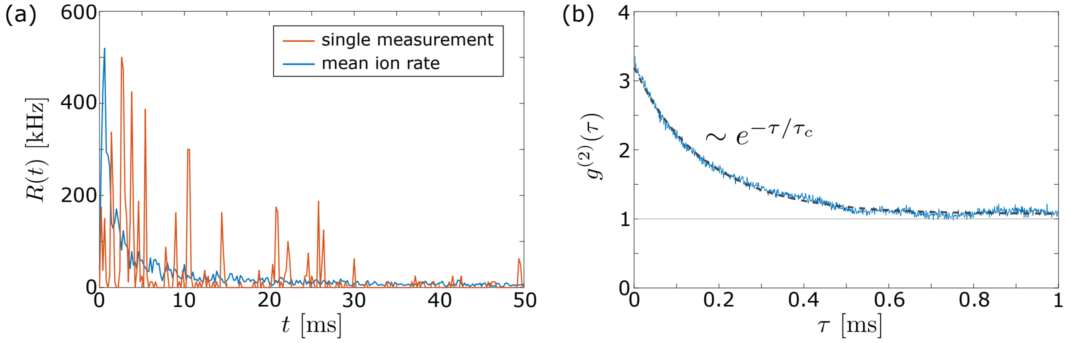

Figure 2.4: (a) Measured ion signal $R(t)$ for a single (red) and averaged-over-40 (blue) experimental realization. The single measurement already indicates strong number fluctuations beyond Poisson-distributed fluctuations. (b) Corresponding second order temporal correlation function $g^{(2)}(\tau)$ from the ionization signal in (a). Experimental parameters are $\Omega = 2\pi \times 77\,\mathrm{kHz}$ and $\Delta = 2\pi \times 13\,\mathrm{MHz}$. The correlation function shows super-Poissonian fluctuations with a bunching amplitude $g^{(2)}(0) \gg 1$.

Rydberg-Rydberg interaction in a lattice with finite width of the trapping potential [116, 117] will be discussed later.

The excitation dynamics is monitored using ionization of Rydberg atoms with small rate $\Gamma_{\mathrm{ion}} = 2\,\mathrm{kHz}$, which stems from photoionization caused by the dipole trap lasers. Ionized atoms produce vacancies in the 3D optical lattice and may therefore alter the excitation dynamics. Using a weak electric field of strength $90\,\mathrm{mVcm}^{-1}$ ions are guided towards a detector. The retrieved ion rate $R(t)$ is proportional to the number of excited Rydberg atoms $N(t)$, corrected by the detector efficiency of 40%,

$$R(t) = \Gamma_{\mathrm{ion}} N(t). \tag{2.22}$$

More details on the experimental setup can be found in Ref. [FL4] and [118]. The experimental observation time $T \simeq 100\,\mathrm{ms}$ is several orders of magnitude larger than the Rydberg state lifetime. This is an indication that the experiment probes the steady state regime. In contrast, other experiments probe the excitation dynamics on timescales $T \simeq 10\,\mu\mathrm{s}$ [92, 93]. We assume that atom loss due to ionization does not alter the steady state properties. The detector signal $R(t)$ is recorded over several individual experimental trajectories.

Using the ion rate $R(t)$ we calculate the ensemble averaged second order temporal correlation function

$$g^{(2)}(\tau) \equiv \frac{\langle R(t+\tau)R(t)\rangle}{\langle R(t+\tau)\rangle\langle R(t)\rangle}. \tag{2.23}$$

Since atoms are lost during the ionization process, the temporal correlation function strictly speaking depends on two points of time. However, atom loss does alter the excitation dynamics only on longer timescales and thus $g^{(2)}(\tau)$ should only depend on the relative time τ between two detector events.

In Fig. 2.4a a typical ionization signal is shown. An individual trajectory (red line) shows strong fluctuations of the Rydberg excitation number. The coarse-grained ion signal (blue line) shows a decreasing ion signal in time displaying the slow atom loss of the system. The corresponding temporal correlation function is shown in Fig. 2.4b. Using an exponential fit function

$$g^{(2)}(\tau) = \left(g^{(2)}(0) - 1\right) e^{-\tau/\tau_c} + 1, \tag{2.24}$$

we extract the two relevant parameters discussed in the following, namely the correlation time τ_c and the bunching amplitude $g^{(2)}(0)$. For a noninteracting system of atoms, the excitation dynamics follows a Poisson distribution and the bunching parameter is $g^{(2)}(0) = 1$ [34, 36]. In this case, the correlation time $\tau_c = \tau_s$ is determined by the Rydberg state lifetime. The experimental data clearly show the fingerprints of a strongly interacting gas of Rydberg atoms with an off-resonant laser excitation scheme. Besides strong excitation bunching $g^{(2)}(0) \gg 1$, an increase in the correlation time $\tau_c \gg \tau_s$ is observed. As will be discussed later in details, this behavior can be attributed to the formation of excitation clusters. While an excitation event in a spatially extended region of ground state atoms is rare using a strongly detuned laser, the first *seed* excitation can trigger an excitation cascade. This leads to a strong bunching in the detected ion signal. Now, the cluster grows and shrinks in time. The size of the cluster is limited by the finite Rydberg state lifetime and collisions with other clusters. Thus, the retrieved correlation time is a measure of the cluster lifetime.

2.2.2 Microscopic Description

We describe the experiment in a system-reservoir approach using the Lindblad master equation introduced in Sec. 1.1. The coherent dynamics of the system is described by a Hamiltonian ($\hbar = 1$)

$$\hat{\mathcal{H}} = \sum_k \left[\Omega\left(\hat{\sigma}^k_{eg} + \hat{\sigma}^k_{ge}\right) - \Delta\hat{\sigma}^k_{ee}\right] + \sum_{k>k'} V(\mathbf{r}_k, \mathbf{r}_{k'})\, \hat{\sigma}^k_{ee} \otimes \hat{\sigma}^{k'}_{ee}. \tag{2.25}$$

We assume a spatially and temporally uniform laser field driving the transition between ground state $|g\rangle$ and Rydberg state $|e\rangle$ with laser carrier frequency ω and Rabi frequency Ω. In particular, we are interested in the excitation dynamics for large detunings $\Delta = \omega - \omega_{ge} \gg \Omega$, where ω_{ge} is the atomic transition frequency. Here, $\hat{\sigma}^k_{eg} = |e\rangle_k \langle g|$ denote the atomic transition and $\hat{\sigma}^k_{ee} = |e\rangle_k \langle e|$ the projection operators to the Rydberg state of the kth atom. Atoms in their Rydberg state interact via a potential $V(r) = C_p/r^p$. The potential curves for two atoms at distance r were calculated by Oliver Thomas and are shown in Fig. 2.5a. To this end, an exact diagonalization of the interaction Hamiltonian up to quadrupole-quadrupole interaction was used in a subspace containing ~ 1600 pair states in the energetic vicinity of the state $|ee\rangle$ [119]. Since the experiment operates on small length scales $a_{x,y}$ (compared to the extent of the Rydberg wavefunction) we expect deviations from a van der Waals type scaling with $p = 6$. Indeed, we fit a repulsive interaction curve and obtain an approximate

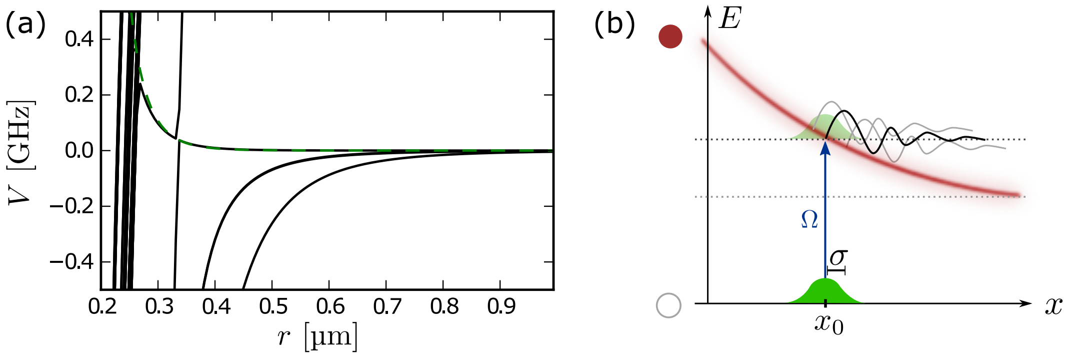

Figure 2.5: (a) Interaction potentials of the pair state $|25P_{1/2}, 25P_{1/2}\rangle$ obtained from exact diagonalization of the interaction Hamiltonian up to quadrupole-quadrupole interaction. The different potential curves correspond to different superpositions of m_j states. We fit a repulsive interaction curve (green dashed line) $V(r) = C_9/r^9$ with $C_9 = 2\pi \times 2.1\,\mathrm{kHz µm}^9$. (b) Schematic of the inhomogeneous broadening. The ground state atom wavefunction (green shaded region) has a finite width σ. Using an off-resonant excitation scheme, the effective detuning $\Delta - V(x)$ depends strongly on the distance x between ground state and Rydberg state atom. The coupling to the manifold of scattering states (black line) introduces an effective broadening mechanism.

scaling $V(r) = C_9/r^9$ with $C_9 \simeq 2\pi \times 2.1\,\mathrm{kHz\,µm}^9$. Note that a black-body induced transition to neighboring Rydberg states may introduce a second energy scale stemming from resonant dipole-dipole interactions. This drastically increases the complexity of the problem and we do not include these effects in the description.

Furthermore, let us discuss incoherent contributions to the system dynamics. First, we include the finite Rydberg state lifetime. We model this process using a Lindblad jump operator of the kth atom from the Rydberg state back to the ground state,

$$\hat{L}_s^k = \sqrt{\Gamma_s}\hat{\sigma}_{ge}^k. \tag{2.26}$$

Second, we include the ionization of Rydberg atoms leading to atom loss. We mimic this process by a transition to an auxiliary state $|a\rangle$ which is decoupled from the system dynamics,

$$\hat{L}_{\mathrm{ion}}^k = \sqrt{\Gamma_{\mathrm{ion}}}\hat{\sigma}_{ae}^k. \tag{2.27}$$

An atom transferred to the auxiliary state $|a\rangle$ is decoupled from the residual excitation dynamics. Therefore, this process is similar to an atom loss. Next, we include dephasing of the Rydberg state by a Lindblad jump operator,

$$\hat{L}_d^k = \sqrt{\Gamma_d}\hat{\sigma}_{ee}^k, \tag{2.28}$$

with $\gamma_0 = \frac{1}{2}(\Gamma_s + \Gamma_d) \simeq \Gamma_d/2$. Furthermore, we include an additional inhomogeneous broadening mechanism, which is discussed below and results from a finite spatial distribution of atoms with width σ and the strong Rydberg-Rydberg interaction [116, 117]. To this end, we add to the bare decoherence rate γ_0 an inhomogeneous broadening rate depending on the positions of all surrounding excited Rydberg atoms,

$$\gamma = \gamma_0 + \sum_{j'} \left|\partial_r V(r = r_j)\right| \sigma/\sqrt{\pi}. \tag{2.29}$$

In the experimental relevant parameter regime, dephasing is dominant, i.e. $\gamma \gg \Omega$. Thus, a rate equation approximation as discussed in Sec. 1.1.2 is suitable for the numerical simulation of the excitation dynamics [31, 34].

Inhomogeneous broadening

We can give an intuitive explanation of the additional dephasing mechanism Eq. (2.29) in a 1D lattice geometry. As shown in Fig. 2.5b a ground state atom is excited to a Rydberg state in the presence of a Rydberg atom fixed at position $x = 0$. The effective detuning of the ground state atom $\Delta - V(x)$ depends sensitively on the atomic position x. Atoms in an optical lattice are localized within a finite spatial width σ. Importantly, a steep gradient $\partial_x V(x)$ of an interaction potential $V(x)$ on the relevant length scale σ can introduce a broad energy scale and a strong mechanical force. As discussed in Ref. [116, 117] the coupling to the manifold of scattering states with different energies introduces then a strong decoherence mechanism in the excitation dynamics. Here, we will justify the inhomogeneous broadening introduced in Ref. [116, 117] using a simpler semi-classical ansatz.

The rate equation approach assumes point-like atoms. In this case, we can cast the excitation rate of a ground state atom at position x in the presence of an already excited Rydberg atom at position $x = 0$ as

$$\Gamma_\uparrow^0(x) = \frac{2\Omega^2\gamma_0}{\gamma_0^2 + (\Delta - V(x))^2}. \tag{2.30}$$

Now, we consider a ground state atom trapped in an optical lattice. Note that Rydberg atoms are typically not trapped [120]. In a semi-classical approximation we analyze the excitation rate weighted by a probability distribution $p(x)$ for finding an atom centered around the position x_0 with width $\sigma = 60\,\mathrm{nm}$. A derivation of the experimental trap width can be found in Appendix A. The resulting excitation rate

$$\Gamma_\uparrow = \int_{-\infty}^{\infty} \mathrm{d}x \; p(x)\, \Gamma_\uparrow^0(x) \tag{2.31}$$

strongly depends on the spatial width σ. In Fig. 2.6a we show $\Gamma_\uparrow$ for different lattice distances x_0 to the Rydberg state using typical experimental parameters versus the detuning Δ. For distances $x_0 \gtrsim 2a_x$ the effect of the Rydberg level shift is negligible. However, for the nearest neighbor ($x_0 = a_x$) and next nearest neighbor ($x_0 = \sqrt{2}a_x$) we observe a strong broadening and suppression of the excitation rate for blue detuning $\Delta > 0$. In the case where we are close to the resonance, i.e. when $\Delta \simeq V(x_0)$,

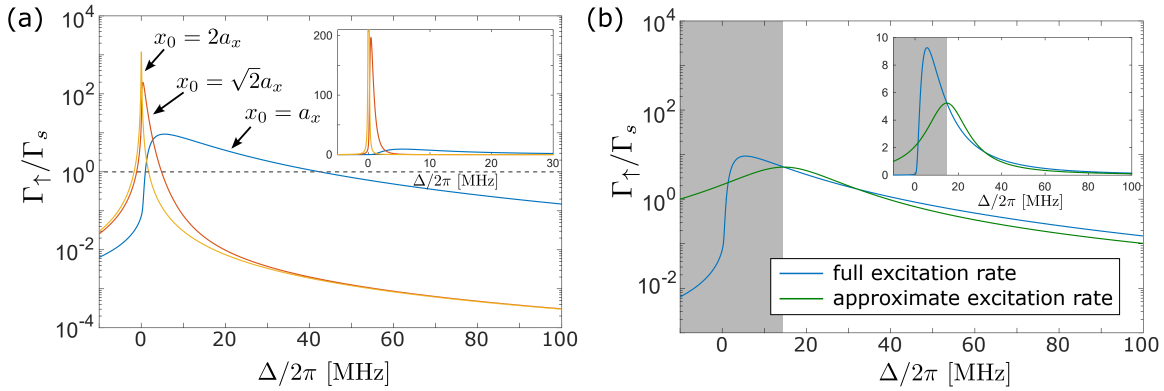

Figure 2.6: (a) Excitation rate versus detuning Δ in Eq. (2.31) for three relevant lattice distances x_0. The Rabi frequency is $\Omega = 2\pi \times 500\,\text{kHz}$ and the bare decoherence rate is $\gamma_0 = 300\,\text{kHz}$. We use the fitted interaction coefficient from Fig. 2.5. The excitation rate for $x_0 = 2a_x$ matches already the uncorrelated excitation rate for $x_0 \to \infty$. (b) Comparison of the full excitation rate Eq. (2.31) and the approximate excitation rate using the inhomogeneous decoherence rate Eq. (2.29). We use the same parameters as in (a) with $x_0 = a_x$. While for $\Delta/2\pi \gtrsim 18\,\text{MHz}$ both rates agree well, the rates differ substantially for $\Delta/2\pi \lesssim 18\,\text{MHz}$ (gray shaded area) . Insets: Some plot with linear scale.

we can approximate the excitation rate Eq. (2.31) using a linear interaction potential. In this limit we obtain a suppressed excitation rate $\Gamma_\uparrow \simeq \frac{2\Omega^2}{\gamma_{\text{inh}}}$ with $\gamma_{\text{inh}} = |\partial_x V(x = x_0)|\,\sigma/\sqrt{\pi}$ [116]. However, as discussed in Ref. [117] the linearized interaction potential cannot describe the excitation rate for all detunings.

In general, we have to evaluate a 3D integral taking into account the interaction shift of all excited Rydberg atoms at positions $\mathbf{r}_j$. Consider a ground state atom localized at position $\mathbf{r}$ with spatial distribution $p(\mathbf{r})$. Then we can cast Eq. (2.31) as

$$\Gamma_\uparrow = \int \mathrm{d}^3\mathbf{r}\; p(\mathbf{r})\, \frac{2\Omega\gamma_0}{\gamma_0^2 + \left(\Delta - \sum_j V(\mathbf{r}, \mathbf{r}_j)\right)^2}, \tag{2.32}$$

where the sum in the denominator includes all positions $\mathbf{r}_j$ of Ryberg excited atoms. The numerical evaluation of a 3D integral for $N_{\text{at}} \gg 1$ atoms using a stochastic rate equation model is challenging. Instead, we replace the bare decoherence rate γ_0 in Eq. (2.30) with a rate including the inhomogeneous broadening γ_{inh} as per Eq. (2.29). The decoherence rate γ depends on the position of all excited Rydberg atoms and can be easily evaluated for large-scale numerical simulations. In Fig. 2.6b we compare this ansatz with the full excitation rate $\Gamma_\uparrow$ as per Eq. (2.31). This suggests that for detunings $\Delta \gtrsim 2\pi \times 18\,\text{MHz}$, both excitation rates agree well. However, for $\Delta \lesssim 2\pi \times 18\,\text{MHz}$ the approximate decoherence rate γ is not valid and both excitation rates deviate substantially. This indicates that the approximate decoherence rate is a good estimate of the excitation rates for $\Delta \gtrsim 2\pi \times 18\,\text{MHz}$.

Besides the inhomogeneous broadening we include in the simulated excitation dynamics an uncorrelated background noise signal with rate Γ_n. The noise follows a Poisson distribution with mean time Γ_n^{-1} between two subsequent events. In particular for large detunings, where all excitation rates are suppressed, noise has a strong influence on the second order correlation function $g^{(2)}(\tau)$. For our discussion we choose a noise rate $\Gamma_n = 1\,\mathrm{kHz}$, which is of similar magnitude than the ionization rate Γ_{ion}. Noise may originate from atoms trapped in the outer region of the optical lattice. Since the atomic density falls off exponentially, the mean particle distance is larger and Rydberg atoms do not interact with each other. The noise signal may depend on Ω and Δ, which we disregard from now on.

We perform stochastic rate equation simulations on a lattice with up to $N_{\text{at}} = 8000$ atoms using the approximations described above. A snapshot of a 3D lattice is shown in Fig. 2.3 including excited atoms (in red) and ionized atoms (in blue). Open circles denote ground state atoms. Already for $N_{\text{at}} = 1000$ finite size effects are reduced. We use the simulated Rydberg excitation signal to calculate the second order temporal correlation function $g^{(2)}(\tau)$. As discussed later on, the results are then compared to the experimental data.

2.3 Single Cluster Model & Dynamics in a 1D lattice

Before we turn to the discussion of the experiment and their full numerical simulation, we start the discussion of the excitation dynamics using a simplified 1D model. Consider a chain of atoms in an equidistant lattice described by the Hamiltonian (2.25). We include only finite Rydberg state lifetime and strong dephasing as per Eq. (2.26) and (2.28). In particular, we discuss the steady state properties in a regime of strong decoherence. The simplified cluster model is capable of describing many of the experimentally accessible observables. Later, we compare this simple model to the experimental data.

2.3.1 Facilitation and Timescales

Consider a blue detuned ($\Delta > 0$) excitation laser and a repulsive interaction potential $V(r)$. In the so called facilitation regime [25, 26, 89], the Rydberg-Rydberg interaction shift is compensated by the detuning Δ leading to an enhanced excitation mechanism. Suppose two atoms are separated by a distance a. We denote the ground state with $|g\rangle$ and the excited Rydberg state with $|e\rangle$. As shown in Fig. 2.7a and in Ref. [77, 121] there are two different excitation scenarios: (i) shows a two-photon transition ($|gg\rangle \leftrightarrow |ee\rangle$) which is resonant at $2\Delta = V(r)$. Here, the resulting effective Rabi frequency scales as $\sim \Omega^2/\Delta$ and is therefore suppressed for $\Omega/\Delta \ll 1$. (ii) corresponds to a two-step process ($|gg\rangle \rightarrow |ge\rangle \rightarrow |ee\rangle$), where a first atom is excited off-resonantly with a small probability $\sim \frac{\Omega^2}{\Delta^2}$, followed by a subsequent fast excitation at $\Delta = V(r)$.

Both processes can be distinguished by probing the full spectrum of small lattice systems with

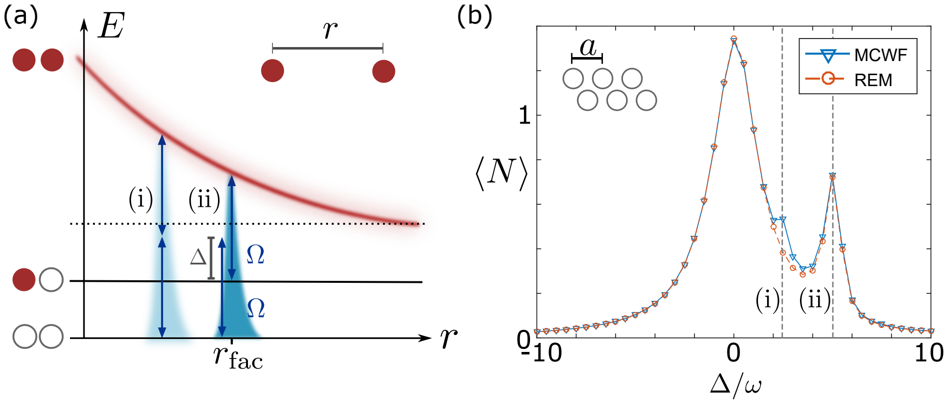

Figure 2.7: (a) Schematics of the two different facilitation mechanisms in the antiblockade regime. Ground state atoms are indicated by open circles and Rydberg states by red circles. In (i) the laser couples via a two-photon transition from the ground state $|gg\rangle$ to the two Rydberg excitation state $|ee\rangle$. In (ii) a two-step excitation is indicated. (b) The steady state Rydberg excitation number $\langle N\rangle$ is shown versus the detuning Δ. For a small 2D lattice indicated in the inset, we compare an approximate rate equation method (REM) to a full Monte Carlo wavefunction (MCWF) approach. The parameters are $\Gamma_d/\Omega = 1.5$, $\Gamma_s/\Omega = 0.1$ and $V(a) = 5w$ where a is the lattice constant and w the single particle linewidth. Apart from the two-photon transition (i) the REM agrees well with the MCWF simulations.

discrete resonance peaks. In Fig. 2.7b we show the mean number of Rydberg atoms $\langle N\rangle$ using an exact numerical simulation. The configuration consists of 6 atoms arranged in a small 2D lattice as indicated in the inset. Probing the spectrum we can identify (i) the two-photon excitation mechanism at $\Delta = V(a)/2$ and (ii) the two-step excitation mechanism at $\Delta = V(a)$. In addition, we compare the exact result to a rate equation approach introduced in Sec. 1.1.2. The rate equation model matches very well the mean excitation number for a broad range of detunings. The coherent two-photon transition (indicated by the gray dashed line (i) in Fig. 2.7b) cannot be described by a rate equation approach and thus leads to a small error. For strong decoherence $\gamma \gg \Omega^2/\Delta$, the two-photon process is highly suppressed and can be neglected in the further discussion. Importantly, for our further discussions the two-step excitation process is the most relevant one and is well described by the rate equation approximation.

Consequently, we deduce the relevant timescales in the facilitation regime using the rate equation model. To start with, the timescale for an initial *seed* excitation is determined by the seed rate

$$\Gamma_{\text{seed}} = \frac{2\Omega^2\gamma}{\gamma^2 + \Delta^2}. \tag{2.33}$$

For a system containing L atoms, we expect a first excitation within τ_{seed}/L, where $\tau_{\text{seed}} = \Gamma_{\text{seed}}^{-1}$.

The seed process is strongly suppressed whenever $\Omega/\Delta \ll 1$. Suppose we have a second atom with distance a to the first one. The excitation rate of the second atom is modified by the presence of the first excited Rydberg atom. Including the interaction strength $V(a)$, we obtain an excitation rate

$$\Gamma_{\uparrow} = \frac{2\Omega^2\gamma}{\gamma^2 + (\Delta - V(a))^2}. \tag{2.34}$$

The rate $\Gamma_{\uparrow}$ is peaked at $\Delta = V(a)$. Upon changing the detuning Δ, we can change the ratio $\Gamma_{\uparrow}/\Gamma_{\mathrm{seed}}$. For $\Gamma_{\uparrow} \gg \Gamma_{\mathrm{seed}}$, i.e. $\Delta \simeq V(a)$, we expect an excitation avalanche in a large lattice system. This will lead to the formation of large excitation clusters [90, 92, 93]. For $\Gamma_{\uparrow} \lesssim \Gamma_{\mathrm{seed}}$ we expect primarily uncorrelated excitation events. Besides the rates $\Gamma_{\uparrow}, \Gamma_{\mathrm{seed}}$, we also have to take into account deexcitation. Having two excited neighboring Rydberg atoms, each of them decays with rate $\Gamma_{\downarrow} + \Gamma_s$, where the induced deexcitation rate is $\Gamma_{\downarrow} = \Gamma_{\uparrow}$ and Γ_s is the decay rate of the Rydberg state. Here, we are interested in a regime, where we have the following hierarchy of rates,

$$\Gamma_{\mathrm{seed}} \ll \Gamma_s \ll \Gamma_{\uparrow}, \Gamma_{\downarrow}, \tag{2.35}$$

corresponding to facilitated excitation dynamics.

2.3.2 Single Cluster Model

Now, we discuss the microscopic dynamics of the birth, growth and decay of a single cluster starting from an initial seed excitation. The detuning is chosen to compensate the interaction shift for the neighboring atoms, i.e. $\Delta = V(a)$. As an example we show in Fig. 2.8a configurations of the initial dynamics as well as the relevant transition rates. The first seed is the starting point of the cluster formation process with a cluster size $m = 1$. This triggers a fast excitation cascade of the two neighboring atoms in the 1D chain with distance a. The number of facilitated ground state atoms is mainly determined by the geometry of the system. In the 1D chain facilitated excitations occur at both ends of the cluster and we introduce a coordination number $z_0 = 2$. Thus, we have a transition rate $z_0\Gamma_{\uparrow}$ between a configuration with cluster size $m = 1$ to a cluster with $m = 2$. The excitation cluster may shrink again with rate $z_0(\Gamma_{\uparrow} + \Gamma_s)$ which includes that each of the two atoms can decay spontaneously. Without the spontaneous decay rate Γ_s, the cluster dynamics renders a random walk where the spreading is proportional to $\sim \sqrt{z_0\Gamma_{\uparrow}t}$. In our example in Fig. 2.8a, the cluster grows further with rate $z_0\Gamma_{\uparrow}$ to a cluster with size $m = 3$. Then, a spontaneous decay of the middle Rydberg states splits the cluster into two parts. Importantly, the reexcitation of the middle ground state atom is highly suppressed and happens only with the very small seed rate Γ_{seed}. While one of the neighboring Rydberg states compensates the detuning, the second Rydberg excitation leads to an additional energy shift $V(a)$ and therefore reduces the excitation rate again. Hence, we can assume that the two parts of the cluster cannot merge to a single one on the relevant timescale of the

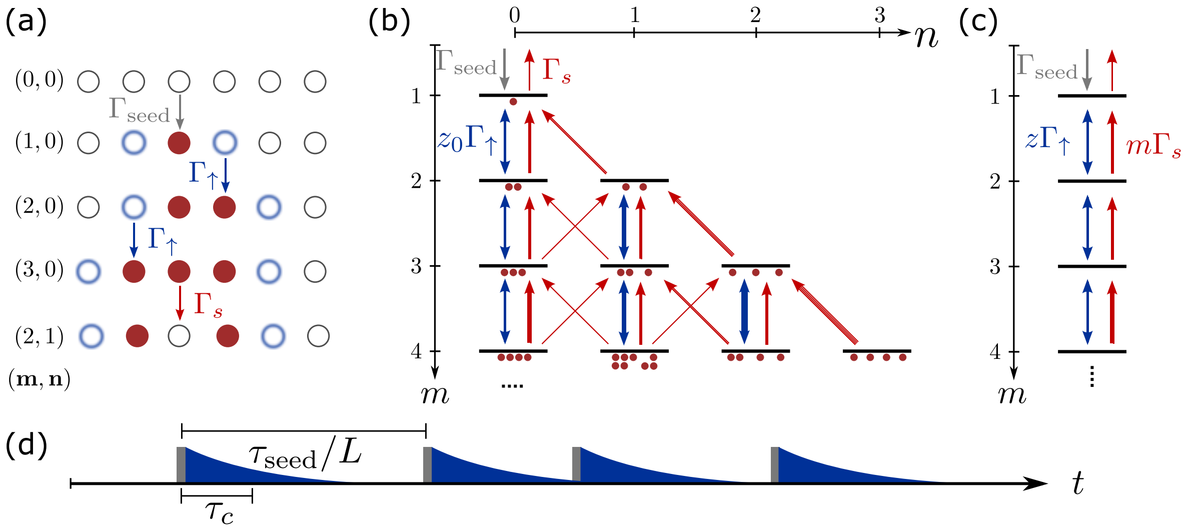

Figure 2.8: (a) Sketch of the initial dynamics of a single cluster starting from a seed excitation. Red circles correspond to Rydberg excitations and white open circles to ground state atoms. Facilitated atoms are indicated with a blue glowing ring. In the last configuration, the two Rydberg states prevent the excitation of the atom in the middle. Thus, a cluster which is split cannot merge. (b) The configuration space can be spanned by the size of the cluster m and the number of splittings n. The transition rates between different configurations are indicated by arrows. The thickness of the arrows indicates the strength of the transition. (c) Simplified cluster model projecting to the cluster size axis. To this end the bare geometric coordination number z_0 is replaced by an effective coordination number z. (d) Sketch of the cluster dynamics. The temporal separation between two seeded excitations is determined by τ_{seed}. The lifetime of the corresponding cluster is determined by τ_c.

cluster dynamics. In principle the two parts perform their own random walk and may separate from each other. If the separation is larger than two lattice sites, each constituent will contribute to an increase in the coordination number. In Fig. 2.8b we illustrate various transitions in a small part of the configuration space spanned by the cluster size m and the number of splittings n.

We are mostly interested in the cluster size m and not in the internal microscopic structure of an individual cluster. Thus, we disregard the number of splittings n and project the cluster dynamics to the cluster size axis m, see Fig. 2.8c. In the weak driving regime clusters are small and splittings can be neglected. In this case we approximately have a constant coordination number z_0. However, for stronger driving we expect that splitting of clusters becomes important and thus we can no longer neglect the impact of an increased coordination number. To this end, we introduce a single effective coordination number z, which will be determined self-consistently later. This allows us to obtain a simple cluster model as sketched in Fig. 2.8c, which is still valid at stronger drive. The equations of

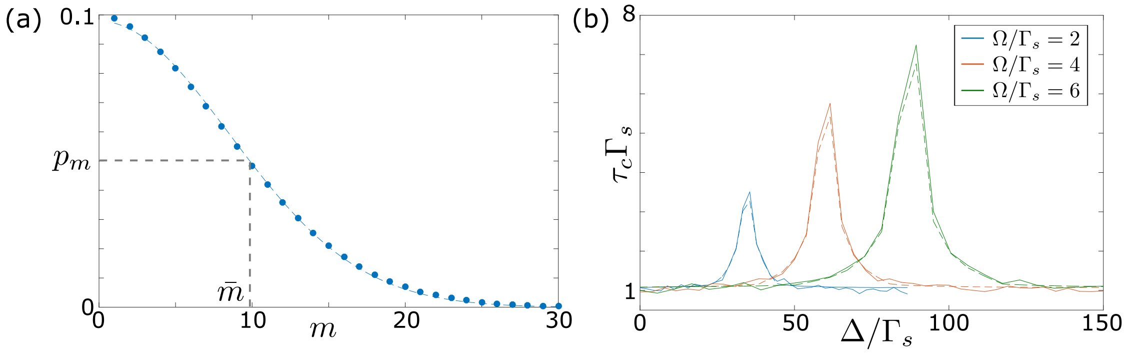

Figure 2.9: (a) Quasi-equilibrium distribution p_m of the cluster size m. The parameters are $\gamma/\Gamma_s = 2$, $\Omega/\Gamma_s = 6$, $z = 2$ and $V(a) = \Delta = 10w$, where w is the single atom linewidth. We use the full width half maximum value $\bar{m}$ as an estimate for a typical cluster size. (b) Comparison of Monte Carlo simulations (solid lines) of the cluster lifetime using Eq. (2.36) and the quasi-equilibrium distribution (dashed lines) with Eq. (2.37). The parameters are the same as in (a) with varying Rabi frequency Ω. The simulations include 1000 individual trajectories. Error bars are small and neglected for simplicity.

motion for the probabilities p_m of having a cluster of size $m \geq 0$ are

$$\partial_t p_0 = -L\Gamma_{\text{seed}} p_0 + \Gamma_s p_1, \tag{2.36a}$$

$$\partial_t p_1 = +L\Gamma_{\text{seed}} p_0 - (z\Gamma_\uparrow + \Gamma_s) p_1 + (z\Gamma_\uparrow + 2\Gamma_s) p_2, \tag{2.36b}$$

$$\partial_t p_m = +z\Gamma_\uparrow p_{m-1} + (2z\Gamma_\uparrow + m\Gamma_s) p_m + (z\Gamma_\uparrow + (m+1)\Gamma_s) p_{m+1} \quad \text{for } m \geq 2. \tag{2.36c}$$

To estimate the lifetime of a single cluster we precede in two ways: First, we use a stochastic Monte Carlo simulation of the Eq. (2.36) and measure the cluster lifetime distribution using many individual realizations. The distribution decays exponentially and we extract the lifetime τ_c by an exponential fit $\sim \exp(-t/\tau_c)$. Second, we use the probability distribution p_m to retrieve a typical cluster size $\bar{m}$. We conjecture that the approximate lifetime is determined by

$$\tau_c = \bar{m}/\Gamma_s. \tag{2.37}$$

Intuitively, it requires on average $\bar{m}$ consecutive decay events of timescale τ_s for the cluster to vanish. This heuristic approach will be compared to full-scale stochastic cluster simulations later on.

To obtain a stationary probability distribution of a single cluster we have to neglect the initial creation process with rate Γ_{seed} and the final cluster annihilation process with rate Γ_s. In this way we project to the case of having always one cluster. We consider the case where the rate $\Gamma_\uparrow \gg \Gamma_s, \Gamma_{\text{seed}}$ is much faster such that the system relaxes to a quasi-equilibrium state before it finally decays. Then,

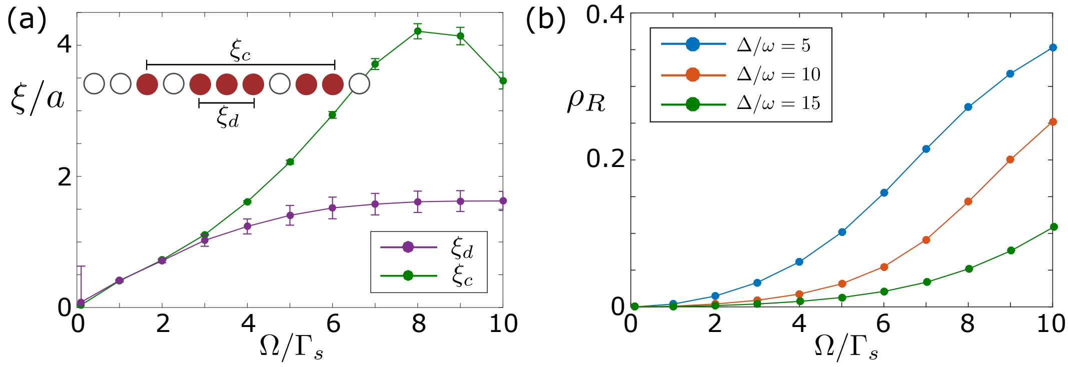

Figure 2.10: (a) Correlation length ξ_c and Rydberg state chain length ξ_d versus the Rabi frequency Ω in a system with parameters $\Gamma_d/\Gamma_s = 10$, $\gamma = \Gamma_s/2 + 2\Gamma_d$ and $V(a) = \Delta = 10w$, where $w = \sqrt{4\Omega^2\gamma/\Gamma_s + \gamma^2}$ is the linewidth. The system size is $L = 1000$ with periodic boundary conditions. (b) Rydberg excitation density ρ_R versus Rabi frequency Ω for different detuning Δ. For each detuning we set interaction strength $V(a) = \Delta$. Other parameters as in (a).

assuming detailed balance we obtain a recursive relation for the cluster distribution

$$p_m = \frac{z\Gamma_\uparrow}{z\Gamma_\uparrow + m\Gamma_s} p_{m-1}. \tag{2.38}$$

With the additional constraint $\sum_{m\geq 1} p_m = 1$, we can determine all probabilities p_m. As an example we show the quasi-equilibrium distribution p_m in Fig. 2.9a. We use the full width half maximum value $\bar{m}$ as a definition of the cluster size in Eq. (2.37). Finally, we compare the stochastic simulations and the cluster distribution ansatz in Fig. 2.9b and find excellent agreement. In turn, we now can estimate a typical cluster size $\bar{m}$ from the measurement of the lifetime τ_c.

2.3.3 Full Numerical Simulation

Using the rate equation approximation, we simulate the facilitated excitation dynamics in a large 1D chain. We observe the system for timescales $T \gg \tau_s$ and thus probe the steady state. Numerically, we checked that for system sizes $L \gg 100$ finite size effects are negligible. Using the rate equation simulation we have access to the microscopic details of the Rydberg excitation clusters. To this end, we calculate the second order spatial correlation function (defined on a discrete lattice)

$$g^{(2)}(d) = \frac{\langle \hat{\sigma}^i_{ee} \hat{\sigma}^{i+d}_{ee} \rangle}{\langle \hat{\sigma}^i_{ee} \rangle \langle \hat{\sigma}^{i+d}_{ee} \rangle}. \tag{2.39}$$

Using an exponential fit similar to Eq. (2.24) we extract a correlation length ξ_c. As long as different clusters are spatially separated, the correlation length ξ_c is a measure of the cluster extent. Additionally, we extract a length scale ξ_d for the individual constituents of a cluster. We calculate a probability distribution p_l for having a Rydberg excitation chain of length $l \geq 1$. Using an exponential fit $\sim \exp(-(l-1)/\xi_d)$ we obtain a length scale for the constituents ξ_d. In Fig. 2.10a we compare both length scales for different driving strength Ω. For the discussed parameter regime all correlation length are small $\xi_c, \xi_d \ll L$ and we do not have long-range order. For weak driving $\Omega/\Gamma_s \lesssim 3$ both correlation length are similar, $\xi_c \simeq \xi_d$. This is intuitive, since in the weak driving regime clusters are small and the splitting of clusters can be neglected. For larger driving strength, the cluster extent ξ_c grows while the length of the individual constituents saturates at $\xi_d \leq 2$. The correlation length reaches a maximum at $\Omega/\Gamma_s \simeq 8$ and decreases then. This can be attributed to cluster collisions and will be explained later on.

In Fig. 2.10b we show the Rydberg excitation density $\rho_R = \sum_j \langle \hat{\sigma}_{ee}^j \rangle / L$ for varying Ω/Γ_s and different interaction strengths $V(a) = \Delta$. As expected, the excitation density ρ_R increases with increasing Rabi frequency Ω. With an increase in the detuning Δ the seed time τ_{seed} increases as well, see Fig. 2.8d. This is the relevant timescale with which new clusters are created. For larger seed time, the number of clusters and thus the number of Rydberg excitations is reduced. Note that the Rydberg excitation density is bounded by $\rho_R \leq 0.5$.

We now analyze the $g^{(2)}(\tau)$ function defined in Eq. (2.23), which is a measure of the temporal correlations in the Rydberg excitation signal. In particular we extract the correlation timescale τ_c and the bunching amplitude $g^{(2)}(0)$. The timescale τ_c measures the time of correlated excitation growth. While individual seed excitations are Poisson distributed, the subsequent excitation cascade will be identified in the correlation time τ_c. Thus, measuring τ_c allows to quantify the lifetime of a cluster and a typical cluster size.

To compare these results to the simple cluster model, we first determine the coordination number z as discussed above in a self-consistent way. While the bare coordination number $z_0 = 2$ stems from the geometry of the lattice, we have to include an increase in z due to splitting of clusters. We presume the number of splittings increases with the cluster lifetime and set

$$z = z_0 + \frac{\tau_c - \tau_s}{\tau_s}. \tag{2.40}$$

We use this ansatz to evaluate the cluster model and compare it to our full rate equation description. In Fig. 2.11a we show the cluster lifetime versus the Rabi frequency Ω for three different interaction strength. While for small driving $\Omega/\Gamma_s \lesssim 3$ all curves, including the result from the cluster model (dashed line) match, for stronger driving deviations occur. These can be attributed to cluster collisions which become more important for smaller detunings Δ. To understand this, let us consider first the rates needed for determining the cluster size distribution $\Gamma_\uparrow, \Gamma_s$. Both are independent on the detuning for $\Delta = V(a)$ and the single cluster model estimates the cluster lifetime τ_c independent on the detuning Δ, as shown in Fig. 2.11a (dashed line). However, the seed rate Γ_{seed} scales as $\sim \frac{1}{\Delta^2}$

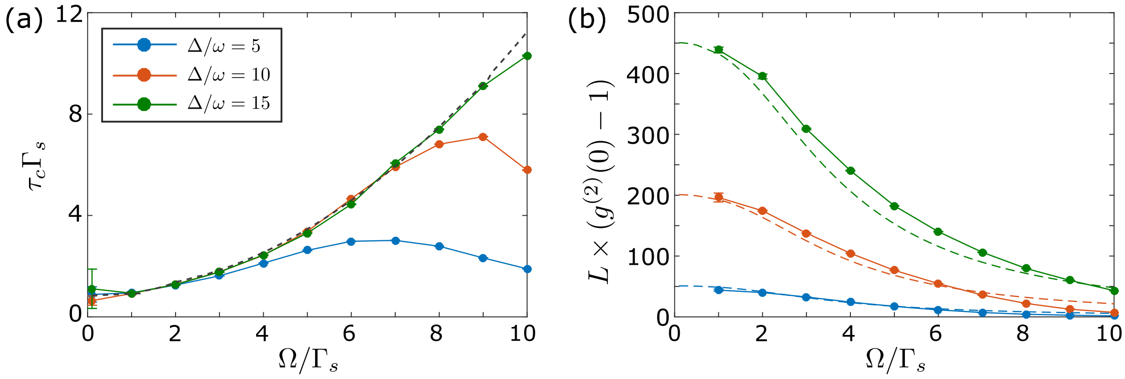

Figure 2.11: Evaluation of the second order temporal correlation function $g^{(2)}(\tau)$ using the same parameters as in Fig. 2.10. Dashed lines correspond to results of the single cluster model. We use $z \simeq z_0 + (\Omega/\Gamma_s)^2/8$ from the initial correlation time growth with Ω/Γ_s as per Eq. (2.40). (a) The correlation time τ_c as per Eq. (2.24) versus the driving strength Ω/Γ_s (b) The bunching amplitude $(g^{(2)}(0) - 1)$ scaled by the system size L versus the driving strength Ω/Γ_s.

and thus for smaller detuning more clusters are created. The increase in the number of clusters will lead to cluster collisions and limit the free growth of excitation clusters. Comparing the maximal cluster lifetime to the Rydberg density in Fig. 2.10 we deduce a critical Rydberg excitation density $\rho_R \simeq 0.2$, where cluster collisions become important. A detailed analysis of the interactions between clusters is beyond the scope of this thesis.

Finally, let us consider the bunching amplitude of the temporal correlation function shown in Fig. 2.11b. The value $g^{(2)}(0) - 1$ measures intrinsic fluctuations of the system. These fluctuations stem from the competition between processes occurring on different timescales, namely a slow seed process and a fast excitation cascade. Note that the bunching amplitude scales with the inverse system size L. To compare the bunching value to our cluster model we scale it with the system size. We interpret the scaled value $L \times (g^{(2)}(0) - 1)$ as a measure for intrinsic fluctuations of a single cluster. Using the cluster size distribution in Eq. (2.38) we can easily evaluate

$$g^{(2)}(0) = \frac{\langle m(m-1)\rangle}{\langle m\rangle^2}. \tag{2.41}$$

Since now the initial seed process is relevant for determining fluctuations, we include creation and annihilation of a single cluster from Eq. (2.36) and normalize the probability distribution accordingly, i.e. $\sum_{m\geq 0} p_m = 1$. We find good agreement between the numerical simulation and the cluster model. Hence, we believe that also fluctuations are well described by the cluster model. The bunching parameter decreases with increasing driving strength Ω, which can be explained as follows: First, the seed time $\tau_{\text{seed}} \sim \frac{\Delta^2}{\Omega^2}$ shrinks leading to the creation of many independent clusters. Second, the

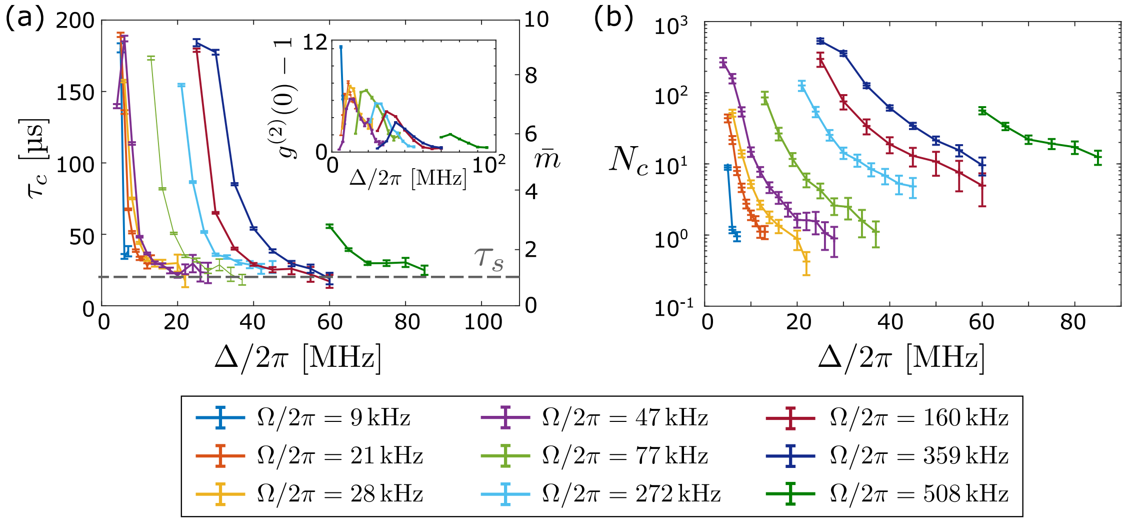

Figure 2.12: (a) Experimentally measured correlation time τ_c versus detuning Δ for different Rabi frequencies Ω. The right axis denotes the corresponding cluster size $\bar{m}$ per Eq. (2.37). The gray dashed line indicates the Rydberg state lifetime τ_s. Inset: Corresponding bunching amplitudes $g^{(2)}(0)-1$. Error bars correspond to the uncertainty in the exponential fit Eq. (2.24). (b) Experimentally determined number of clusters N_c as per Eq. (2.42) versus detuning Δ for different Rabi frequencies Ω.

lifetime of each cluster grows as well. Both increase the number of Poisson distributed events and therefore reduce $g^{(2)}(0)-1$.

2.4 Experimental Results & Cluster Dynamics in 3D Lattices

Now, we turn back to the original question whether the steady state properties observed in the experiment can be attributed to a bistable or metastable phase. We use the cluster model presented in the previous section to interpret the experimental data. While the cluster model was a good approximation to the full system dynamics in a 1D chain, we have to verify it using the 3D experimental data. Using a rate equation model, we discuss hysteresis behavior and Rydberg number distributions which are not directly accessible in the experiment.

2.4.1 Experimental Results

Cluster size

The experimental results of the second order temporal correlation function are shown in Fig. 2.12a. Using the cluster model we extract a typical cluster size $\bar{m}$ versus the detuning Δ for various Rabi frequencies Ω. As seen in the 1D chain, by increasing the driving strength, the cluster size increases.

Experimentally, we retrieve a maximal cluster size $\bar{m} \leq 10$. For large detunings all rates are strongly suppressed and we obtain a cluster size of $\bar{m} \simeq 1$ corresponding to an uncorrelated Rydberg excitation. Decreasing the detuning Δ the cluster size increases. This is compatible with an increase in the facilitated excitation rate $\Gamma_\uparrow$ as can be seen in Fig. 2.6. Note that for small detuning or large Rabi frequency atom loss may dominates and the system decays on a timescale comparable to or faster than the cluster lifetime. In this regime we do not probe the steady state of the system and neglect these data points. The inset in Fig. 2.12a shows Rydberg excitation number fluctuations encoded in $g^{(2)}(0)$. Probing the spectrum for $\Delta > 0$ we obtain values up to ~ 13 indicating strong excitation bunching. The bunching amplitude peaks at a detuning value, which coincides with a cluster size $\bar{m} \simeq 2$. While for larger detuning the cluster size approaches unity and uncorrelated noise dominates the bunching parameter, for smaller detuning the cluster size increases leading to an increase in a Poisson distributed Rydberg excitation signal. Both reduce the bunching amplitude to a value $g^{(2)}(0) \simeq 1$.

Number of clusters

To estimate the number of clusters, we assume a nearly constant atom number $N_{\mathrm{at}} \simeq 20\,000$ and thereby neglect atom loss due to photoionization on a timescale of τ_c. Furthermore, we assume a small Rydberg excitation density $\rho_R \ll 1$. Then, new seed events occur on a timescale $\sim \tau_{\mathrm{seed}}/N_{\mathrm{at}}$. Comparing this time to the cluster lifetime τ_c we can estimate the number of clusters N_c in the system,

$$N_c \simeq N_{\mathrm{at}} \Gamma_{\mathrm{seed}} \tau_c. \tag{2.42}$$

The seed rate Γ_{seed} is determined experimentally independently by an analysis of the first ion signal arrived at the detector. As can be seen in Fig. 2.12b, the number of clusters increases strongly with the driving frequency Ω. For large detuning, when all excitation rates are suppressed, the number of clusters decreases. We estimate a maximal cluster number of $N_c \simeq 500$ in the experimentally accessible regime.

Both, the analysis of cluster size $\bar{m}$ and cluster number N_c suggest that the steady state of the large 3D system is composed of many individual clusters of small size. The correlation length should be of similar magnitude as the cluster size $\bar{m}$ and thus the system size exceeds the typical correlation length. Since both, correlation length as well as correlation time remain finite, we conclude the corresponding phase is incompatible with a global bistable phase. Nevertheless, the characteristic relaxation time given by the cluster lifetime well exceeds the typical relaxation time given by the Rydberg state lifetime. This suggests that the system is metastable.

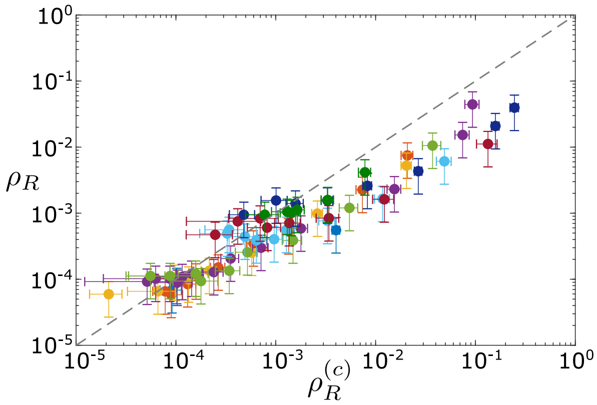

Figure 2.13: Validation of the cluster model. Using the maximum of the ion signal $R(t)$ we can estimate the Rydberg excitation density ρ_R. Similarly, we use the cluster model parameters and calculate the expected Rydberg excitation density $\rho_R^{(c)}$. The color code denotes different Rabi frequencies and was already used in Fig. 2.12. The dashed line indicates ideal agreement with unity slope, i.e. $\rho_R = \rho_R^{(c)}$.

Validity of the cluster model

So far we assumed that the cluster model discussed in Sec. 2.3 is a reasonable description for the 3D experimental setup. To further support the interpretation in terms of excitation clusters, we compare the Rydberg excitation density ρ_R retrieved experimentally from independent data to an estimate of the Rydberg excitation density $\rho_R^{(c)}$ using the cluster model. In the ideal case, we have $\rho_R = \rho_R^{(c)}$, which would indicate that the cluster model is a fairly good description of the steady state phase.

The experimental Rydberg excitation density ρ_R is estimated using the maximal ionization signal $R_{\text{ion}}^{\text{max}} = \max[R(t)]$. Using Eq. (2.22) we find

$$\rho_R = \frac{R_{\text{ion}}^{\text{max}}}{N_{\text{at}}\Gamma_{\text{ion}}}. \tag{2.43}$$

Here, we assume that the maximal ion signal $R_{\text{ion}}^{\text{max}}$ reflects the steady state value without atom loss. However, we expect that in the strong driving regime where many Rydberg atoms are immediately ionized the true steady state value may be larger and we obtain a smaller excitation density $\rho_R \leq \rho_R^{(c)}$. The Rydberg excitation density can be estimated from the cluster model by a combination of the cluster number N_c and cluster size $\bar{m}$. We obtain

$$\rho_R^{(c)} = \frac{N_c \bar{m}}{N_{\text{at}}}, \tag{2.44}$$

assuming that the system is described by independent clusters.

In Fig. 2.13 the results of the Rydberg excitation density are shown. As can be seen directly, all data

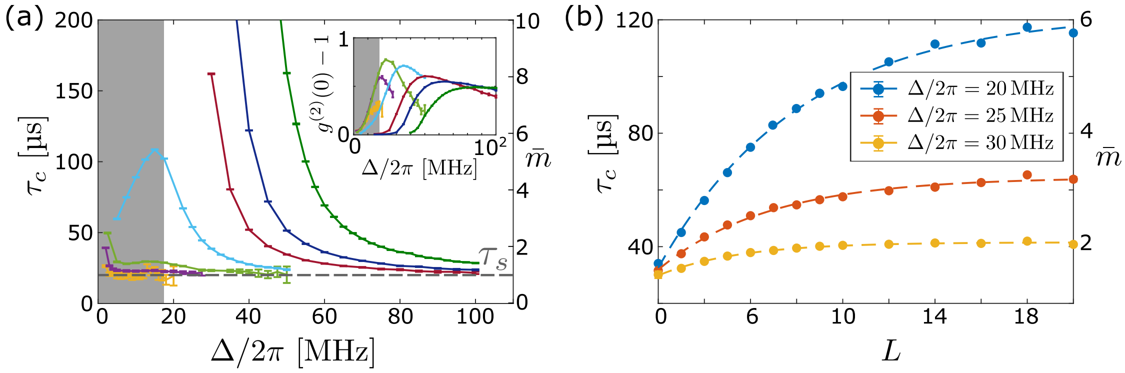

Figure 2.14: (a) Numerical simulation of the system dynamics using the rate equation method. The evaluation of $g^{(2)}(\tau)$ results in the cluster lifetime τ_c and bunching amplitude $g^{(2)}(0)-1$ (inset). The parameters are chosen according to the experiment discussed in Sec. 2.2 with $N_{\text{at}} = 1000$. The color code used is the same as in Fig. 2.12. The gray shaded region indicates the parameter regime where the inhomogeneous decoherence rate is no longer a good approximation. The gray dashed line indicates the Rydberg state lifetime τ_s. (b) Finite size scaling of the cluster lifetime with the linear system size L. We used a Rabi frequency $\Omega/2\pi = 160\,\text{kHz}$ and three different detunings Δ. The dashed lines indicate an exponential fit discussed in the main text.

points for different Rabi frequencies (color-coded) fall on top of each other. For weak driving and small excitation density $\rho_R \lesssim 10^{-3}$, the cluster model approach agrees well with the experimentally retrieved excitation density. Deviations are seen for strong driving and $\rho_R \gtrsim 10^{-3}$. We believe that in this regime cluster collisions and atomic loss become important and the simple cluster model cannot describe all features of the experiment. We have already seen in Sec. 2.3, that for strong driving and thus large Rydberg excitation density, cluster collisions become relevant. Since cluster collisions reduce the actual cluster growth we may overestimate the Rydberg excitation density by the cluster model, $\rho_R \leq \rho_R^{(c)}$.

2.4.2 Full Rate Equation Simulations

The experimental setup only give access to volume-integrated obervables and precludes the observation of microscopic structures. To gain insight to the latter, we simulate the full system dynamics using the rate equation method discussed in Sec. 1.1.2. Since the rate equation model goes well beyond the single cluster model, we have full access to the microscopic details of the system. We can explore finite size effects and hysteresis behavior that are not easily accessible in the experiment. All parameters are given or estimated by the experiment in Sec. 2.2. In particular, we include the inhomogeneous broadening approximation and a weak ionization channel. Similar to the experiment we calculate the second order temporal correlation function $g^{(2)}(\tau)$ and extract the correlation time τ_c and bunching parameter $g^{(2)}(0)$. The results of the numerical simulation, shown in Fig. 2.14a,

$\Delta/2\pi$ [MHz]	τ_c^∞ [µs]	$\bar{m} = \tau_c^\infty/\tau_s$	L_0	c
20	122(3)	6.1	6.2(6)	1.00(4)
25	64(1)	3.2	4.8(7)	0.76(6)
30	41(1)	2.5	3.5(4)	0.49(4)

Table 2.1: Fitted parameters for the finite size scaling in Fig. 2.14b using the fit function (2.45).

are compared to the experimental data in Fig. 2.12a. Despite the large parameter space given by the microscopic model, the experimental data and numerical simulations show qualitatively the same behavior. In particular, the magnitude of the cluster lifetime τ_c agrees fairly well with the experimental results. Since the approximation for the inhomogeneous broadening is only valid for $\Delta \gtrsim 2\pi \times 18\,\mathrm{MHz}$, the evaluation of the temporal correlation function in the gray shaded region is not reliable. The structure of the $g^{(2)}(0)$ peak corresponds to a cluster size $\bar{m} \simeq 2$, as it was already seen in the experiment. However, the numerically simulated system size is a factor of 20 smaller than the experimental system size. Thus, we would expect a much larger bunching amplitude $g^{(2)}(0)$ in the numerical simulations than in the experiment, which is however not the case. This discrepancy is yet not fully understood. A possible explanation may be black-body induced transitions to other Rydberg states or atomic motion which effectively reduce the system size. Overall the numerical simulations agree sufficiently well with the experimental results and thus are a good approximation for the Rydberg excitation dynamics.

Finite size scaling of the cluster size

We have already seen that the system is metastable in the relevant parameter regime with a relaxation timescale determined by the cluster lifetime. To check whether the system is bistable we consider the scaling of the cluster lifetime with the linear system size L with $N_{\mathrm{at}} = L^3$. In Fig. 2.14b we display the scaling behavior of the cluster lifetime for typical parameters in the experiment. We identify an exponential scaling of the cluster lifetime and fit the numerical data using a function

$$\tau_c = \tau_c^\infty \left(1 - c e^{-L/L_0}\right). \tag{2.45}$$

The extracted data are summarized in Table 2.1. The cluster lifetime saturates for a linear system size $L \gg L_0$. The characteristic relaxation length scale L_0 is thereby comparable or larger than the cluster size $\bar{m} = \tau_c^\infty/\tau_s$. Since we extract an exponential saturation rather than an algebraic divergence of the cluster lifetime we infer, as discussed in Sec. 2.1 that the system is not bistable in the relevant parameter regime amenable to a rate equation model.

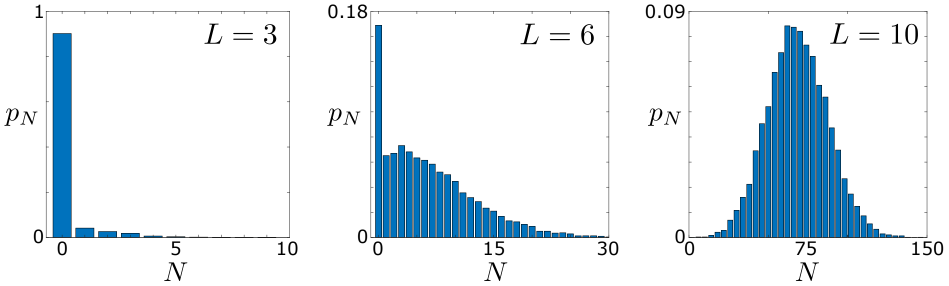

Figure 2.15: Excitation number distribution p_N obtained from the numerical simulation for Rabi frequency $\Omega = 2\pi \times 185\,\text{kHz}$ and detuning $\Delta = 2\pi \times 15\,\text{MHz}$. The counting statistics is recorded after $1\,\text{ms}$ for three different linear system sizes L.

Counting distribution

In Ref. [92, 93] the Rydberg excitation number distribution p_N was experimentally observed. The retrieved bimodal distribution shows peaks at low ($N = 0$) and high Rydberg excitation number N. It was argued that bi-modality is an indicator of a bistable system. However, we will argue here that a bimodal counting distribution can also occur as a finite size effect for metastable systems when correlation length ξ become comparable to the system size L.

Using our numerical simulation we extract the distribution p_N for three different linear system sizes L, see Fig. 2.15. The distribution is determined after $1\,\text{ms}$ continuous excitation and thus probes the steady state. For $L = 3$ we obtain a single peaked distribution at a low Rydberg excitation number. In this case, seed events are rare and clusters cannot grow due to the smallness of the system size. The excitation dynamics in a system of linear size $L = 6$ shows a dynamical switching between low and high Rydberg excitation number N. In this case the cluster size $\bar{m}$ is comparable to the system size and we obtain a bimodal counting statistics. For an even larger system size $L = 10$ the bimodal structure disappears and finite size effects are already strongly reduced. Instead the distribution p_N is now a single peaked Gaussian with a large mean Rydberg excitation number.

We conclude that the bimodal structure strongly depends on the cluster size $\bar{m}$ and thus the correlation length $\xi \sim \bar{m}$ relative to the system size L: For a system where correlation length and system size are similar, bimodality can be observed. However, when the system size far exceeds the correlation length, we can subdivide the 3D system into $\sim (L/\xi)^3$ independent spatial regions. For $L/\xi \gg 1$ the central limit theorem applies and we obtain a single peaked Gaussian distribution p_N.

Dynamic hysteresis

Finally, we discuss the hysteresis behavior as seen in Ref. [94, 98]. It was argued that the observed hysteresis upon parameter changes on a timescale τ_{sweep} is an indicator for bistability. Hysteresis can however be observed in metastable systems, too. Interestingly, the characteristic sweep time

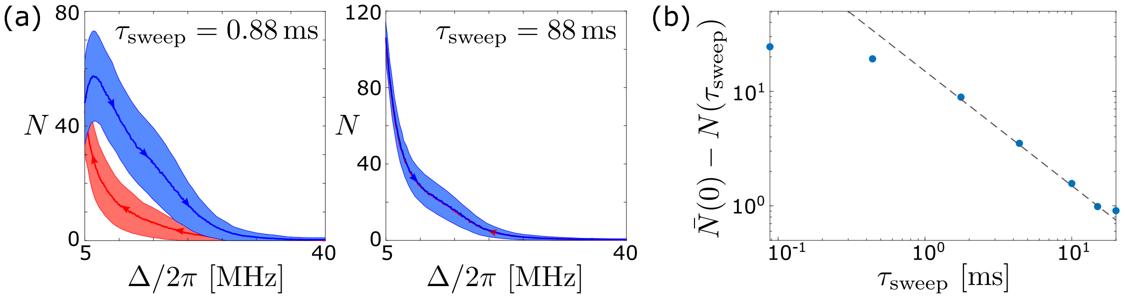

Figure 2.16: (a) Hysteresis scan in the detuning parameter for $\Omega = 2\pi \times 160\,\text{kHz}$ and $L = 10$. The sweep time in the forward (blue line) and backward (red line) directions are $\tau_{\text{sweep}} = 0.88\,\text{ms}$ and $\tau_{\text{sweep}} = 88\,\text{ms}$. The Rydberg excitation number is averaged over 500 trajectories and the standard deviations are shown by the shaded area. (b) Mismatch between the equilibrium Rydberg excitation number $\bar{N}(0)$ and the Rydberg excitation number $N(\tau_{\text{sweep}})$ after a finite sweep time τ_{sweep}. The hysteresis scan starts at a detuning $\Delta = 2\pi \times 40\,\text{MHz}$ and ends at $\Delta = 2\pi \times 10\,\text{MHz}$. Same parameters as in (a). The dashed line shows a scaling with $\sim 1/\tau_{\text{sweep}}$.

at which the hysteresis disappears can be surprisingly large. Naively, one would expect that this happens when the sweep time τ_{sweep} is longer than the relaxation timescale T. However, due to algebraic corrections hysteresis can be seen even for timescales $\tau_{\text{sweep}} \gtrsim T$, see e.g. [122]. While, as we have seen before, finite size effects vanish when the system size L exceeds the correlation length ξ, a hysteresis can still persist independent on the system size.

In Fig. 2.16a we numerically perform sweeps in the detuning Δ and observe the Rydberg excitation number N. We linearly increase the detuning from an initial value Δ_0 to a final value Δ_1 within a time τ_{sweep}. For the relevant detuning regime, the relaxation rate T is on the order of the cluster lifetime $\tau_c \sim 100\,\mu\text{s}$. We numerically verified this by simulating quench dynamics for different detunings. Although a sweep time $\tau_{\text{sweep}} = 0.88\,\text{ms}$ exceeds the relaxation time, we can clearly identify a hysteresis area. For a sweep time $\tau_{\text{sweep}} = 88\,\text{ms}$, which is three orders of magnitude larger as the relaxation timescale, the dynamic hysteresis disappears. We will show below that the relaxation of the Rydberg excitation number N towards the equilibrium value $\bar{N}$ attains besides the exponential relaxation algebraic corrections scaling as $\sim T/\tau_{\text{sweep}}$.

As will be outlined in detail in the following, we model the relaxation behavior using a sequence of small parameter quenches. Linearizing the equilibrium Rydberg excitation number $\bar{N}(x)$ with $x = \frac{\Delta_1 - \Delta}{\Delta_1 - \Delta_0} \in (0, 1)$ we obtain after a finite sweep time τ_{sweep} and assuming a constant relaxation time T,

$$\begin{aligned} N(\tau_{\text{sweep}}) - \bar{N}(0) = &\big(N(0) - \bar{N}(0)\big)\, e^{-\tau_{\text{sweep}}/T} \\ &+ \frac{T}{\tau_{\text{sweep}}} \times \left.\frac{\mathrm{d}\bar{N}(x)}{\mathrm{d}x}\right|_{x=0} \left[1 - e^{-\tau_{\text{sweep}}/T}\left(1 + \frac{\tau_{\text{sweep}}}{T}\right)\right] + \mathcal{O}\left(\frac{T^2}{\tau_{\text{sweep}}^2}\right). \end{aligned} \tag{2.46}$$

The first term corresponds to the usual exponential relaxation, while the second term indicates algebraic corrections in lowest order in T/τ_{sweep}. Importantly, in the long time dynamics, the algebraic relaxation becomes important and we expect a slow decrease of the hysteresis area. As an example, in Fig. 2.16b we show the relaxation of the Rydberg excitation number $N(\tau_{\text{sweep}})$ with respect to the equilibrium Rydberg excitation number $\bar{N}(x = 0)$ versus the sweep time. To conclude, hysteresis behavior is expected in metastable systems with a slow algebraic relaxation behavior. This may explain the experimental results seen in Ref. [94, 97].

Model for the hysteresis relaxation behavior

We now want to describe the hysteresis relaxation behavior based on a model of many small parameter quenches. This yields algebraic corrections in time t to the otherwise exponential relaxation to the equilibrium value. To be specific, we discuss the relaxation behavior of the Rydberg excitation number $N(t)$ upon parameter changes in the detuning Δ.

Single quench First, we consider the relaxation after a single parameter quench. Starting from a Rydberg excitation number N_0 and detuning Δ_0, we quench the system to another detuning Δ_1. For a detuning Δ_1, we denote the equilibrium Rydberg excitation number $\bar{N}_1$ and the relaxation timescale T_1. Then, typically the system relaxes exponentially in time and is described by

$$N(t) = \bar{N}_1 + (N_0 - \bar{N}_1)e^{-t/T_1}. \tag{2.47}$$

Multiple quenches Now, we consider the relaxation dynamics of the Rydberg excitation number for a finite parameter sweep. We describe the hysteresis as a sequence of M small parameter quenches $\Delta_j \to \Delta_{j+1}$ as illustrated in Fig. 2.17. We denote the equilibrium Rydberg excitation number at detuning Δ_j with $\bar{N}_j \equiv \bar{N}(\Delta_j)$ and the relaxation time $T_j \equiv T(\Delta_j)$. After each quench the system relaxes on a timescale $\tau = t/M$ before the next quench starts, where t is the total sweep time. We denote the Rydberg excitation number after time $t = j\tau$ with $N_j \equiv N(j\tau)$. Starting from a nonequilibrium Rydberg excitation number N_0 the system can relax on a timescale τ after a parameter

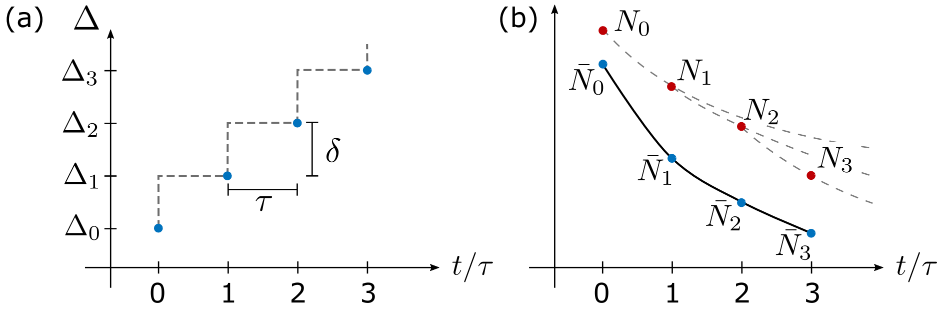

Figure 2.17: Schematic model for the hysteresis relaxation behavior in the number of Rydberg excitations N. We model the relaxation behavior as a sequence of small parameter quenches $\Delta_j \to \Delta_{j+1}$ with relaxation time step τ. (a) The tuning parameter Δ versus time t. (b) Corresponding relaxation of the Rydberg excitation number N_j and the equilibrium Rydberg excitation number $\bar{N}_j$ in time t (or detuning as shown in (a)). The gray dashed line indicates the relaxation as per Eq. (2.47) after each parameter quench.

quench $\Delta_0 \to \Delta_1$ to a Rydberg excitation number

$$N_1 = N_0 e^{-\tau/T_1} + \bar{N}_1 \left(1 - e^{-\tau/T_1}\right). \tag{2.48}$$

Subsequently, we quench the system from Δ_1 to Δ_2 and let it relax for time τ. The resulting excitation number is

$$\begin{aligned} N_2 &= N_1 e^{-\tau/T_2} + \bar{N}_2 \left(1 - e^{-\tau/T_2}\right) \\ &= N_0 e^{-\tau/T_1} e^{-\tau/T_2} + \bar{N}_1 \left(1 - e^{-\tau/T_1}\right) e^{-\tau/T_2} + \bar{N}_2 \left(1 - e^{-\tau/T_2}\right) \end{aligned} \tag{2.49}$$

Iteration yields a formula for the nonequilibrium Rydberg excitation number after M subsequent quenches,

$$N_M = N_0 \exp\left(-\sum_{j=1}^{M} \frac{\tau}{T_j}\right) + \sum_{j=1}^{M} \left[\bar{N}_j \left(1 - e^{-\tau/T_j}\right) \exp\left(-\sum_{k=j+1}^{M} \frac{\tau}{T_j}\right)\right]. \tag{2.50}$$

We perform a continuum limit $M \to \infty$ and assume a constant sweep rate $\dot{\Delta} = \delta/\tau$, where $\delta \equiv \Delta_{j+1} - \Delta_j \to 0$ and $\tau \to 0$. This allows us to approximate,

$$1 - e^{-\tau/T_j} \simeq \frac{\tau}{T_j}, \tag{2.51}$$

where we assumed a finite relaxation time T_j. Replacing the sum with an integral we directly obtain

$$N(t) = N_0 \exp\left(-\frac{1}{\dot{\Delta}}\int_{\Delta_0}^{\Delta_M}\frac{\mathrm{d}\Delta}{T(\Delta)}\right) + \frac{1}{\dot{\Delta}}\int_{\Delta_0}^{\Delta_M}\mathrm{d}\Delta\left[\frac{\bar{N}(\Delta)}{T(\Delta)}\exp\left(-\int_{\Delta}^{\Delta_M}\frac{\mathrm{d}\tilde{\Delta}}{T(\tilde{\Delta})}\right)\right]. \tag{2.52}$$

In the case of a constant relaxation rate T we can further simplify the excitation number $N(t)$

$$N(t) = N_0 e^{-t/T} + \frac{t}{T}\int_0^1 \mathrm{d}x\, \bar{N}(x) e^{-\frac{t}{T}x}, \tag{2.53}$$

with $x = \frac{\Delta_M - \Delta}{\Delta_M - \Delta_0} \in (0,1)$. Clearly, for a constant mean excitation number $\bar{N}$ we obtain the previous result for a single quench in Eq. (2.47). In the case, where the mean excitation number changes with the detuning Δ, we obtain algebraic corrections in (T/t). To see this, we use a Taylor expansion of $\bar{N}(x)$ around $x = 0$,

$$\bar{N}(x) = \bar{N}(0) + \frac{\mathrm{d}\bar{N}(x=0)}{\mathrm{d}x}x + \frac{\mathrm{d}^2\bar{N}(x=0)}{\mathrm{d}x^2}x^2 + \mathcal{O}(x^3). \tag{2.54}$$

Inserting into Eq. (2.52) yields

$$\begin{aligned} N(t) \simeq{} & N_0 e^{-t/T} + \bar{N}_M\left(1 - e^{-t/T}\right) \\ & + \left(\frac{t}{T}\right)^{-1}\left.\frac{\mathrm{d}\bar{N}(x)}{\mathrm{d}x}\right|_{x=0}\left[1 - e^{-t/T}\left(1 + \frac{t}{T}\right)\right] \\ & + \left(\frac{t}{T}\right)^{-2}\left.\frac{\mathrm{d}^2\bar{N}(x)}{\mathrm{d}x^2}\right|_{x=0}\left[2 - e^{-t/T}\left(2 + 2\frac{t}{T}\right) + \frac{t^2}{T^2}\right] \end{aligned} \tag{2.55}$$

This is equivalent to Eq. (2.46) upon replacing t with τ_{sweep} and $\bar{N}_M$ with $\bar{N}(x=0)$ Clearly, for timescales $t \gtrsim T$, the algebraic correction scaling as $\sim 1/t$ becomes the dominant part for relaxation.

Conclusion

In this chapter we discussed the possibility of a phase transition to a bistable steady state in a driven dissipative Rydberg lattice gas in the antiblockade regime. Both, a careful experimental analysis and numerical simulations suggest the absence of a global bistable phase in the experimentally relevant decoherence-dominated regime.

In particular, we characterized and analyzed the experimental data and compared them to a cluster model and a numerical simulation of a rate equation model. The simplified cluster model agrees well with the experimental results and suggests that the system consists of many small independent excitation clusters. This shows that correlation lengths are finite within the experimentally accessible parameter regime. Furthermore, using the cluster model we explained the prolongation of the characteristic timescales, which is compatible with a metastable state.

Moreover, we found that a bistable steady states has in the thermodynamic limit long-range order and a diverging relaxation time. Using a rate equation model of the full microscopic model, we numerically checked that correlation lengths and correlation times remain finite even in the thermodynamic limit. This suggests the absence of a bistable phase in the experimentally relevant parameter regime of strong decoherence. However, our results on bimodal counting distributions and hysteresis sweeps show that it is possible to observe both in finite and metastable systems. Our results are therefore compatible with experiments in the antiblockade regime.

The controversial discussion in literature shows that the identification of open system phase transitions in small atomic ensembles requires a careful analysis in terms of system size scaling and correlation functions. Due to the large complexity of the problem, numerical simulations should be contrasted to experimental data. While our results suggest the absence of a bistable phase in a system with strong decoherence, it remains an open question whether a bistable phase can exist in the coherent regime. However, numerical simulations in this regime can only be performed for small system sizes which makes it difficult to gain insight into the properties in the thermodynamic limit.

Chapter 3

Hole Dynamics in a Chain of Rydberg Superatoms

When a sufficiently confined mesoscopic ensemble of atoms is driven to a high lying Rydberg state, the strong Rydberg-Rydberg interactions may suppress all but one Rydberg excitation [24, 33, 36]. This leads to the concept of *Rydberg superatoms* [33, 41, 42, 123] representing an effective spin-$1/2$ model. Due to the large number of atoms within a superatom the coupling to an electromagnetic field is collectively enhanced. Furthermore, as pointed out in Ref. [41, 59] dissipation can lead to an increase of the steady state excitation probability exceeding the one for a single atom. Thus, arrays of Rydberg superatoms allow to study many-body spin dynamics with enhanced coupling to laser fields and the potential of preparing fully polarized states.

For a long time much interest lay in the study of the Rydberg blockade phenomena realizing Ising type spin models. Driving these systems resonantly to the Rydberg state with an additional laser field led to the observation of strong but short-range spatial correlations of Rydberg excitations [10, 21, 22, 32, 33, 124–127]. Ref. [59] investigated 2D arrays of Rydberg superatoms which may allow to reach a regime exhibiting long-range correlations. As discussed already in Sec. 2.1, the enhanced driving strength of superatoms can also lead to a phase transition to a bistable steady state.

Here, we discuss superatoms in the *facilitation regime* [25, 26, 89], i.e. using an off-resonant laser excitation scheme. In the previous chapter we discussed facilitation of a lattice gas with individual atoms. We found that in the experimentally accessible regime of the many-body dynamics metastable states occur consisting of small Rydberg excitation clusters. In the present chapter, we discuss a chain of superatoms realizing an effective spin lattice model. Due to the strong superatom driving mechanism, large Rydberg excitation clusters are expected to form. We show that the steady state has a high and almost universal Rydberg excitation density of $\rho_R = 2/3$. Exploring the dynamics in the system we find that the steady state can be described using a new quasi particle – an excitation hole. These holes behave similar to hard rods with a liquid-type correlation function.

This chapter is based on the publication [FL5], partially with text overlap.

3.1 1D Chain of Superatoms

3.1.1 Microscopic Model

We consider an ensemble of atoms arranged as depicted in Fig. 3.1 realizing a chain of superatoms. All atoms are driven by a laser field from their ground state $|g\rangle$ to a Rydberg state $|e\rangle$ with Rabi frequency Ω and carrier frequency ω. The coherent excitation dynamics is described by a Hamiltonian ($\hbar = 1$)

$$\hat{\mathcal{H}} = \sum_{k} \left[\Omega\left(\hat{\sigma}_{eg}^{k} + \hat{\sigma}_{ge}^{k}\right) - \Delta\hat{\sigma}_{ee}^{k}\right] + \sum_{k<k'} V(\mathbf{r}_k, \mathbf{r}_{k'})\,\hat{\sigma}_{ee}^{k} \otimes \hat{\sigma}_{ee}^{k'}, \tag{3.1}$$

where we introduced the detuning $\Delta = \omega - \omega_{ge}$ from the atomic transition frequency ω_{ge}. Here, $\hat{\sigma}_{\mu\nu}^{k} = |\mu\rangle_k \langle\nu|$ denote the transition ($\mu \neq \nu$) or projection ($\mu = \nu$) operator for the kth atom. Atoms at positions $\mathbf{r}_k, \mathbf{r}_{k'}$ in a Rydberg state $|e\rangle$ interact with a potential $V(\mathbf{r}_k, \mathbf{r}_{k'}) = \frac{C_p}{|\mathbf{r}_k - \mathbf{r}_{k'}|^p}$ where C_p is the interaction coefficient and p the corresponding power law. To be specific, we consider $p = 6$ for van der Waals interaction and $p = 3$ for static dipole-dipole interaction (in the presence of an electric field) [13].

Besides the coherent excitation dynamics, we include incoherent processes described by Lindblad jump operators as discussed in Sec. 1.1. First, we consider the finite lifetime of the Rydberg states with decay rate Γ_s,

$$\hat{L}_s^k = \sqrt{\Gamma_s}\hat{\sigma}_{ge}^k. \tag{3.2}$$

Furthermore we include dephasing of the Rydberg state with rate Γ_d,

$$\hat{L}_d^k = \sqrt{\Gamma_d}\hat{\sigma}_{ee}^k. \tag{3.3}$$

Now, the dynamics of the system is described by a master equation for the density matrix $\hat{\rho}$,

$$\partial_t \hat{\rho} = -i[\hat{\mathcal{H}}, \hat{\rho}] + \sum_{k} \sum_{\alpha=s,d} \left(\hat{L}_\alpha^k \hat{\rho} \hat{L}_\alpha^{k\dagger} - \frac{1}{2}\{\hat{L}_\alpha^{k\dagger}\hat{L}_\alpha^k, \hat{\rho}\}\right). \tag{3.4}$$

This is the starting point for our derivation of an effective rate equation model for Rydberg superatoms.

3.1.2 Superatom Rate Equation Model

We assume that each superatom in the one-dimensional lattice with lattice constant a contains N atoms. These atoms are confined within a region of linear dimension $\delta r \ll a$, as can be seen in Fig. 3.1. In the case where the interaction energy $C_p/\delta r^p$ within a single superatom exceeds all relevant energy scales, we can restrict the excitation dynamics to the subspace of having at most one excited Rydberg atom per superatom (Rydberg blockade). In particular, we require $w, \Delta \ll C_p/\delta r^p$, where $w = \sqrt{4\Omega^2\gamma/\Gamma_s + \gamma^2}$ is the excitation linewidth of a single atom and $\gamma = \frac{1}{2}(\Gamma_s + \Gamma_d)$

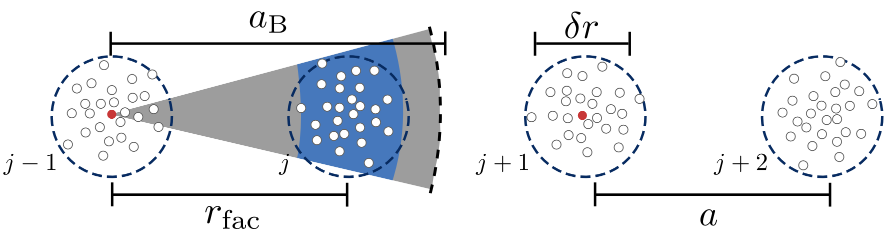

Figure 3.1: Schematics of a superatom chain. Each superatom (indicated by the dashed line) contains on average N atoms and is labeled with an index j. Open white circles indicate ground state atoms and the dark red dots atoms excited to a Rydberg state. The width of the confinement is δr. We choose a configuration where the blockade radius a_B exceeds the distance to a nearest neighbor superatom (gray shaded region) and the lattice constant a matches the facilitation distance r_fac. The facilitation region is indicated by the blue shaded region.

the decoherence rate [24, 33]. Note that the interaction energy C_p/a^p between the neighboring superatom can still be large and comparable to the detuning Δ.

Suppose one superatom on lattice site j is in the collective ground state $|G^j\rangle \equiv |g_1 g_2 \ldots g_N\rangle$. If the excitation laser is uniform on a scale of the superatom width δr, the collective ground state is coupled to the symmetric single-excitation state $|E_s\rangle \equiv \frac{1}{\sqrt{N}} \sum_k |g_1 g_2 \ldots e_k \ldots g_N\rangle$ with enhanced Rabi frequency $\sqrt{N}\Omega$. In addition, there are $N-1$ non-symmetric states $|E_{ns}\rangle_m$, labeled by an index $m = 1, 2, \ldots, N-1$, which are decoupled from the laser field. The single superatom excitation scheme is shown in Fig. 3.2a. Thus the Hamiltonian in Eq. (3.1) can be approximated by

$$\hat{\mathcal{H}} \simeq \sum_j \left[\sqrt{N}\Omega\Big(|G^j\rangle\langle E_s^j| + |E_s^j\rangle\langle G^j|\Big)\right] - \Delta \hat{P}_{EE}^j + \sum_{j>i} \frac{C_p}{|\mathbf{r}_j - \mathbf{r}_i|^p} \hat{P}_{EE}^j \otimes \hat{P}_{EE}^i, \tag{3.5}$$

where $\hat{P}_{EE}^j \equiv |E_s^j\rangle\langle E_s^j| + \sum_m |E_{ns}^j\rangle_m \langle E_{ns}^j|$ is the projector onto the manifold of N single Rydberg excitation states of a superatom at site j. The position of a superatom at lattice site j is approximated by the center of mass coordinate $\mathbf{r}_j = \frac{1}{N}\sum_{k_j} \mathbf{r}_{k_j}$. All states with more than one Rydberg excitation are highly suppressed by the strong interactions between atoms in the Rydberg state. First, let us discuss the dynamics of a single superatom. Later, we include the interactions between them using an effective detuning [31–33].

Single superatom

Each superatom is driven coherently from the collective ground state $|G\rangle$ to the symmetric Rydberg state $|E_s\rangle$. In addition to the coherent dynamics, all single excitation states $\{|E_s\rangle, |E_{ns}\rangle_m\}$ decay back to the ground state with rate Γ_s. We distinguish two cases: First, when the dephasing rate is much smaller than the coherent drive and the decay rate, $\Gamma_d \ll \Omega, \Gamma_s$, the superatom dynamics

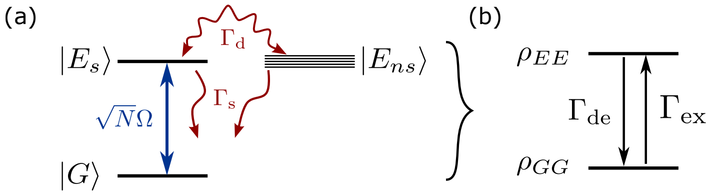

Figure 3.2: (a) Level scheme of a single superatom. The collective ground state $|G\rangle$ is coupled to the symmetric single excitation state $|E_s\rangle$ with enhanced Rabi frequency $\sqrt{N}\Omega$, where N is the number of atoms within the superatom. Dephasing with rate Γ_d tries to equilibrate the states in the single excitation manifold including $(N-1)$ nonsymmetric states $|E_{ns}\rangle$. Spontaneous decay with rate Γ_s couples the excited states to the collective ground state. (b) Simplified superatom rate equation model. The superatom is excited with rate Γ_ex to the collective state ρ_{EE} and deexcited with rate Γ_de to the state ρ_{GG}.

resembles a two-level atom with enhanced coupling strength $\sqrt{N}\Omega$ to the radiation field. Second, we consider the case when $\Gamma_s \ll \Omega, \Gamma_d$. For simplicity we replace the manifold of nonsymmetric states $\{|E_{ns}\rangle_m\}$ with a single state $|E_{ns}\rangle$. Then, dephasing tries to equilibrate all single excitation states, i.e. the symmetric state $|E_s\rangle$ is coupled incoherently with rate $(N-1)/N\ \Gamma_d$ to the nonsymmetric state $|E_{ns}\rangle$. In turn the transition rate from the nonsymmetric state to the symmetric states is Γ_d/N. In this regime, a superatom resembles a three level system with relevant states $\{|G\rangle, |E_s\rangle, |E_{ns}\rangle\}$ as illustrated in Fig. 3.2a.

Using a master equation for the evolution of the density matrix, we obtain for the full equations of motion,

$$\partial_t \rho = \hat{\mathcal{L}}\rho, \tag{3.6}$$

with Lindbladian

$$\hat{\mathcal{L}} = \begin{pmatrix} 0 & \Gamma_s & i\sqrt{N}\Omega & -i\sqrt{N}\Omega & \Gamma_s \\ 0 & -\Gamma_s - \frac{N-1}{N}\Gamma_d & -i\sqrt{N}\Omega & i\sqrt{N}\Omega & \frac{1}{N}\Gamma_d \\ i\sqrt{N}\Omega & -i\sqrt{N}\Omega & -i\Delta-\gamma & 0 & 0 \\ -i\sqrt{N}\Omega & i\sqrt{N}\Omega & 0 & i\Delta-\gamma & 0 \\ 0 & \frac{N-1}{N}\Gamma_d & 0 & 0 & -\Gamma_s - \frac{1}{N}\Gamma_d \end{pmatrix} \tag{3.7}$$

and $\rho = (\rho_{GG}, \rho_{E_sE_s}, \rho_{GE_s}, \rho_{E_sG}, \rho_{E_{ns}E_{ns}})^T$ is a vector of density matrix elements. Since the coupling to the nonsymmetric state $|E_{ns}\rangle$ is incoherent, the corresponding coherences $\rho_{E_{ns}G}, \rho_{E_{ns}E_s}$ remain decoupled, i.e. $\rho_{E_{ns}G} = \rho_{E_{ns}E_s} = 0$.

For the case $N = 1$ we retrieve the two-level atom result discussed in Sec. 1.1.2, where the excitation population in the steady state is bounded by $\rho_{ee} \leq 0.5$. The excited state population and linewidth are given in Eq. (1.17) and (1.18), respectively. For a superatom with $N > 1$, dephasing leads to a population of nonsymmetric states [34, 41]. Solving Eq. (3.6) for the steady state, $\partial_t \rho = 0$, we obtain the excited state population of a superatom

$$\rho_{EE} \equiv \rho_{E_sE_s} + \rho_{E_{ns}E_{ns}} = \frac{2N\Omega^2\gamma}{\Omega^2(N+1)\left(\Gamma_d + \frac{2N}{N+1}\Gamma_s\right) + \Gamma_s(\gamma^2+\Delta^2)} \tag{3.8}$$

and the corresponding superatom linewidth reads

$$w_{\mathrm{SA}} \simeq \sqrt{2N\Omega^2\gamma/\Gamma_s + \gamma^2}. \tag{3.9}$$

In the following, we consider the case $\Gamma_s \ll \Gamma_d, \Omega^2/\Gamma_d$ where dephasing dominates the superatom dynamics. For a resonant excitation and in the limit of large atom number N, the excited state population is approximately

$$\rho_{EE} \simeq \frac{N}{N+1}. \tag{3.10}$$

Clearly, for large $N \gg 1$ the steady state population approaches $\rho_{EE} \simeq 1$. This is in contrast to a coherent superatom $\Omega \gg \Gamma_s \gg \Gamma_d$, where the steady state population is limited by $\rho_{EE} \leq 0.5$. Comparing the superatom linewidth in Eq. (3.9) with the single atom linewidth in Eq. (1.18), we notice the analogy upon replacement $\Omega^2 \to \frac{1}{2}N\Omega^2$. Naively we would expect to replace the Rabi frequency Ω by the collective Rabi frequency $\sqrt{N}\Omega$. The factor $\frac{1}{2}$ originates from the increased excitation probability of a saturated superatom approaching unity, rather than $\rho_{EE} \simeq 0.5$.

Superatom rate equation model To obtain a superatom rate equation model in the limit $\Gamma_d \gtrsim \Omega$ we first eliminate the coherences $\rho_{E_{ns}G}, \rho_{GE_{ns}}$. Setting $\dot\rho_{E_{ns}G} = \dot\rho_{E_{ns}E_s} = 0$, we obtain for the populations $\rho_3 = (\rho_{GG}, \rho_{E_sE_s}, \rho_{E_{ns}E_{ns}})^T$

$$\partial_t\rho_3 = \hat{\mathcal{L}}_3\rho_3, \qquad \text{with} \qquad \hat{\mathcal{L}}_3 = \begin{pmatrix} -N\chi & N\chi + \Gamma_s & \Gamma_s \\ N\chi & -N\chi - \Gamma_s - \frac{N-1}{N}\Gamma_d & \frac{1}{N}\Gamma_d \\ 0 & \frac{N-1}{N}\Gamma_d & -\Gamma_s - \frac{1}{N}\Gamma_d \end{pmatrix}. \tag{3.11}$$

Here we defined

$$\chi \equiv \frac{2\Omega^2\gamma}{\gamma^2+\Delta^2}, \tag{3.12}$$

which is equal to the excitation rate for the two-level rate equation model in Sec. 1.1.2. On one hand for small decay rate $\Gamma_s \ll \chi, \Gamma_d$ the laser tends to equalize the populations ρ_{GG} and $\rho_{E_sE_s}$. On the other hand dephasing transfers population from the symmetric state $\rho_{E_sE_s}$ to the nonsymmetric states $\rho_{E_{ns}E_{ns}}$. The reverse process is suppressed by a factor $1/N$. This leads to an imbalance in excited state populations, where for large N the population of the symmetric state $\rho_{E_sE_s} \sim \rho_{E_{ns}E_{ns}}/N$ is small. Thus, the symmetric state plays the role of an intermediate state. By adiabatic elimination of $\rho_{E_sE_s}$ we obtain a simple rate equation model between two states, the collective ground state

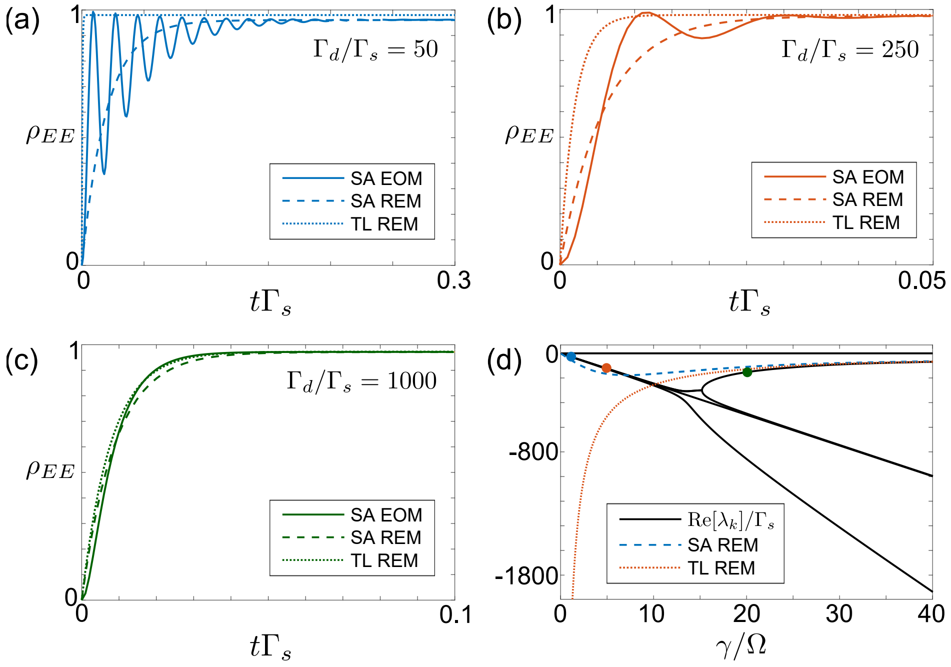

Figure 3.3: (a)-(c) Excitation dynamics of a single superatom containing $N = 50$ atoms. The solid lines correspond to a solution of the full superatom density matrix equations of motion (SA EOM) in Eq. (3.6) projected to the single excitation Hilbert space. The dashed lines correspond to the superatom rate equation model (SA REM) in Eq. (3.13) and the dotted line to the two-level rate equation model (TL REM) in Eq. (3.14). The laser is resonant ($\Delta = 0$) with Rabi frequency $\Omega/\Gamma_s = 25$ and dephasing rates $\Gamma_d/\Gamma_s = 50$, $\Gamma_d/\Gamma_s = 250$ and $\Gamma_d/\Gamma_s = 1000$, respectively. (d) Real part of the eigenvalues λ_k of $\hat{\mathcal{L}}$ in Eq. (3.7) versus the decoherence rate γ/Ω. The blue dashed line shows the total relaxation rate Γ_{tot} of the superatom rate equation model (SA REM) and the red dotted line shows the total relaxation rate $\tilde{\Gamma}_{\text{tot}}$ of the two-level rate equation model (TL REM). The blue, red and green circle correspond to (a), (b) and (c), respectively.

ρ_{GG} and collective single excited state ρ_{EE} with approximately $\rho_{GG} + \rho_{EE} \simeq 1$, as can be seen in Fig. 3.2b. The corresponding rate for excitation Γ_{ex} and deexcitation Γ_{de} are given by

$$\Gamma_{\text{ex}} = \frac{(N-1)\chi}{N\chi + 2\gamma}\Gamma_d, \qquad \Gamma_{\text{de}} = \frac{\chi}{N\chi + 2\gamma}\Gamma_d + \Gamma_s. \tag{3.13}$$

The superatom rate equation approximation is valid in the limit $N \gg 1$. In this limit and for $\Gamma_s \ll \Gamma_d$ the total relaxation rate $\Gamma_{\text{tot}} = \Gamma_{\text{ex}} + \Gamma_{\text{de}}$ is approximately given by the dephasing rate $\Gamma_{\text{tot}} \simeq \Gamma_d$.

Two-level rate equation model This result is in contrast to the commonly used two-level rate equation approach, which is discussed in Sec. 1.1.2 and will be presented here shortly: Again in the limit of strong Rydberg blockade we reduce the superatom subspace to the collective ground state and N single excitation states. Now, using the rate equation approximation, we find the following excitation and deexcitation rates

$$\tilde{\Gamma}_{\text{ex}} = N\chi, \qquad \tilde{\Gamma}_{\text{de}} = \chi + \Gamma_s, \tag{3.14}$$

which differ from the superatom rate equation model Eq. (3.13). The excitation rate $\tilde{\Gamma}_{\text{ex}}$ is enhanced by the number of atoms per superatom N. The deexcitation rate is given by the deexcitation rate for a single excited atom. While the total two-level relaxation rate $\tilde{\Gamma}_{\text{tot}} = \tilde{\Gamma}_{\text{ex}} + \tilde{\Gamma}_{\text{de}} \sim N\chi$ scales with the number of atoms N for small decay rates Γ_s and $N \gg 1$, the total superatom relaxation rate approaches a constant given by the dephasing rate $\Gamma_{\text{tot}} \simeq \Gamma_d$. Thus, we expect a large discrepancy in this parameter regime.

In Fig. 3.3a-c we compare the full coherent relaxation dynamics of a resonantly driven superatom to the approximate rate equation models. Both rate equation models approximate well the steady state population ρ_{EE}. Comparing the dynamics for different ratios Γ_d/Γ_s the superatom rate equation model compares more favorably. While the superatom rate equation model Eq. (3.13) agrees well with the exact relaxation dynamics over a broad parameter regime $\gamma \gtrsim \sqrt{N}\Omega$, the two-level rate equation approach is only valid when $\gamma \gg \sqrt{N}\Omega$.

This can be further investigated by considering the real parts of the eigenvalues λ_k of the matrix $\hat{\mathcal{L}}$ in Eq. (3.7). As discussed in Sec. 1.1 the real part of λ_k denotes the relaxation rate of the system. The eigenvalue $\lambda_0 = 0$ corresponds to the steady state solution. All other eigenvalues λ_k $(k = 1, 2, 3, 4)$ have a nonvanishing negative real part. The smallest value of $|\text{Re}[\lambda_k]|$ describes the slowest timescale for relaxation of a single superatom. This can be compared to the total relaxation rate Γ_{tot} and $\tilde{\Gamma}_{\text{tot}}$ of both rate equation models. In Fig. 3.3d we can see that the exact relaxation rate is approximated well by the superatom rate equation model even for $\sqrt{N}\Omega \simeq \gamma$. As discussed before, in this regime the two-level rate equation model predicts a much faster relaxation rate. However, for $\gamma \gg \sqrt{N}\Omega$ both agree nicely with the exact relaxation rate. Importantly, the superatom rate equation model approximates well the characteristic relaxation timescale and steady state population ρ_{EE} and is therefore used throughout this chapter for describing the superatom excitation dynamics.

Many superatoms

To include interactions between individual superatoms, we reintroduce the effective detuning seen by a superatom due to the energy shift of all neighboring superatoms. The population dynamics is then described by many-body rate equations

$$\begin{aligned} \partial_t \rho^j_{EE} &= \Gamma_{\text{ex}}(\Delta_j)\rho^j_{GG} - \Gamma_{\text{de}}(\Delta_j)\rho^j_{EE}, \qquad (3.15)\\ \rho^j_{GG} + \rho^j_{EE} &\simeq 1. \qquad (3.16) \end{aligned}$$

Excitation and deexcitation rates are given by

$$\Gamma_{\text{ex}}(\Delta_j) = \frac{(N-1)\,\chi(\Delta_j)}{N\,\chi(\Delta_j) + 2\gamma}\Gamma_d, \tag{3.17a}$$

$$\Gamma_{\text{de}}(\Delta_j) = \frac{\chi(\Delta_j)}{N\,\chi(\Delta_j) + 2\gamma}\Gamma_d + \Gamma_s, \tag{3.17b}$$

respectively with $\chi(\Delta_j) \equiv \frac{2\Omega^2\gamma}{\gamma^2+(\Delta_j)^2}$. Here the effective detuning of the jth superatom,

$$\Delta_j = \Delta - \sum_{i\neq j} \frac{C_p}{|\mathbf{r}_i - \mathbf{r}_j|^p}\rho^i_{EE}, \tag{3.18}$$

includes the Rydberg level shift due to the interaction with all other superatoms in the excited state. The superatom rate equation model is the basis of all further numerical simulations of a 1D chain of Rydberg superatoms.

3.1.3 Facilitation, Timescales and Holes

In the so called facilitation regime the 1D array of superatoms is driven off-resonantly to a Rydberg state. Hereby, the laser detuning Δ is chosen such that it compensates the interaction level shift on the neighboring lattice site, i.e. $\Delta = C_p/a^p \equiv V_{\text{N}}$. For simplicity we neglect the level shift on the next nearest neighbor $C_p/(2a)^p$. The validity of this assumption will be discussed in the Sec. 3.1.4.

If the detuning exceeds the superatom linewidth $\Delta \gg w_{\text{SA}}$, a first *seed* excitation is highly suppressed. The timescale for this excitation is determined by the seed rate

$$\Gamma_{\text{seed}} = \Gamma_{\text{ex}}(\Delta). \tag{3.19}$$

Starting with a chain of L superatoms in their ground state a first excitation is created within a timescale $1/(L\Gamma_{\text{seed}})$. Now, a seed excitation triggers an excitation cascade similar to the case discussed in Chapter 2. Since the detuning compensates the interaction level shift, the effective detuning for a neighboring atom is $\Delta_{\text{eff}} = \Delta - V_{\text{N}} = 0$. Thus, the superatom excitation and deexcitation rate are given by

$$\Gamma_\uparrow = \Gamma_{\text{ex}}(\Delta_{\text{eff}} = 0), \qquad \Gamma_\downarrow = \Gamma_{\text{de}}(\Delta_{\text{eff}} = 0). \tag{3.20}$$

In contrast to a chain of individual atom, a regime where $\Gamma_\uparrow \gg \Gamma_\downarrow$ can be easily realized for superatoms and we expect a rapid growth of large excitation clusters comparable to the system size [FL4]. However, spontaneous decay of a superatom with rate Γ_s or collisions of two excitation clusters will produce *excitation holes* in the steady state of the system. We call each ground state superatom an excitation hole if and only if it is surrounded by two excited superatoms. While two ground state superatoms can be on neighboring lattice sites, a hole, in the sense of this definition, is always in between two excited superatoms. A hole is stable since the interaction energy of the middle ground state atom is shifted by the two neighboring excited superatoms. Thus the effective detuning is $\Delta_{\text{eff}} = \Delta - 2V_{\text{N}} = -\Delta$ and the hole will be refilled with the strongly suppressed seed rate Γ_{seed}. Typically, we have the following hierarchy of the relevant rates

$$\Gamma_{\text{seed}} \ll \Gamma_s, \Gamma_\downarrow \ll \Gamma_\uparrow. \tag{3.21}$$

Note that in the regime of large number of atoms N per superatom and strong dephasing rate Γ_d, the resonant deexcitation rate $\Gamma_\downarrow \gtrsim \Gamma_s$ is of similar magnitude as the decay rate Γ_s.

3.1.4 Experimental Considerations

We discuss the experimental prerequisites to realize a 1D chain of superatoms in the facilitation regime. We assume a repulsive interaction potential $V(r) = C_p/r^p$ with $C_p > 0$ and single particle linewidth w. Then the blockade radius [24, 33] is defined as

$$a_{\text{B}} = \sqrt[p]{\frac{C_p}{w}}. \tag{3.22}$$

We assume each superatom can be characterized by its center of mass coordinate $\mathbf{r}_j$ and linear extent δr determined by the trapping potential of the atoms. In Fig. 3.1 a sketch can be found for the relevant length scales. A superatom should accommodate at most one Rydberg excitation and thus we require the blockade condition

$$\delta r \ll a_{\text{B}}. \tag{3.23}$$

In the facilitation regime we have a strong separation of timescales $\Gamma_\uparrow \gg \Gamma_{\text{seed}}$. Clearly the excitation of a superatom is suppressed whenever the laser detuning exceeds the excitation linewidth of a superatom $\Delta > w_{\text{SA}} \simeq \sqrt{N/2}w$. Now, to enhance the excitation rate $\Gamma_\uparrow$ in the presence of an already excited superatom, the distance between two superatoms $r_{\text{fac}} = |\mathbf{r}_{j+1} - \mathbf{r}_j|$ is chosen such that $\Delta = V(r_{\text{fac}})$. Thus, the interaction induced level shift compensates the detuning and we set the lattice constant

$$a = r_{\text{fac}} = \sqrt[p]{\frac{C_p}{\Delta}}. \tag{3.24}$$

Since $\Delta > w$, the *facilitation distance* r_{fac} is smaller than the blockade radius a_{B}. To facilitate all atoms within a superatom, the resulting induced level shift $|\Delta - V(r_{\text{fac}} \pm \delta r)| \lesssim w_{\text{SA}}$ should be within the superatom linewidth. Linearizing the interaction potential for $\delta r/r_{\text{fac}} \ll 1$ we obtain a condition for the extent of a superatom

$$\delta r \lesssim \frac{1}{p}\frac{r_{\text{fac}}^{p+1}}{C_p/w_{\text{SA}}} = \frac{1}{p}\frac{w_{\text{SA}}}{\Delta}a. \tag{3.25}$$

To neglect the induced interaction shift on the next neighbor, we require $V(2a) \lesssim w_{\text{SA}}$. This can be expressed as a condition on the power law scaling of the interaction potential

$$p\log(2) \geq \log(\Delta/w_{\text{SA}}). \tag{3.26}$$

Let us discuss a specific example: We assume atoms are confined in an array of microtraps or a long wavelength optical lattice [36, 45, 128–130] each containing $N \simeq 50$ atoms. Choosing Rubidium atoms, the atomic ground state $|g\rangle \equiv |5S_{1/2}\rangle$ is coupled via a two-photon transition to an excited Rydberg state $|e\rangle \equiv |nS_{1/2}\rangle$ with principal quantum number $n \simeq 90$ [21, 125]. The decay rate is $\Gamma_s = 5\,\text{kHz}$ and a Rabi frequency $\Omega = 25\Gamma_s = 2\pi \times 20\,\text{kHz}$ can be easily achieved. Atoms in their Rydberg state can be strongly dephased due to atomic collisions and motion in an inhomogeneous trapping potential or intermediate state decay for a two-photon transition [21, 35, 131, 132]. With a realistic dephasing rate $\Gamma_d \simeq 250\Gamma_s$, we have a single atom linewidth of $w = 2\pi \times 450\,\text{kHz}$ and a superatom linewidth $w_{\text{SA}} = 5w$. Choosing a detuning $\Delta = 2\pi \times 10\,\text{MHz}$ and with a van der Waals coefficient $C_6 = 2\pi \times 16.8\,\text{THz}\,\mu\text{m}^6$ [133] we obtain a lattice constant $a \simeq 11\,\mu\text{m}$ as well as a superatom extent $\delta r \lesssim 0.4\,\mu\text{m}$. However, this implies a high atomic density $10^{15}\,\text{cm}^{-3}$, which may lead to strong dephasing and collisional losses of the ground state atoms.

Another possibility is to apply a strong static electric field in a direction perpendicular to the superatom array. The corresponding Stark eigenstates possess large dipole moments $\sim \frac{3}{2}n^2 a_0 e$, where a_0 is the Bohr radius and e the electric charge, and lead to strong dipole-dipole interactions. Using $n = 60$ we obtain a dipole-dipole coefficient $C_3 \simeq 2\pi \times 28.5\,\text{GHz}\,\mu\text{m}^3$. In this case the lattice constant is $a \simeq 14\,\mu\text{m}$ and the superatom extent $\delta r \simeq 1\,\mu\text{m}$. Thus we have experimentally feasible atomic densities $5 \times 10^{13}\,\text{cm}^{-3}$. In both scenarios we can neglect the level shift on the next nearest neighbor superatom as per Eq. (3.26).

Finally, let us comment on the aspect of atom losses due to the strong Rydberg-Rydberg interactions. While in a lattice with unity filling a loss of a single atom has a strong impact on the excitation dynamics, a lattice of superatoms with $N \gg 1$ is much more robust against a single atom loss. Preparing experimentally a lattice with exactly N atoms per microtrap may be challenging. However, in the case of superatoms and for $N \gg 1$ a single atom loss only slightly changes the relevant excitation and deexcitation rates.

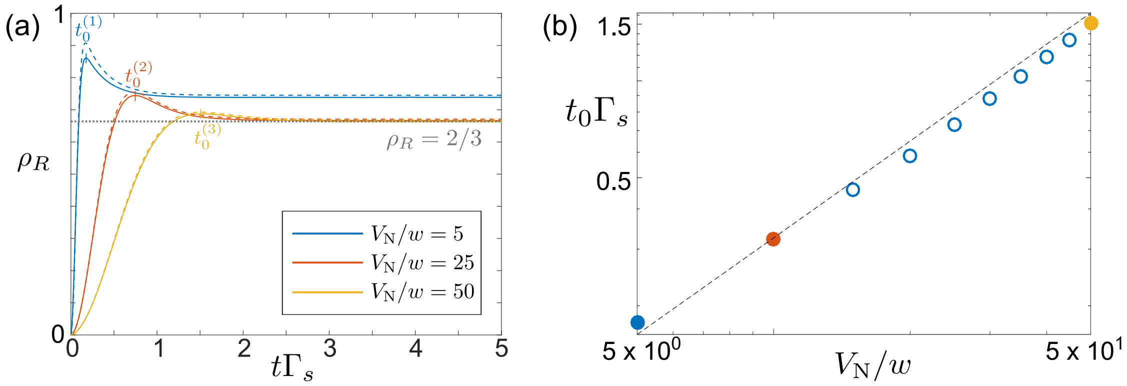

Figure 3.4: (a) Numerical simulation of the Rydberg excitation density ρ_R using the superatom rate equation model (solid lines) and the macroscopic model (dashed lines) in a 1D chain of superatoms. Initially, the system is in a state where all except of one (seed) atom are in the ground state. The parameters are $N = 50$, $\Omega = 25\Gamma_s$ and $\Gamma_d = 250\Gamma_s$. We use periodic boundary conditions in a chain of $L = 5000$ superatoms. The simulations are averaged over 500 individual realizations. The color code represents different interaction strength with respect to the single atom linewidth $w \simeq 570\Gamma_s$. The gray dotted line indicates a Rydberg excitation density $\rho_R = 2/3$. A peak in the excitation density is indicated by time t_0. (b) Scaling of the peak time t_0 with interaction strength V_{N}/w. The dashed line corresponds to the analytic estimate $t_0 \simeq 2/\sqrt{\Gamma_{\mathrm{seed}}\Gamma_{\uparrow}}$. The filled circles denote the peak time in (a) using the same color code.

3.2 Transient Relaxation Dynamics

Now, we discuss the transient excitation dynamics of the system under facilitation conditions on a timescale $t \lesssim \Gamma_s^{-1}$. Initially, all atoms are prepared in the ground state. To start the excitation cascade at a well defined time, we put one seed excitation in the system. A numerical simulation is shown in Fig. 3.4a. After turning on the excitation laser, the system reaches a peak Rydberg excitation density within a timescale $t \lesssim \Gamma_s^{-1}$. Then, the density relaxes to a lower steady state value. With increasing interaction strength V_{N}/w the Rydberg excitation density approaches $\rho_R \simeq 2/3$. Similarly, we observe the time evolution of the hole density ρ_h in Fig. 3.5a relaxing to a steady state value $\rho_h \simeq 1/3$.

3.2.1 Macroscopic Model

To gain insight into the characteristics of the transient relaxation dynamics, we construct a simple model based on three essential states: We start with all atoms in the ground state having zero Rydberg excitation density $\rho_R = 0$. The probability of this state is denoted by p_g with $p_g(t = 0) = 1$. Now, a first seed excitation triggers an excitation cascade to a state where almost all superatoms are excited with a corresponding probability p_e. While this state has unity Rydberg excitation density, we have already seen in Fig. 3.4a that the steady state, denoted by probability p_s, has a density $\rho_R = 2/3$. Initially, we have $p_e(t = 0) = p_s(t = 0) = 0$. We construct a simple model for the transient relaxation dynamics. The equations of motion for the state probabilities are

$$\partial_t p_g = -p_{\text{seed}}(t)\, 2\Gamma_\uparrow\, p_g, \tag{3.27a}$$

$$\partial_t p_e = +p_{\text{seed}}(t)\, 2\Gamma_\uparrow\, p_g - 3\Gamma_s\, p_e + \Gamma_{\text{seed}}\, p_s, \tag{3.27b}$$

$$\partial_t p_s = +3\Gamma_s\, p_e - \Gamma_{\text{seed}}\, p_s. \tag{3.27c}$$

The initial probability p_g is depleted to the excited state p_e by the growth of large excitation clusters. Each cluster originates from a seed and grows with rate $2\Gamma_\uparrow$ to both sides of the 1D chain. For short times, we assume a linear growth rate of seed excitations. Thus we approximate a seed probability $p_{\text{seed}}(t) \simeq p_{\text{seed}}(0) + \Gamma_{\text{seed}} t$, which is only a valid assumption for short times. However, since the initial state probability p_g is depleted on a fast timescale, the role of seed excitations becomes irrelevant. Now the excited state probability p_e relaxes to the steady state probability p_s with a rate $3\Gamma_s$, where on average every third superatom is an excitation hole. We verified the relaxation rate by numerical simulations starting with all superatoms excited. In turn, holes are refilled with the seed rate Γ_{seed} from the steady state with $2/3$ Rydberg excitation density to the excited state with unity density. We compare the resulting excitation density

$$\rho_R(t) = p_e(t) + \frac{2}{3} p_s(t) \tag{3.28}$$

to the full numerical simulation in Fig. 3.4a. Although the macroscopic model does not include microscopic details it approximates well the mean Rydberg excitation density evolution. In particular cluster collisions producing additional holes are not included in the model. This may explain the slight overestimation of the excitation density in the macroscopic model.

Now, we estimate the time t_0 where the excitation density ρ_R reaches its maximum. To this end, we integrate the initial state probability p_g. We assume that the maximum in the excitation density is reached when the initial state is depleted. Solving Eq. (3.27a) with $p_{\text{seed}}(0) \simeq 0$, we obtain

$$p_g(t) = \exp\left(-\Gamma_{\text{seed}}\Gamma_\uparrow t^2\right). \tag{3.29}$$

Thus, using the seed rate from Eq. (3.19) we expect a scaling of the peak time $t_0 \propto 1/\sqrt{\Gamma_{\text{seed}}\Gamma_\uparrow} \propto V_{\text{N}}$, which is verified by our numerical simulation in Fig. 3.4b.

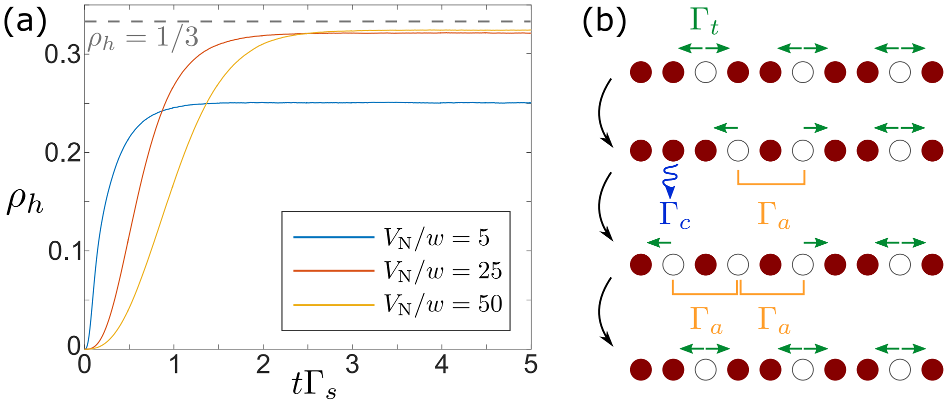

Figure 3.5: Numerical simulation of the hole density ρ_h using the superatom rate equation model (solid lines) in a 1D chain of superatoms. The parameters are the same as in Fig. 3.4 with different interaction strength V_N/w. The gray dotted line indicates a hole density $\rho_h = 1/3$. (b) Schematics of the effective model for the hole dynamics including hole creation with rate Γ_c, annihilation with rate Γ_a and transport from site to site with rate Γ_t.

3.3 Steady State Hole Dynamics

Next, we study the nonequilibrium dynamics of the system for times $t \gg \Gamma_s^{-1}$. Instead of considering Rydberg excited superatoms, we study the dynamics of excitation holes, i.e. a ground state superatom which is surrounded by two excited ones. Holes originate from collisions of Rydberg excitation clusters or from spontaneous decay of a Rydberg state within a cluster. The dynamics of the hole density ρ_h is shown in Fig. 3.5a. In the limit of strong interactions $V_\mathrm{N}/w \gg 1$ holes cannot be refilled and we obtain an almost universal hole density of $\rho_h \simeq 1/3$ in the steady state. To understand this and the nonequilibrium dynamics of holes we construct an effective model.

3.3.1 Effective Hole Model

Holes appear as stable quasi-particles for two reasons: First, an excitation hole can only be refilled by an off-resonant excitation of a Rydberg state with a strongly suppressed seed rate Γ_seed. In the limit $\Delta/w = V_\mathrm{N}/w \gg 1$ and for our discussion of an effective hole model we neglect this process. Second, whenever two or more unexcited superatoms are next to each other they will be immediately reexcited with rate $\Gamma_\uparrow$. These configurations are short lived since $\Gamma_\uparrow$ determines the shortest timescale in our system. By adiabatic elimination of these states we can construct an effective model for holes. Hence, the relevant subspace of the hole model includes only states where ground state superatoms are separated by one or more lattice sites. This behavior is reminiscent of a hard rod lattice gas with rod length $2a$ and was already used for describing Rydberg systems in the blockade regime [33, 134].

Before we derive the model, let us summarize the results: The many-body dynamics of holes can be described by three relevant processes, which are illustrated in Fig. 3.5b. It is convenient to express these processes in terms of Lindblad jump operators acting on the corresponding subspace for holes.

1. *Creation*: Holes are created by spontaneous decay of a Rydberg superatom in the center of a sequence of at least three consecutive excited superatoms with a rate $\Gamma_c = \Gamma_s$. This can be described by a non-local jump operator

   $$\hat{L}_c^{(j)} = \sqrt{\Gamma_c}\,\hat{\sigma}_+^{(j)}[1-\hat{n}_h^{(j+1)}][1-\hat{n}_h^{(j-1)}], \tag{3.30}$$

   which creates a hole on lattice site j if there is no hole on the neighboring sites (hard rod constraint). Here, the $\hat{\sigma}_\pm^{(j)}$ is the hole creation/annihilation operator for site j of the lattice and $\hat{n}_h^{(j)} \equiv \hat{\sigma}_+^{(j)}\hat{\sigma}_-^{(j)}$ is the number operator for a hole.

2. *Annihilation*: When two holes are separated by one excited superatom, one of the holes can be annihilated. This process is initiated by spontaneous decay of the middle superatom which triggers fast excitation of two superatoms from one or both sides of the three-site region. The hole annihilation is described by

   $$\hat{L}_a^{(j)} = \sqrt{\Gamma_a/2}\,\hat{\sigma}_+^{(j)}\hat{\sigma}_-^{(j+1)}\hat{\sigma}_-^{(j-1)}, \tag{3.31a}$$

   $$\hat{L}_{a\pm}^{(j)} = \sqrt{\Gamma_a/4}\,\hat{\sigma}_-^{(j\pm1)}\hat{n}_h^{(j)}, \tag{3.31b}$$

   with the total annihilation rate given by $\Gamma_a = \Gamma_s$. The remaining hole can then occupy either the middle site with half of the total probability, or one of the side sites, each with quarter of the total probability.

3. *Transport*: Holes can hop from site to site. This process is mediated by deexcitation of the superatom next to a hole with rate $\Gamma_\downarrow$ followed by facilitated excitation of one of the ground state superatoms. The hole transport is described by

   $$\hat{L}_{t\pm}^{(j)} = \sqrt{\Gamma_t}\,\hat{\sigma}_+^{(j\pm1)}\hat{\sigma}_-^{(j)}[1-\hat{n}_h^{(j\pm2)}], \tag{3.32}$$

   where $\Gamma_t = \Gamma_\downarrow/2$ is the transport rate and the last term ensures that the hole cannot hop to a site next to an existing hole.

Derivation

We derive the resulting effective model in a small chain of superatoms shown in Fig. 3.6. In particular, we consider three superatoms in a row where each superatom can be in the ground state (g) or excited Rydberg state (e). We assume that the chain of three superatoms is surrounded by excited superatoms on both sides. The probability of having a state in a configuration $\{abc\}$ with $a, b, c \in \{g, e\}$ is p_{abc}.

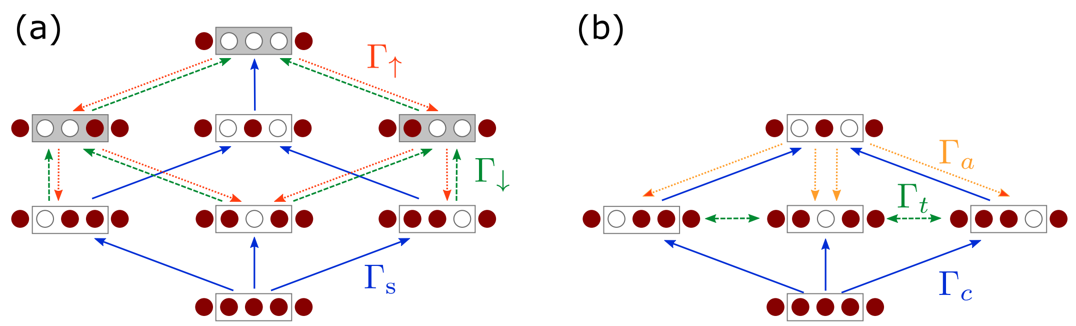

Figure 3.6: (a)-(b) Sketch of the transition rates of the full rate equation model (a) and effective hole model (b). Filled (red) circles denote excited superatoms, and open (white) circles the non-excited ones. (a) Using a three-site chain of superatoms, and fixed excited superatoms on the left and right of the chain, we identify the transition rates $\Gamma_s, \Gamma_\downarrow, \Gamma_\uparrow$ between the various excitation configurations. All configurations with two or more neighboring non-excited superatoms are adiabatically eliminated (gray shaded configurations). (b) The resulting effective model for hole dynamics involves three processes: creation of holes with rate Γ_c, annihilation of holes with rate Γ_a, and transport of holes with rate Γ_t.

In Fig. 3.6a we show all relevant transition rates. We obtain the following set of equations based on the superatom rate equation model

$$\partial_t p_{eee} = -3\Gamma_s p_{eee}, \tag{3.33a}$$

$$\partial_t p_{gee} = -(\Gamma_s + \Gamma_\downarrow) p_{gee} + \Gamma_s p_{eee} + \Gamma_\uparrow p_{gge}, \tag{3.33b}$$

$$\partial_t p_{ege} = -2\Gamma_\downarrow p_{ege} + \Gamma_s p_{eee} + \Gamma_\uparrow p_{gge} + \Gamma_\uparrow p_{egg}, \tag{3.33c}$$

$$\partial_t p_{eeg} = -(\Gamma_s + \Gamma_\downarrow) p_{eeg} + \Gamma_s p_{eee} + \Gamma_\uparrow p_{egg}, \tag{3.33d}$$

$$\partial_t p_{geg} = -\Gamma_s (p_{geg} - p_{gee} - p_{eeg}), \tag{3.33e}$$

$$\partial_t p_{gge} = -(2\Gamma_\uparrow + \Gamma_\downarrow) p_{gge} + \Gamma_\uparrow p_{ggg} + \Gamma_\downarrow (p_{gee} + p_{ege}), \tag{3.33f}$$

$$\partial_t p_{egg} = -(2\Gamma_\uparrow + \Gamma_\downarrow) p_{egg} + \Gamma_\uparrow p_{ggg} + \Gamma_\downarrow (p_{eeg} + p_{ege}), \tag{3.33g}$$

$$\partial_t p_{ggg} = -2\Gamma_\uparrow p_{ggg} + \Gamma_\downarrow (p_{gge} + p_{egg}) + \Gamma_s p_{geg}. \tag{3.33h}$$

To give an example, a state with all superatoms excited $\{eee\}$ may decay to any of the states $(\{gee\}, \{ege\}, \{eeg\})$ with overall rate $3\Gamma_s$ and one hole. Starting e.g. with $\{gee\}$ an excited superatom next to the hole may be deexcited with rate $\Gamma_\downarrow$ and results in a state $\{gge\}$. Now, any of the two ground state superatoms may be facilitated with rate $\Gamma_\uparrow$.

The probability of having three excited superatoms can only decay with rate $3\Gamma_s$ and is then no longer relevant for the dynamics of the three atom chain. All states containing more than one neighboring ground state superatom decay with a fast rate $\sim \Gamma_\uparrow$. We adiabatically eliminate these states setting $\partial_t p_{gge} = \partial_t p_{egg} = \partial_t p_{ggg} = 0$. Finally, we assume a strong facilitation rate $2\Gamma_\uparrow \gg \Gamma_\downarrow$

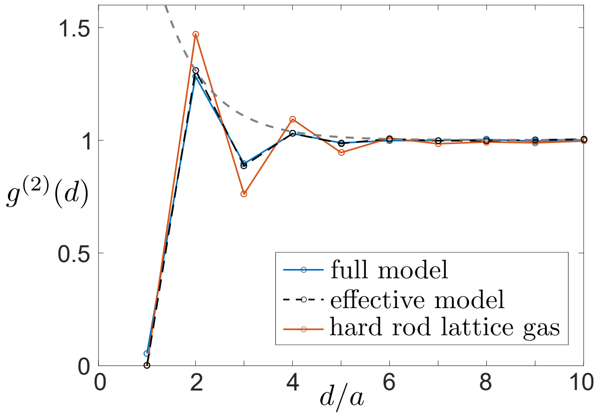

Figure 3.7: Second order spatial correlation function $g^{(2)}(d)$ for non-exited superatoms (solid blue line) obtained from the full rate equation simulation with $\Gamma_t/\Gamma_s \simeq 2.15$. Additionally, we show the correlation function for the effective hole model (black dashed line) and for a hard rod lattice gas (red line) with rod length $2a$ and constant density $1/3$ ($\Gamma_a = \Gamma_c = 0$). Using an exponential fit (gray dashed line) at even values of d/a we extract a correlation length $\xi = 0.86 \pm 0.14$.

and that states with two neighboring ground state atoms are strongly suppressed, $\frac{\Gamma_\downarrow}{\Gamma_s} p_{gge}, \frac{\Gamma_\downarrow}{\Gamma_s} p_{egg} \ll p_{geg}$. Then, we obtain transition rates for the hole dynamics

$$\partial_t p_{gee} = -(\Gamma_s + \tfrac{1}{2}\Gamma_\downarrow)p_{gee} + \tfrac{1}{2}\Gamma_\downarrow p_{ege} + \tfrac{1}{4}\Gamma_s p_{geg}, \tag{3.34a}$$

$$\partial_t p_{ege} = -\Gamma_\downarrow p_{ege} + \tfrac{1}{2}\Gamma_s p_{geg} + \tfrac{1}{2}\Gamma_\downarrow (p_{gee} + p_{eeg}), \tag{3.34b}$$

$$\partial_t p_{eeg} = -(\Gamma_s + \tfrac{1}{2}\Gamma_\downarrow)p_{eeg} + \tfrac{1}{2}\Gamma_\downarrow p_{ege} + \tfrac{1}{4}\Gamma_s p_{geg}, \tag{3.34c}$$

$$\partial_t p_{geg} = -\Gamma_s p_{geg} + \Gamma_s (p_{gee} + p_{eeg}). \tag{3.34d}$$

The corresponding transitions are illustrated in Fig. 3.6b and correspond to creation, annihilation and transport processes explained in detail for a large lattice system at the beginning of this chapter.

3.3.2 Hole Correlation Function

In the steady state of the system we expect a strong suppression of the probability of finding two neighboring ground state superatoms. This can be verified by calculating the second order spatial correlation function $g^{(2)}(d)$. Explicitly, the correlation function is defined in terms of excitation holes as

$$g^{(2)}(d_k) \equiv \frac{\langle \hat{n}_h^{(j)} \hat{n}_h^{(j+k)} \rangle}{\langle \hat{n}_h^{(j)} \rangle^2}, \tag{3.35}$$

where $d_k = ka$ with $k \in \mathbb{N}$ is the distance between holes. We assume a spatially uniform average hole density $\langle \hat{n}_h^{(j)} \rangle = \rho_h$.

In Fig. 3.7, we compare the $g^{(2)}(d)$ correlation function for ground state superatoms, the effective hole model and a hard rod liquid with rod length $2a$ and density $1/3$. In the case of the hard rod liquid and effective hole model $g^{(2)}(1a) = 0$ by definition. The full rate equations simulations also predict a strong suppression of $g^{(2)}(1a) \simeq 0$ and the effective model and the full model agree very well. The correlation function resembles a liquid of holes where we extract a small correlation length $\xi \lesssim 1a$. Although the hard rod lattice gas ($\Gamma_c = \Gamma_a = 0$) qualitatively shows the same behavior, it cannot reproduce the correlation function quantitatively. We believe the good agreement of full superatom rate equation simulations and the effective hole model fully justifies the interpretation of the steady state in terms of excitation holes.

3.3.3 Liquid-Crystal Crossover

In the current setup the transport rate is limited to $\Gamma_t \geq \Gamma_s/2$. Below, we discuss a hypothetical case where the transport rate of hole excitations can be reduced to arbitrarily small values. The more general case displays however interesting new phases in the steady state of the many-body system and may be realized with a more complicated laser excitation scheme.

Let us start with the case where all transport processes are suppressed, i.e. $\Gamma_t = 0$. Neglecting the small rate for refilling excitation holes Γ_{seed} we then have three stable steady state configurations. These correspond to a structure where each hole is separated by two excitations from the next hole (see initial configuration in Fig. 3.5b). Translational invariance upon a shift in the lattice of three sites results in a triply degenerate steady state. These configurations may be termed dark states, since the action of operators for creation $\hat{L}_c^{(j)}$ in Eq. (3.30) and annihilation $\hat{L}_a^{(j)}$ in Eq. (3.31) onto these configurations is zero. Thus, for a vanishing transport rate we have a crystalline ordered steady state where the peaks in the density-density correlation function $g^{(2)}(d)$ appear with period $d = 3a$. The hole density is $\rho_h = 1/3$ with no hole number fluctuations. We characterize fluctuations of the number of holes using the Mandel Q parameter

$$Q \equiv \frac{\langle \hat{n}_h^2 \rangle - \langle \hat{n}_h \rangle^2}{\langle \hat{n}_h \rangle} - 1, \tag{3.36}$$

where $\hat{n}_h = \sum_j \hat{n}_h^{(j)}$ is the total number of holes. The Mandel Q parameter is defined such that a value $Q < 0$ corresponds to sub-Poissonian number distribution. A value $Q = -1$ means no number fluctuations at all.

By increasing the transport rate Γ_t for holes we introduce fluctuations of the hole number. Since holes are now mobile again, creation and annihilation processes are possible. In Fig. 3.8a-b we plot the hole density ρ_h and the Q parameter versus the transport rate Γ_t. While the hole density $\rho_h \simeq 1/3$ remains constant, number fluctuations and thus the Q parameter increase. Nevertheless, even for large transport rates we obtain a sub-Poissonian hole number statistics. Using an algebraic

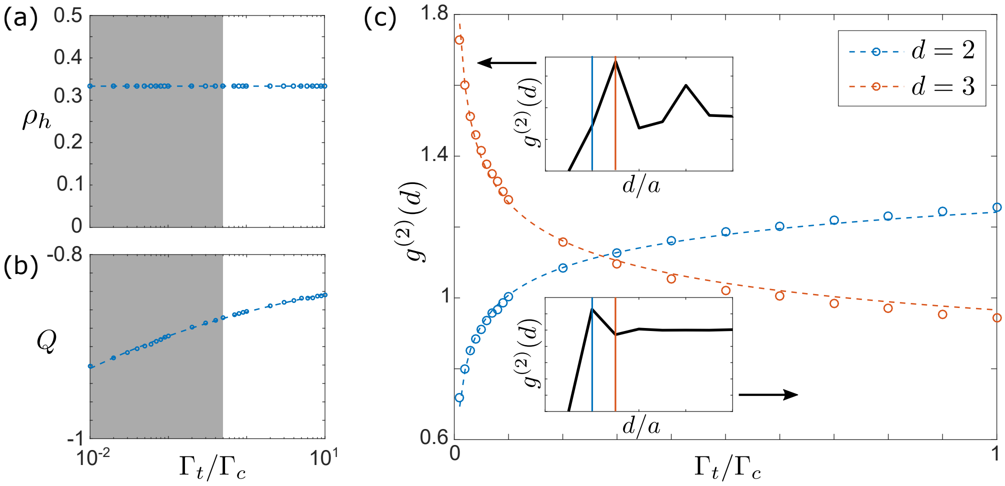

Figure 3.8: (a) Average hole density ρ_h and (b) Mandel Q parameters for the total number of holes versus the hopping rate Γ_t. The shaded area in (a) and (b) indicate the hypothetical case $\Gamma_t < \Gamma_s/2$, which is not accessible experimentally in the current model. (c) Amplitudes of the correlation function $g^{(2)}(d)$ for $d = 2a$ (blue circles) and $d = 3a$ (red circles) versus the hopping rate Γ_t. Dashed lines are algebraic fit functions. Exemplary, we show as an inset the second order spatial correlation function defined in Eq. (3.35) for small and large transport rate Γ_t.

fit function we find

$$Q\left(\frac{\Gamma_t}{\Gamma_c}\right) \simeq -0.8071 + 0.0546\left(\frac{\Gamma_t}{\Gamma_c}\right)^{-0.17}, \tag{3.37}$$

leading to a value $Q \simeq -0.81$ in the limit $\Gamma_t \to \infty$. Since both the annihilation rate and creation rate are equal to the decay rate in our setup, $\Gamma_c = \Gamma_a = \Gamma_s$, the number of holes is constant. We checked numerically that changing these rates independently the hole density changes as well.

Fluctuations of the hole number and associated transport processes lead to a melting of the crystalline structure with period $d = 3a$. Interestingly, the crystal does not simply melt into a liquid with short-range density correlations peaked at $d = 3a$, but at $d = 2a$. This crystal-liquid crossover upon increasing the transport rate Γ_t is indicated in Fig. 3.8c. While for small transport rates Γ_t it is more likely to find two holes with distance $d = 3a$ ($g^{(2)}(d = 3a) > 1$) than having distance $d = 2a$ ($g^{(2)}(d = 2a) < 1$), in the limit of large transport rates the situation is reversed. Since holes cannot move closer than two lattice sites, the liquid of holes has a correlation function similar to that of a hard rod liquid with rod length $2a$ and density $1/3$.

Conclusion

In this chapter we showed that interesting steady states can be realized in a 1D chain of Rydberg superatoms in the facilitation regime. Each superatom consists of a mesoscopic ensemble of atoms sharing at most one Rydberg excitation. We showed that in the steady state a new quasi-particle – a hole – emerges with an almost universal hole density of $\rho_h = 1/3$. A hole is a ground state superatom whenever it is surrounded by two excited superatoms.

We developed an efficient superatom rate equation model to simulate the many-body excitation dynamics. This description is valid in the regime of moderate and strong dephasing and is the basis of the discussion of the excitation dynamics. We showed that the relaxation towards the steady state can be easily described using a coarse grained macroscopic model. Furthermore, numerical simulations show that the steady state has an almost universal Rydberg excitation density of $\rho_R = 2/3$. We found that this can be understood in terms of holes, which can move through the lattice. Although, new holes can be created and annihilated, the hole number fluctuations are strongly suppressed with a Mandel Q parameter $Q \simeq -0.81$. In the experimentally accessible regime holes essentially behave as hard rods of length $d = 2a$ with short-range spatial correlations.

We envision that using a more complicated laser excitation scheme holes may become less mobile and allow to study a crossover to a crystalline regime with period $d = 3a$. This may be realized by coupling the ground state atoms to metastable long-lived states. Moreover, we believe it is interesting to investigate different lattice geometries of superatoms in the facilitation regime.

Chapter 4

Anomalous Excitation Facilitation in Dense Inhomogeneously Broadened Rydberg Gases

In the previous two chapters, we have seen that the facilitation regime in large ensembles of driven Rydberg atoms allows to observe interesting relaxation dynamics and steady state properties [90, 92, 93]. In particular, we investigated a large 3D system composed of single atoms (Chapter 2) and a 1D chain consisting of Rydberg superatoms (Chapter 3). In both cases, the facilitation dynamics manifests itself in a strong separation of timescales. While the rate for an off-resonant excitation to a Rydberg state is strongly suppressed, a subsequent excitation rate of a neighboring atom is enhanced, since the interaction energy shift can compensate the detuning. The interplay between these different timescales and the lifetime of a Rydberg state can lead to kinetically constrained excitation dynamics [59, 83–85, 135]

While strong decoherence is typically a limiting factor for quantum simulations, its influence on the system may lead to novel effects. In this chapter we discuss an anomalous facilitation mechanism arising in a dense inhomogeneously broadened Rydberg gas. This mechanism may appear on the "wrong" side of the laser detuning. Since in this case the interaction shift cannot compensate the detuning, it appears rather unexpected. Specifically, we discuss an attractively interacting Rydberg gas where facilitated excitations can appear on the red detuned side (*usual case*) as well as on the blue detuned side (*anomalous case*).

This chapter is based on the publication [FL3]. Several paragraphs have been taken from [FL3] and are partially modified.

4.1 Two Particle Dynamics: Usual Case

Let us briefly review the usual facilitation mechanism. Specifically, we discuss two repulsively interacting atoms on the blue detuned ($\Delta > 0$) side of the resonance. We consider the incoherent excitation rate of a ground state atom at distance r from an excited Rydberg state atom,

$$\Gamma_{\uparrow}(r) = \frac{2\Omega^2\gamma_0}{\gamma_0^2 + (\Delta - V(r))^2}. \tag{4.1}$$

A detailed derivation of the rate equation model and its validity can be found in Sec. 1.1.2. Due to the long-range interactions, a single Rydberg excitation alters dramatically the excitation rate

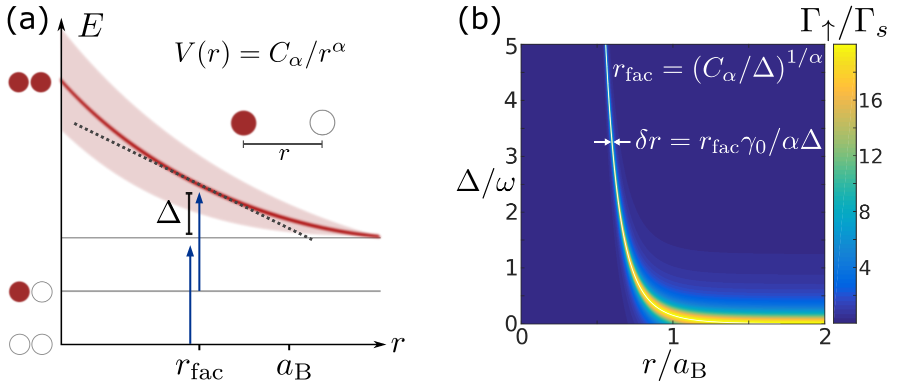

Figure 4.1: (a) Schematic overview of the two-step excitation mechanism in the incoherent antiblockade regime. An inhomogeneous broadening is indicated by the red shaded region. At the facilitation radius r_{fac} the interaction shift compensates the detuning shift, i.e. $\Delta = V(r_{\text{fac}})$. The blockade radius $a_{\text{B}} = (C_\alpha/\gamma_0)^{(1/\alpha)}$ is always larger than the facilitation radius r_{fac}. (b) Incoherent excitation rate normalized to the spontaneous decay rate Γ_s of the Rydberg state in the presence of one Rydberg excitation with distance r for different detunings Δ. We set the Rabi frequency $\Omega = 1$ as the natural energy scale and $a = 1$ the characteristic length scale. In these units, the parameters are $\Gamma_s = 0.05$, $\gamma_0 = 2$ and $C_6 = 10\omega$ with linewidth $\omega = \gamma_0\sqrt{4\Omega^2/\Gamma_s\gamma_0 + 1}$.

$\Gamma_\uparrow(r)$ of surrounding atoms. We consider repulsive interactions between Rydberg atoms of the form $V(r) = C_\alpha/r^\alpha$ ($\hbar = 1$) with $\alpha = 6$, corresponding to van der Waals type interaction. For repulsive interactions $V(r) > 0$ the interaction term in the denominator of Eq. (4.1) can compensate the detuning $\Delta > 0$. Here, Ω denotes the Rabi frequency and γ_0 is the decoherence rate including spontaneous decay and dephasing.

Figure 4.1a illustrates the antiblockade regime starting from both atoms in the ground state. While the first excitation is strongly off-resonant, the interaction shift $V(r)$ can compensate the detuning Δ exciting the second atom to the Rydberg state. For a fixed detuning Δ, the subsequent excitation rate $\Gamma_\uparrow(r)$ reaches its maximum at the so called facilitation radius

$$r_{\text{fac}} = \sqrt[\alpha]{C_\alpha/\Delta}, \tag{4.2}$$

at which the transition is moved exactly into resonance.

Assuming a linear slope and that the excitation linewidth is determined by the decoherence rate γ_0, the spatial extent of the facilitation region can be expressed as

$$\delta r \simeq \frac{\gamma_0}{\alpha\Delta} r_{\text{fac}}. \tag{4.3}$$

The spatial extent δr becomes smaller and smaller if the detuning Δ is increased. However, the peak value $2\Omega^2/\gamma_0$ is unaltered. This can be seen in Fig. 4.1b, where we show the excitation rate (4.1) for different detunings Δ illustrating the transition between blockade regime ($\Delta \lesssim w$) and antiblockade regime ($\Delta \gtrsim w$).

4.2 Inhomogeneous Broadening

In many experiments with Rydberg atoms strong broadening in the atomic spectrum has been observed [136–139]. Although this may limit the observation of fully coherent quantum dynamics, it may also lead to interesting new effects.

There are several possibilities for inhomogeneous broadening which strongly depend on the microscopic details of the system. Therefore, a full theory of possible broadening mechanisms in Rydberg gas experiments is not available. Yet, we want to mention a few possible scenarios: Firstly, the strong and long-range interaction may induce additional dephasing mechanisms [136, 137]. Secondly, black-body induced or spontaneous transitions to neighboring Rydberg levels may lead to a dipole-dipole interaction induced broadening [138–141]. Another effect is motion in Rydberg gases, which goes beyond the frozen gas approximation [39, 142]. In particular, the off-resonant excitation of two atoms to Rydberg states in optical lattices can induce an inhomogeneous broadening as discussed in Ref [116, 117] and in Sec. 2.2. In the latter case an asymmetric line shape is expected as can be seen in Fig. 2.6. Crucially, they all originate from a strong and quasi long-range interaction potential $V(r) = C_\alpha/r^\alpha$ and therefore depend on the mutual distance r between the two atoms.

We assume a special type of interaction induced broadening,

$$\gamma(r) = \gamma_0 + \frac{D_\beta}{r^\beta}. \tag{4.4}$$

Besides the bare decoherence rate γ_0 we added a dephasing rate seen by a ground state atom with distance r to an excited atom. The coefficient β determines the range and D_β the strength of the broadening. Specifically, we discuss here the case $\beta = 6$. However, similar results can be obtained for different exponents β, such as $\beta = 12$ expected for van der Waals interaction induced broadening. Importantly, with decreasing distance between two atoms, the interaction induced broadening $\gamma(r)$ increases strongly. In this case, the full excitation rate is

$$\Gamma_\uparrow(r) = \frac{2\Omega^2\gamma(r)}{\gamma(r)^2 + (\Delta - V(r))^2}. \tag{4.5}$$

Note that we assume a symmetric inhomogeneous broadening mechanism centered at the resonance position $\Delta = V(r_{\text{fac}})$. In the limit $r \to \infty$, we retrieve the excitation rate for uncorrelated atoms.

4.3 Two & Many Particle Dynamics: Anomalous Case

Below, we will show that contrary to the intuition from the previous discussion also attractive interactions with strong inhomogeneous broadening can result in an *anomalous facilitation* on the blue detuned side of the resonance. Specifically, we discuss an attractive interaction potential $V(r) = C_6/r^6 < 0$. Responsible for the anomalous facilitation mechanism is the additional inhomogeneous decoherence rate $\gamma(r)$ as in Eq. (4.4). The line broadening $\gamma(r)$ strongly increases with decreasing mutual distance r between two atoms in the ground and Rydberg state. The resulting excitation rate (4.5) is shown in Fig. 4.2 as a false-color contour plot.

On the red detuned side $\Delta < 0$, i.e. the detuning has the same sign as the interaction potential $V(r)$, we recognize the usual facilitation mechanism, see Fig. 4.2b. Here, the broadening mainly reduces the excitation rate compared to (4.1) without additional broadening. At the facilitation radius r_{fac}, the excitation rate $\Gamma_{\uparrow}(r)$ reaches approximately its maximum. We obtain a broader spatial width approximately given by $\delta r \simeq r_{\text{fac}}\gamma(r_{\text{fac}})/6\Delta$ upon replacing γ_0 by $\gamma(r_{\text{fac}})$ in Eq. (4.3).

Interestingly, we can identify an anomalous facilitation radius $\tilde{r}_{\text{fac}}$ also on the blue detuned side $\Delta > 0$, as shown in the inset of Fig. 4.2a. Similar to the usual case, the anomalous facilitation rate at $\tilde{r}_{\text{fac}}$ decreases with increasing detuning Δ and approximately follows the same scaling as r_{fac}. While in the usual case facilitation results from an interaction term compensating the detuning, in the anomalous case, the peak in the excitation rate at the anomalous radius $\tilde{r}_{\text{fac}}$ originates from the inhomogeneity of the broadening mechanism. Overall, the excitation rate for an atom at distance $\tilde{r}_{\text{fac}}$ with blue detuning is of course much smaller than in the red detuned case. However, the spatial width of the facilitation profile $\Gamma_{\uparrow}(r)$ is broadened, too.

Naively, we do not expect any cascaded excitations since the magnitude of the rates is strongly reduced on the blue detuned side of the resonance for attractive interaction. However, we will show that facilitation can be possible for certain detunings Δ in sufficiently dense atomic gases. So far, we discussed the excitation rate of a single ground state atom in the presence of one other already excited Rydberg atom at distance r. However, a single Rydberg excitation influences the excitation rate of *all* surrounding atoms within a blockade radius a_{B}. Therefore, we have to consider the integrated facilitation rate

$$\bar{\Gamma}_{\uparrow} = \sum_{j}^{N} \Gamma_{\uparrow}(r_j) \tag{4.6}$$

over all atoms j with distance r_j to the excited Rydberg atom. Here N is the number of atoms within the blockade radius a_{B}. Atoms with distance larger than the blockade radius, i.e. $r > a_{\text{B}}$, are only weakly affected by the interaction shift and therefore neglected. To observe facilitated excitations, we require two ingredients: Firstly, for an excitation cascade, we have to compare the integrated

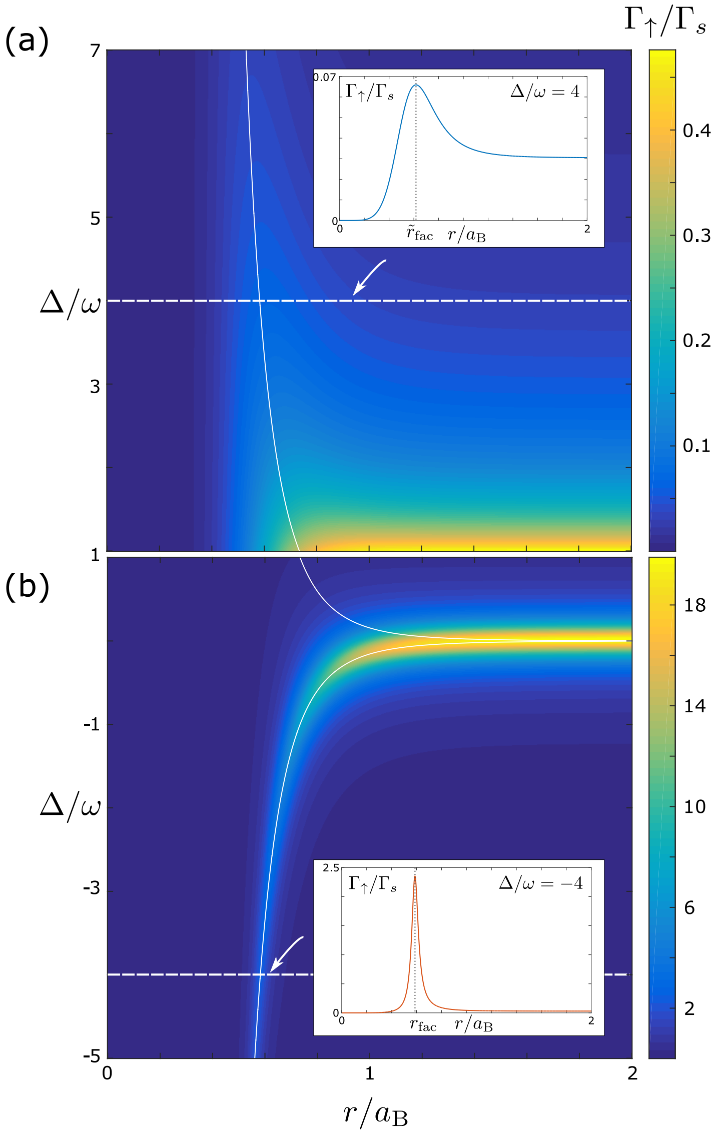

Figure 4.2: Incoherent excitation rate $\Gamma_\uparrow(\Delta, r)/\Gamma_s$ in the presence of one Rydberg atom at distance r with detuning Δ for an attractive interaction $C_6 = -10\omega$ for the same parameters as in Fig. 4.1 and $D_6 = 0.3C_6$. (a) *Anomalous facilitation* on the blue detuned side and (b) *usual facilitation* on the red detuned side with attractive interaction. The insets show the excitation profile $\Gamma_\uparrow(r)$ for (a) blue ($\Delta/\omega = -4$) and (b) red ($\Delta/\omega = 4$) detuning. The white solid line follows $|C_6/\Delta|^{(1/6)}$.

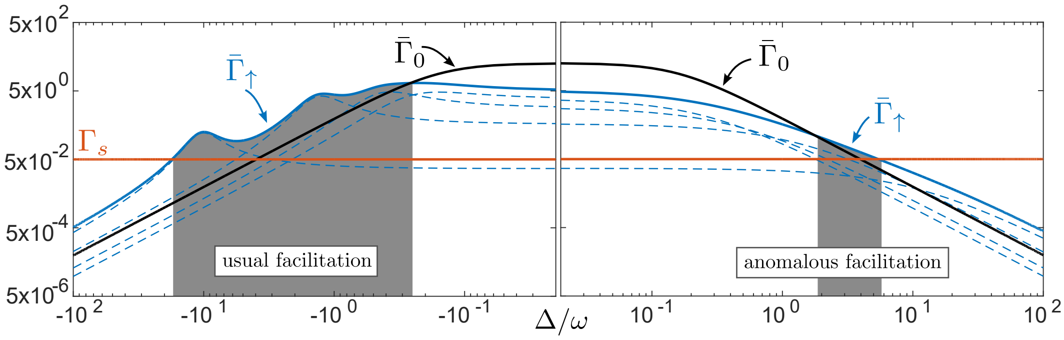

Figure 4.3: For a cubic lattice with lattice spacing a we calculate the total facilitation rate $\bar{\Gamma}_\uparrow$ for all atoms within a blockade radius $a_\mathrm{B}/a \simeq 2$. We determine the region (gray shaded) where both conditions for facilitation (i) $\bar{\Gamma}_\uparrow > \bar{\Gamma}_0$ and (ii) $\bar{\Gamma}_\uparrow > \Gamma_s$ are fulfilled. The blue dashed lines show the facilitation rate for different distances r_j to the excited Rydberg atom. Due to the lattice structure, we encounter a discrete set of resonances. The blue solid line is the total facilitation rate. We used the same parameters as in Fig. 4.2.

facilitation rate $\bar{\Gamma}_\uparrow$ to the uncorrelated total excitation rate

$$\bar{\Gamma}_0 = N\Gamma_\uparrow(r \to \infty). \tag{4.7}$$

Secondly, we have to ensure, that one Rydberg excitation triggers a subsequent excitation before it decays with rate Γ_s back to the ground state. This leads to the following two conditions for facilitation

$$\bar{\Gamma}_\uparrow > \bar{\Gamma}_0, \tag{4.8}$$

$$\bar{\Gamma}_\uparrow > \Gamma_s. \tag{4.9}$$

The conditions (4.8) and (4.9) may be fulfilled easily in the usual facilitation case even in the case of a single neighboring atom (see Fig. 4.2), whereas in the anomalous case, the individual excitation rates are much weaker. Nevertheless, since the spatial excitation width of the anomalous case is much larger, many more atoms can contribute and conditions (4.8) and (4.9) can be fulfilled for a sufficiently dense atomic gas.

4.3.1 Example and Experimental Considerations

To give an example, we calculate the integrated excitation rates $\bar{\Gamma}_\uparrow$ and $\bar{\Gamma}_0$ using realistic experimental parameters for a cubic lattice with lattice spacing $a_\mathrm{B}/a \simeq 2$ and we choose a weight $D_6/C_6 = 0.3$. Within a blockade radius a_B, we count $N = 32$ atoms. The results are shown for both, blue and red detuning, in Fig. 4.3. While we can identify individual resonance peaks (dashed blue lines) on the red detuned side corresponding to specific lattice distances, on the blue detuned side only the residual line broadening of the resonances remain. Due to the inhomogeneous broadening, the resonance lines on the red detuned side are strongly broadened. Here, conditions Eq. (4.8) and Eq. (4.9) are fulfilled for a broad range of detunings (gray shaded region) and we observe usual facilitation. Surprisingly, on the blue detuned side both facilitation conditions in Eq. (4.8) and (4.9) are fulfilled for several detunings, too. Although, the extent of allowed detunings Δ is much larger on the red detuned side, an anomalous facilitation is possible on the blue side of the detuning Δ. Note that the anomalous facilitation range strongly depends on the density, the microscopic geometry, the interaction and the line broadening.

Finally, let us comment on a possible observation of the anomalous facilitation mechanism in a pump-probe experiment. A first excitation pulse, which is resonant with the atomic transition, creates a small number of Rydberg excitations in a cold atomic sample. Choosing, for instance, Rubidium p-states with principal quantum number $n < 38$ will provide the required attractive van der Waals interaction. Subsequently, a probe beam with tunable frequency is applied and the number of Rydberg excitations is recorded. This is then compared to the bare excitation rate without the pump pulse. To enhance the visibility of the effect, it might be favorable to increase the number of atoms within a blockade sphere, which suggests the use of a three-dimensional setup. We checked that a continuous system without an underlying lattice structure fulfills the anomalous facilitation condition, too. The parameters chosen here are compatible with current experiments. Nevertheless, we want to point out that other parameters can lead to similar results.

Conclusion

We discovered an anomalous facilitation mechanism allowing to observe cascaded excitations in an experimentally accessible and unexpected parameter regime. In contrast to the usual facilitation, where the interaction compensates the detuning, the anomalous facilitation appears on the opposite side of the detuning. Our discussion was motivated by the observation of an interaction induced inhomogeneous broadening mechanism in recent experiments [138, 139]. While we here assumed an additional decoherence proportional to the van der Waals interaction, we would like to point out that other spatially dependent broadening mechanisms may lead to similar results. We discussed the general conditions for facilitation in the many particle dynamics.

We believe that the anomalous facilitation is an interesting extension to the usual facilitation, which may be observable in current experiments. In particular, it may lead to unexpected correlations on the "wrong" side of the resonance. For instance, attractive interactions may lead to the formation of molecular bound states suppressing an excitation cascade on the red detuned side. However, the observation of strongly correlated excitation growth may be seen on the blue detuned side of the resonance. Finally, we hope that our discussion further motivates to study the origin of excitation line broadening in ultracold Rydberg gases and may trigger applications thereof.

Chapter 5

Mobile Bound States of Rydberg Excitations in a Lattice

Spin lattice models play a fundamental role in the theoretical description of solid state phenomena, such as magnetism and superconductivity. They are relevant for both, the study of quantum and thermal phase transitions [57, 58]. While these models arise naturally in condensed matter systems, it is still experimentally challenging to create interesting spin models in a controlled environment with tunable interactions. Of particular interest are systems, where the interplay between transport of spin excitations and the interaction between spins may lead to interesting dynamics [143–146].

Although, the realization of tunable and coherent spin models is challenging, there exist several experimental platforms exploring these models. Among them are trapped ions [11, 147], superconducting circuits [148, 149] and quantum dots [150]. One promising route for large scale spin models and good coherent control are cold atoms in optical lattices [12, 151]. However, the relevant interaction energies in these systems are on the order of a few Hz, which makes them susceptible to thermal effects and decoherence.

Rydberg system offer another possibility to exploit strong spin interactions [37, 38]. So far, many experiments concentrate on either strong van der Waals interactions [10, 21, 22, 125–127], realizing Ising type models, or resonant dipole-dipole interactions [46, 152–155]. The latter allows to realize spin models with spin-exchange interaction. Here, we propose a scheme realizing an extended XXZ model with tunable and long-range interactions. To this end, we combine both dipole-dipole interactions and van der Waals interactions in a setup of dressed Rydberg atoms [117, 156, 157]. This allows to tune the spin-exchange strength by changing the amplitude of the dressing laser field. Due to the rather long lifetimes of Rydberg states, this setup is suitable to study coherent and incoherent spin dynamics alike.

In particular, we investigate the dynamics of a few spin excitations. We show that in our setup mobile bound states of excitations exist. Similar to the binding mechanism of e.g. repulsively bound pairs in the Bose Hubbard model [145, 158–161], Rydberg excitations can form a tightly bound pair due to the strong van der Waals interaction. The long-range spin-exchange process leads to an increased mobility in comparison with the Bose Hubbard model.

This chapter is based on the publication [FL6], partially with text overlap.

5.1 Extended XXZ Model

In this section we consider a spin lattice model with long-range interactions, which is described by the Hamiltonian ($\hbar = 1$)

$$\hat{\mathcal{H}} = \sum_{i<j} J_{ij} \left(\hat{\sigma}_+^i \hat{\sigma}_-^j + \hat{\sigma}_-^i \hat{\sigma}_+^j \right) + \sum_{i<j} U_{ij} \hat{n}_i \hat{n}_j. \tag{5.1}$$

We define the spin lowering $\hat{\sigma}_-^i = |\downarrow\rangle_i \langle\uparrow|$ and raising operators $\hat{\sigma}_+^i = |\uparrow\rangle_i \langle\downarrow|$ for the ith spin in the lattice. The operator $\hat{n}_i \equiv \hat{\sigma}_+^i \hat{\sigma}_-^i = |\uparrow\rangle_i \langle\uparrow|$ projects onto the spin-up state. The first term in Eq. (5.1) corresponds to a long-range spin-flip process with exchange interaction J_{ij}. We assume a lattice with $L \gg 1$ sites. The second term describes interactions between spins in the state $|\uparrow\rangle$ with an interaction strength U_{ij}. We assume that both interaction strengths depend only on the mutual distance $|i - j|$ between two spins at positions i and j. This model preserves the total number of spin excitations $\hat{N} = \sum_i \hat{n}_i$.

Single excitation For a single spin excitation ($N = 1$) – a *magnon* – the interaction part becomes irrelevant. We can label each state with the position x of the spin excitation $|x\rangle \equiv \hat{\sigma}_+^x |\downarrow_1 \downarrow_2 \ldots \downarrow_L\rangle$. The Hamiltonian (5.1) can be written as

$$\hat{\mathcal{H}}^{(1)} = \sum_{x \neq y}^{L} J_{xy} |x\rangle \langle y| = \sum_{x=1}^{L} \sum_{d \geq 1} J_d (|x\rangle \langle x + d| + |x\rangle \langle x - d|). \tag{5.2}$$

The magnon can hop from one site to an other site at distance d with a hopping strength J_d depending on the hopping distance d. We can easily diagonalize the Hamiltonian (5.2) using a discrete Fourier transform $|x\rangle = \frac{1}{\sqrt{L}} \sum_q e^{iqx} |q\rangle$. Here, q is the lattice quasi momentum which has values $q = \frac{2\pi n}{L}$ with $n \in \{-\frac{L-1}{2}, \ldots, \frac{L-1}{2}\}$. The transformed Hamiltonian,

$$\hat{\mathcal{H}}_J^{(1)} = \sum_q E^{(1)}(q) |q\rangle \langle q|, \tag{5.3}$$

is diagonal in the lattice quasi momentum q with energy

$$E^{(1)}(q) = \sum_{d \geq 1} 2 J_d \cos(qd). \tag{5.4}$$

Two excitations Next, let us consider the case of two magnons ($N = 2$). We label states with excitations at positions x and y with $|x, y\rangle \equiv \hat{\sigma}_+^x \hat{\sigma}_+^y |\downarrow_1 \downarrow_2 \ldots \downarrow_L\rangle$. Since $|x, y\rangle = |y, x\rangle$ we use the convention $x < y$ for a state $|x, y\rangle$ to avoid double counting. Within the $N = 2$ excitation subspace we can cast the Hamiltonian (5.1) as

$$\begin{aligned}\hat{\mathcal{H}}^{(2)} = \sum_{x<y}\Big[&\sum_{d} J_d(|x,y\rangle\langle x-d,y| + |x,y\rangle\langle x,y+d|) \\ &+ \sum_{d<y-x} J_d(|x,y\rangle\langle x+d,y| + |x,y\rangle\langle x,y-d|) \\ &+ \sum_{d>y-x} J_d(|x,y\rangle\langle y,x+d| + |x,y\rangle\langle y-d,x|) \\ &+ U_{xy}|x,y\rangle\langle x,y|\Big]. \end{aligned} \tag{5.5}$$

The hopping part of Eq. (5.5) includes processes where two excitations approach or separate each other or hop over one another. Besides the individual hopping elements of each spin excitation we include an interaction U_{xy} between magnons at lattice sites x and y. We assume the interaction depends only on the relative distance between the spin excitations $r \equiv y - x$. Thus we use center of mass coordinate $R \equiv \frac{x+y}{2}$ and relative coordinate r to further simplify the Hamiltonian and obtain

$$\begin{aligned}\hat{\mathcal{H}}^{(2)} = \sum_{R,r}\Big[&\sum_{d} J_d(|R\rangle\langle R-d/2| \otimes |r\rangle\langle r+d| + |R\rangle\langle R+d/2| \otimes |r\rangle\langle r+d|) \\ &+ \sum_{d<r} J_d(|R\rangle\langle R+d/2| \otimes |r\rangle\langle r-d| + |R\rangle\langle R-d/2| \otimes |r\rangle\langle r-d|) \\ &+ \sum_{d>r} J_d(|R\rangle\langle R+d/2| \otimes |r\rangle\langle d-r| + |R\rangle\langle R-d/2| \otimes |r\rangle\langle d-r|) \\ &+ U_r|R\rangle\langle R| \otimes |r\rangle\langle r|\Big]. \end{aligned} \tag{5.6}$$

Here, $R = 1 + \frac{1}{2}, 2, 2 + \frac{1}{2}, \ldots, L - \frac{1}{2}$ takes $\tilde{L} = 2L - 3$ discrete values, and $r = 1, 2, \ldots, L - 1$ takes $L - 1$ values. We perform a Fourier transformation $|R\rangle = \frac{1}{\sqrt{\tilde{L}}}\sum_K e^{iKR}|K\rangle$ and introduce the center of mass lattice quasi momentum $K = \frac{2\pi n}{\tilde{L}}$ with $n \in \{-\frac{\tilde{L}-1}{2}, \ldots, \frac{\tilde{L}-1}{2}\}$. Finally, using $J_{d,K} \equiv 2J_d\cos(Kd/2)$ we can recast Hamiltonian (5.1) for two excitations as

$$\begin{aligned}\hat{\mathcal{H}}^{(2)} &= \sum_K \hat{\mathcal{H}}_K|K\rangle\langle K|, \\ \hat{\mathcal{H}}_K &= \sum_r\Big[\sum_d J_{d,K}|r\rangle\langle r+d| + \sum_{d<r} J_{d,K}|r\rangle\langle r-d| + \sum_{d>r} J_{d,K}|r\rangle\langle d-r| + U_r|r\rangle\langle r|\Big]. \end{aligned} \tag{5.7}$$

5.2 Effective Rydberg-dressed Spin Lattice Model

The spin model discussed in Sec. 5.1 can be realized using two different Rydberg states and exploiting dipole-dipole and van der Waals interactions. We assume that single atoms are trapped in a 1D array and can be excited to Rydberg states $|s\rangle$ and $|e\rangle$ as indicated in Fig. 5.1. Initially, N atoms are

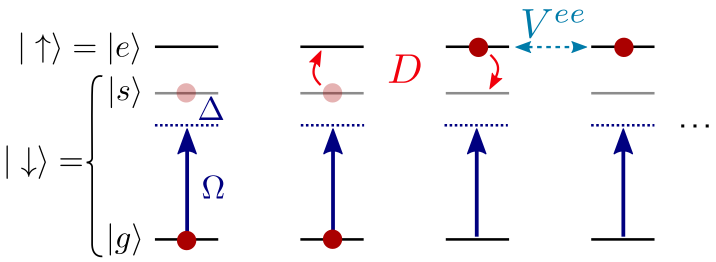

Figure 5.1: Simplified level scheme for Rydberg-dressed spin model. A ground state $|g\rangle$ is dressed to a Rydberg state $|s\rangle$ with Rabi frequency Ω and detuned by Δ. The spin-down state is approximately $|\downarrow\rangle \simeq |g\rangle + \frac{\Omega}{\Delta}|s\rangle$ and the spin-up state is another Rydberg state, $|\uparrow\rangle = |e\rangle$. While the interaction between spin-up states maintains the full Rydberg interaction strength V^{ee}, the spin flip processes induced by the dipole-exchange interaction D is reduced approximately by a factor $\frac{|\Omega|^2}{\Delta^2}$.

prepared in the Rydberg state $|e\rangle$, while the remaining atoms are prepared in the other Rydberg state $|s\rangle$. Let us assume that the transition between states $|s\rangle$ and $|e\rangle$ are dipole allowed. Then two atoms in states $|e\rangle$ and $|s\rangle$ with distance d will undergo resonant dipole-dipole interaction with strength $D_d = C_3/d^3$ [47, 154], which realizes the first part of Eq. (5.1), i.e. the hopping of magnons. In addition, we have interactions between two atoms in Rydberg states $|s\rangle$ and $|e\rangle$ [40]. For simplicity, let us assume that only the interaction between two Rydberg $|e\rangle$ states is relevant. Then, we have a van der Waals interaction $V_d^{ee} = C_6/d^6$, which corresponds to the second part of the Hamiltonian Eq. (5.1).

The interaction coefficients C_3 and C_6 are determined by the microscopic details of the atomic states. Typically, the resonant dipole-dipole interaction D_d is much stronger than the van der Waals interaction V_d. As already discussed in Sec. 1.2, the van der Waals interaction originates from second order perturbation theory in $D_d/\delta\omega \ll 1$, where $\delta\omega$ is a large Förster defect [38]. Thus, the van der Waals interaction $V_d \sim D_d^2/\delta\omega$ is smaller than the resonant dipole-dipole interaction and therefore precludes the study of the strong interaction regime $V_d \gtrsim D_d$. However, this is the regime where we expect interesting spin excitation dynamics to happen and therefore want to study.

To this end, we propose a scheme which allows to approximately realize the spin lattice model Hamiltonian Eq. (5.1) with tunable parameter J_{ij}/U_{ij}. Instead of directly exciting atoms to the Rydberg $|s\rangle$ state, this Hamiltonian might be realized by dressing ground state atoms with the Rydberg $|s\rangle$ state. The small admixture of the Rydberg state mediates the spin exchange process with tunable interaction strength, while the van der Waals interaction strength of the $|e\rangle$ excitation remains unaltered. The idea to employ Rydberg-dressing to realize tunable interactions has been proposed already in Ref. [117, 156, 157] and Rydberg dressing has been realized in recent experiments [126, 127, 162]. This may pave the way to study exotic phases of condensed matter systems [92, 143, 144, 146, 163–165].

5.2.1 Microscopic Model

We consider a translational invariant array of atoms trapped in a 1D optical lattice with lattice constant a. The level scheme including the external drive and interactions is depicted in Fig. 5.1. Each lattice site contains a single atom, which is assumed to be in its motional ground state. We assume that initially a fixed number N of atoms in the Rydberg states $|e\rangle$ are created. A spatially uniform laser drives the transition from the ground state $|g\rangle$ to a Rydberg state $|s\rangle$ with Rabi frequency Ω. The mismatch between the laser carrier frequency ω and the atomic transition frequency ω_{gs} determines the detuning $\Delta = \omega_{ge} - \omega$. In a rotating frame and neglecting a constant energy offset the Hamiltonian is ($\hbar = 1$)

$$\hat{\mathcal{H}}_{\text{at}} = \sum_j \left[\Delta\hat{\sigma}_j^{ss} - \Omega\hat{\sigma}_j^{gs} - \Omega^*\hat{\sigma}_j^{sg}\right] + \sum_{i<j} D_{ij}\left(\hat{\sigma}_i^{es}\hat{\sigma}_j^{se} + \hat{\sigma}_i^{se}\hat{\sigma}_j^{es}\right) \\ + \sum_{i<j}\left(V_{ij}^{ee}\hat{\sigma}_i^{ee}\hat{\sigma}_j^{ee} + V_{ij}^{ss}\hat{\sigma}_i^{ss}\hat{\sigma}_j^{ss} + V_{ij}^{es}\hat{\sigma}_i^{ee}\hat{\sigma}_j^{ss}\right). \quad (5.8)$$

Here $\hat{\sigma}_j^{\mu\nu} = |\mu\rangle_j\langle\nu|$ is a transition ($\mu \neq \nu$) or a projection ($\mu = \nu$) operator for the jth atom. We include interactions between Rydberg states and assume them to be of van der Waals type $V_{jk}^{\mu\nu} = V_{r_{jk}} = C_6^{\mu\nu}/r_{jk}^6$. $C_6^{\mu\nu}$ denotes the van der Waals coefficient and $r_{jk} = |j-k|a$ is the distance between two atoms at lattice sites j and k. Furthermore, we include dipole-dipole coupling between two atoms in the Rydberg states $|se\rangle \leftrightarrow |es\rangle$ via $D_{kj} = D_{r_{jk}} = C_3/r_{jk}^3$. We neglect all decoherence mechanisms e.g. decay from the Rydberg states. This is justified when the experimental timescales are sufficiently shorter than the lifetime of the Rydberg states. In this case, the number N of atoms in the $|e\rangle$ state is a conserved quantity. In the following discussion we set the lattice constant a to unity. Thus the distance r_{jk} between two atoms at lattice sites j and k is a positive integer.

5.2.2 Rydberg Dressing

For dressing the ground state with a Rydberg state, we consider a regime where the detuning is the largest energy scale in the system,

$$\Delta \gg |\Omega|, D_d > V_d^{ee}, V_d^{es}, V_d^{ss}, \quad (5.9)$$

where d is the distance between Rydberg atoms. While the Rabi frequency Ω can be comparable to the dipole-dipole interactions, the relevant van der Waals interaction $V_d^{\mu\nu}$ can be much smaller.

Zero excitations ($N = 0$)

Let us first recall dressing of an isolated atom [165]. In this case we neglect all interactions and the system is described by the Hamiltonian (in a rotating frame)

$$\hat{\mathcal{H}}_0 = \Delta \left|s\right\rangle \left\langle s\right| - \Omega \left|g\right\rangle \left\langle s\right| - \Omega^* \left|s\right\rangle \left\langle g\right| . \tag{5.10}$$

For convenience we set the ground state energy to zero. For $|\Omega|/\Delta = 0$ the low-energy state $|g\rangle$ is decoupled from the high energy state $|s\rangle$ with energy Δ. In the case $|\Omega|/\Delta \neq 0$, we diagonalize the system and obtain eigenstates and corresponding eigenenergies

$$|\pm\rangle = \frac{\varepsilon_\mp |g\rangle + \Omega |s\rangle}{\sqrt{\varepsilon_\mp^2 + |\Omega|^2}}, \quad \varepsilon_\pm = \frac{\Delta \pm \sqrt{\Delta^2 + 4|\Omega|^2}}{2}. \tag{5.11}$$

In the dressing regime ($\Delta \gg |\Omega|$), the low-energy state $|g\rangle$ is modified. The new eigenstate $|-\rangle \simeq |g\rangle + \frac{\Omega}{\Delta} |s\rangle$ has a small admixture of the Rydberg state $|s\rangle$. Its eigenenergy $\epsilon_- \simeq -\frac{|\Omega|^2}{\Delta}$ is shifted by $\delta = -\frac{|\Omega|^2}{\Delta}$ (ac Stark shift). We will use the dressed ground state as the spin-down state $|\downarrow\rangle \equiv |-\rangle$.

Now we consider a chain of L ground state atoms dressed with the Rydberg $|s\rangle$ state. Since atoms are excited with probability $\frac{|\Omega|^2}{\Delta^2}$ to the Rydberg $|s\rangle$ state, the interaction is reduced to $\frac{|\Omega|^4}{\Delta^4} V_r^{ss}$. In the case discussed here we assume that this is small and we neglect interactions between spin-down states. The total energy shift

$$E_0 = \sum_x^L \delta_x = -L \frac{|\Omega|^2}{\Delta} \tag{5.12}$$

is constant and can be disregarded by redefining the zero-point energy.

Single excitation ($N = 1$)

We identify the spin-up state $|\uparrow\rangle \equiv |e\rangle$ with a Rydberg state $|e\rangle$. Now we consider a single atom in the Rydberg state $|e\rangle$ immersed in a gas of dressed ground state atoms. In this case we have to take into account the residual dipole-dipole interaction D_d and van der Waals interaction V_r^{es} between the single $|e\rangle$ state and the dressed ground states. This will lead to an effective hopping and a modified Stark shift depending on the distance to the $|e\rangle$ Rydberg state.

We consider interatomic interactions up to second order in $\frac{|\Omega|}{\Delta}$. Then, it is sufficient to consider atomic states involving no more than one $|s\rangle$ excitation. Consequently, we consider here two atoms, with one atom being in state $|e\rangle$ and the other atom either in state $|g\rangle$ or $|s\rangle$. The positions of the two atoms are x and y. In this subspace the corresponding Hamiltonian is

$$\begin{aligned}\hat{\mathcal{H}}_1 =&(\Delta + V^{es}_{xy})\Big[\,|s\rangle\langle s|\otimes|e\rangle\langle e| + |e\rangle\langle e|\otimes|s\rangle\langle s|\Big]\\ &-\Big[\Omega\big(\,|g\rangle\langle s|\otimes|e\rangle\langle e| + |e\rangle\langle e|\otimes|g\rangle\langle s|\,\big) + \text{h.c.}\Big] + D_{xy}\big(\,|s\rangle\langle e|\otimes|e\rangle\langle s| + \text{h.c.}\big),\end{aligned} \tag{5.13}$$

where x and y are the positions of the two atoms. The two-atom wavefunction can be written as

$$|\phi\rangle = c_{ge}\,|ge\rangle + c_{eg}\,|eg\rangle + c_{se}\,|se\rangle + c_{es}\,|es\rangle\,. \tag{5.14}$$

For the amplitudes $c_{\nu\mu}$ we obtain the following equations of motion

$$i\dot{c}_{ge} = -\Omega c_{se}, \tag{5.15a}$$

$$i\dot{c}_{eg} = -\Omega c_{es}, \tag{5.15b}$$

$$i\dot{c}_{se} = (\Delta + V^{es}_{xy})c_{se} - \Omega^* c_{ge} + D_{xy}c_{es}, \tag{5.15c}$$

$$i\dot{c}_{es} = (\Delta + V^{es}_{xy})c_{es} - \Omega^* c_{eg} + D_{xy}c_{se}. \tag{5.15d}$$

Since Δ is the largest energy scale in the system and we are interested in the low-energy dynamics we adiabatically eliminate states containing Rydberg states $|s\rangle$. In particular, we set $\dot{c}_{se} = 0$ and $\dot{c}_{es} = 0$ and solve for c_{se} and c_{es}. Inserting into the first two equations, we obtain

$$i\dot{c}_{ge} = -\frac{|\Omega|^2(\Delta + V^{es}_{xy})}{(\Delta + V^{es}_{xy})^2 - D^2_{xy}}c_{ge} + \frac{|\Omega|^2 D_{xy}}{(\Delta + V^{es}_{xy})^2 - D^2_{xy}}c_{eg}, \tag{5.16a}$$

$$i\dot{c}_{eg} = -\frac{|\Omega|^2(\Delta + V^{es}_{xy})}{(\Delta + V^{es}_{xy})^2 - D^2_{xy}}c_{eg} + \frac{|\Omega|^2 D_{xy}}{(\Delta + V^{es}_{xy})^2 - D^2_{xy}}c_{ge}. \tag{5.16b}$$

We can interpret these equations as follows: The dressed ground state atom at position x acquires an energy shift depending on the position y of the $|e\rangle$ excitation. The energy shift is given by

$$\delta^{(y)}_x = -\frac{|\Omega|^2(\Delta + V^{es}_{xy})}{(\Delta + V^{es}_{xy})^2 - D^2_{xy}}. \tag{5.17}$$

Additionally we obtain an exchange coupling between the $|e\rangle$ excitation and the dressed ground state with strength

$$J_{xy} = \frac{|\Omega|^2 D_{xy}}{(\Delta + V^{es}_{xy})^2 - D^2_{xy}}. \tag{5.18}$$

Both, the energy shift $\delta^{(y)}_x$ and the effective hopping $J_{xy} = J_d$ depend only on the relative distance $d = |x - y|$ between the two atoms. Note that setting $D_{xy} = V^{es}_{xy} = 0$ we obtain the previous zero-excitation result with Stark shift $\delta = -\frac{|\Omega|^2}{\Delta}$.

The total energy shift in a system with $L-1$ atoms in the dressed ground state and one atom at position y in the $|e\rangle$ state is

$$E_1 = \sum_{x\neq y} \delta_x^{(y)}. \tag{5.19}$$

Note that E_1 is a constant and does not depend on the position y of the $|e\rangle$ excitation (assuming the thermodynamic limit $L\to\infty$). We can disregard this energy shift by redefining the zero-point energy. Thus, we obtain an effective Hamiltonian for the single excitation dynamics

$$\hat{\mathcal{H}}_1^{\text{eff}} = \sum_{x\neq y} J_{xy} |x\rangle\langle y| = \sum_{x=1}^{L}\sum_{d\geq 1} J_d\big(|x\rangle\langle x+d| + |x\rangle\langle x-d|\big). \tag{5.20}$$

This realizes the single spin-up Hamiltonian in Eq. (5.2). The hopping strength can be approximated by

$$J_d \simeq \frac{|\Omega|^2}{\Delta^2} D_d \propto \frac{1}{d^3} \tag{5.21}$$

for $\Delta \gg D_d, V_d^{es}$.

Two excitations $(N=2)$

For the case of two $|e\rangle$ excitations we follow the same procedure as before. We restrict our discussion to interatomic interactions up to second order in $\frac{|\Omega|}{\Delta}$ and discuss the case of at most one $|s\rangle$ excitation. Therefore it is sufficient to consider the subspace having three atoms where two are in the $|e\rangle$ state and one atom is either in the ground state $|g\rangle$ or Rydberg $|s\rangle$ state. Later, we will extend our discussion to the case of large lattice systems with L atoms. We assume a weak interaction $V_d^{ee} \ll |\Omega|, D_d$ between the $|e\rangle$ excitations, which we will neglect in the following derivation. Later when we introduce the effective Hamiltonian we will account for the full interaction potential including V_d^{ee}. The three-atom Hamiltonian with two $|e\rangle$ excitations is

$$\begin{aligned}
\hat{\mathcal{H}}_2 = &\Big(\Delta_x^{(y,z)} |s\rangle\langle s| - [\Omega |g\rangle\langle s| + \text{h.c.}]\Big) \otimes |e\rangle\langle e| \otimes |e\rangle\langle e| \\
&+ |e\rangle\langle e| \otimes \Big(\Delta_y^{(x,z)} |s\rangle\langle s| - [\Omega |g\rangle\langle s| + \text{h.c.}]\Big) \otimes |e\rangle\langle e| \\
&+ |e\rangle\langle e| \otimes |e\rangle\langle e| \otimes \Big(\Delta_z^{(x,y)} |s\rangle\langle s| - [\Omega |g\rangle\langle s| + \text{h.c.}]\Big) \\
&+ D_{xy}(|s\rangle\langle e| \otimes |e\rangle\langle s| \otimes |e\rangle\langle e| + \text{h.c.}) \\
&+ D_{xz}(|s\rangle\langle e| \otimes |e\rangle\langle e| \otimes |e\rangle\langle s| + \text{h.c.}) \\
&+ D_{yz}(|e\rangle\langle e| \otimes |s\rangle\langle e| \otimes |e\rangle\langle s| + \text{h.c.}),
\end{aligned} \tag{5.22}$$

where x, y and z denote the positions of the three atoms. We introduce an effective detuning $\Delta_z^{(x,y)} \equiv \Delta + V_{xz}^{es} + V_{yz}^{es}$ seen by the $|s\rangle$ excitation at position z in the presence of two $|e\rangle$ excitations at positions x and y. Analogously, we define $\Delta_y^{(x,z)}$ and $\Delta_x^{(y,z)}$. Using a three-atom wavefunction

$$|\phi\rangle = c_{gee}\,|gee\rangle + c_{ege}\,|ege\rangle + c_{eeg}\,|eeg\rangle + c_{see}\,|see\rangle + c_{ese}\,|ese\rangle + c_{ees}\,|ees\rangle\,, \tag{5.23}$$

we derive the equations of motion for the coefficients $c_{\lambda\nu\mu}$ and obtain

$$i\dot{c}_{gee} = -\Omega c_{see}, \tag{5.24a}$$

$$i\dot{c}_{ege} = -\Omega c_{ese}, \tag{5.24b}$$

$$i\dot{c}_{eeg} = -\Omega c_{ees}, \tag{5.24c}$$

$$i\dot{c}_{see} = -\Omega^* c_{gee} + \Delta_x^{(y,z)} c_{see} + D_{xy} c_{ese} + D_{xz} c_{ees}, \tag{5.24d}$$

$$i\dot{c}_{ese} = -\Omega^* c_{ege} + \Delta_y^{(x,z)} c_{ese}, + D_{xy} c_{see} + D_{yz} c_{ees}, \tag{5.24e}$$

$$i\dot{c}_{ees} = -\Omega^* c_{eeg} + \Delta_z^{(x,y)} c_{ees} + D_{xz} c_{see} + D_{yz} c_{ese}. \tag{5.24f}$$

Adiabatic elimination of the amplitudes containing the detuned $|s\rangle$ state, i.e. $\dot{c}_{see} = \dot{c}_{ese} = \dot{c}_{ees} = 0$, allows us to solve for the coefficients c_{see}, c_{ese} and c_{ees}. Inserting these into the first three equations, we obtain effective equations of motion for the low-energy dynamics

$$\begin{aligned}\dot{c}_{eeg} =& \frac{|\Omega|^2(\Delta_y^{(x,z)}\Delta_x^{(y,z)} - D_{xy}^2)}{\Gamma(x,y,z)} c_{eeg} \\ &+ \frac{|\Omega|^2(D_{xy}D_{xz} - D_{yz}\Delta_x^{(y,z)})}{\Gamma(x,y,z)} c_{ege} + \frac{|\Omega|^2(D_{xy}D_{yz} - D_{xz}\Delta_y^{(x,z)})}{\Gamma(x,y,z)} c_{gee},\end{aligned} \tag{5.25a}$$

$$\begin{aligned}\dot{c}_{ege} =& \frac{|\Omega|^2(\Delta_z^{(x,y)}\Delta_x^{(y,z)} - D_{xz}^2)}{\Gamma(x,y,z)} c_{ege} \\ &+ \frac{|\Omega|^2(D_{xy}D_{xz} - D_{yz}\Delta_x^{(y,z)})}{\Gamma(x,y,z)} c_{eeg} + \frac{|\Omega|^2(D_{xz}D_{yz} - D_{xy}\Delta_z^{(x,y)})}{\Gamma(x,y,z)} c_{gee},\end{aligned} \tag{5.25b}$$

$$\begin{aligned}\dot{c}_{gee} =& \frac{|\Omega|^2(\Delta_y^{(x,z)}\Delta_z^{(x,y)} - D_{yz}^2)}{\Gamma(x,y,z)} c_{gee} \\ &+ \frac{|\Omega|^2(D_{xy}D_{yz} - D_{xz}\Delta_y^{(x,z)})}{\Gamma(x,y,z)} c_{eeg} + \frac{|\Omega|^2(D_{xz}D_{yz} - D_{xy}\Delta_z^{(x,y)})}{\Gamma(x,y,z)} c_{ege},\end{aligned} \tag{5.25c}$$

with

$$\Gamma(x,y,z) \equiv -\Delta_z^{(x,y)}\Delta_y^{(x,z)}\Delta_x^{(y,z)} - 2D_{xy}D_{xz}D_{yz} + \Delta_z^{(x,y)}D_{xy}^2 + \Delta_y^{(x,z)}D_{xz}^2 + \Delta_x^{(y,z)}D_{yz}^2. \tag{5.26}$$

The effective equations of motion in Eq. (5.25) include an energy shift as well as an exchange process between a dressed ground state $|g\rangle$ and the Rydberg state $|e\rangle$. Using a series expansion in $\frac{|\Omega|}{\Delta}$ we can further simplify the energy shift and the excitation hopping strength and gain insight into the relevant processes. In Fig. 5.2a-c we visualize the individual contributions to the energy shift and hopping strength. In particular, Fig. 5.2a allows to determine the hopping strength and energy shift diagrammatically. For a ground state atom at position z and two $|e\rangle$ excitations at positions x and y we obtain an energy shift

$$\delta_z^{(x,y)} = -\frac{|\Omega|^2}{\Delta_z^{(x,y)}} - \frac{|\Omega|^2 D_{xz}^2}{\left(\Delta_z^{(x,y)}\right)^2 \Delta_x^{(z,y)}} - \frac{|\Omega|^2 D_{yz}^2}{\left(\Delta_z^{(x,y)}\right)^2 \Delta_y^{(x,z)}} + \mathcal{O}\left(\frac{|\Omega|^4}{\Delta^4}\right). \tag{5.27}$$

The first term corresponds to a virtual excitation of the $|g\rangle$ state to the $|s\rangle$ state via a nonresonant laser field. The latter two terms are higher order processes involving an additional exchange process back and forth, see Fig. 5.2b. Likewise, we can identify an excitation hopping process, see Fig. 5.2c. To give an example, the hopping of an excitation from position x to z, $|eeg\rangle \leftrightarrow |gee\rangle$, is given by

$$J_{xz}^{(y)} = \frac{|\Omega|^2 D_{xz}}{\Delta_z^{(x,y)} \Delta_x^{(z,y)}} - \frac{|\Omega|^2 D_{yz} D_{xy}}{\Delta_z^{(x,y)} \Delta_x^{(y,z)} \Delta_y^{(z,x)}} + \mathcal{O}\left(\frac{|\Omega|^4}{\Delta^4}\right). \tag{5.28}$$

Here, the first term describes the direct excitation hopping of the dressed ground state atom between positions x and z. The second term is a higher order term involving two dipole-dipole-exchange processes. First, an exchange process between position y and z followed by exchange process between x and y ($|eeg\rangle \rightarrow |ege\rangle \rightarrow |gee\rangle$). Note that the second term has a different sign and therefore may cancels the first term.

Using Eq. (5.28) and (5.27), we can construct a low-energy Hamiltonian for three atoms with two excitations and one dressed ground state. Including the interaction potential V_d^{ee} between the two excitations $|e\rangle$ we have

$$\begin{aligned}\hat{\mathcal{H}}_2^{\text{eff}} =& (\delta_x^{(y,z)} + V_{yz}^{ee}) |gee\rangle \langle gee| + (\delta_y^{(x,z)} + V_{xz}^{ee}) |ege\rangle \langle ege| + (\delta_z^{(x,y)} + V_{xy}^{ee}) |eeg\rangle \langle eeg| \\ &+ J_{xy}^{(z)}(|gee\rangle \langle ege| + \text{h.c.}) + J_{xz}^{(y)}(|eeg\rangle \langle gee| + \text{h.c.}) + J_{yz}^{(x)}(|ege\rangle \langle eeg| + \text{h.c.}).\end{aligned} \tag{5.29}$$

In Fig. 5.2d we compare the spectrum of this effective Hamiltonian (dashed lines) to the full Hamiltonian in Eq. (5.22) (solid lines) including the interaction potential V_d^{ee}. Thereby we vary the position z of the third atom while keeping the positions of the first two atoms, $x = 0$ and $y = a$. The effective Hamiltonian reproduces the low-energy part of the full Hamiltonian very well. In the limit $\frac{\Omega}{\Delta} \rightarrow 0$, the deviation vanishes and we obtain the exact low-energy result of the full model.

Now, we extend the three-atom model to the case of a chain of L atoms. We start with the transport term Eq. (5.28). Let us denote the positions of the two $|e\rangle$ excitations with x and y. The hopping rate $J_{xz}^{(y)} \equiv J_d(r)$ of the $|e\rangle$ excitation from site x to z depends on the position of the spectator $|e\rangle$ excitation at site y. Due to the translational invariance of the system, the hopping rate depends on the mutual distance $r \equiv |y - x|$ between the two $|e\rangle$ excitations and the hopping distance $d \equiv |z - x|$.

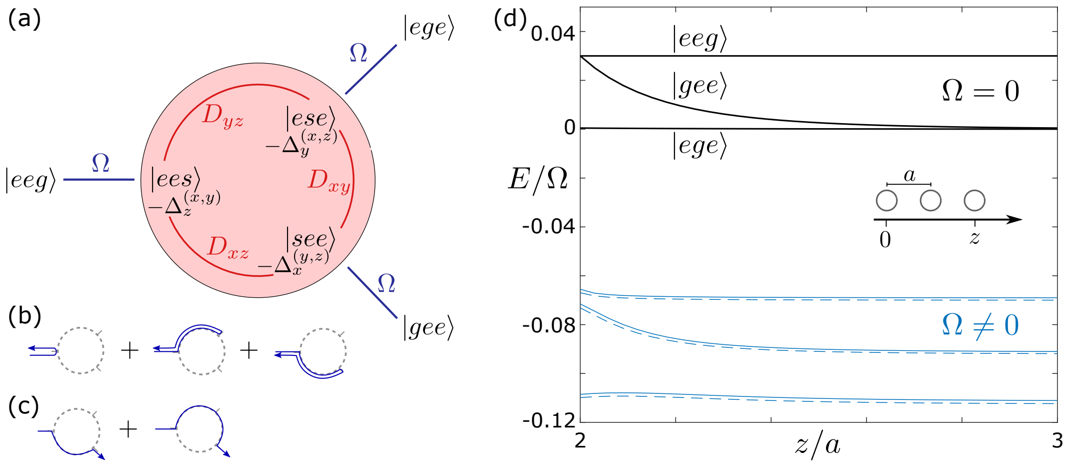
(a)
$|ege\rangle$
Ω
D_{yz}
$|ese\rangle$
$-\Delta_y^{(x,z)}$
$|eeg\rangle$
Ω
$|ees\rangle$
$-\Delta_z^{(x,y)}$
D_{xy}
D_{xz}
$|see\rangle$
$-\Delta_x^{(y,z)}$
Ω
$|gee\rangle$
(b)
+
+
(c)
+
(d)
0.04
0
-0.04
-0.08
-0.12
E/Ω
$|eeg\rangle$
$|gee\rangle$
$|ege\rangle$
$\Omega = 0$
a
0
z
$\Omega \neq 0$
2
z/a
3

Figure 5.2: (a) Diagram of transitions for retrieving the perturbative energy shifts and excitation hopping rates for two excited $|e\rangle$ and one ground $|g\rangle$ state atoms. The atomic positions are x, y, z. Red-shaded region denotes the high energy subspace, $\Delta \gg \Omega, D$, which is eliminated adiabatically. (b) Illustration of three virtual processes contributing to the energy shift of $|eeg\rangle$, as per Eq. (5.27). (c) Two possible paths for the hopping process $|eeg\rangle \leftrightarrow |gee\rangle$ given by Eq. (5.28). (d) Comparison of the low-energy spectra of the exact Hamiltonian (5.22) including the interactions V_r^{ee} (solid lines), and the effective Hamiltonian (5.29) (dashed lines). The positions of the first and second atoms are fixed, $x = 0$ and $y = a$, while the position of the third atom vary, $z \geq 2a$. Black lines at $E \geq 0$ show the exact spectrum for $\Omega = 0$, corresponding to the bare states $|ege\rangle$, $|gee\rangle$ and $|eeg\rangle$. Blue lines show the spectra for the dressed states with the parameters $\Delta/\Omega = 10$, $D_1/\Omega = 1$, $V_1^{es}/\Omega = -1/8$ and $V_1^{ee}/\Omega = 0.03$ ($D_r \propto 1/r^3$, $V_r \propto 1/r^6$).

Thus, the transport Hamiltonian can be written as

$$\begin{aligned}\hat{\mathcal{H}}_J^{(2)} = \sum_{x<y} \Big[& \sum_{d} J_d(r) (|x,y\rangle \langle x-d, y| + |x,y\rangle \langle x, y+d|) \\ & + \sum_{d<y-x} J_d(r) (|x,y\rangle \langle x+d, y| + |x,y\rangle \langle x, y-d|) \\ & + \sum_{d>y-x} J_d(r) (|x,y\rangle \langle y, x+d| + |x,y\rangle \langle y-d, x|) \Big].\end{aligned} \tag{5.30}$$

The Hamiltonian has a similar structure to the hopping part in the two-excitation spin model Eq. (5.5). However, here the hopping elements depend on the relative distance between the spin-up excitations. To the leading order $J_d(r) \propto D_d \sim 1/d^3$ scales with the dipole-dipole interaction. We truncate the range of the hopping distance to $d \leq d_J = 2$. This will be justified later in this chapter. Analogously to Sec. 5.1 we introduce center of mass R and relative r coordinates and transform the center of mass

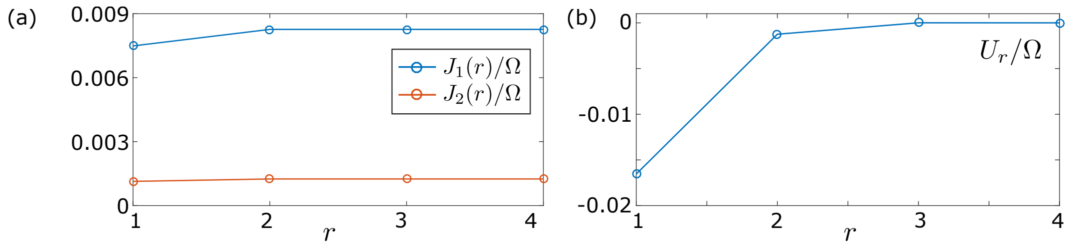

Figure 5.3: (a) One- and two-site hopping rates $J_1(r)$ and $J_2(r)$ versus distance r between the two excitations as in Table 5.1. (b) Interaction potential U_r as in Table 5.2 for $V_1^{ee} = 0$. The parameters are $\Delta/\Omega = 10$, $D_1/\Omega = 1$ and $V_1^{es}/\Omega = 1$.

d	$J_d(r=1)$	$J_d(r \geq 2)$	$J'_d(r=1)$
1	$\frac{\lvert\Omega\rvert^2 D_1}{(\Delta + V_1^{es})(\Delta + 2V_1^{es})}\left(1 - \frac{D_2}{\Delta + V_1^{es}}\right)$	$\frac{\lvert\Omega\rvert^2 D_1}{(\Delta + V_1^{es})^2}$	–
2	$\frac{\lvert\Omega\rvert^2 D_2}{\Delta(\Delta + V_1^{es})}$	$\frac{\lvert\Omega\rvert^2 D_2}{\Delta^2}$	$\frac{\lvert\Omega\rvert^2 D_2}{(\Delta + V_1^{es})^2}\left(1 - \frac{D_1^2/D_2}{\Delta + 2V_1^{es}}\right)$

Table 5.1: Approximate hopping rates for the two-excitation spin model depending on the hopping distance d and the distance r between two Rydberg $|e\rangle$ excitations.

coordinate R to the center of mass quasi momentum K, using $|R\rangle = \frac{1}{\sqrt{L}} \sum_K e^{iKR} |K\rangle$ and obtain

$$\begin{aligned}\hat{\mathcal{H}}_J^{(2)} = \sum_K |K\rangle \langle K| \otimes \Big\{ \sum_{r \geq 1} \Big[& 2J_1(r)\cos(K/2)(|r\rangle\langle r+1| + |r+1\rangle\langle r|) \\ & + 2J_2(r)\cos(K)(|r\rangle\langle r+2| + |r+2\rangle\langle r|)\Big] + 2J'_2(r=1)\cos(K)\,|1\rangle\langle 1| \Big\}. \end{aligned} \tag{5.31}$$

Note that the hopping $J'_2(r=1)$ indicates the case where an $|e\rangle$ excitation hops over another $|e\rangle$ excitation with a different hopping strength than $J_2(r=1)$. From Eq. (5.28) we can directly deduce the hopping rates. We further assume an interaction range $d_U \leq 1$ and therefore set $V_{d\geq 2}^{es} = 0$ and $D_{d\geq 3} = 0$. In Table 5.1 we summarize all relevant hopping rates within the approximations discussed above. The dependence of the hopping rate $J_1(r)$ and $J_2(r)$ on the relative distance between the spin-up excitations for a specific parameter set is shown in Fig. 5.3a. While the next nearest neighbor hopping rate $J_2(r)$ stays almost constant, the nearest neighbor hopping rate $J_1(r)$ shows a small dip at $r = 1$ for large $V_1^{es} \sim \Omega$. We can deduce from Table 5.1 that $J_1(r)$ becomes r-independent for $V_1^{es} = -D_2$. In the case where the interaction coefficients C_3 and C_6^{es} have opposite sign, we can determine a lattice constant $a = 2\sqrt[3]{-C_6^{es}/C_3}$, such that this condition is fulfilled.

Next, we consider the effective interaction strength. The total energy shift in a lattice of L sites

r	U_r
1	$V_1^{ee} - 2\left(\frac{\lvert\Omega\rvert^2}{\Delta} - \frac{\lvert\Omega\rvert^2}{\Delta + V_1^{es}}\right) + 2\frac{\lvert\Omega\rvert^2 D_1^2}{(\Delta + V_1^{es})^2}\left(\frac{2}{\Delta + V_1^{es}} - \frac{1}{\Delta + 2V_1^{es}}\right) + 2\lvert\Omega\rvert^2 D_2^2\left(\frac{2}{\Delta^3} - \frac{1}{\Delta^2(\Delta + V_1^{es})} - \frac{1}{(\Delta + V_1^{es})^3}\right)$
2	$V_2^{ee} - \left(\frac{\lvert\Omega\rvert^2}{\Delta} - \frac{\lvert\Omega\rvert^2}{\Delta + V_1^{es}}\right) + 2\frac{\lvert\Omega\rvert^2 D_1^2}{\Delta + V_1^{es}}\left(\frac{1}{(\Delta + V_1^{es})^2} - \frac{1}{(\Delta + 2V_1^{es})^2}\right) + 2\frac{\lvert\Omega\rvert^2 D_2^2}{\Delta^3}$
3	$V_3^{ee} + 2\frac{\lvert\Omega\rvert^2 D_2^2}{\Delta}\left(\frac{1}{\Delta^2} - \frac{1}{(\Delta + V_1^{es})^2}\right)$

Table 5.2: Approximate interaction elements for the two-excitation spin model depending on the relative distance r between both $|e\rangle$ excitations.

having two $|e\rangle$ excitations at positions x and y is given by

$$E_2(x, y) = \sum_{z \neq x,y} \delta_z^{(x,y)}. \tag{5.32}$$

The total energy shift is no longer constant and depends on the relative distance $r = |y - x|$. For large r, when the two $|e\rangle$ excitations are well separated, the sum approaches a constant value. We set $E_2(r \to \infty)$ the zero-point energy of the system. The energy difference $E_2(r) - E_2(r \to \infty)$ adds to the interaction potential V_r^{ee}. We define an interaction potential between two spin-up excitations

$$U_r = V_r^{ee} + E_2(r) - E_2(r \to \infty). \tag{5.33}$$

The interaction strengths for the spin model are listed in Table 5.2 for the relative distances of the particles $r = 1, 2, 3$. Note that we truncated the interaction V_d^{es} at $d_U = 1$, while we included the full interaction strength V_d^{ee} up to $d = 3$. In Fig. 5.3b we show the interaction potential U_r for a specific parameter set, where we have chosen $V_r^{ee} = 0$. Clearly, the nearest neighbor interaction is much stronger than the next nearest neighbor interaction. Using the center of mass R and relative r coordinates and Fourier transform with respect to R we end up with an interaction Hamiltonian

$$\hat{\mathcal{H}}_U^{(2)} = \sum_K |K\rangle\langle K| \otimes \sum_{r=1}^{3} U_r |r\rangle\langle r|. \tag{5.34}$$

To summarize, the total Hamiltonian $\hat{\mathcal{H}}^{(2)} = \hat{\mathcal{H}}_J^{(2)} + \hat{\mathcal{H}}_U^{(2)}$ based on Eq. (5.31) and Eq. (5.34) for the two Rydberg excitations $|e\rangle$ in a lattice of dressed ground states approximates well the spin model Hamiltonian Eq. (5.5). This model allows to investigate the impact of longer-range spin-exchange processes and interactions. There are small differences to the exact model Eq. (5.5) in the dependence of the hopping elements on the distance r between two excitations and a reduced transport rate for one excitation hopping over the other. We will derive now the two magnon bound state solution of the spin lattice model and compare it to the full Rydberg-dressed Hamiltonian $\hat{\mathcal{H}}^{(2)}$. The discussion of the full many-body physics, i.e. $N > 2$ Rydberg excitations, is beyond the scope of this thesis.

5.3 Magnon Dynamics and Bound States

Now, let us return to the spin model Eq. (5.1). Using center of mass R and relative r coordinate we simplified the extended XXZ Hamiltonian for the case $N = 2$. In this case the two-body wavefunction can be written as

$$|\Psi(x, y)\rangle = \sum_{x<y} \Psi(x, y) |x, y\rangle = \frac{1}{\sqrt{\tilde{L}}} \sum_K e^{iKR} |K\rangle \otimes \sum_{r\geq 1} \psi_K(r) |r\rangle . \tag{5.35}$$

As usual, we obtain a one-body problem for the relative coordinate r with a wavefunction $\psi_K(r)$ depending on the center of mass momentum K. Our aim is to solve the eigenvalue problem

$$\hat{\mathcal{H}}_K |\psi_K\rangle = E_K |\psi_K\rangle \tag{5.36}$$

for the relative coordinate wavefunction $|\psi_K\rangle = \sum_{r\geq 1} \psi_K(r) |r\rangle$. This problem has scattering and bound state solutions.

5.3.1 Free Magnon Dynamics and Scattering States

Let us briefly comment on the scattering solutions of the problem Eq. (5.36). Assume two magnons are far separated and the interactions have a finite range d_U. Then for the total energy we can simply add the energies of two free magnons [159, 160] with quasi momenta q_1, q_2 in Eq. (5.4)

$$E_{K,k}^{(\mathrm{s})} = E_{q_1}^{(1)} + E_{q_2}^{(1)} = \sum_d 4J_d \cos(Kd/2) \cos(kd). \tag{5.37}$$

Here, $K = q_1 + q_2$ and $k = \frac{q_1 - q_2}{2}$ are the center of mass and relative quasi momenta, respectively. The corresponding wavefunction $\psi_K(r)$ for $r > d_U$ is given by plane waves,

$$\psi_K(r) = e^{ikr} + e^{-2i\delta_{K,k}} e^{-ikr}. \tag{5.38}$$

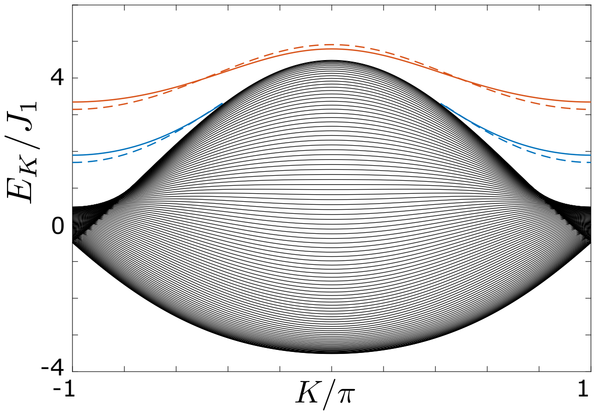

Figure 5.4: Spectrum of two spin (Rydberg) excitations in a lattice versus the center of mass quasi momentum K. The scattering states form a continuum spectrum (black), Eq. (5.37). The bound states for strong (red lines) and weak (blue lines) repulsive interactions are obtained from the spin-lattice Hamiltonian (dashed lines), Eq. (5.45), and from exact diagonalization of the dressed Rydberg Hamiltonian (solid lines). The system parameters are $\Delta/\Omega = 10$, $D_1/\Omega = 1$, $V_1^{es}/\Omega = -0.125$, and $V_1^{ee}/\Omega = 0.03, 0.015$ for the red and blue solid lines, respectively. In the simulations, we used a lattice of size $L = 100$. The corresponding spin model parameters are $J_2/J_1 = 1/8$, $U_1/J_1 = 3.4, 1.9$ for the red and blue dashed lines, respectively.

The scattering phase shift $\delta_{K,k}$ depends on the interaction U_r and is not relevant for our further discussion. The scattering spectrum is shown in Fig. 5.4 (black lines) for a hopping range $d_J \leq 2$. At $K = \pm\pi$ the energy spectrum has a finite width $E^{(s)}_{K=\pm\pi,k} \in [-4J_2, 4J, 2]$ determined by the long-range hopping [159]. This is in contrast to the case of nearest neighbor hopping discussed in Ref. [151, 158, 160, 161] reducing the energy width to a single point $E^{(s)}_{K=\pm\pi,k} = 0$. Thus, even at a center of mass momentum $K = \pm\pi$, the two free magnons are mobile.

5.3.2 Bound Magnons

We discuss here magnon bound states in a lattice with a strong (repulsive or attractive) nearest neighbor interaction U_1. Our discussion assumes an interaction range $d_U = 1$ and hopping range $d_J \leq 2$. Although, we truncate here the hopping range to next nearest neighbor, it allows multiple pathways for the spin excitations to move, which makes a calculation of the eigenfunctions more difficult. Later we will see that the truncation is a good approximation for Rydberg systems, where the interaction scales as $\sim 1/d^6$ and the hopping as $\sim 1/d^3$ with distance d. Thus, the relevant

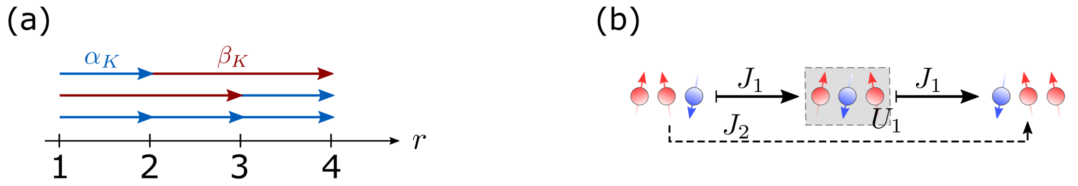

Figure 5.5: (a) Schematic sketch of the recurrence relation Eq. (5.41) for excitation hopping from $r = 1$ to $r = 4$. (b) Illustration of the motion of the bound pair via resonant two-site hopping J_2 and second order hopping J_1^2/U_1 as per Eq. (5.45).

Hamiltonian for a given center of mass momentum K is (see Eq. (5.7))

$$\hat{\mathcal{H}}_K = \sum_{r\geq 1} \Big[J_{1,K}(|r\rangle\langle r+1| + |r+1\rangle\langle r|) + J_{2,K}(|r\rangle\langle r+2| + |r+2\rangle\langle r|) \Big] \\ + (U_1 + J_{2,K})\,|1\rangle\langle 1|\,. \tag{5.39}$$

Using the wavefunction $|\psi_K\rangle$ the eigenvalue problem reads

$$E_K^{(b)}\psi_K(r) = J_{1,K}\big[\psi_K(r+1) + \psi_K(r-1)\big] + J_{2,K}\big[\psi_K(r+2) + \psi_K(r-2)\big] \\ + (U_1 + J_{2,K})\delta_{r,1}\psi_K(r). \tag{5.40}$$

For a bound magnon solution we expect an exponentially in r localized wavefunction $\psi_K(r)$, which is normalizable and fulfills $\psi_K(r \to \infty) = 0$. To determine the wavefunction we make an ansatz

$$\psi_K(r) = \alpha_K\psi_K(r-1) + \beta_K\psi_K(r-2), \quad r \geq 2, \tag{5.41}$$

where we set the (initial) values $\psi_K(0) = 0$ and $\psi_K(1) = \mathcal{N}$. The constant $\mathcal{N}$ is determined by the normalization. The physical intuition behind this recurrence relation is as follows: Each wavefunction amplitude $\psi_K(r)$ is determined by the previous two wavefunction amplitudes $\psi_K(r-1)$ and $\psi_K(r-2)$. The coefficients $\alpha_K \sim J_1$ and $\beta_K \sim J_2$ correspond to nearest neighbor and next nearest neighbor hopping, respectively and have to be determined. Starting from the minimal relative distance $r = 1$, we can construct a wavefunction at any r

$$\psi_K(r) = \mathcal{N} \sum_{n=0}^{\lfloor (r-1)/2 \rfloor} \binom{r-1-2n}{n} \alpha_K^{r-1-2n}\beta_K^n, \tag{5.42}$$

which is a solution of the recurrence relation. Here, $\lfloor\cdot\rfloor$ denotes the floor function. The binomial coefficients count the corresponding weight of each path starting from site $r = 1$. To give an example: We can reach $r = 4$ from $r = 1$ by three successive one-site hoppings α_K^3 or by a combination of a one-site and two-site hopping $\alpha_K\beta_K$ or $\beta_K\alpha_K$, as indicated in Fig. 5.5a. In total, the wavefunction

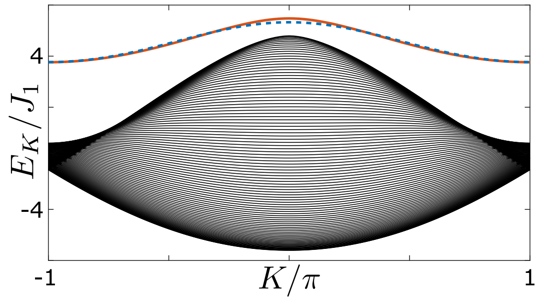

Figure 5.6: Scattering (black) and bound state (red solid line) spectra obtained by exact numerical diagonalization of the Hamiltonian Eq. (5.7) with long-range interactions $J_d = J_1/d^3$ and $U_r = U_1/r^6$ ($U_1/J_1 = 4$). The bound state energy $E_K^{(b)}$ of Eq. (5.45) (dashed blue line), obtained with truncated interactions ($d_J = 2$ and $d_U = 1$), is nearly indistinguishable from the exact result.

is $\psi_K(4) = (\alpha_K^3 + 2\alpha_K\beta_K)\psi_K(1)$.

Using the wavefunction Eq. (5.42) for the eigenvalue equation (5.40) with $r = 1, 2, 3$, we obtain three equations for the unknowns α_K, β_K and E_K,

$$E_K^{(b)} = (U_1 + J_{2,K}) + J_{1,K}\alpha_K + J_{2,K}(\alpha_K^2 + \beta_K), \tag{5.43a}$$

$$E_K^{(b)}\alpha_K = J_{1,K}(\alpha_K^2 + \beta_K + 1) + J_{2,K}(\alpha_K^3 + 2\alpha_K\beta_K), \tag{5.43b}$$

$$E_K^{(b)}(\alpha_K^2 + \beta_K) = J_{1,K}(\alpha_K + \alpha_K^3 + 2\alpha_K\beta_K) + J_{2,K}(1 + \alpha_K^4 + 3\alpha_K^2\beta_K + \beta_K^2). \tag{5.43c}$$

This is a nonlinear system in α_K, β_K and $E_K^{(b)}$ with a unique solution. We obtain for the coefficients

$$\alpha_K = \frac{J_{1,K}}{U_1}, \quad \beta_K = \frac{J_{2,K}}{U_1 + J_{2,K}}. \tag{5.44}$$

Note that this is consistent with our ansatz $\alpha_K \sim J_1$ and $\beta_K \sim J_2$. Furthermore, we obtain for the bound pair energy

$$E_K^{(\mathrm{b})} = 2J_{2,K} + \frac{J_{1,K}^2}{U_1} + \frac{J_{1,K}^2 J_{2,K}}{U_1^2} + \frac{U_1^2}{U_1 + J_{2,K}}. \tag{5.45}$$

The bound pair energy admits a simple interpretation: The first term does not depend on U_1 and describes resonant two-site tunneling. An excitation can hop over the other excitation, $|x-1, x\rangle \leftrightarrow |x, x+1\rangle$, with coupling strength $\sim J_2$. This process is resonant since both states have the same interaction energy. The second term is a second order hopping process ($\propto J_1^2/U_1$) already known from Ref. [151, 158, 160, 161]. Both processes are indicated in Fig. 5.5b. The third term is a third order tunneling ($\propto J_1^2 J_2/U_1^2$). The last term describes the energy offset due to the strong nearest neighbor interaction U_1. Note that even in the limit of large interaction strength $U_1 \gg J_1$, bound magnon pairs stay mobile with transport rate $\sim J_2$.

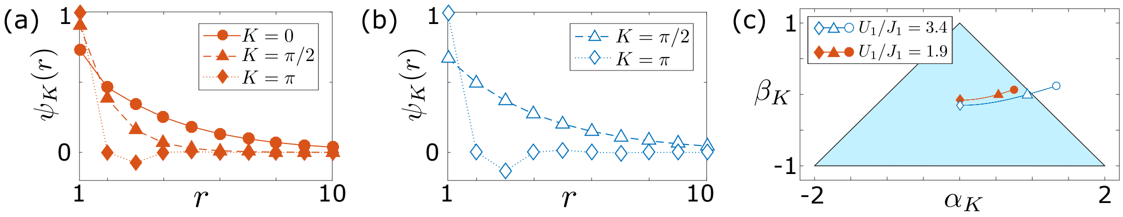

Figure 5.7: (a),(b) Wavefunction $\psi_K(r)$ versus the relative distance r for several values of the center of mass quasi momentum K. The parameters are the same as in Fig. 5.4 and (a) $U_1/J_1 = 3.4$, (b) $U_1/J_1 = 1.9$. (c) Diagram of values of α_K, β_K for the existence of bound states (light-blue shaded region). The red line corresponds to the parameters in (a) and the blue line to the parameters in (b). Note that no bound states exist in the vicinity of $K = 0$ for (b).

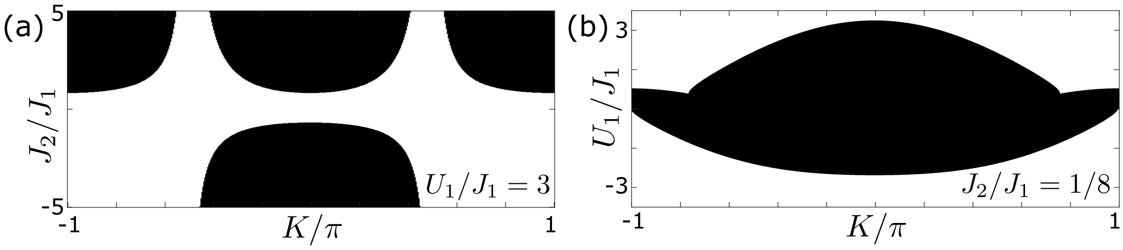

Figure 5.8: Diagram of values of J_2/J_1, for fixed $U_1 = 3J_1$ (a), and U_1/J_1, for fixed $J_2 = J_1/8$ (b), versus K, for the existence (white regions) and absence (black regions) of the bound states.

In order to demonstrate the quality of the above made truncation of the interaction to range $d_U = 1$ and hopping to range $d_J \leq 2$, let us compare these results to the full long-range potential. Since we are mostly interested in a Rydberg system as discussed in Sec. 5.2 we have a scaling of the hopping element $J_d \propto 1/d^3$ and interaction potential $U_d \propto 1/d^6$ with distance d. They originate from the dipole-dipole and van der Waals interaction, respectively. In Fig. 5.6 we show the spectrum of the scattering and bound states obtained from diagonalization of the long-range potentials without truncation and the bound pair energy solution Eq. (5.45). The good agreement demonstrates that our approximations are valid in the relevant regime of Rydberg systems. Now, we compare the result of the truncated spin model solution to full diagonalization of the Rydberg-dressed Hamiltonian with two excitations. In Fig. 5.4 we see that the spin lattice model approximates well the properties of the dressed Rydberg system. The corresponding bound pair wavefunctions are shown in Fig. 5.6a-b. Interestingly, a bound pair solution does not exist for all K, which will be discussed below.

Existence of bound states

The above recurrence relation in Eq. (5.41) can be easily extended to longer range hopping processes $d_J > 2$. In general, we assume an exponential ansatz $\psi_K(r) \propto \lambda^r$. Inserting into the recurrence relation, Eq. (5.41), we obtain a quadratic equation $\lambda^2 = \alpha_K \lambda + \beta_K$. Solving for λ, we find two solutions

$$\lambda_{1,2} = \frac{\alpha_K \pm \sqrt{\alpha_K^2 + 4\beta_K^2}}{2}. \tag{5.46}$$

Thus, the wavefunction can be written as

$$\psi_K(r) = c_1 \lambda_1^r + c_2 \lambda_2^r, \tag{5.47}$$

where the coefficients c_1, c_2 are determined by the initial values $\psi_K(0) = 0$ and $\psi_K(1) = \mathcal{N}$. This yields

$$c_2 = -c_1 = \frac{\mathcal{N}}{\sqrt{\alpha_K^2 + 4\beta_K^2}} \tag{5.48}$$

This is the same wavefunction as in Eq. (5.42). However, the ansatz also allows to determine conditions when the bound pair solution $\psi_K(r)$ is normalizable, i.e. $\sum_{r\geq 1} |\psi_K(r)|^2 = 1$. This is the case when the bound state solution decays exponentially in r. For this we require

$$|\lambda_{1,2}| = \tfrac{1}{2}|\alpha_K \pm \sqrt{\alpha_K^2 + 4\beta_K^2}| < 1. \tag{5.49}$$

Therefore, we can deduce a parameter regime (α_K, β_K) where a bound state solution can exist. In Fig. 5.7c the regime of an exponentially localized wavefunction (blue shaded region) forms a triangular region. For the case of $J_2 = 0$, i.e. having only nearest neighbor hopping, we retrieve the result of Ref. [160, 161]. For a given set of parameters J_1, J_2 and U_1 the bound state does not exist for all values of center of mass quasi momentum K. This can be seen in Fig. 5.4, where for small interaction strength the bound state dissolves into the scattering states. In Fig. 5.7a-b the corresponding bound pair wavefunctions are shown. A wavefunction closer to the boundary of the blue shaded region becomes less localized. In Fig. 5.8 we show diagrams for the existence of bound states for parameters (a) J_2/J_1 and fixed $U_1/J_1 = 3$ and (b) U_1/J_1 and fixed $J_2/J_1 = 1/8$. This shows that there are parameter regimes where bound states do not exist at all or only within a certain interval of K values.

5.4 Experimental Considerations

Let us briefly discuss the preparation and observation of magnon bound states in a Rydberg-dressed spin lattice model as indicated in Fig. 5.1. We envision a defect free chain of atoms trapped in a 1D optical lattice or an array of microtraps [4, 5]. With a focused laser beam selected atoms are transferred from ground state $|g\rangle$ to the Rydberg state $|e\rangle$. During this preparation, the global dressing laser is turned off, i.e. $\Omega = 0$. Upon turning on the dressing laser between the ground state $|g\rangle$

and the Rydberg state $|s\rangle$, the $|e\rangle$ excitation hopping starts. The transport is induced by the dipole-dipole interaction between the Rydberg state $|e\rangle$ and the dressed ground state, which is a mixture of the ground state $|g\rangle$ and the Rydberg state $|s\rangle$. This will allow to observe interesting Rydberg excitation dynamics on a timescale limited by the Rydberg state lifetime. Free magnon dynamics can be distinguished from the magnon bound state dynamics spectroscopically or by discriminating the fast and slow dynamics, respectively [151, 158]. Turning off the dressing laser freezes the magnon dynamics and individual Rydberg excitations can be detected with high efficiency and single-site resolution [10, 22, 166].

To give an example of the characteristic timescales and length scales, we discuss parameters of the experimental setup in Refs. [37, 40, 154]: In an array of microtraps, atoms can be confined with typical lattice spacing $a \simeq 5\,\mu\mathrm{m} - 20\,\mu\mathrm{m}$ and a spatial width $\Delta a \simeq 1\,\mu\mathrm{m}$. The ground state of Rubidium $|g\rangle = |5S_{1/2}\rangle$ can be dressed with a high lying Rydberg state $|s\rangle = |63P_{1/2}\rangle$ using an off-resonant UV laser with a Rabi frequency $\Omega/(2\pi) \simeq 5\,\mathrm{MHz}$ and detuning $\Delta/(2\pi) \simeq 33\,\mathrm{MHz}$ ($\Omega/\Delta = 0.15$). The spin-up state can be the Rydberg state $|e\rangle = |62D_{2/3}\rangle$. Shining focused laser beams onto the desired atoms, the Rydberg states can be populated via a two-photon transition. Using the above Rydberg states we have a dipole-dipole interaction coefficient $C_3 = 7950\,\mathrm{MHz}\,\mu\mathrm{m}^3$ and a van der Waals coefficient $C_6 = 730\,\mathrm{GHz}\,\mu\mathrm{m}^6$. The lifetime of the state $|e\rangle$ is $\tau_e \simeq 100\,\mu\mathrm{s}$ and of the state $|s\rangle$ is $\tau_s \simeq 135\,\mu\mathrm{s}$. The decay of the state $|s\rangle$ is further suppressed by a factor $|\Omega|^2/\Delta^2$ due to the dressing. Now, assuming a lattice constant $a = 10\,\mu\mathrm{m}$, we have $U_1 \simeq 730\,\mathrm{kHz}$, $J_1 \simeq 180\,\mathrm{kHz}$ and $J_2 \simeq 22\,\mathrm{kHz}$. Importantly, the hopping rates are larger than the spontaneous decay rate of the Rydberg states. This allows the observation of coherent excitation dynamics. Since $U_1/J_1 = 4$, we are in a regime where we expect strongly bound states of Rydberg excitations. Similar spin model parameters can be obtained for atoms in optical lattices with a smaller lattice constant $a \simeq 1\,\mu\mathrm{m}$. Here, one has to choose lower lying Rydberg states with less interaction strength [21, 125–127]. However, these states have shorter Rydberg state lifetimes and thus higher hopping rates are required.

A further requirement for the observation of coherent spin dynamics is that the system relaxes on a much longer timescale than the coherent processes given by J_d^{-1}. As discussed in Ref. [138, 139, 141] Rydberg dressing in large systems may suffer from black-body induced transitions to other Rydberg states. The populations of different Rydberg states and the strong dipole-dipole interaction can cause additional dephasing mechanisms. To mitigate this issue cryogenic setups or pulsed dressing schemes may be employed.

Another aspect are fluctuations of the dressing laser. While small variations in the laser carrier frequency can be typically neglected when $\Delta \gg |\Omega|$, phase fluctuations and Doppler shifts of thermal atoms contribute to additional decoherence. In particular, the hopping elements $J_d \simeq \Omega D_d \Omega^*/\Delta^2$ involve an absorption (Ω) of a photon by one atom and a subsequent emission (Ω^*) by a different atom. Thus the hopping elements are susceptible to dephasing of ground to Rydberg transitions. To reduce these effects laser with a narrow linewidth of less than $10\,\mathrm{kHz}$ and cooling of atoms to the regime of $10\,\mathrm{nK}$ are required.

While dressed ground state atoms are tightly confined in microtraps or optical lattices, atoms in Rydberg states are typically free. The strong interactions between Rydberg states will lead to a strong repulsive ($C_6 > 0$) or attractive ($C_6 < 0$) force $F(r) = -\partial_r V_r^{ee} = 6C_6/r^7$ and thus induce atomic motion. We estimate the displacement Δr from the equilibrium position assuming a constant force $F(a)$ between two neighboring excited Rydberg atoms. The resulting displacement is $\Delta r \simeq \frac{F(a)}{2m}t^2$, where m is the atomic mass. For the case discussed above and the relevant interaction timescales $t \simeq J_{1,2}^{-1}$ we obtain a displacement $\Delta r \simeq 3 - 200\,\mathrm{nm}$. Since $\Delta r \ll \Delta a$ we expect that the atomic motion on a timescale of excitation hopping will not have a detrimental effect. Another option to mitigate this problem is the use of a magic wavelength optical lattice which traps ground state and Rydberg state atoms simultaneously [120].

Conclusion

The realization of tunable and coherent spin models is experimentally challenging. Here, we showed that tunable and even long-range XXZ spin lattice models can be realized in a setup of Rydberg atoms. Interestingly, this model allows to study the few and many-body spin dynamics of a system with competing interaction strength. As an example we discussed the case of two spin excitations and the existence of mobile bound states of Rydberg excitations.

In particular, we studied the realization of this spin model using a Rydberg dressing scheme. Here, the spin-down state is a ground state atom dressed to a Rydberg state and the spin-up state is another Rydberg state. The spin-exchange is mediated by the strong dipole-dipole interaction and the spin-spin interactions by van der Waals interaction between Rydberg states.

Furthermore, we discussed magnon bound states appearing in an extended XXZ spin lattice model. We found an increased mobility of the magnon bound states which is determined by a combination of nonresonant one-site hoppings and a resonant two-site hopping even in the limit of large interactions. We shortly discussed the experimental preparation and detection of the bound states and showed that observation of bound states is possible in existing setups.

So far we discussed the case of a few spin excitations. However, we believe it will be interesting to go beyond the few excitation case and study interactions emerging between many spin excitations or clusters in this system. Furthermore, it might be interesting to study the long-time dynamics where dissipative processes such as dephasing become important. While in the coherent case, ballistic transport is expected, one may find a transition to a regime dominated by diffusive processes for the incoherent case.

Chapter 6

Laughlin State Preparation for Cavity Rydberg Polaritons

Over the last years the interest in creating topological states of matter in photonic or atomic systems has increased tremendously. One goal is to realize and study fractional quantum Hall physics in a well controlled environment, where the large length scales offer direct manipulation of the states. To this end, strong magnetic fields, strong inter-particle interactions and low temperatures are required. In solid-state systems, this has been demonstrated many years ago [51]. However, the realization of ground states in the fractional quantum Hall effect (*Laughlin states*) remains challenging in photonic systems and ultracold gases.

While strong magnetic fields have been realized in atomic [167–170] and photonic [171–175] [FL8] systems, the cooling below the many-body gap in interacting systems has not yet been achieved. On the one hand, most experimental setups rely on lattice structures where the many-body gap is typically small [176, 177] and thus even lower temperatures are required to prepare the many-body ground state. Therefore lattice-free systems, as in Ref. [174], are preferable. On the other hand, photonic systems lack the ability to realize nonlinearities on the single photon level. Here, as was demonstrated in Ref. [178, 179] coupling photons to high lying Rydberg states could allow to generate strong and even long-range photon-photon interactions. Systems with a flat-top interaction potential are particularly interesting and allow to study phases beyond what is known in the fractional quantum Hall effect [180].

Since cooling of photons is still not possible due to the lack of thermalization mechanisms, we follow here a different approach. We will make use of the good coherent control and large length scales in these systems to prepare the ground state. Instead of an efficient cooling mechanism, here laser with a narrow linewidth and low-loss cavities are required. One approach is to use these good coherence properties and directly excite the Laughlin state in a coherent process [181]. However, since the transition amplitudes between the ground state and a Laughlin state with high photon number is rather small, it is quite challenging to prepare a true many-body state. Another approach suggests to rapidly refill holes in a lossy system and thereby stabilize a steady state that is close to the ground state dynamically [60].

Here, we study an alternative approach for the preparation of Laughlin states in the setup of Ref. [174] based on the growing scheme suggested in [FL1],[FL2]. The scheme consists of two steps: First, flux is inserted into the cavity by transferring orbital angular momentum of a classical laser beam via an atomic medium to the cavity photons. This creates a hole excitation in the center which will be replenished in the second step of the growing scheme inserting exactly one photon. Subsequent iteration of the scheme allows to grow large Laughlin liquids. In Ref. [182] a similar growing scheme is presented, which relies on different orbital angular momentum beams for each step of the protocol. This is in contrast to our method which relies solely on two beams carrying orbital angular momentum. Furthermore, since we continuously pump photons into the center of the Laughlin liquid, our protocol allows to investigate almost defect free Hall physics in the central region of the cavity.

This chapter is based on the manuscript [FL7] and the publications [FL1],[FL2], partially with text overlap.

6.1 Photonic Cavity Setup and Rydberg Polaritons

The two essential ingredients needed to study fractional quantum Hall physics are strong magnetic fields and strong particle interactions. In a photonic cavity setup the first requirement can be realized by twisting the cavity mirrors to induce an image rotation and the second by coupling the photons to a high lying Rydberg state.

6.1.1 Experiment and Microscopic Model

Similar to neutral atoms, photons do not carry a net electric charge and therefore do not couple to an applied magnetic field. However, as already shown for ultracold atoms by inducing a rotation of atoms confined in a harmonic trap an artificial magnetic field can be produced [55, 56, 183, 184]. This is a direct consequence of the formal similarity between the Lorentz force in a magnetic field and a Coriolis force. The same ideas can be applied to massless photons using a rotating dispersive medium [185, 186] or a non-planar ring resonator [174, 187]. The latter setup is sketched in Fig. 6.1a and consists of four cavity mirrors, which confine the photons in a 2D harmonic potential. The cavity mirrors are aligned in such a way that they induce an image rotation after each round-trip. This creates a Coriolis force and an anti-binding potential seen by the photons. The anti-binding potential may reduce or even cancel the harmonic potential by fine-tuning of the system parameters. In the experiment in Ref. [174] the resonator length is changed within a range of a few microns to create a flat Landau level structure. The total resonator length lies in the regime of a few centimeters and the magnetic length $\ell_B = w_0/2$ is given by the mode waist $w_0 = 43\,\mu\mathrm{m}$ of the resonator.

The usual Landau level structure is however unstable due to astigmatism. As discussed in Ref. [174], astigmatism drives transitions between states with an angular momentum difference $\Delta\ell = 2$. When the Landau level states become degenerate, the angular momentum of the photons is steadily increased and eventually leads to photon loss. To avoid this instability the system parameters are tuned to

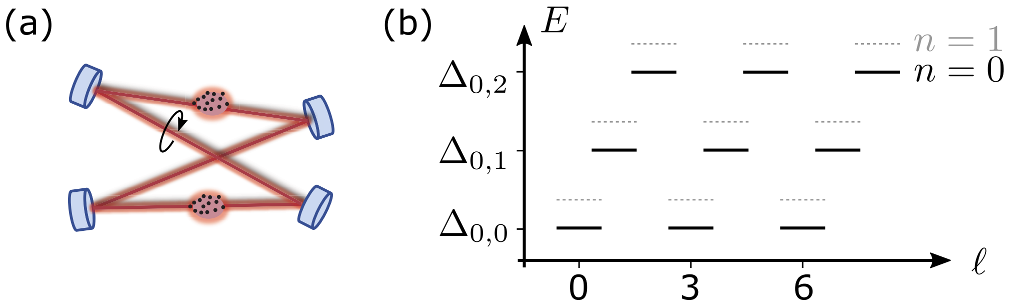

Figure 6.1: (a) Sketch of the photonic cavity setup to study fractional quantum Hall phases. A twisted ring resonator is used to induce an image rotation creating an artificial magnetic field for photons. We envision two clouds of atoms within the resonator. One of them is used to introduce a strong photon-photon nonlinearity by coupling the photons to high lying Rydberg states. The second atomic cloud is used as a mediator to transfer orbital angular momentum from an external light beam to the cavity photons. (b) Schematic photonic Landau level structure $\Delta_{n,q}$ versus angular momentum ℓ. Here, n denotes the Landau level quantum number and $q = 0, 1, 2$ one out of three sub-manifolds. The lowest Landau level (LLL) corresponds to states with energy $\Delta_{0,0}$.

another set of states with high degeneracy containing photon modes with angular momentum in multiples of $3\hbar$ – the *photonic Landau levels*. The schematic energy structure is illustrated in Fig. 6.1b. The former Landau levels n are split in three degenerate sub-manifolds, which we label with $q = 0, 1, 2$. Within a sub-manifold, the angular momentum $\ell = 3m + q$, where m is an integer, increases in multiples of $3\hbar$ and thus suppresses loss due to astigmatism.

The corresponding Hamiltonian can be written as

$$\hat{\mathcal{H}}_0 = \sum_{q=0}^{2} \sum_{n,m} \Delta_{n,q} \hat{a}^\dagger_{n,3m+q} \hat{a}_{n,3m+q}, \tag{6.1}$$

where the $\Delta_{n,q}$ determine the photonic Landau level energy spectrum. We introduced the creation $\hat{a}^\dagger_{n,\ell}$ and annihilation $\hat{a}_{n,\ell}$ operator of a cavity photon in a mode defined by the two integers (n, ℓ). The corresponding mode function

$$f_{n,\ell}(r,\varphi) = \sqrt{\frac{2^{|\ell|+1} n!}{\pi(|\ell|+n)! w_0^2}} \left(\frac{r}{w_0}\right)^{|\ell|} e^{i\ell\varphi} e^{-r^2/w_0^2} L_n^{|\ell|}\left(2\frac{r^2}{w_0^2}\right) \tag{6.2}$$

are Laguerre-Gaussian modes and form an orthogonal basis in the 2D plane. The function $L_n^{|\ell|}$ denote the generalized Laguerre polynomials. For our discussion we refer to the states of the lowest Landau level (LLL) having $n = q = 0$ and $\ell = 0, 3, 6, \ldots$.

One way to reach a regime of strongly interacting photons is to couple the photonic cavity field $\hat{\mathcal{E}}$

to a high lying Rydberg state. As we have seen in the previous chapters, Rydberg atoms provide a strong and quasi long-range interaction. Consider an additional dense atomic ensemble in the ring resonator, as sketched in Fig. 6.1a. We discuss how to achieve strong interactions within the LLL photonic modes. To this end, it is convenient to decompose the photonic cavity field $\hat{\mathcal{E}} = \sum_q \sum_n \hat{\mathcal{E}}_{n,q}$ into Laguerre-Gaussian modes

$$\hat{\mathcal{E}}_{n,q} = \sum_m f_{n,3m+q}(r,\varphi)\hat{a}_{n,3m+q}. \tag{6.3}$$

The cavity field $\hat{\mathcal{E}}_{0,0}$ with energy $\Delta_{0,0}$ is coupled to a Rydberg state $|p\rangle$ under conditions of electromagnetically induced transparency (EIT) [188, 189]. Consider the case without interactions between Rydberg states, where the system can be easily diagonalized. Then, the relevant zero-energy eigenstate is a mixture of the photonic cavity field $\hat{\mathcal{E}}_{0,0}$ and the Rydberg state $|p\rangle$, a *Rydberg cavity polariton*, $\hat{\Psi}_p = \cos\theta\hat{\mathcal{E}}_{0,0} - \sin\theta\hat{\sigma}_{gp}$. The mixing angle θ can be controlled by an external laser field. The case of interacting Rydberg polaritons has been discussed in Ref. [42, 190, 191]. This leads to an effective interaction potential between photons in the LLL and has already been demonstrated in a photonic cavity setup [178, 179]. A similar scheme can be used to induce interactions between photons in higher or different Landau level at the expense of a more complicated laser excitation scheme.

We assume an effective interaction potential $V(r) = C_6/(r^6 + \xi^6)$ between photons with distance r and interaction coefficient C_6. The length scale ξ provides a cut-off for small distances $r \ll \xi$ and stems from the dipole blockade [192, 193]. We can cast the interaction Hamiltonian between photonic modes in the LLL $(n = q = 0)$ as $(\hbar = 1)$

$$\hat{\mathcal{H}}_{\text{int}} = \sum_{\ell_1,\ell_2} \sum_{\ell_3,\ell_4} V^{\ell_1\ell_2}_{\ell_3\ell_4} \hat{a}^\dagger_{0,\ell_1} \hat{a}^\dagger_{0,\ell_2} \hat{a}_{0,\ell_3} \hat{a}_{0,\ell_4}, \tag{6.4}$$

where $\ell_i = 3m$ denotes the angular momentum. In the basis of angular momentum states $|\ell_i\rangle$, the interaction coefficients are $V^{\ell_1\ell_2}_{\ell_3\ell_4} = \langle \ell_1, \ell_2|\, V(r)\, |\ell_3, \ell_4\rangle$.

In the following, we assume that the magnetic length $\ell_B \gg \xi$ is much larger than the blockade distance ξ, which can be realized by choosing an appropriate Rydberg state. This allows us to approximate the interaction potential $V(r)$ with a contact type interaction [182]. Then, all interaction coefficients are determined by Haldane's zeroth pseudopotential V_0 [53], which can be approximated in the case of the flat-top interaction potential in Rydberg states [180] by

$$V_0 \simeq \frac{3C_6}{8\ell_B^2\xi^4}. \tag{6.5}$$

The strength V_0 can be tuned by changing the mixing angle θ and thus the proportion of photonic to matter component or by coupling to different Rydberg states. Within this approximation the interaction coefficients are

$$V_{\ell_3\ell_4}^{\ell_1\ell_2} = \frac{V_0}{2}(\ell_1 + \ell_2)!\sqrt{\frac{2^{-2(\ell_1+\ell_2)}}{\ell_1!\ell_2!\ell_3!\ell_4!}}\delta_{\ell_1+\ell_2,\ell_3+\ell_4}. \tag{6.6}$$

Clearly, the interaction Hamiltonian (6.4) preserves the total angular momentum L_z. We assume that the cyclotron frequency equivalent of the photonic Landau levels $\Delta \equiv \Delta_{0,1} - \Delta_{0,0}$ is much larger than the interaction coefficients $V_{\ell_3\ell_4}^{\ell_1\ell_2} \sim V_0$ within the LLL. In this case, mixing of states in the LLL with those in higher Landau levels is suppressed.

6.1.2 Laughlin States and Quasi-hole Excitations

The combination of photonic Landau levels (6.1) and Rydberg interactions (6.4) may lead to ground states similar to the one observed in the fractional quantum Hall effect and discussed in Sec. 1.3. Indeed, for a fixed number of photons N the state with lowest total angular momentum L_z,

$$\Psi_{\mathrm{LN}} = \langle z_1, \ldots, z_N \left|\mathrm{LN}, N\right\rangle = \mathcal{N}_{\mathrm{LN}} \prod_{i<j} \left(z_i^3 - z_j^3\right)^2 \exp\left(-\sum_j \frac{|z_j|^2}{4\ell_B^2}\right), \tag{6.7}$$

which we term *photonic Laughlin state*, is a unique ground state [174, 193, 194]. Here, $\mathcal{N}_{\mathrm{LN}}$ is a normalization constant and $z_j = x_j - iy_j$ is the complex coordinate of the jth photon. This state has a similar form as the filling $\nu = 1/2$ Laughlin state introduced in Sec. 1.3. The additional exponents $\sim z_j^3$ ensure that the state lies within the photonic LLL and Eq. (6.7) represents the filling $\nu = 1/2$ photonic Laughlin state. For the case of contact interaction, the Jastrow factors $\prod_{i<j}\left(z_i^3 - z_j^3\right)^2$ fully screen Haldane's zeroth pseudopotential and thus Eq. (6.7) is an exact zero-energy eigenstate. The total angular momentum of the photonic Laughlin state is

$$L_z(\left|\mathrm{LN}, N\right\rangle) = 3N(N-1). \tag{6.8}$$

Zero-energy excitations of the photonic Laughlin state are photonic quasi-hole excitations. A state with m quasi-holes located at the center of the system is

$$\Psi_{m\mathrm{qh}} = \langle z_1, \ldots, z_N \left|m\mathrm{qh}, N\right\rangle = \mathcal{N}_{m\mathrm{qh}} \left(\prod_j z_j^{3m}\right) \Psi_{\mathrm{LN}}, \tag{6.9}$$

where $\mathcal{N}_{m\mathrm{qh}}$ is a normalization constant. The additional factor $\prod_j z_j^3$ adds flux to the system and

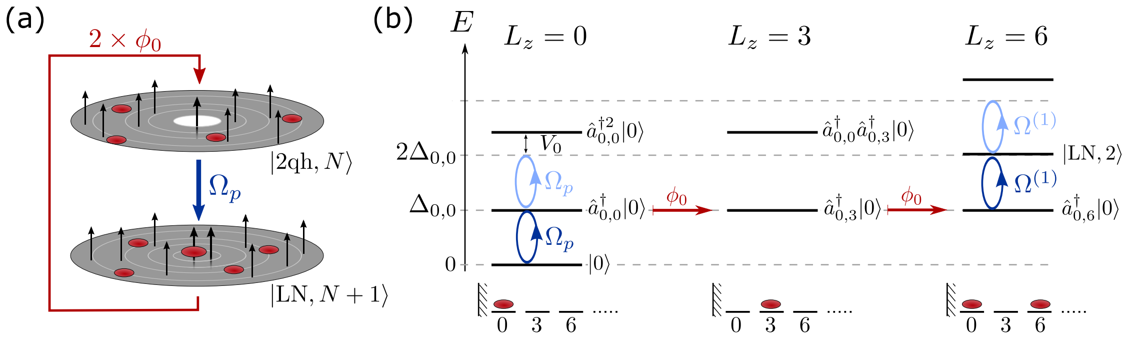
(a)
$2 \times \phi_0$
$|2\mathrm{qh}, N\rangle$
Ω_p
$|\mathrm{LN}, N+1\rangle$
(b)
E
$L_z = 0$
$L_z = 3$
$L_z = 6$
$2\Delta_{0,0}$
$\Delta_{0,0}$
0
V_0
$\hat{a}^{\dagger 2}_{0,0}|0\rangle$
Ω_p
$\hat{a}^{\dagger}_{0,0}|0\rangle$
Ω_p
$|0\rangle$
ϕ_0
$\hat{a}^{\dagger}_{0,0}\hat{a}^{\dagger}_{0,3}|0\rangle$
$\hat{a}^{\dagger}_{0,3}|0\rangle$
ϕ_0
$\Omega^{(1)}$
$|\mathrm{LN}, 2\rangle$
$\Omega^{(1)}$
$\hat{a}^{\dagger}_{0,6}|0\rangle$
0 3 6
0 3 6
0 3 6

Figure 6.2: (a) Growing scheme of the filling $\nu = 1/2$ photonic Laughlin state: First, two flux quanta ϕ_0 are inserted into the center of the system. Second, the resulting hole excitation is refilled with exactly one photon using a coherent pump Ω_p and the strong photon blockade mechanism. (b) The first steps of the growing scheme for the preparation of the Laughlin state $|\mathrm{LN}, 2\rangle$ are illustrated and explained in the main text. By inserting flux quanta ϕ_0, the total angular momentum L_z is increased by $6\hbar$. The lowest line shows the schematics of the state preparation process in terms of Landau orbitals. Note that this is a simplified picture and the structure of the photonic Laughlin state at $L_z = 6$ is more complicated.

therefore the state $\Psi_{m\mathrm{qh}}$ with N photons has a higher total angular momentum

$$L_z(|m\mathrm{qh}, N\rangle) = \frac{3}{2} m N(N+1). \tag{6.10}$$

Note that a state with two quasi-holes and N photons has the same angular momentum as the Laughlin state with $N+1$ photons, $L_z(|2\mathrm{qh}, N\rangle) = L_z(|\mathrm{LN}, N+1\rangle)$.

6.2 Growing Scheme

To grow a filling $\nu = 1/2$ photonic Laughlin state, we use a two-step protocol similar to that presented in Ref. [FL1] and [FL2] and illustrated in Fig. 6.2a: Assume we start initially with a Laughlin state $|\mathrm{LN}, N\rangle$ with N photons. The goal is to prepare the Laughlin state $|\mathrm{LN}, N+1\rangle$ with $N+1$ photons. In the first step we adiabatically insert two flux quanta $\phi_0 = 3\hbar$ in the center of the system. Thereby, we increase the total angular momentum by $\Delta L_z = 6N\hbar$ and produce a hole excitation. Now, we are already in the correct total angular momentum sector for the Laughlin state with $N+1$ photons. In the second step, we replenish the hole with a single photon by exploiting the strong photon-photon interactions caused by coupling to Rydberg atoms. In this step, we increase the number of photons by one without changing the total angular momentum. This leads to the controlled preparation of the $N+1$ Laughlin state. Below, we discuss the two steps in more details.

6.2.1 Flux Insertion

The idea of adiabatic flux insertion was first introduced by Laughlin [195] providing an explanation of the quantized Hall conductivity. Inserting locally in the center of the system flux ϕ produces an outwards Hall current $j_r \sim \sigma_\mathrm{H}\partial_t\phi$ in radial direction, where σ_H is the Hall conductivity. This results in a hole excitation in the center as indicated in Fig. 6.2a. In the case of photonic Landau levels, we add two *photonic flux quanta* $\phi_0 = 3\hbar$ to grow a Laughlin state with $\frac{1}{2}$-filling in time T_ϕ. The adiabatic increase of flux ensures that we maintain a zero-energy state and create a two quasi-hole excitation $|2\mathrm{qh}, N\rangle$. In this step the total angular momentum is increased by $\Delta L_z = 6N\hbar$. A detailed protocol of flux insertion in a photonic cavity setup will be discussed in Sec. 6.3.

6.2.2 Single Photon Pump

In the next step the hole is replenished with a single photon. To this end, a coherent pump is coupled to the center of the system. If the applied laser field profile matches with the $\ell = 0$ photonic mode in the LLL, no additional angular momentum will be transferred. The corresponding Hamiltonian can be written as

$$\hat{\mathcal{H}}_{\Omega_p} = \Omega_p \left(\hat{a}^\dagger_{0,0} e^{-i\omega t} + \mathrm{h.c.}\right), \tag{6.11}$$

where Ω_p is the pump Rabi frequency. We choose the oscillation frequency $\omega = \Delta_{0,0}$ resonant with the energy of the LLL. Without interactions, the laser excites a state with superpositions of many photons. Including a strong photon blockade, we can insert at most one photon into the center of the system. In the given total angular momentum sector, the only energetically relevant state is the Laughlin state $|\mathrm{LN}, N+1\rangle$ with $N+1$ photons. The energy offset to any other state in the $N+1$ particle sector is given by the many-body gap $\Delta_\mathrm{LN} \sim 0.2V_0$ (*Laughlin gap*). Note that the Laughlin gap weakly depends on the photon number N, see e.g. [182]. For the photon blockade mechanism we require $\Omega_p \ll \Delta_\mathrm{LN}, V_0$.

To insert rapidly one photon, we suggest to use a π-pulse. The duration of the pulse is given by $T_p = \pi/(2\Omega_p^{(N)})$, where

$$\Omega_p^{(N)}/\Omega_p = \langle \mathrm{LN}, N+1|\, \hat{a}^\dagger_{0,0}\, |2\mathrm{qh}, N\rangle\,, \tag{6.12}$$

accounts for the finite overlap between the initial two quasi-hole excitation and the final Laughlin state. The overlaps weakly depend on the photon number N and converge for $N \to \infty$ [FL2].

In Fig. 6.2b we illustrate the initial steps of the growing scheme. The protocol starts with zero photons in the cavity with vacuum state $|0\rangle$. First, we apply the coherent laser excitation to insert a single photon. Making use of the photon blockade, we pump one photon into the state $\hat{a}^\dagger_{0,0}|0\rangle$. The two-photon state $\hat{a}^{\dagger 2}_{0,0}|0\rangle$ is gapped by an energy mismatch V_0. In the next step, we add two flux quanta ϕ_0 to the system and thereby increase the total angular momentum. The state is transferred to $\hat{a}^\dagger_{0,0}|0\rangle \xrightarrow{\phi_0} \hat{a}^\dagger_{0,3}|0\rangle \xrightarrow{\phi_0} \hat{a}^\dagger_{0,6}|0\rangle$, which corresponds to the trivial two quasi-hole state. Next, we couple again the coherent laser field to the cavity and thus excite the zero-energy Laughlin state $|\mathrm{LN}, 2\rangle \sim \left(\sqrt{20}\hat{a}^{\dagger}_{0,0}\hat{a}^{\dagger}_{0,6} - \hat{a}^{\dagger 2}_{0,3}\right)|0\rangle$. The photon-photon interactions and the overlap $\Omega_p^{(1)}/\Omega_p = \sqrt{10/11}$ ensure that we add exactly one photon into the cavity. Repeating the protocol allows to grow the desired N photon Laughlin liquid.

6.3 Flux Insertion in a Photonic Cavity

Now, we present a protocol for the controlled insertion of flux quanta $\phi_0 = 3\hbar$ into a twisted photonic cavity setup. This will lead to a transfer of photons between modes

$$\hat{a}_{0,3m} \xrightarrow{\text{(i)}} \hat{a}_{0,3m+1} \xrightarrow{\text{(ii)}} \hat{a}_{0,3m+3} \tag{6.13}$$

in two steps. In the first step (i) we populate a higher Landau level $n = 0, q = 1$ and add $1\hbar$ angular momentum to each photon. In the second step (ii), we add another $2\hbar$ angular momentum and transfer all photons back to the LLL. In this way we prevent errors from direct coupling between the modes $\hat{a}_{0,3m}$ and $\hat{a}_{0,3m+3}$ and break time reversal symmetry. We show that these two steps can be performed by coupling an external laser field to a dense atomic medium in one of the resonator arms as is indicated in Fig. 6.1a. The medium acts as a mediator between the photonic cavity field $\hat{\mathcal{E}}$ and an external orbital angular momentum (OAM) beam. The angular momentum will be first transferred to the atomic cloud and later to the cavity field. To this end, we employ a STIRAP technique [196], which is robust and insensitive to small variations of the coupling strength. First, we discuss the noninteracting case of flux insertion, which can be realized without coupling photons to Rydberg states. Later, we comment on the interacting case.

6.3.1 Microscopic Model

Consider a dense atomic ensemble with four relevant atomic states as shown in Fig. 6.3. Besides the ground state $|g\rangle$, we consider a metastable state $|s\rangle$ and two excited states $|e\rangle$ and $|r\rangle$. Both excited states have a finite lifetime with decay rate γ_e and γ_r. The cavity fields $\hat{\mathcal{E}}_{0,0}$ and $\hat{\mathcal{E}}_{0,1}$ drive the transitions $|g\rangle \leftrightarrow |e\rangle$ and $|g\rangle \leftrightarrow |r\rangle$ with coupling strength g_0 and g_1, respectively. We assume real coupling strength $g_{0,1}$, which are proportional to the relevant transition dipole moment and include the corresponding mode volume. In addition, we assume a large single photon detuning $\delta \gg g_{0,1}$ to avoid any direct transition to the excited states and thus decay via the excited states. Furthermore, we assume that all other cavity modes with $n \neq 0$ and $n = 0, q = 3$ are highly off-resonant and can be disregarded.

Additionally, we consider external laser fields with Rabi frequency $\bar{\Omega}_\ell$ which couple the atomic transitions $|s\rangle \leftrightarrow |e\rangle$ ($\ell = 1, -2$) and $|s\rangle \leftrightarrow |r\rangle$ ($\ell = 0$) and carry OAM $\hbar\ell$. The fields Ω_0 ($\Omega_{\ell=1,-2}$)

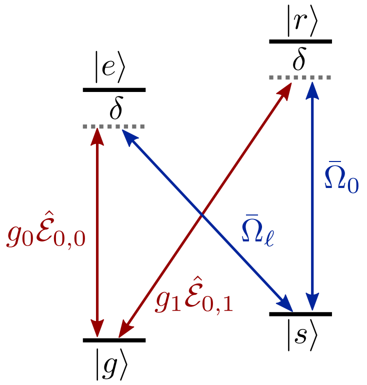

Figure 6.3: The relevant atomic states consist of a ground state $|g\rangle$, a metastable state $|s\rangle$ and two excited states $|e\rangle, |r\rangle$. The transitions $|g\rangle \leftrightarrow |e\rangle$ and $|g\rangle \leftrightarrow |r\rangle$ are driven by the cavity fields $\hat{\mathcal{E}}_{0,0}$ and $\hat{\mathcal{E}}_{0,1}$ with coupling constants g_0 and g_1, respectively. The external laser fields $\bar{\Omega}_0$ and $\bar{\Omega}_\ell$ drive the transitions $|s\rangle \leftrightarrow |e\rangle$ and $|s\rangle \leftrightarrow |r\rangle$, respectively. The Rabi frequency $\bar{\Omega}_\ell$ carries $\ell\hbar$ orbital angular momentum. The laser frequencies are chosen such that the two-photon transition is resonant, while the single-photon detuning δ is large compared to the coupling strength g_0, g_1.

and $\hat{\mathcal{E}}_{0,1}$ ($\hat{\mathcal{E}}_{0,0}$) are in two-photon resonance with the transition $|g\rangle \leftrightarrow |s\rangle$, as indicated in Fig. 6.3. The external laser field can be written as

$$\bar{\Omega}_\ell = \Omega_\ell(t)\kappa_\ell(r)e^{i\ell\varphi}, \tag{6.14}$$

where $\kappa_\ell(r)$ denotes the spatial profile and $\Omega_\ell(t)$ the time-dependent coupling strength. Laser beams carrying OAM have already been used in experiments to transfer OAM of light to an atomic medium [197]. We assume a spatially uniform excitation laser $\bar{\Omega}_0 = \Omega_0$ having $\ell = 0$ angular momentum.

In a rotating frame and projected to the lowest two Landau levels $n = 0$ with $q = 0, 1$, the light-matter coupling Hamiltonian can be written as ($\hbar = 1$)

$$\begin{aligned}\hat{\mathcal{H}}_\phi = &\int \mathrm{d}^2\mathbf{r}\ \rho(r)\delta\left[\hat{\sigma}_{ee} + \hat{\sigma}_{rr}\right] \\ &- \int \mathrm{d}^2\mathbf{r}\ \rho(r)\left[g_0\hat{\mathcal{E}}_{0,0}\hat{\sigma}_{eg} + g_1\hat{\mathcal{E}}_{0,1}\hat{\sigma}_{rg} + \bar{\Omega}_\ell\hat{\sigma}_{se} + \Omega_0\hat{\sigma}_{sr} + \text{h.c.}\right].\end{aligned} \tag{6.15}$$

We assume a high atomic density $\rho(r)$, which varies only slightly over the relevant experimental length scales. In particular, we assume a weak trapping potential of the dense atomic medium, which can be neglected in the description of the collective atomic modes. Thus, we discuss in the following the case of a homogeneous constant density ρ. Furthermore, we introduced in Eq. (6.15) spatially coarse-grained atomic flip operators

$$\hat{\sigma}_{\mu\nu}(\mathbf{r},t) = \frac{1}{\Delta N} \sum_{j\in\Delta V} |\mu\rangle_j \langle\nu| , \tag{6.16}$$

with $\mu,\nu \in \{g,s,e,r\}$. Here, the sum is taken over $\Delta N \gg 1$ atoms in a small volume ΔV centered around the position $\mathbf{r}$. This can be used as an approximation in the high density limit $\rho = \frac{\Delta N}{\Delta V}$ and when the density is smooth on a length scale on which the light field varies. Then, the operators $\hat{\sigma}_{\mu\nu}(\mathbf{r})$ approximately fulfill the commutation relation

$$\left[\hat{\sigma}_{\alpha\beta}(\mathbf{r}), \hat{\sigma}_{\gamma\delta}(\mathbf{r}')\right] = \frac{\delta(\mathbf{r}-\mathbf{r}')}{\rho} \left[\delta_{\beta\gamma}\hat{\sigma}_{\alpha\delta}(\mathbf{r}) - \delta_{\alpha\delta}\hat{\sigma}_{\gamma\beta}(\mathbf{r})\right]. \tag{6.17}$$

Initially, all atoms are in the ground state $|g\rangle$. We assume weak cavity fields $g_0\langle\hat{\mathcal{E}}_{0,0}\rangle, g_1\langle\hat{\mathcal{E}}_{0,1}\rangle \ll \Omega$ and discuss the linear response regime. Within this approximation, we set $\hat{\sigma}_{gg} \simeq 1$ while all other states have a vanishing population. It is convenient to introduce scaled atomic field operators for the coherences, namely we set $\hat{P} = \sqrt{\rho}\hat{\sigma}_{ge}$, $\hat{S} = \sqrt{\rho}\hat{\sigma}_{gs}$ and $\hat{R} = \sqrt{\rho}\hat{\sigma}_{gr}$. We decompose the atomic cavity field operators into the Laguerre-Gaussian basis, i.e.

$$\hat{P} = \sum_{n,m} f_{n,m}(r,\varphi)\hat{P}_{n,m}, \tag{6.18}$$

$$\hat{S} = \sum_{n,m} f_{n,m}(r,\varphi)\hat{S}_{n,m}, \tag{6.19}$$

$$\hat{R} = \sum_{n,m} f_{n,m}(r,\varphi)\hat{R}_{n,m}, \tag{6.20}$$

and use Eq. (6.3) for the decomposition of the cavity fields $\hat{\mathcal{E}}_{0,0}$ and $\hat{\mathcal{E}}_{0,1}$. Then, we can express the Hamiltonian (6.15) as

$$\begin{aligned}\hat{\mathcal{H}}_\phi =& \delta\sum_{n,m}\left(\hat{P}^\dagger_{n,m}\hat{P}_{n,m} + \hat{R}^\dagger_{n,m}\hat{R}_{n,m}\right) - \sum_m \left[g_0\sqrt{\rho}\hat{P}^\dagger_{0,3m}\hat{a}_{0,3m} + g_1\sqrt{\rho}\hat{R}^\dagger_{0,3m+1}\hat{a}_{0,3m+1} + \text{h.c.}\right] \\ &- \sum_{n,m}\left[\Omega_0\hat{S}^\dagger_{n,m}\hat{R}_{n,m} + \text{h.c.}\right] - \sum_{n,n'}\sum_{m,m'}\left[\Omega_\ell\chi^{n,n'}_{m,m'}\hat{S}^\dagger_{n,m}\hat{P}_{n',m'} + \text{h.c.}\right],\end{aligned} \tag{6.21}$$

where the coefficient

$$\chi^{n,n'}_{m,m'} = \int \mathrm{d}^2\mathbf{r}\; f^*_{n,m}(r,\varphi)\kappa_\ell(r)e^{i\ell\varphi}f_{n',m'}(r,\varphi) \tag{6.22}$$

determines the overlap between the different atomic modes and the spatial profile of the OAM beam.

6.3.2 Dark States and Orbital Angular Momentum Transfer

The main feature of our flux insertion scheme is a versatile OAM beam $\bar{\Omega}_\ell$. We will see below that our scheme only relies on two different OAM beams. In the first step (i) of the flux insertion process we add $\Delta l = 1$ angular momentum and in the second step (ii) we add $\Delta\ell = 2$ angular momentum to all photons. This is in contrast to the scheme presented in Ref. [182], which requires for each step a different OAM beam.

Step (i): In the first step we use an OAM beam $\bar{\Omega}_1 = \Omega_1 \kappa_1(r) e^{i\varphi}$. Using the Heisenberg-Langevin equation [198], we obtain for the relevant cavity and atomic modes,

$$\partial_t \hat{a}_{0,3m} = i g_0 \sqrt{\rho} \hat{P}_{0,3m}, \tag{6.23a}$$

$$\partial_t \hat{a}_{0,3m+1} = i g_1 \sqrt{\rho} \hat{R}_{0,3m+1}, \tag{6.23b}$$

$$\partial_t \hat{P}_{n,3m} = -\left(i\delta + \gamma_e\right) \hat{P}_{n,3m} + i g_0 \sqrt{\rho} \hat{a}_{0,3m} \delta_{n,0} + i\Omega_1^* \sum_{n'} \left(\chi_m^{n',n}\right)^* \hat{S}_{n',3m+1}, \tag{6.23c}$$

$$\partial_t \hat{S}_{n,3m+1} = i\Omega_1 \sum_{n'} \chi_m^{n,n'} \hat{P}_{n',3m} + i\Omega_0 \hat{R}_{n,3m+1}, \tag{6.23d}$$

$$\partial_t \hat{R}_{n,3m+1} = -\left(i\delta + \gamma_r\right) \hat{R}_{n,3m+1} + i g_1 \sqrt{\rho} \hat{a}_{0,3m+1} \delta_{n,0} + i\Omega_0^* \hat{S}_{n,3m+1}, \tag{6.23e}$$

with coefficients

$$\chi_m^{n,n'} = \int \mathrm{d}^2\mathbf{r}\, f_{n,3m+1}^*(r,\varphi) \kappa_1(r) e^{i\varphi} f_{n',3m}(r,\varphi). \tag{6.24}$$

We assume a high-finesse cavity with small photon losses on the experimentally relevant timescale and therefore neglect these in the equations of motion. However, since atomic decay might be relevant on the experimental timescale, we include decay of excited states with rate γ_e, γ_r. To maintain the commutation relations Langevin noise operators can be introduced, which are δ-correlated in space and time with zero mean value. Since we discuss a regime where the excited state population is negligible we however omit the noise operators here and in what follows.

Choosing a spatial profile $\kappa_1(r) = \frac{1}{r/w_0}$, we have $\chi_m^{0,n'} \propto \delta_{n',0}$ in Eq. (6.24) and thus the coupling from the atomic mode $\hat{S}_{0,3m+1}$ to higher atomic modes with $n' > 0$ vanishes. Then, we can directly construct a dark state for an OAM transfer of $\Delta\ell = 1$,

$$\hat{\Psi}_{0,3m+1}^{(1)} = \sqrt{\rho} g_1 \Omega_1 \sqrt{\frac{2}{3m+1}} \hat{a}_{0,3m} + \sqrt{\rho} g_0 \Omega_0 \hat{a}_{0,3m+1} - \rho g_0 g_1 \hat{S}_{0,3m+1}, \tag{6.25}$$

which fulfills $\partial_t \hat{\Psi}_{0,3m+1}^{(1)} = 0$. For simplicity we omit here a proper normalization factor. Since the dark state $\hat{\Psi}_{0,3m+1}^{(1)}$ contains only the cavity fields $\hat{a}_{0,3m}$, $\hat{a}_{0,3m+1}$ and the coherence $\hat{S}_{0,3m+1}$ with the metastable state, it is immune to excited state decay. The transfer of photons from the LLL with $q = 0$ and angular momentum $\ell = 3m$ to the first Landau level with $q = 1$ and angular momentum

$\ell = 3m+1$ can be achieved by increasing the ratio Ω_0/Ω_1.

The choice of the above spatial profile ensures to remain within the manifold of states with $n = 0$. However, since the spatial profile diverges in the center at $r = 0$, this cannot be realized experimentally as the intensity of a light beam with a vortex has to vanish in the center. Instead, we approximate the spatial profile with

$$\kappa_1(r)/w_0 = \frac{r^2}{r_0^3 + r^3}, \tag{6.26}$$

with a cut-off length r_0. While the intensity vanishes now for $r \to 0$, the spatial profile maintains the scaling $\sim 1/r$ for large $r \gg r_0$. Choosing $r_0 \ll w_0$, we approximately obtain $\chi_m^{0,n'} \simeq \delta_{n',0}$ as per Eq. (6.24). We will discuss below that a residual coupling to states with $n > 0$ leads to a small loss rate to states outside the dark state manifold.

Let us assume, that initially only photonic cavity modes with $n = 0$ and $\ell = 3m$ are populated. Starting with a strong external field $\Omega_1 \gg \sqrt{\frac{3m+1}{2}\frac{g_0}{g_1}}\Omega_0, \sqrt{\frac{3m+1}{2}}\sqrt{\rho}g_0$ carrying $\ell = 1$ OAM, the system is approximately in its dark state $\hat{\Psi}^{(1)}_{0,3m+1} \simeq \hat{a}_{0,3m}$. Upon adiabatically increasing the ratio Ω_0/Ω_1, we follow the zero-energy state $\hat{\Psi}^{(1)}_{0,3m+1}$. For values $\Omega_0 \gg \sqrt{\frac{2}{3m+1}\frac{g_0}{g_1}}\Omega_1, \sqrt{\rho}g_1$, we obtain approximately a dark state with all photons in higher Landau level $q = 1$, $\hat{\Psi}^{(1)}_{0,3m+1} \simeq \hat{a}_{0,3m+1}$. This concludes the first step of the flux insertion protocol.

Step (ii): In the second step, the goal is to transfer photons in mode $\hat{a}_{0,3m+1}$ back to the LLL and add $2\hbar$ of angular momentum. Analogously, to obtain a dark state only between the modes $\hat{a}_{0,3m+3}$ and $\hat{a}_{0,3m+1}$, we choose an OAM beam $\bar{\Omega}_{-2} = \Omega_{-2}\kappa_{-2}(r)e^{-2i\varphi}$. This results in a similar set of Heisenberg-Langevin equations for the photonic cavity and atomic modes,

$$\partial_t \hat{a}_{0,3m+3} = ig_0\sqrt{\rho}\hat{P}_{0,3m+3}, \tag{6.27a}$$

$$\partial_t \hat{a}_{0,3m+1} = ig_1\sqrt{\rho}\hat{R}_{0,3m+1}, \tag{6.27b}$$

$$\partial_t \hat{P}_{n,3m+3} = -\left(i\delta + \gamma_e\right)\hat{P}_{n,3m+3} + ig_0\sqrt{\rho}\hat{a}_{0,3m+3}\delta_{n,0} + i\Omega_{-2}^*\sum_{n'}\left(\tilde{\chi}_m^{n',n}\right)^*\hat{S}_{n',3m+1}, \tag{6.27c}$$

$$\partial_t \hat{S}_{n,3m+1} = i\Omega_1\sum_{n'}\tilde{\chi}_m^{n,n'}\hat{P}_{n',3m+3} + i\Omega_0\hat{R}_{n,3m+1}, \tag{6.27d}$$

$$\partial_t \hat{R}_{n,3m+1} = -\left(i\delta + \gamma_r\right)\hat{R}_{n,3m+1} + ig_1\sqrt{\rho}\hat{a}_{0,3m+1}\delta_{n,0} + i\Omega_0^*\hat{S}_{n,3m+1}, \tag{6.27e}$$

with coefficients

$$\tilde{\chi}_m^{n,n'} = \int \mathrm{d}^2\mathbf{r}\, f^*_{n,3m+1}(r,\varphi)\kappa_{-2}(r)e^{-2i\varphi}f_{n',3m+3}(r,\varphi). \tag{6.28}$$

Choosing a spatial profile $\kappa_{-2}(r) = \frac{r^2}{w_0^2}$, we have $\tilde{\chi}_m^{0,n'} \propto \delta_{n',0}$. Thus, the atomic modes $\hat{S}_{0,3m+1}$ do not couple to atomic modes with higher $n' > 0$. We obtain a dark state for an OAM transfer of $\Delta\ell = 2$ as

$$\hat{\Psi}^{(2)}_{0,3m+1} = \sqrt{\rho} g_1 \Omega_{-2} \frac{1}{2} \sqrt{\frac{(3m+3)!}{(3m+1)!}} \hat{a}_{0,3m+3} + \sqrt{\rho} g_0 \Omega_0 \hat{a}_{0,3m+1} - \rho g_0 g_1 \hat{S}_{0,3m+1}, \tag{6.29}$$

which fulfills $\partial_t \hat{\Psi}^{(2)}_{0,3m+1} = 0$. Note that the spatial profile $\kappa_{-2}(r)$ can be realized experimentally and thus Eq. (6.29) is an exact dark state.

The first step is completed with a strong Rabi frequency Ω_0 and all photons in the modes $n = 0$ and $\ell = 3m + 1$. We further require $\Omega_0 \gg \frac{1}{2}\sqrt{(3m+3)(3m+2)}\frac{g_1}{g_0}\Omega_{-2}$ and therefore start the second step in the dark state $\hat{\Psi}^{(2)}_{0,3m+1} \simeq \hat{a}_{0,3m+1}$. Upon adiabatically increasing the ratio Ω_{-2}/Ω_0, we transfer all photons back to the LLL. For $\Omega_{-2} \gg \frac{g_0}{g_1}\frac{2\Omega_0}{\sqrt{(3m+3)(3m+2)}}, \sqrt{\rho} g_0$ we approximately obtain the dark state $\hat{\Psi}^{(2)}_{0,3m+1} \simeq \hat{a}_{0,3m+3}$. Thus, in total we increased the angular momentum of all photons by $\Delta\ell = 3$. The total time T_ϕ for the flux insertion process has to be chosen to fulfill adiabaticity, which will be discussed below.

In Fig. 6.4 the results of a numerical simulation of the flux insertion process is shown using the full equations of motion (6.23) and (6.27) including the small residual couplings out of the dark state in the first step of the protocol. We change the strength of the orbital angular momentum beams Ω_0, Ω_1 and Ω_{-2} in time t as shown in Fig. 6.4a. In the first step, i.e. for $0 \leq t < T_\phi/2$, we choose

$$\Omega_1(t) = \frac{\Omega}{\sqrt{1 + e^{+(t - T_\phi/4)/\tau}}}, \qquad \Omega_0(t) = \frac{\Omega}{\sqrt{1 + e^{-(t - T_\phi/4)/\tau}}}, \tag{6.30a}$$

where τ denotes the characteristic pulse duration. For the second step, i.e. $T_\phi/2 \leq t < T_\phi$, we choose

$$\Omega_0(t) = \frac{\Omega}{\sqrt{1 + e^{+(t - 3T_\phi/4)/\tau}}}, \qquad \Omega_{-2}(t) = \frac{\Omega}{\sqrt{1 + e^{-(t - 3T_\phi/4)/\tau}}}. \tag{6.30b}$$

As can be seen in Fig. 6.4b, our protocol robustly transfers photons from a state with angular momentum $\ell = 0$ to a state with $\ell = 3$ with a small cut-off length $r_0 \ll w_0$.

Adiabatic flux insertion: interacting case

The generalization of the adiabatic flux insertion protocol to the case of interacting photons is not straightforward. However, we will argue below that the quantized insertion of flux quanta is still possible.

Consider the first step of our growing protocol, which consists of inserting one photon and adiabatically inserting two flux quanta $\phi_0 = 3\hbar$ as is shown in Fig. 6.2b. The photon blockade ensures

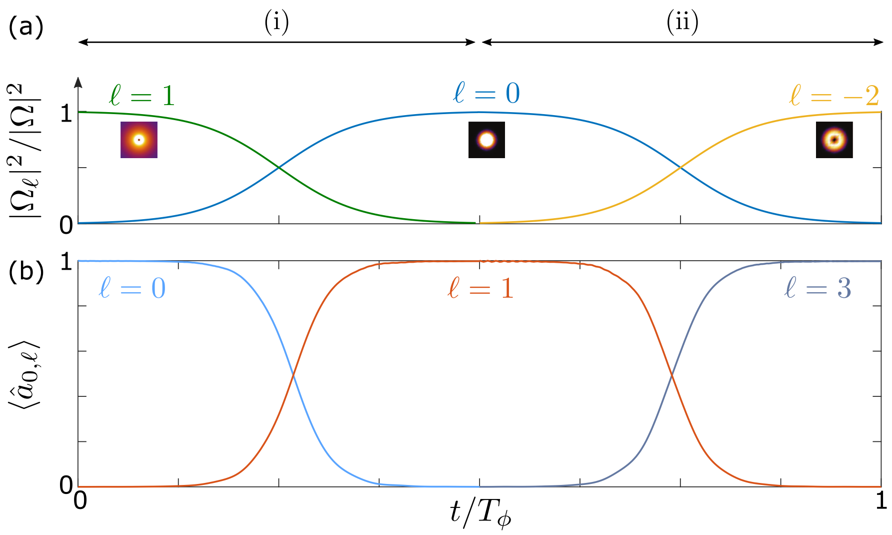

Figure 6.4: The adiabatic flux insertion protocol consisting of two steps, (i) and (ii) in time T_ϕ. (a) The laser intensity $|\Omega_\ell|^2$ is changed adiabatically in time t according to Eq. (6.30). In the insets, the intensity profile of the three different laser beams with $\ell = 1, 0, -2$ are shown. (b) Numerical simulation of the flux insertion protocol using the full equations of motion (6.23) and (6.27). Initially, we assume a coherent amplitude $\langle \hat{a}_{0,0} \rangle (t = 0) = 1$. In the first step, at $t = T_\phi/2$ the amplitude is transferred to the $\ell = 1$ mode in a higher Landau level and at $t = T_\phi$ back to the LLL with $\ell = 3$. The parameters are $\Omega = 2\pi \times 12.4\,\mathrm{MHz}$, $\sqrt{\rho} g_0 = \sqrt{\rho} g_1 = 2\pi \times 0.45\,\mathrm{MHz}$ and $\delta = 2\pi \times 1.27\,\mathrm{MHz}$ and $\gamma_e = \gamma_r = 0$. The cut-off length in the $\ell = 1$ orbital angular momentum beam is $r_0 = w_0/100$. The duration of the flux insertion process is $T_\phi = 40\tau$, where $\tau = 1\,\mu\mathrm{s}$ is a characteristic timescale. The simulations were performed by Peter Ivanov.

coherent pumping of a single photon into the state $\hat{a}^\dagger_{0,0} |0\rangle$. Using the flux insertion protocol we increase the angular momentum and reach a single photon state $\hat{a}^\dagger_{0,6} |0\rangle$. In the second step the coherent pump couples to the unique zero-energy Laughlin state with $N = 2$ photons, namely $|\mathrm{LN}, 2\rangle \sim \left(\sqrt{20}\hat{a}^\dagger_{0,0}\hat{a}^\dagger_{0,6} - \hat{a}^{\dagger 2}_{0,3}\right) |0\rangle$. Without interactions, we expect that after inserting two more flux quanta ϕ_0 we create a state $\sim \left(\sqrt{20}\hat{a}^\dagger_{0,6}\hat{a}^\dagger_{0,12} - \hat{a}^{\dagger 2}_{0,9}\right) |0\rangle$. This is however not the two quasi-hole state $|2\mathrm{qh}, 2\rangle \sim \left(\sqrt{55/21}\hat{a}^\dagger_{0,6}\hat{a}^\dagger_{0,12} - \hat{a}^{\dagger 2}_{0,9}\right) |0\rangle$ and thus has a higher energy in the interacting case.

Now, consider the case of interacting photons. During flux insertion the dark state remains a zero-energy state and we do not transfer energy into the system in the adiabatic limit, which requires that the change of system parameters is slow compared to the many-body gap, i.e. $\Delta_{\mathrm{LN}} T_\phi \gg 1$. We presume that we stay within the manifold of zero-energy states consisting of the Laughlin state $|\mathrm{LN}, N\rangle$ and the quasi-hole states $|1\mathrm{qh}, N\rangle$, $|2\mathrm{qh}, N\rangle$. Importantly, this means that in the state transfer the prefactor in the photonic Laughlin state is modified ($\sqrt{20} \to \sqrt{55/21}$). Thus, after two times of flux insertion, we create the two quasi-hole state $|2\mathrm{qh}, N\rangle$. Later, we will verify this by numerical simulations.

To maintain a finite Laughlin gap Δ_{LN} during the whole protocol we need interactions between the photons also in the first Landau level ($n = 0$, $q = 1$). To this end, we envision that the photonic mode $\hat{\mathcal{E}}_{0,1}$ is also coupled to another Rydberg state in an EIT configuration. Then, the same discussion as in Sec. 6.1 applies. While the interaction potential between two photons in the same or in different Landau levels might differ, we assume in the following a single interaction potential for all cases.

6.3.3 Performance

Using the single photon pump and the flux insertion process, we add one particle after another in time $T = 2T_\phi + T_p$. After N steps of the growing scheme, we prepare a state $|\Psi_N\rangle$. To quantify the accuracy of the growing scheme, we summarize in the following the main contributions to the fidelity,

$$\mathcal{F}_N = |\langle\Psi_N|\, \text{LN}, N\rangle|^2. \tag{6.31}$$

In essence, we identify two main errors in the growing scheme: Firstly, we assume an effective photon loss rate γ_{eff} including cavity losses, Rydberg state decay as well as residual couplings to higher Landau level in the flux insertion protocol. For small loss rate $\gamma_{\text{eff}} \ll 1/T$, we can estimate the probability of a single decay process after N steps by

$$P_\gamma = 1 - \exp\left(-\gamma_{\text{eff}} T \sum_{k=1}^{N} k\right) \simeq \frac{1}{2}\gamma_{\text{eff}} T N(N+1). \tag{6.32}$$

Secondly, we account for nonadiabatic errors in the flux insertion and single photon pump. These result from coupling to high energy states or states with a photon number different from N with many-body gap $\sim \Delta_{\text{LN}}$. We estimate that the probabilities for exciting these states scale as

$$P_\phi \sim \frac{1}{(\Delta_{\text{LN}} T_\phi)^2}, \qquad P_p \sim \frac{1}{(\Delta_{\text{LN}} T_p)^2}, \tag{6.33}$$

for flux insertion and coherent pump, respectively. In total, we obtain an estimate for the fidelity,

$$\mathcal{F}_N = e^{-(P_\gamma + P_\phi + P_p)} \simeq \exp\left[-N\left(\frac{1}{2}\gamma_{\text{eff}} T(N+1) + \frac{\Lambda^2}{\Delta_{\text{LN}}^2 T^2}\right)\right], \tag{6.34}$$

where we combined both nonadiabatic contributions P_ϕ, P_p and introduced a parameter Λ. Numerical simulations in Ref. [FL2] showed that $\Lambda \simeq 10$ for lattice systems, where angular momentum is not a conserved quantity. We expect similar values for Λ in the case discussed here.

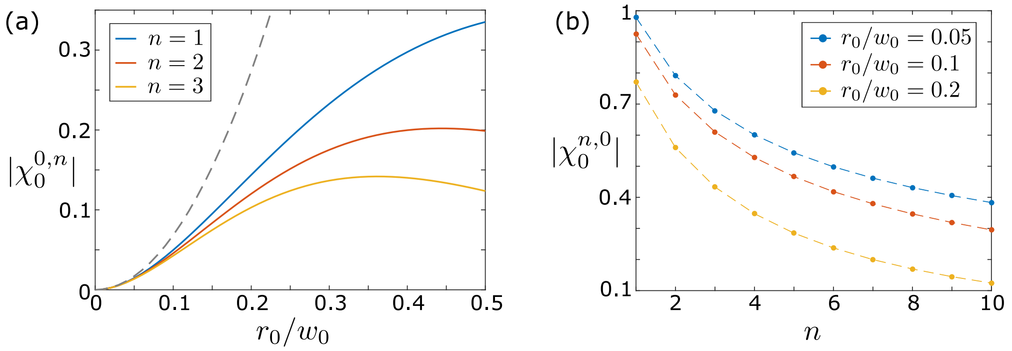

Figure 6.5: Residual coupling to higher Landau level $n > 0$ in the first step of the flux insertion procotol for spatial profile $\kappa_1(r)/w_0 = r^2/(r^3 + r_0^3)$ with cut-off length r_0. (a) Overlap $|\chi_0^{0,n}|$ versus the cut-off length r_0 for $n = 1, 2, 3$. The gray dashed line indicates an approximate scaling with r_0 as $|\chi_0^{0,n}| = \frac{8\pi}{3}\sqrt{\frac{2}{3}}\frac{r_0^2}{w_0^2}$. (b) Overlap $|\chi_0^{n,0}|$ versus the Landau level quantum number n for three different cut-off lengths r_0.

Residual coupling to higher Landau levels with $n > 0$

In the adiabatic flux insertion protocol discussed here, we encounter another error due to the cut-off in the spatial profile of the OAM beam in Eq. (6.26). This leads to a reduced angular momentum transfer probability and is a source of additional excited state decay. To see this, we consider again the first step of the flux insertion protocol in Eq.(6.23). As discussed before, the case $\kappa_1(r)/w_0 = 1/r$ results in $\chi_m^{0,n'} \propto \delta_{n',0}$. Then, the state Eq. (6.25) remains a dark state, as can be seen directly by evaluating $\partial_t \hat{\Psi}_{0,3m+1}^{(1)}$. However, the experimentally realizable spatial profile $\kappa_1(r)/w_0 = r^2/(r_0^3 + r^3)$ as in Eq. (6.26) yields small coupling elements $\sim \chi_m^{0,n'}$ to higher Landau level $n' > 0$ for $r_0 \ll w_0$. This is illustrated for different cut-off lengths r_0/w_0 in Fig. 6.5a. Clearly, the overlaps $|\chi_0^{0,n'}| \ll |\chi_0^{0,0}| \simeq \sqrt{2}$ decrease with increasing Landau level quantum number n' and approximately scale as $\chi_0^{0,n'} \propto r_0^2$ for $r_0/w_0 \ll 1$. The coupling elements between higher angular momentum states with $m > 0$ are even smaller and can be neglected. Note that the coefficients $\chi_m^{n,0}$ do not necessarily have to be small to maintain a dark state. Indeed, this is the case as shown in Fig. 6.5b for several cut-off length r_0/w_0.

Let us assume we are initially in the dark state manifold, where we can neglect the contributions from the excited states and the coherences $\hat{S}_{n,3m+1}$ with $n > 0$. The residual coupling between $\hat{S}_{0,3m+1}$ and the excited state coherences $\hat{P}_{n,3m}$ with $n > 0$ introduces a loss mechanism. We adiabatically eliminate the atomic state coherences $\hat{E}_{n,3m}$, which decay on a fast timescale with rate γ_e and reinsert into Eq. (6.23d). This yields

$$\partial_t \hat{S}_{0,3m+1} \simeq i\Omega_1 \chi_m^{0,0} \hat{P}_{0,3m} + i\Omega_0 \hat{R}_{n,3m+1} - \sum_{n>0} \frac{|\Omega_1 \chi_m^{0,n}|^2}{\delta^2 + \gamma_e^2} \left(-i\delta + \gamma_e\right) \hat{S}_{0,3m+1}, \tag{6.35}$$

which includes an effective decay channel for the coherences $\hat{S}_{0,3m+1}$ and thus the dark state $\hat{\Psi}^{(1)}_{0,3m+1}$. For sufficiently small cut-off length r_0 or small population of the metastable state, the additional decay can be neglected.

6.4 Exact Diagonalization of Small Systems

A full simulation of all photonic modes including the interactions between all photons and atomic modes is challenging due to the large Hilbert space. However, the simulation of small systems involving only the photonic modes with $n = 0$ with a certain maximal total angular momentum $L_z^{\max}$ is feasible. To this end, we shortly present a simplified adiabatic flux insertion protocol used for simulating the dynamics of up to three photons. While this model might not be realized in an experiment, it serves as a toy model for a similar adiabatic flux insertion process and suggests that the adiabatic flux insertion protocol should work.

Similar to the STIRAP technique, we use an adiabatic transfer protocol to increase the angular momentum of the system. The coupling scheme relies on photonic cavity modes within the Landau levels $n = 0$ with $q = 0, 1$. As before, we use a two-step protocol,

$$\hat{a}_{0,3m} \xrightarrow{\text{(i)}} \hat{a}_{0,3m+1} \xrightarrow{\text{(ii)}} \hat{a}_{0,3m+3}, \tag{6.36}$$

to increase the angular momentum of each photon by $\Delta\ell = 3$. Each step, (i) and (ii), is a combination of a coupling between two photonic modes and a dynamically controlled energy mismatch $\Delta(t) \equiv \Delta_{0,1} - \Delta_{0,0}$ between the lowest and first photonic Landau level. This process is reminiscent of a Landau-Zener sweep or a rapid adiabatic passage technique.

The corresponding coupling Hamiltonian can be written as

$$\hat{\mathcal{H}}_\phi = \sum_m \left[\chi_1(t)\hat{a}^\dagger_{0,3m}\hat{a}_{0,3m+1} + \chi_2(t)\hat{a}^\dagger_{0,3m+1}\hat{a}_{0,3m+3} + \text{h.c.}\right], \tag{6.37}$$

where the coupling constants $\chi_1, \chi_2 \ll \Delta_{\text{LN}} \ll \Delta(0) = \Delta(T_\phi)$ are much weaker than the Laughlin gap and the original Landau level energy gap. This avoids mixing between different angular momentum states before and after the flux insertion protocol and thus weakly affects the relevant many-body states, namely the Laughlin state and the quasi-hole states.

The system parameters χ_1, χ_2 and Δ are changed in time as shown in Fig. 6.6a. For simplicity, we sweep the energy mismatch linearly in time,

$$\Delta(t) = -\Delta(0) + \frac{4\Delta(0)}{T_\phi}\left|t - \frac{T_\phi}{2}.\right| \tag{6.38}$$

Clearly, this is not an optimal parameter sweep and will be therefore slow compared to more

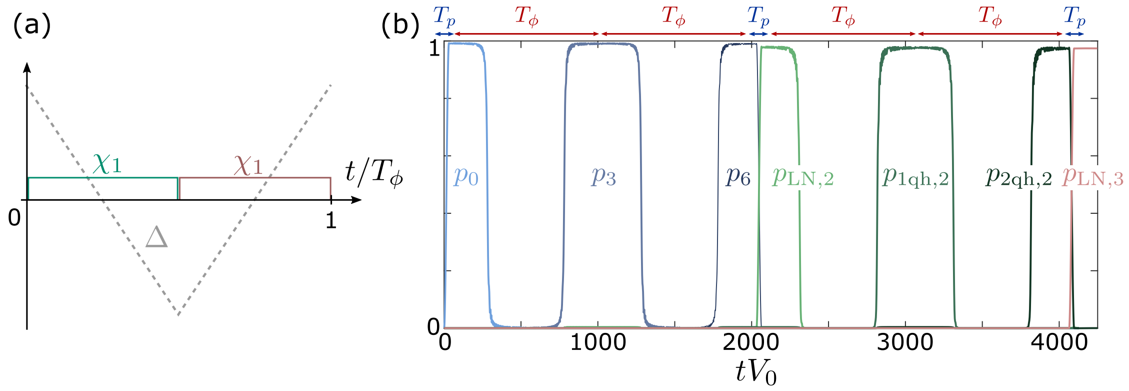

Figure 6.6: (a) Schematic sketch of the system parameter changes during the simplified flux insertion protocol. The coupling elements χ_1 (χ_2) between the photonic modes as per Eq. (6.37) are turned on during the first (second) half of the protocol. The energy mismatch between the lowest photonic Landau levels $\Delta = \Delta_{0,1} - \Delta_{0,0}$ is changed in time as per Eq. (6.38). After a full step of flux insertion in time T_ϕ we have $\Delta(0) = \Delta(T_\phi)$. (b) Results of an exact diagonalization of the growing scheme for up to $N = 3$ photons in the $n = 0$ Landau level subspace with maximal total angular momentum $L_z^{\max} = 19$. Shown are the probabilities for the relevant states in the LLL with respect of the simulated state $|\Psi(t)\rangle$. The single-photon probabilities are denoted by $p_\ell = |\langle\Psi|\,\hat{a}^\dagger_{0,\ell}\,|0\rangle|^2$. The probability of being in the Laughlin state with N photons is $p_{\mathrm{LN},N}$ and the probability of being in the m quasi-hole state with N photons is $p_{m\mathrm{qh},N}$. A step in the growing scheme consists of a coherent pump Eq. (6.11) during time T_p and insertion of two flux quanta ϕ_0 as shown in (a) during time T_ϕ. The parameters are $\Delta(0)/V_0 = 10$, $\Omega_p/V_0 = 1/20$ and $\chi_1/V_0 = \chi_2/V_0 = 1/5$.

sophisticated protocols. We estimate the timescale T_ϕ needed to fulfill adiabaticity and obtain

$$T_\phi \gg \frac{4\Delta(0)}{\Delta_{\mathrm{LN}}^2}. \tag{6.39}$$

Let us start to discuss the noninteracting case, where all photons are in the LLL. Within the first half of the protocol, $0 \leq t < T_\phi/2$, photons are transferred from the LLL to the first Landau level. During this time, the coupling strength χ_1 is turned on and the energy mismatch slowly decreases to a value $-\Delta(0)$. In the adiabatic limit the prepared state remains in the ground state and the angular momentum per photon is increased by $\Delta\ell = 1$. In the second part of the flux insertion protocol, $T_\phi/2 \leq t < T_\phi$, the coupling χ_2 is turned on and the energy mismatch increases to its original value. All photons are now transferred back to LLL and the angular momentum per photon is increased by $\Delta\ell = 2$. In total, we added one flux quantum ϕ_0 to the system.

Finally, let us discuss the full protocol presented in Sec. 6.2 consisting of a coherent pump Eq. (6.11) and the flux insertion process described above. We assume a contact-type interaction Hamiltonian of the form (6.4) between photons in the LLL and first Landau level. In Fig. 6.6b the simulation of the growing scheme up to $N = 3$ particles is shown. We show the probabilities of the relevant many-body states in the LLL. The protocol ends after three steps in a state $|\Psi_3\rangle$, which has a high overlap with the 3-photon Laughlin state, $\mathcal{F}_3 = |\langle\Psi_3|\,\mathrm{LN},3\rangle|^2 = 0.97$.

Conclusion

The creation of interesting fractional quantum Hall states of light is experimentally challenging due to the lack of efficient cooling mechanism. Here, we demonstrated that using a simple growing scheme photonic Laughlin states can be prepared in a cavity setup with high fidelity. The studies are motivated by recent experiments realizing strong magnetic fields in a photonic twisted cavity setup [174] and strong photon-photon interactions by coupling the cavity fields to Rydberg states [178].

The growing scheme consists of two steps: In the first step, flux is inserted into the cavity creating a quasi-hole excitation. We discussed a flux insertion protocol using an external laser beam with orbital angular momentum to transfer additional flux to the system. We showed that upon adiabatic parameter changes in two steps, the angular momentum of each photon increases by $3\hbar$. In the second step, a coherent pump replenishes the hole with exactly one photon due to the strong photon-photon interactions. We discussed the performance of the protocol including photon loss and non-adiabatic transitions to high energy states. Using an exact diagonalization we simulated a similar protocol and showed that it is possible to grow a Laughlin state with high fidelity.

While we studied here the case of short-range interactions realizing a photonic Laughlin state, it may also be interesting to investigate different states in the case of a long-range flat-top interaction potential [180]. In addition, the good coherent control of photonic systems may allow to study bilayer quantum Hall phases by exploring different photonic Landau levels.

List of publications

Publications relevant for this thesis

The following papers are already published or submitted to a peer reviewed journal. In each paper all authors contributed to the research project.

[FL1] Fabian Grusdt, Fabian Letscher, Mohammad Hafezi and Michael Fleischhauer
Topological growing of Laughlin states in synthetic gauge fields
Phys. Rev. Lett. **113** 155301 (2014)

This publication is a collaboration with Mohammad Hafezi and the group of Michael Fleischhauer and was developed during the time of my diploma thesis. In particular, I contributed to the discussion and estimate of the fidelity. All authors contributed to the data interpretation and manuscript.

[FL2] Fabian Letscher, Fabian Grusdt and Michael Fleischhauer
Growing quantum states with topological order
Phys. Rev. B **91** 184302 (2015)

This is a follow-up publication of [FL1]. In particular, I made the numerical simulations of the effective composite fermion model. Furthermore, I wrote and edited the early versions of the manuscript. All authors contributed to the data interpretation and manuscript.

[FL3] Fabian Letscher, Oliver Thomas, Thomas Niederprüm, Herwig Ott and Michael Fleischhauer
Anomalous excitation facilitation in inhomogeneously broadened Rydberg gases
Phys. Rev. A **95** 023410 (2017)

This publication is a collaboration with the group of Herwig Ott and Michael Fleischhauer. In particular, I contributed to the analysis and made the numerical simulations. Furthermore, I wrote and edited the main parts of the publication. All authors contributed to the data interpretation and manuscript.

[FL4] Fabian Letscher, Oliver Thomas, Thomas Niederprüm, Michael Fleischhauer and Herwig Ott
Bistability vs. Metastability in Driven Dissipative Rydberg Gases
Phys. Rev. X **7** 021020 (2017)

This publication is a collaboration with the group of Herwig Ott and Michael Fleischhauer. M. F. and H. O. conceived the study of off-resonant Rydberg excitation dynamics. O. T and T. N. performed the experiment and analyzed the data. H. O. supervised the experiment. F. L. and M. F. developed the theoretical model. F. L. performed the numerical simulations of the many-body rate equation model. F. L. and O. T. performed numerical simulations of the single cluster model. M. F. supervised the numerical simulations. F. L. and O. T. prepared the early version of the manuscript. All authors contributed to the data interpretation and manuscript.

[FL5] Fabian Letscher, David Petrosyan and Michael Fleischhauer
Many-body dynamics of holes in a driven, dissipative spin chain of Rydberg superatoms
New J. Phys. **19** 113014 (2017)

This publication is a collaboration with David Petrosyan and Michael Fleischhauer. M. F. conceived the study of a superatom chain. I derived the superatom rate equation model and performed all numerical simulations. All authors contributed to the data interpretation and manuscript.

[FL6] Fabian Letscher and David Petrosyan
Mobile bound states of Rydberg excitations in a lattice
Phys. Rev. A **97** 043415 (2018)

This manuscript is a collaboration with David Petrosyan. I derived the effective dressed model for the Rydberg spin model and performed all numerical simulations. All authors contributed to the interpretation and manuscript.

[FL7] Peter Ivanov, Fabian Letscher, Jonathon Simon and M. Fleischhauer
Adiabatic flux insertion and growing of Laughlin-type states of cavity Rydberg polaritons
submitted (2018)

This work is a collaboration with Peter Ivanov, Jonathan Simon and Michael Fleischhauer. I contributed to the numerical simulation of the growing scheme. All authors contributed to the interpretation and manuscript.

Publications not related to this thesis

[FL8] Christina Jörg, Fabian Letscher, Michael Fleischhauer and Georg von Freymann
Dynamic defects in photonic Floquet topological insulators
New J. Phys. **19** 083003 (2017)

Appendices

Appendix A

A single atom in an optical lattice

We estimate the relevant wavefunction and spatial width σ of the experimental setup in Chapter 2. For simplicity, we discuss a 1D lattice where the standing wave forms a periodic trapping potential

$$V(x) = V_0 \sin^2(kx). \tag{A.1}$$

Here, $k = \frac{2\pi}{\lambda_0}$ is the wavevector of the trapping laser with wavelength $\lambda_0 = 748\,\mathrm{nm}$ and V_0 is the lattice depth. The trap potential depths is $V_0 = 20E_r$, where $E_r = \frac{\hbar^2 k^2}{2m}$ is the recoil energy of Rubidium with mass m. In the case of a deep optical lattice and low temperatures, atoms are localized near the center of the periodic potential. Consider an atom trapped in a potential minimum at position $x = x_0$, where x_0 is a multiple of the lattice constant $a_x = \lambda_0/2$. We can estimate the corresponding Wannier wavefunction by approximating the lattice potential with a harmonic potential (*tight-binding approximation*),

$$\begin{aligned}\hat{\mathcal{H}}_{\mathrm{lat}} &= \frac{p_x^2}{2m} + V_0 \sin^2(kx) \\ &\simeq \frac{p_x^2}{2m} + \frac{1}{2} m\omega^2 (x - x_0)^2.\end{aligned} \tag{A.2}$$

This is a valid approximation at low temperatures $k_B T \ll \hbar\omega$, when the atom is well localized in the lowest eigenstate of the Hamiltonian. Then, the corresponding wavefunction is

$$\psi(x) = \left(\frac{1}{\pi\sigma^2}\right)^{1/4} e^{-\frac{(x-x_0)^2}{2\sigma^2}}, \tag{A.3}$$

with the harmonic oscillator length $\sigma = \sqrt{\frac{\hbar}{m\omega}}$ and trapping frequency $\omega = \sqrt{\frac{2V_0 k^2}{m}}$. We obtain for the experimental parameters $\omega = 2\pi \times 37\,\mathrm{kHz}$ and $\sigma = 60\,\mathrm{nm}$.

We use $p(x) = |\psi(x)|^2$ as a semi-classical approximation of the probability distribution of an atom within a lattice.

References

[1] M. H. Anderson, J. R. Ensher, M. R. Matthews, C. E. Wieman, and E. A. Cornell. Observation of Bose-Einstein Condensation in a Dilute Atomic Vapor. *Science*, **269**, (1995), 198–201.

[2] M. Greiner, O. Mandel, T. Esslinger, T. W. Hänsch, and I. Bloch. Quantum phase transition from a superfluid to a Mott insulator in a gas of ultracold atoms. *Nature*, **415**, (2002), 39–44.

[3] I. Bloch, J. Dalibard, and W. Zwerger. Many-body physics with ultracold gases. *Reviews of Modern Physics*, **80**, (2008), 885–964.

[4] M. Endres, H. Bernien, A. Keesling, H. Levine, E. R. Anschuetz, A. Krajenbrink, C. Senko, V. Vuletić, M. Greiner, and M. D. Lukin. Atom-by-atom assembly of defect-free one-dimensional cold atom arrays. *Science*, **354**, (2016), 1024–1027.

[5] D. Barredo, S. de Léséleuc, V. Lienhard, T. Lahaye, and A. Browaeys. An atom-by-atom assembler of defect-free arbitrary two-dimensional atomic arrays. *Science*, **354**, (2016), 1021–1023.

[6] J. Cirac and P. Zoller. Quantum Computations with Cold Trapped Ions. *Physical Review Letters*, **74**, (1995), 4091–4094.

[7] a. Y. Kitaev. Fault-tolerant quantum computation by anyons. *Annals of Physics*, **303**, (2003), 2–30.

[8] C. Nayak, S. H. Simon, A. Stern, M. Freedman, and S. Das Sarma. Non-Abelian anyons and topological quantum computation. *Reviews of Modern Physics*, **80**, (2008), 1083–1159.

[9] M. Saffman. Quantum computing with atomic qubits and Rydberg interactions: progress and challenges. *Journal of Physics B: Atomic, Molecular and Optical Physics*, **49**, (2016), 202001.

[10] H. Bernien, S. Schwartz, A. Keesling, H. Levine, A. Omran, H. Pichler, S. Choi, A. S. Zibrov, M. Endres, M. Greiner, V. Vuletić, and M. D. Lukin. Probing many-body dynamics on a 51-atom quantum simulator. *Nature*, **551**, (2017), 579–584.

[11] J. Zhang, G. Pagano, P. W. Hess, A. Kyprianidis, P. Becker, H. Kaplan, A. V. G. Z.-X. Gong, and C. Monroe. Observation of a many-body dynamical phase transition with a 53-qubit quantum simulator. *Nature*, **551**, (2017), 601–604.

[12] C. Gross and I. Bloch. Quantum simulations with ultracold atoms in optical lattices. *Science*, **357**, (2017), 995–1001.

[13] T. F. Gallagher. *Rydberg Atoms*. Cambridge, England: Cambridge University Press, 1994. isbn: 9780511524530.

[14] T. Peyronel, O. Firstenberg, Q.-Y. Liang, S. Hofferberth, A. V. Gorshkov, T. Pohl, M. D. Lukin, and V. Vuletić. Quantum nonlinear optics with single photons enabled by strongly interacting atoms. *Nature*, **488**, (2012), 57–60.

[15] O. Firstenberg, T. Peyronel, Q.-Y. Liang, A. V. Gorshkov, M. D. Lukin, and V. Vuletić. Attractive photons in a quantum nonlinear medium. *Nature*, **502**, (2013), 71–75.

[16] S. Baur, D. Tiarks, G. Rempe, and S. Dürr. Single-Photon Switch Based on Rydberg Blockade. *Physical Review Letters*, **112**, (2014), 073901.

[17] C. Tresp, C. Zimmer, I. Mirgorodskiy, H. Gorniaczyk, A. Paris-Mandoki, and S. Hofferberth. Single-Photon Absorber Based on Strongly Interacting Rydberg Atoms. *Physical Review Letters*, **117**, (2016), 223001.

[18] C. H. Greene, A. S. Dickinson, and H. R. Sadeghpour. Creation of Polar and Nonpolar Ultra-Long-Range Rydberg Molecules. *Physical Review Letters*, **85**, (2000), 2458–2461.

[19] M. Schlagmüller, T. C. Liebisch, F. Engel, K. S. Kleinbach, F. Böttcher, U. Hermann, K. M. Westphal, A. Gaj, R. Löw, S. Hofferberth, T. Pfau, J. Pérez-Ríos, and C. H. Greene. Ultracold Chemical Reactions of a Single Rydberg Atom in a Dense Gas. *Physical Review X*, **6**, (2016), 031020.

[20] T. Niederprüm, O. Thomas, T. Eichert, C. Lippe, J. Pérez-Ríos, C. H. Greene, and H. Ott. Observation of pendular butterfly Rydberg molecules. *Nature Communications*, **7**, (2016), 12820.

[21] P. Schauss, M. Cheneau, M. Endres, T. Fukuhara, S. Hild, A. Omran, T. Pohl, C. Gross, S. Kuhr, and I. Bloch. Observation of spatially ordered structures in a two-dimensional Rydberg gas. *Nature*, **491**, (2012), 87–91.

[22] H. Labuhn, D. Barredo, S. Ravets, S. de Léséleuc, T. Macrì, T. Lahaye, and A. Browaeys. Tunable two-dimensional arrays of single Rydberg atoms for realizing quantum Ising models. *Nature*, **534**, (2016), 667–670.

[23] D. Jaksch, J. I. Cirac, P. Zoller, S. L. Rolston, R. Côté, and M. D. Lukin. Fast Quantum Gates for Neutral Atoms. *Physical Review Letters*, **85**, (2000), 2208–2211.

[24] M. D. Lukin, M. Fleischhauer, R. Cote, L. M. Duan, D. Jaksch, J. I. Cirac, and P. Zoller. Dipole Blockade and Quantum Information Processing in Mesoscopic Atomic Ensembles. *Physical Review Letters*, **87**, (2001), 037901.

[25] C. Ates, T. Pohl, T. Pattard, and J. M. Rost. Antiblockade in Rydberg Excitation of an Ultracold Lattice Gas. *Physical Review Letters*, **98**, (2007), 23002.

[26] T. Amthor, C. Giese, C. S. Hofmann, and M. Weidemüller. Evidence of Antiblockade in an Ultracold Rydberg Gas. *Physical Review Letters*, **104**, (2010), 013001.

[27] M. Fleischhauer. Intensivkurs: Offene Quantensysteme. 2016.

[28] H. J. Carmichael. *Statistical Methods in Quantum Optics 1: Master Equations and Fokker-Planck Equations.* Springer Berlin Heidelberg, 1999. isbn: 978-3-540-54882-9.

[29] H.-P. Breuer and F. Petruccione. *The Theory of Open Quantum Systems.* Oxford University Press, 2007. isbn: 9780199213900.

[30] C. Gerry and P. Knight. *Introductory Quantum Optics.* Cambridge University Press, 2005. isbn: 9780521527354.

[31] C. Ates, T. Pohl, T. Pattard, and J. M. Rost. Many-body theory of excitation dynamics in an ultracold Rydberg gas. *Physical Review A*, **76**, (2007), 013413.

[32] M. Höning, D. Muth, D. Petrosyan, and M. Fleischhauer. Steady-state crystallization of Rydberg excitations in an optically driven lattice gas. *Physical Review A*, **87**, (2013), 023401.

[33] D. Petrosyan, M. Höning, and M. Fleischhauer. Spatial correlations of Rydberg excitations in optically driven atomic ensembles. *Physical Review A*, **87**, (2013), 053414.

[34] M. Hoening. *Many-body phases of open Rydberg systems and signatures of topology in quantum gases.* PhD thesis. Technischen Universitaet Kaiserslautern, 2014.

[35] A. Gaj, A. T. Krupp, J. B. Balewski, R. Löw, S. Hofferberth, and T. Pfau. From molecular spectra to a density shift in dense Rydberg gases. *Nature Communications*, **5**, (2014), 4546.

[36] T. M. Weber, M. Höning, T. Niederprüm, T. Manthey, O. Thomas, V. Guarrera, M. Fleischhauer, G. Barontini, and H. Ott. Mesoscopic Rydberg-blockaded ensembles in the superatom regime and beyond. *Nature Physics*, **11**, (2015), 157–161.

[37] A. Browaeys, D. Barredo, and T. Lahaye. Experimental investigations of dipole–dipole interactions between a few Rydberg atoms. *Journal of Physics B: Atomic, Molecular and Optical Physics*, **49**, (2016), 152001.

[38] M. Saffman, T. G. Walker, and K. Mølmer. Quantum information with Rydberg atoms. *Reviews of Modern Physics*, **82**, (2010), 2313–2363.

[39] I. Mourachko, D. Comparat, F. de Tomasi, A. Fioretti, P. Nosbaum, V. M. Akulin, and P. Pillet. Many-Body Effects in a Frozen Rydberg Gas. *Physical Review Letters*, **80**, (1998), 253–256.

[40] L. Béguin, a. Vernier, R. Chicireanu, T. Lahaye, and a. Browaeys. Direct Measurement of the van der Waals Interaction between Two Rydberg Atoms. *Physical Review Letters*, **110**, (2013), 263201.

[41] J. Honer, R. Löw, H. Weimer, T. Pfau, and H. P. Büchler. Artificial Atoms Can Do More Than Atoms: Deterministic Single Photon Subtraction from Arbitrary Light Fields. *Physical Review Letters*, **107**, (2011), 093601.

[42] D. Petrosyan, J. Otterbach, and M. Fleischhauer. Electromagnetically induced transparency with Rydberg atoms. *Physical Review Letters*, **107**, (2011), 213601.

[43] R. Heidemann, U. Raitzsch, V. Bendkowsky, B. Butscher, R. Löw, L. Santos, and T. Pfau. Evidence for Coherent Collective Rydberg Excitation in the Strong Blockade Regime. *Physical Review Letters*, **99**, (2007), 163601.

[44] Y. O. Dudin, L. Li, F. Bariani, and A. Kuzmich. Observation of coherent many-body Rabi oscillations. *Nature Physics*, **8**, (2012), 790–794.

[45] M. Ebert, M. Kwon, T. G. Walker, and M. Saffman. Coherence and Rydberg Blockade of Atomic Ensemble Qubits. *Physical Review Letters*, **115**, (2015), 093601.

[46] S. Ravets, H. Labuhn, D. Barredo, L. Béguin, T. Lahaye, and A. Browaeys. Coherent dipole–dipole coupling between two single Rydberg atoms at an electrically-tuned Förster resonance. *Nature Physics*, **10**, (2014), 914–917.

[47] S. de Léséleuc, D. Barredo, V. Lienhard, A. Browaeys, and T. Lahaye. Optical Control of the Resonant Dipole-Dipole Interaction between Rydberg Atoms. *Physical Review Letters*, **119**, (2017), 053202.

[48] J. Jain. *Composite fermions.* Cambridge University Press, 2007. isbn: 9780521862325.

[49] Z. Ezawa. *Quantum Hall Effects: Field Theoretical Approach and Related Topics.* World Scientific, 2008. isbn: 9789812700322.

[50] K. V. Klitzing, G. Dorda, and M. Pepper. New method for high-accuracy determination of the fine-structure constant based on quantized hall resistance. *Physical Review Letters*, **45**, (1980), 494–497.

[51] D. C. Tsui, H. L. Stormer, and a. C. Gossard. Two-Dimensional Magnetotransport in the Extreme Quantum Limit. *Physical Review Letters*, **48**, (1982), 1559–1562.

[52] H. Stormer. Nobel Lecture: The fractional quantum Hall effect. *Reviews of Modern Physics*, **71**, (1999), 875–889.

[53] F. D. M. Haldane. Fractional quantization of the hall effect: A hierarchy of incompressible quantum fluid states. *Physical Review Letters*, **51**, (1983), 605–608.

[54] R. B. Laughlin. Anomalous quantum Hall effect: An incompressible quantum fluid with fractionally charged excitations. *Physical Review Letters*, **50**, (1983), 1395–1398.

[55] N. R. Cooper and N. K. Wilkin. Composite fermion description of rotating Bose-Einstein condensates. *Physical Review B*, **60**, (1999), R16279–R16282.

[56] N. K. Wilkin and J. M. F. Gunn. Condensation of “Composite Bosons” in a Rotating BEC. *Physical Review Letters*, **84**, (2000), 6–9.

[57] S. Sachdev. *Quantum Phase Transitions.* 2nd ed. Cambridge University Press, 2011. isbn: 9780521514682.

[58] F. Schwabl. *Statistische Mechanik.* 3rd ed. Springer-Verlag Berlin Heidelberg, 2006. isbn: 978-3-540-31095-2.

[59] M. Hoening, W. Abdussalam, M. Fleischhauer, and T. Pohl. Antiferromagnetic long-range order in dissipative Rydberg lattices. *Physical Review A*, **90**, (2014), 021603.

[60] E. Kapit, M. Hafezi, and S. H. Simon. Induced Self-Stabilization in Fractional Quantum Hall States of Light. *Physical Review X*, **4**, (2014), 031039.

[61] S. Diehl, A. Tomadin, A. Micheli, R. Fazio, and P. Zoller. Dynamical Phase Transitions and Instabilities in Open Atomic Many-Body Systems. *Physical Review Letters*, **105**, (2010), 015702.

[62] E. M. Kessler, G. Giedke, A. Imamoglu, S. F. Yelin, M. D. Lukin, and J. I. Cirac. Dissipative phase transition in a central spin system. *Physical Review A*, **86**, (2012), 012116.

[63] K. Mølmer, Y. Castin, and J. Dalibard. Monte Carlo wave-function method in quantum optics. *Journal of the Optical Society of America B*, **10**, (1993), 524.

[64] W. Casteels, R. Fazio, and C. Ciuti. Critical dynamical properties of a first-order dissipative phase transition. *Physical Review A*, **95**, (2017), 012128.

[65] J. J. Mendoza-Arenas, S. R. Clark, S. Felicetti, G. Romero, E. Solano, D. G. Angelakis, and D. Jaksch. Beyond mean-field bistability in driven-dissipative lattices: Bunching-antibunching transition and quantum simulation. *Physical Review A*, **93**, (2016), 023821.

[66] J. Jin, A. Biella, O. Viyuela, L. Mazza, J. Keeling, R. Fazio, and D. Rossini. Cluster Mean-Field Approach to the Steady-State Phase Diagram of Dissipative Spin Systems. *Physical Review X*, **6**, (2016), 031011.

[67] H. Weimer. Variational Principle for Steady States of Dissipative Quantum Many-Body Systems. *Physical Review Letters*, **114**, (2015), 040402.

[68] H. Weimer. Variational analysis of driven-dissipative Rydberg gases. *Physical Review A*, **91**, (2015), 063401.

[69] M. F. Maghrebi and A. V. Gorshkov. Nonequilibrium many-body steady states via Keldysh formalism. *Physical Review B*, **93**, (2016), 014307.

[70] L. M. Sieberer, M. Buchhold, and S. Diehl. Keldysh field theory for driven open quantum systems. *Reports on Progress in Physics*, **79**, (2016), 096001.

[71] M. Buchhold, B. Everest, M. Marcuzzi, I. Lesanovsky, and S. Diehl. Nonequilibrium effective field theory for absorbing state phase transitions in driven open quantum spin systems. *Physical Review B*, **95**, (2017), 014308.

[72] C. Ates, B. Olmos, J. P. Garrahan, and I. Lesanovsky. Dynamical phases and intermittency of the dissipative quantum Ising model. *Physical Review A*, **85**, (2012), 043620.

[73] T. E. Lee, S. Gopalakrishnan, and M. D. Lukin. Unconventional magnetism via optical pumping of interacting spin systems. *Physical Review Letters*, **110**, (2013), 257204.

[74] M. Marcuzzi, E. Levi, S. Diehl, J. P. Garrahan, and I. Lesanovsky. Universal Nonequilibrium Properties of Dissipative Rydberg Gases. *Physical Review Letters*, **113**, (2014), 210401.

[75] N. Lang and H. P. Büchler. Exploring quantum phases by driven dissipation. *Physical Review A*, **92**, (2015), 012128.

[76] R. M. Wilson, K. W. Mahmud, A. Hu, A. V. Gorshkov, M. Hafezi, and M. Foss-Feig. Collective phases of strongly interacting cavity photons. *Physical Review A*, **94**, (2016), 033801.

[77] D. W. Schönleber, M. Gärttner, and J. Evers. Coherent versus incoherent excitation dynamics in dissipative many-body Rydberg systems. *Physical Review A*, **89**, (2014), 033421.

[78] P. D. Drummond and D. F. Walls. Quantum theory of optical bistability. I. Nonlinear polarisability model. *Journal of Physics A: Mathematical and General*, **13**, (1999), 725–741.

[79] W. Casteels and C. Ciuti. Quantum entanglement in the spatial-symmetry-breaking phase transition of a driven-dissipative Bose-Hubbard dimer. *Physical Review A*, **95**, (2017), 013812.

[80] W. Casteels and M. Wouters. Optically bistable driven-dissipative Bose-Hubbard dimer: Gutzwiller approaches and entanglement. *Physical Review A*, **95**, (2017), 043833.

[81] M. Foss-Feig, P. Niroula, J. T. Young, M. Hafezi, A. V. Gorshkov, R. M. Wilson, and M. F. Maghrebi. Emergent equilibrium in many-body optical bistability. *Physical Review A*, **95**, (2017), 043826.

[82] M. Foss-Feig, J. T. Young, V. V. Albert, A. V. Gorshkov, and M. F. Maghrebi. Solvable Family of Driven-Dissipative Many-Body Systems. *Physical Review Letters*, **119**, (2017), 190402.

[83] I. Lesanovsky and J. P. Garrahan. Kinetic Constraints, Hierarchical Relaxation, and Onset of Glassiness in Strongly Interacting and Dissipative Rydberg Gases. *Physical Review Letters*, **111**, (2013), 215305.

[84] M. M. Valado, C. Simonelli, M. D. Hoogerland, I. Lesanovsky, J. P. Garrahan, E. Arimondo, D. Ciampini, and O. Morsch. Experimental observation of controllable kinetic constraints in a cold atomic gas. *Physical Review A*, **93**, (2016), 040701.

[85] B. Everest, M. Marcuzzi, J. P. Garrahan, and I. Lesanovsky. Emergent kinetic constraints in open quantum systems. *Physical Review E*, **94**, (2016), 052108.

[86] M. Marcuzzi, M. Buchhold, S. Diehl, and I. Lesanovsky. Absorbing State Phase Transition with Competing Quantum and Classical Fluctuations. *Physical Review Letters*, **116**, (2016), 245701.

[87] R. Gutierrez, C. Simonelli, M. Archimi, F. Castellucci, E. Arimondo, D. Ciampini, M. Marcuzzi, I. Lesanovsky, and O. Morsch. Experimental signatures of an absorbing-state phase transition in an open driven many-body quantum system. *Physical Review A*, **96**, (2017), 041602.

[88] C. Pérez-Espigares, M. Marcuzzi, R. Gutiérrez, and I. Lesanovsky. Epidemic dynamics in open quantum spin systems. *Physical Review Letters*, **119**, (2017), 140401.

[89] I. Lesanovsky and J. P. Garrahan. Out-of-equilibrium structures in strongly interacting Rydberg gases with dissipation. *Physical Review A*, **90**, (2014), 011603.

[90] A. Urvoy, F. Ripka, I. Lesanovsky, D. Booth, J. P. Shaffer, T. Pfau, and R. Löw. Strongly Correlated Growth of Rydberg Aggregates in a Vapor Cell. *Physical Review Letters*, **114**, (2015), 203002.

[91] C. Simonelli, M. M. Valado, G. Masella, L. Asteria, E. Arimondo, D. Ciampini, and O. Morsch. Seeded excitation avalanches in off-resonantly driven Rydberg gases. *Journal of Physics B: Atomic, Molecular and Optical Physics*, **49**, (2016), 154002.

[92] H. Schempp, G. Günter, M. Robert-de-Saint-Vincent, C. S. Hofmann, D. Breyel, A. Komnik, D. W. Schönleber, M. Gärttner, J. Evers, S. Whitlock, and M. Weidemüller. Full Counting Statistics of Laser Excited Rydberg Aggregates in a One-Dimensional Geometry. *Physical Review Letters*, **112**, (2014), 013002.

[93] N. Malossi, M. M. Valado, S. Scotto, P. Huillery, P. Pillet, D. Ciampini, E. Arimondo, and O. Morsch. Full Counting Statistics and Phase Diagram of a Dissipative Rydberg Gas. *Physical Review Letters*, **113**, (2014), 023006.

[94] C. Carr, R. Ritter, C. G. Wade, C. S. Adams, and K. J. Weatherill. Nonequilibrium Phase Transition in a Dilute Rydberg Ensemble. *Physical Review Letters*, **111**, (2013), 113901.

[95] N. R. de Melo, C. G. Wade, N. Šibalić, J. M. Kondo, C. S. Adams, and K. J. Weatherill. Intrinsic optical bistability in a strongly driven Rydberg ensemble. *Physical Review A*, **93**, (2016), 063863.

[96] D. S. Ding, C. S. Adams, B. S. Shi, and G. C. Guo. Non-equilibrium phase-transitions in multi-component Rydberg gases (2016), 5. arXiv: 1606.08791.

[97] D. Weller, A. Urvoy, A. Rico, R. Löw, and H. Kübler. Charge-induced optical bistability in thermal Rydberg vapor. *Physical Review A*, **94**, (2016), 063820.

[98] N. Šibalić, C. G. Wade, C. S. Adams, K. J. Weatherill, and T. Pohl. Driven-dissipative many-body systems with mixed power-law interactions: Bistabilities and temperature-driven nonequilibrium phase transitions. *Physical Review A*, **94**, (2016), 011401.

[99] K. Macieszczak, M. Guta, I. Lesanovsky, and J. P. Garrahan. Towards a Theory of Metastability in Open Quantum Dynamics. *Physical Review Letters*, **116**, (2016), 240404.

[100] D. C. Rose, K. Macieszczak, I. Lesanovsky, and J. P. Garrahan. Metastability in an open quantum Ising model. *Physical Review E*, **94**, (2016), 052132.

[101] G. Lindblad and G. On the generators of quantum dynamical semigroups. *Communications in Mathematical Physics*, **48**, (1976), 119–130.

[102] E. Davies. *Quantum Theory of Open Systems.* London: Academic Press, 1976, 171. isbn: 0122061500.

[103] H. Spohn. Approach to equilibrium for completely positive dynamical semigroups of N-level systems. *Reports on Mathematical Physics*, **10**, (1976), 189–194.

[104] H. Spohn. An algebraic condition for the approach to equilibrium of an open N-level system. *Letters in Mathematical Physics*, **2**, (1977), 33–38.

[105] S. Wolff, A. Sheikhan, and C. Kollath. Dissipative time evolution of a chiral state after a quantum quench. *Physical Review A*, **94**, (2016), 043609.

[106] P. A. Pearce and K. A. Seaton. A classical theory of hard squares. *Journal of Statistical Physics*, **53**, (1988), 1061–1072.

[107] H. C. M. Fernandes, J. J. Arenzon, and Y. Levin. Monte Carlo simulations of two-dimensional hard core lattice gases. *Journal of Chemical Physics*, **126**, (2007), 114508.

[108] T. Nath and R. Rajesh. Multiple phase transitions in extended hard-core lattice gas models in two dimensions. *Physical Review E*, **90**, (2014), 012120.

[109] P. C. Hohenberg and B. I. Halperin. Theory of dynamic critical phenomena. *Reviews of Modern Physics*, **49**, (1977), 435.

[110] M. P. Nightingale and H. W. J. Blöte. Dynamic Exponent of the Two-Dimensional Ising Model and Monte Carlo Computation of the Subdominant Eigenvalue of the Stochastic Matrix. *Physical Review Letters*, **76**, (1996), 4548–4551.

[111] K. Binder. Finite size scaling analysis of ising model block distribution functions. *Zeitschrift für Physik B Condensed Matter*, **43**, (1981), 119–140.

[112] K. Binder. Monte Carlo calculation of the surface tension for two- and three-dimensional lattice-gas models. *Physical Review A*, **25**, (1982), 1699–1709.

[113] S. Miyashita and H. Takano. Dynamical Nature of the Phase Transition of the Two-Dimensional Kinetic Ising Model. *Progress of Theoretical Physics*, **73**, (1985), 1122–1140.

[114] T. E. Lee, H. Häffner, and M. C. Cross. Collective Quantum Jumps of Rydberg Atoms. *Physical Review Letters*, **108**, (2012), 023602.

[115] V. R. Overbeck, M. F. Maghrebi, A. V. Gorshkov, and H. Weimer. Multicritical behavior in dissipative Ising models. *Physical Review A*, **95**, (2017), 042133.

[116] W. Li, C. Ates, and I. Lesanovsky. Nonadiabatic Motional Effects and Dissipative Blockade for Rydberg Atoms Excited from Optical Lattices or Microtraps. *Physical Review Letters*, **110**, (2013), 213005.

[117] T. Macrì and T. Pohl. Rydberg dressing of atoms in optical lattices. *Physical Review A*, **89**, (2014), 011402.

[118] T. Manthey, T. M. Weber, T. Niederprüm, P. Langer, V. Guarrera, G. Barontini, and H. Ott. Scanning electron microscopy of Rydberg-excited Bose–Einstein condensates. *New Journal of Physics*, **16**, (2014), 083034.

[119] M. R. Flannery, D. Vrinceanu, and V. N. Ostrovsky. Long-range interaction between polar Rydberg atoms. *Journal of Physics B: Atomic, Molecular and Optical Physics*, **38**, (2005), S279–S293.

[120] S. Zhang, F. Robicheaux, and M. Saffman. Magic-wavelength optical traps for Rydberg atoms. *Physical Review A*, **84**, (2011), 043408.

[121] M. Gärttner, K. P. Heeg, T. Gasenzer, and J. Evers. Dynamic formation of Rydberg aggregates at off-resonant excitation. *Physical Review A*, **88**, (2013), 043410.

[122] W. Casteels, F. Storme, A. Le Boité, C. Ciuti, A. L. Boit, A. Le Boité, C. Ciuti, and A. L. Boit. Power laws in the dynamic hysteresis of quantum nonlinear photonic resonators. *Physical Review A*, **93**, (2016), 033824.

[123] M. Gärttner, S. Whitlock, D. W. Schönleber, and J. Evers. Collective Excitation of Rydberg-Atom Ensembles beyond the Superatom Model. *Physical Review Letters*, **113**, (2014), 233002.

[124] D. Petrosyan. Two-dimensional crystals of Rydberg excitations in a resonantly driven lattice gas. *Physical Review A*, **88**, (2013), 43431.

[125] P. Schauss, J. Zeiher, T. Fukuhara, S. Hild, M. Cheneau, T. Macri, T. Pohl, I. Bloch, and C. Gross. Crystallization in Ising quantum magnets. *Science*, **347**, (2015), 1455–1458.

[126] J. Zeiher, R. van Bijnen, P. Schauss, S. Hild, J.-y. Choi, T. Pohl, I. Bloch, and C. Gross. Many-body interferometry of a Rydberg-dressed spin lattice. *Nature Physics*, **12**, (2016), 1095–1099.

[127] J. Zeiher, J.-y. Choi, A. Rubio-Abadal, T. Pohl, R. van Bijnen, I. Bloch, and C. Gross. Coherent many-body spin dynamics in a long-range interacting Ising chain. *Physical Review X*, **7**, (2017), 041063.

[128] R. Dumke, M. Volk, T. Müther, F. B. J. Buchkremer, G. Birkl, and W. Ertmer. Micro-optical Realization of Arrays of Selectively Addressable Dipole Traps: A Scalable Configuration for Quantum Computation with Atomic Qubits. *Physical Review Letters*, **89**, (2002), 097903.

[129] P. Würtz, T. Langen, T. Gericke, A. Koglbauer, and H. Ott. Experimental demonstration of single-site addressability in a two-dimensional optical lattice. *Physical Review Letters*, **103**, (2009), 080404.

[130] F. Nogrette, H. Labuhn, S. Ravets, D. Barredo, L. Béguin, A. Vernier, T. Lahaye, and A. Browaeys. Single-Atom Trapping in Holographic 2D Arrays of Microtraps with Arbitrary Geometries. *Physical Review X*, **4**, (2014), 021034.

[131] J. B. Balewski, A. T. Krupp, A. Gaj, D. Peter, H. P. Büchler, R. Löw, S. Hofferberth, and T. Pfau. Coupling a single electron to a Bose–Einstein condensate. *Nature*, **502**, (2013), 664–667.

[132] M. Schlagmüller, T. C. Liebisch, H. Nguyen, G. Lochead, F. Engel, F. Böttcher, K. M. Westphal, K. S. Kleinbach, R. Löw, S. Hofferberth, T. Pfau, J. Pérez-Ríos, and C. H. Greene. Probing an Electron Scattering Resonance using Rydberg Molecules within a Dense and Ultracold Gas. *Physical Review Letters*, **116**, (2016), 053001.

[133] K. Singer, J. Stanojevic, M. Weidemüller, and R. Côté. Long-range interactions between alkali Rydberg atom pairs correlated to the n s– n s, n p– n p and n d– n d asymptotes. *Journal of Physics B: Atomic, Molecular and Optical Physics*, **38**, (2005), S295.

[134] C. Ates and I. Lesanovsky. Entropic enhancement of spatial correlations in a laser-driven Rydberg gas. *Physical Review A*, **86**, (2012), 013408.

[135] M. Mattioli, A. W. Glätzle, and W. Lechner. From classical to quantum non-equilibrium dynamics of Rydberg excitations in optical lattices. *New Journal of Physics*, **17**, (2015), 113039.

[136] K. Singer, M. Reetz-Lamour, T. Amthor, L. G. Marcassa, and M. Weidemüller. Suppression of Excitation and Spectral Broadening Induced by Interactions in a Cold Gas of Rydberg Atoms. *Physical Review Letters*, **93**, (2004), 163001.

[137] U. Raitzsch, R. Heidemann, H. Weimer, B. Butscher, P. Kollmann, R. Löw, H. P. Büchler, and T. Pfau. Investigation of dephasing rates in an interacting Rydberg gas. *New Journal of Physics*, **11**, (2009), 055014.

[138] E. A. Goldschmidt, T. Boulier, R. C. Brown, S. B. Koller, J. T. Young, A. V. Gorshkov, S. L. Rolston, and J. V. Porto. Anomalous Broadening in Driven Dissipative Rydberg Systems. *Physical Review Letters*, **116**, (2016), 113001.

[139] T. Boulier, E. Magnan, C. Bracamontes, J. Maslek, E. A. Goldschmidt, J. T. Young, A. V. Gorshkov, S. L. Rolston, and J. V. Porto. Spontaneous avalanche dephasing in large Rydberg ensembles. *Physical Review A*, **96**, (2017), 053409.

[140] B. G. Richards and R. R. Jones. Dipole-dipole resonance line shapes in a cold Rydberg gas. *Physical Review A*, **93**, (2016), 042505.

[141] J. T. Young, T. Boulier, E. Magnan, E. A. Goldschmidt, R. M. Wilson, S. L. Rolston, J. V. Porto, and A. V. Gorshkov. Dissipation induced dipole blockade and anti-blockade in driven Rydberg systems. *Physical Review A*, **97**, (2017), 023424.

[142] R. Faoro, C. Simonelli, M. Archimi, G. Masella, M. M. Valado, E. Arimondo, R. Mannella, D. Ciampini, and O. Morsch. Van der Waals explosion of cold Rydberg clusters. *Physical Review A*, **93**, (2016), 030701.

[143] M. Mattioli, M. Dalmonte, W. Lechner, and G. Pupillo. Cluster luttinger liquids of Rydberg-dressed atoms in optical lattices. *Physical Review Letters*, **111**, (2013), 165302.

[144] A. W. Glaetzle, M. Dalmonte, R. Nath, I. Rousochatzakis, R. Moessner, and P. Zoller. Quantum spin-ice and dimer models with Rydberg atoms. *Physical Review X*, **4**, (2014), 041037.

[145] D. Petrosyan, B. Schmidt, J. R. Anglin, and M. Fleischhauer. Quantum liquid of repulsively bound pairs of particles in a lattice. *Physical Review A*, **76**, (2007), 033606.

[146] M. Dalmonte, W. Lechner, Z. Cai, M. Mattioli, A. M. Läuchli, and G. Pupillo. Cluster Luttinger liquids and emergent supersymmetric conformal critical points in the one-dimensional soft-shoulder Hubbard model. *Physical Review B*, **92**, (2015), 045106.

[147] R. Blatt and C. F. Roos. Quantum simulations with trapped ions. *Nature Physics*, **8**, (2012), 277–284.

[148] A. A. Houck, H. E. Türeci, and J. Koch. On-chip quantum simulation with superconducting circuits. *Nature Physics*, **8**, (2012), 292–299.

[149] C. Neill, P. Roushan, K. Kechedzhi, S. Boixo, S. V. Isakov, V. Smelyanskiy, R. Barends, B. Burkett, Y. Chen, Z. Chen, B. Chiaro, A. Dunsworth, A. Fowler, B. Foxen, R. Graff, E. Jeffrey, J. Kelly, E. Lucero, A. Megrant, J. Mutus, M. Neeley, C. Quintana, D. Sank, A. Vainsencher, J. Wenner, T. C. White, H. Neven, and J. M. Martinis. A blueprint for demonstrating quantum supremacy with superconducting qubits. *Science*, **360**, (2017), 195–199.

[150] T. Hensgens, T. Fujita, L. Janssen, X. Li, C. J. V. Diepen, C. Reichl, W. Wegscheider, S. D. Sarma, and L. M. K. Vandersypen. Quantum simulation of a Fermi-Hubbard model using a semiconductor quantum dot array. *Nature*, **548**, (2017), 70–73.

[151] T. Fukuhara, P. Schauss, M. Endres, S. Hild, M. Cheneau, I. Bloch, and C. Gross. Microscopic observation of magnon bound states and their dynamics. *Nature*, **502**, (2013), 76–79.

[152] C. S. E. van Ditzhuijzen, A. F. Koenderink, J. V. Hernández, F. Robicheaux, L. D. Noordam, and H. B. v. L. van den Heuvell. Spatially Resolved Observation of Dipole-Dipole Interaction between Rydberg Atoms. *Physical Review Letters*, **100**, (2008), 243201.

[153] G. Günter, H. Schempp, M. Robert-de-Saint-Vincent, V. Gavryusev, S. Helmrich, C. S. Hofmann, S. Whitlock, and M. Weidemüller. Observing the dynamics of dipole-mediated energy transport by interaction-enhanced imaging. *Science*, **342**, (2013), 954–956.

[154] D. Barredo, H. Labuhn, S. Ravets, T. Lahaye, A. Browaeys, and C. S. Adams. Coherent Excitation Transfer in a Spin Chain of Three Rydberg Atoms. *Physical Review Letters*, **114**, (2015), 113002.

[155] A. P. Orioli, A. Signoles, H. Wildhagen, G. Günter, J. Berges, S. Whitlock, and M. Weidemüller. Relaxation of an Isolated Dipolar-Interacting Rydberg Quantum Spin System. *Physical Review Letters*, **120**, (2018), 063601.

[156] I. Bouchoule and K. Mølmer. Spin squeezing of atoms by the dipole interaction in virtually excited Rydberg states. *Physical Review A*, **65**, (2002), 041803.

[157] J. E. Johnson and S. L. Rolston. Interactions between Rydberg-dressed atoms. *Physical Review A*, **82**, (2010), 033412.

[158] K. Winkler, G. Thalhammer, F. Lang, R. Grimm, J. H. Denschlag, A. J. Daley, A. Kantian, H. P. Büchler, and P. Zoller. Repulsively bound atom pairs in an optical lattice. *Nature*, **441**, (2006), 853–856.

[159] R. Piil and K. Mølmer. Tunneling couplings in discrete lattices, single-particle band structure, and eigenstates of interacting atom pairs. *Physical Review A*, **76**, (2007), 023607.

[160] M. Valiente and D. Petrosyan. Two-particle states in the Hubbard model. *Journal of Physics B: Atomic, Molecular and Optical Physics*, **41**, (2008), 161002.

[161] M. Valiente and D. Petrosyan. Scattering resonances and two-particle bound states of the extended Hubbard model. *Journal of Physics B: Atomic, Molecular and Optical Physics*, **42**, (2009), 121001.

[162] Y.-Y. Jau, A. M. Hankin, T. Keating, I. H. Deutsch, and G. W. Biedermann. Entangling atomic spins with a Rydberg-dressed spin-flip blockade. *Nature Physics*, **12**, (2015), 71.

[163] A. W. Glaetzle, M. Dalmonte, R. Nath, C. Gross, I. Bloch, and P. Zoller. Designing Frustrated Quantum Magnets with Laser-Dressed Rydberg Atoms. *Physical Review Letters*, **114**, (2015), 173002.

[164] R. M. W. V. Bijnen, T. Pohl, R. M. W. van Bijnen, and T. Pohl. Quantum Magnetism and Topological Ordering via Rydberg Dressing near Förster Resonances. *Physical Review Letters*, **114**, (2014), 243002.

[165] L. F. Buchmann, K. Mølmer, and D. Petrosyan. Creation and transfer of nonclassical states of motion using Rydberg dressing of atoms in a lattice. *Physical Review A*, **95**, (2017), 013403.

[166] V. Lienhard, S. de Léséleuc, D. Barredo, T. Lahaye, A. Browaeys, M. Schuler, L.-P. Henry, and A. M. Läuchli. Observing the space- and time-dependent growth of correlations in dynamically tuned synthetic Ising antiferromagnets (2017). arXiv: 1711.01185.

[167] M. Aidelsburger, M. Atala, M. Lohse, J. T. Barreiro, B. Paredes, and I. Bloch. Realization of the Hofstadter Hamiltonian with Ultracold Atoms in Optical Lattices. *Physical Review Letters*, **111**, (2013), 185301.

[168] H. Miyake, G. a. Siviloglou, C. J. Kennedy, W. C. Burton, and W. Ketterle. Realizing the Harper Hamiltonian with Laser-Assisted Tunneling in Optical Lattices. *Physical Review Letters*, **111**, (2013), 185302.

[169] J. Struck, C. Olschläger, M. Weinberg, P. Hauke, J. Simonet, A. Eckardt, M. Lewenstein, K. Sengstock, and P. Windpassinger. Tunable gauge potential for neutral and spinless particles in driven optical lattices. *Physical Review Letters*, **108**, (2012), 225304.

[170] G. Jotzu, M. Messer, R. R. Desbuquois, M. Lebrat, T. Uehlinger, D. Greif, and T. Esslinger. Experimental realization of the topological Haldane model with ultracold fermions. *Nature*, **515**, (2014), 237–240.

[171] Z. Wang, Y. Chong, J. D. Joannopoulos, and M. Soljacić. Observation of unidirectional backscattering-immune topological electromagnetic states. *Nature*, **461**, (2009), 772–775.

[172] M. Hafezi, E. Demler, M. Lukin, and J. Taylor. Robust optical delay lines via topological protection. *Nature Physics*, **7**, (2011), 907–912.

[173] M. C. Rechtsman, J. M. Zeuner, Y. Plotnik, Y. Lumer, D. Podolsky, F. Dreisow, S. Nolte, M. Segev, and A. Szameit. Photonic Floquet topological insulators. *Nature*, **496**, (2013), 196–200.

[174] N. Schine, A. Ryou, A. Gromov, A. Sommer, and J. Simon. Synthetic Landau levels for photons. *Nature*, **534**, (2016), 671–675.

[175] J. Ningyuan, C. Owens, A. Sommer, D. Schuster, and J. Simon. Time- and Site-Resolved Dynamics in a Topological Circuit. *Physical Review X*, **5**, (2015), 021031.

[176] A. S. Sørensen, E. Demler, and M. D. Lukin. Fractional quantum hall states of atoms in optical lattices. *Physical Review Letters*, **94**, (2005), 086803.

[177] M. Hafezi, A. S. Sørensen, E. Demler, and M. D. Lukin. Fractional quantum Hall effect in optical lattices. *Physical Review A*, **76**, (2007), 23613.

[178] J. Ningyuan, A. Georgakopoulos, A. Ryou, N. Schine, A. Sommer, and J. Simon. Observation and characterization of cavity Rydberg polaritons. *Physical Review A*, **93**, (2016), 041802.

[179] N. Jia, N. Schine, A. Georgakopoulos, A. Ryou, A. Sommer, and J. Simon. A Strongly Interacting Polaritonic Quantum Dot. *Nature Physics*, (2018).

[180] F. Grusdt and M. Fleischhauer. Fractional quantum Hall physics with ultracold Rydberg gases in artificial gauge fields. *Physical Review A*, **87**, (2012), 043628.

[181] R. O. Umucalilar and I. Carusotto. Fractional Quantum Hall States of Photons in an Array of Dissipative Coupled Cavities. *Physical Review Letters*, **108**, (2012), 206809.

[182] S. Dutta and E. J. Mueller. Coherent generation of photonic fractional quantum Hall states in a cavity and the search for anyonic quasiparticles. *Physical Review A*, **97**, (2018), 033825.

[183] J. R. Abo-Shaeer, C. Raman, J. M. Vogels, and W. Ketterle. Observation of Vortex Lattices in Bose-Einstein Condensates. *Science*, **292**, (2001), 476–479.

[184] V. Schweikhard, I. Coddington, P. Engels, V. P. Mogendorff, and E. A. Cornell. Rapidly Rotating Bose-Einstein Condensates in and near the Lowest Landau Level. *Physical Review Letters*, **92**, (2004), 040404.

[185] J. B. Götte, S. M. Barnett, and M. Padgett. On the dragging of light by a rotating medium. *Proceedings of the Royal Society A: Mathematical, Physical and Engineering Sciences*, **463**, (2007), 2185–2194.

[186] J. Otterbach, J. Ruseckas, R. G. Unanyan, G. Juzeliunas, and M. Fleischhauer. Effective magnetic fields for stationary light. *Physical Review Letters*, **104**, (2010), 33903.

[187] A. Sommer and J. Simon. Engineering photonic Floquet Hamiltonians through Fabry–Pérot resonators. *New Journal of Physics*, **18**, (2016), 035008.

[188] M. Fleischhauer and M. D. Lukin. Dark-State Polaritons in Electromagnetically Induced Transparency. *Physical Review Letters*, **84**, (2000), 5094–5097.

[189] M. Fleischhauer and M. D. Lukin. Quantum memory for photons: Dark-state polaritons. *Physical Review A*, **65**, (2002), 022314.

[190] J. D. Pritchard, D. Maxwell, a. Gauguet, K. J. Weatherill, M. P. a. Jones, and C. S. Adams. Cooperative atom-light interaction in a blockaded Rydberg ensemble. *Physical Review Letters*, **105**, (2010), 193603.

[191] A. V. Gorshkov, J. Otterbach, M. Fleischhauer, T. Pohl, and M. D. Lukin. Photon-photon interactions via Rydberg blockade. *Physical Review Letters*, **107**, (2011), 133602.

[192] P. Bienias, S. Choi, O. Firstenberg, M. F. Maghrebi, M. Gullans, M. D. Lukin, A. V. Gorshkov, and H. P. Büchler. Scattering resonances and bound states for strongly interacting Rydberg polaritons. *Physical Review A*, **90**, (2014), 053804.

[193] A. Sommer, H. P. Büchler, and J. Simon. Quantum Crystals and Laughlin Droplets of Cavity Rydberg Polaritons (2015). arXiv: 1506.00341.

[194] Y.-H. Wu, H.-H. Tu, and G. J. Sreejith. Fractional quantum Hall states of bosons on cones. *Physical Review A*, **96**, (2017), 033622.

[195] R. B. Laughlin. Quantized Hall Conductivity in 2 Dimensions. *Physical Review B*, **23**, (1981), 5632–5633.

[196] N. V. Vitanov, A. A. Rangelov, B. W. Shore, and K. Bergmann. Stimulated Raman adiabatic passage in physics, chemistry, and beyond. *Reviews of Modern Physics*, **89**, (2017), 015006.

[197] M. Andersen, C. Ryu, P. Cladé, V. Natarajan, A. Vaziri, K. Helmerson, and W. Phillips. Quantized Rotation of Atoms from Photons with Orbital Angular Momentum. *Physical Review Letters*, **97**, (2006), 170406.

[198] M. O. Scully and M. S. Zubairy. *Quantum Optics*. Cambridge University Press, 1997.

Lebenslauf

Persönliche Angaben

Name	Fabian David Letscher
Geburt	21.07.1989 in Ruthweiler
Familienstand	verheiratet
Staatsangehörigkeit	Deutsch

Studium und Ausbildung

10/2014 – 05/2018 **Promotionsstudium in der Arbeitsgruppe von Prof. Dr. M. Fleischhauer**
Technische Universität Kaiserslautern

- Stipendiat der Graduate School of Excellence Materials Science in Mainz
- Angestrebter Abschluss: Dr. rer. nat.

10/2009 – 09/2014 **Studium der Physik**
Technische Universität Kaiserslautern

- Schwerpunkt theoretische Physik mit Nebenfach Mathematik
- Diplomarbeit: *„Topologische Zustände in bosonischen Gittermodellen“* mit Note: 1.0
- Abschluss Diplom mit Abschlussnote: 1.1

08/2000 – 03/2009 **Allgemeine Hochschulreife**
Gymansium Ramstein-Miesenbach

- Abschluss Abitur mit Abschlussnote: 1.7

Berufserfahrung

seit 10/2014 **wissenschaftlicher Mitarbeiter – Promotionsstudent**
Technische Universität Kaiserslautern, Fachbereich Physik

04/2012 – 09/2013 **wissenschaftliche Hilfskraft**
Technische Universität Kaiserslautern, Fachbereich Physik

Qualifikationen

Sprachen	Deutsch (Muttersprache) Englisch (verhandlungssicher) Französisch (Grundkenntnisse)
Anwendungen	MatLab (sehr gut) Mathematica (gut) Latex (gut) Microsoft Office (gut)

Danksagung

Eine Promotion ist ein langer und teils auch beschwerlicher Weg, den man nicht alleine geht. Auf dem Pfad zu einem erfolgreichen Abschluss haben mich viele Menschen begleitet. An dieser Stelle möchte ich mich bei ihnen bedanken.

Allen voran bedanke ich mich bei meinem Doktorvater, Michael Fleischhauer, der mich stets in höchstem Maße unterstützt und gefördert hat. Für meine persönliche Entwicklung war Michael weitaus mehr als nur ein Richtungsweiser. Ich schätze das mir entgegengebrachte Vertrauen sehr und bedanke mich für die wundervollen und lehrreichen Jahre in guter Zusammenarbeit. Danke!

Ich danke David Petrosyan für die unentbehrlichen Diskussionen über die Welt der Rydberg-Atome und die hervorragende Gastfreundschaft während meines Aufenthalts in Heraklion. Mir hat unsere Zusammenarbeit sehr viel Freude bereitet.

Ich bedanke mich ebenso bei meinem Zweitgutachter, Herwig Ott, und meinem Drittgutachter, Igor Lesanovsky für ihre Unterstützung. Insbesondere die gute Zusammenarbeit mit der Arbeitsgruppe von Herwig Ott half mir in der Anfangsphase meiner Promotion den Blick auf den *Ryd-Berg* zu schärfen. Ich danke Thomas Niederprüm, Oliver Thomas, Tanita Eichert und Carsten Lippe.

Auf dem Weg zum Gipfel gibt es viele Stolpersteine, die ich gemeinsam mit der Arbeitsgruppe von Michael Fleischhauer aus dem Weg geräumt habe. Ich bedanke mich für die schöne gemeinsame Zeit, die vielen Anregungen und die große Unterstützung. Gerne möchte ich an dieser Stelle Nikolai Lauk, Matthias Moos und Razmik Unanyan nennen. Ebenso danke ich Christina Jörg für die zahlreichen Diskussionen über die Topologie in Wellenleitern. Ich bedanke mich bei der Graduiertenschule Materials Science in Mainz für deren Unterstützung und den Blick über den Tellerrand, wie etwa durch das Mentorenprogramm.

Zu guter Letzt bedanke ich mich bei meiner Familie und bei meinen Freunden. Ich danke Martin für unsere gemeinsame Zeit. Ihr seid Motivation und Ansporn diesen Weg zu gehen. Ich danke euch! Den Erfolg den Gipfel zu erreichen teile ich mit euch.